AN X-RAY AND NEUTRON SCATTERING STUDY OF AMORPHOUS HYDROGENATED CARBON

A THESIS SUBMITTED TO

THE UNIVERSITY OF KENT AT CANTERBURY

IN THE SUBJECT OF PHYSICS

FOR THE DEGREE

OF DOCTOR OF PHILOSOPHY.

By

Theresa Mary Burke

September 1994

For my mother

Abstract

A series of thin film and powder samples of amorphous hydrogenated carbon (a-C:H) have been deposited in a fast atom source, from one of three hydrocarbon precursor gases, at a deposition energy ranging between 0.5keV and 1.2keV. Neutron scattering studies, sensitive to both the carbon and hydrogen environments, have been carried out on three of these samples, deposited at the same impact energy, having varying degrees of isotopic enrichment. The measured scattering profiles have been used to derive the partial C-C, C-H and H-H correlation functions for the material, affording an insight into the structural configuration of this phase of a-C:H of unique clarity. Complementary X-ray diffraction measurements, dominated by contributions from the carbon matrix, have been made on these isotopically substituted samples and two further samples deposited at a lower deposition energy. A structural reconfiguration from a graphite-like, highly trigonally bonded network, to a more diamond-like atomic arrangement has been observed as the deposition energy falls, accompanied by a progressive change in the void structure. X-ray diffraction studies have also been made of two samples of a-C:H, deposited from the same precursor gas, at impact energies of 0.5keV and 0.85keV. Again a breakdown in the intra- and inter- layer graphite-like structural arrangement has been found to occur as the deposition energy decreases.

The Warren-Mavel fluorescence detection technique has been used to remove the incoherent scattering contribution to the measured X-ray scattering profiles and has been shown to be highly efficient at the removal of such contributions when used in conjunction with a synchrotron X-ray source. In fact, this technique has been so successful that it has highlighted the problem of obtaining suitable theoretical self scattering curves for the coherent data accessed.

Preliminary studies on a novel glancing angle X-ray diffraction technique for the *in situ* analysis of thin film samples of a-C:H, mounted on a crystalline substrate, have been carried out. Two films have been studied, and early results have been encouraging, showing that not only can scattering profiles be collected for these low Z, amorphous systems from films 1μm thick, but that depth profiling of the thin film/substrate system is also possible.

Acknowledgements

There are many people who have contributed significantly, either directly or indirectly to the following work and I only hope that I can do all of them justice in the following paragraphs.

I would like to thank my supervisor, Dr. R. J Newport, for his continued guidance and support and for working well beyond the call of duty throughout this project. I am greatly indebted to both Jane and Michelle for their proof reading, helpful comments, sense of humour, provision of a bed and above all friendship. My thanks must go to Phillip, Mark and Adrian for their enjoyable company and for keeping me laughing. Thanks must also go to Dave, Ashley, Jennifer and to all members of the X-ray and neutron scattering group, both past and present, for their support and friendship.

I would like to thank Tania Noddings for her continual encouragement and my huge telephone bill. Thanks are also due to Andrew Floyd for the use of the cottage.

For helping me to keep the plasma system out of intensive care, my thanks must go to Don Riley, Ken Stevens and all the guys in both the mechanical and electronics workshops. Thanks are due to Joe Franks and Peter Revell of Ion Tech Ltd. for supplying some of the a-C:H samples used in this work, and to Dr. J. Wilson for the thin film polycrystalline diamond sample. For analysing the samples, I would like to thank Tony Fassam (UKC) and Chris Jeynes (Surrey). I gratefully acknowledge receipt of an SERC grant which has made this work possible.

I would like to take this opportunity to thank my parents, Sylvia and Trevor Evans, for their unending support, both emotional and financial, throughout my university career. My thanks must also go to Eileen and Donald Smith for acting as a substitute family in their absence.

Finally, my eternal gratitude must go to Simon for his endless support, encouragement, love and patience throughout the writing of this thesis.

Contents

List of Tables

List of Figures

Chapter 1

Introduction

A particularly active area of solid-state physics research over the last decade has been in the field of non-crystalline, or amorphous, materials. These systems display no long range order in their atomic scale structure and, therefore, cannot be described by the mathematical methods (such as Brillouin zones and Bloch states) available to the crystallographer. The key to the macroscopic properties displayed by such materials lies in their atomic scale bonding configuration and it is only through a detailed analysis of the latter that these phases can be fully understood. Amorphous materials have proved of great interest not only in the context of the fundamental physics questions that they pose, but also from a technological viewpoint. The properties of such materials are critically dependent upon their formation conditions [1, 2] and much work has been carried out on the characterisation and optimisation of the many techniques used for their production [3, 4]. The formation of an amorphous solid is an almost universal property of condensable matter. What is required is to cool the material at a suitably fast rate such that nucleation and growth of crystallites is prevented from occurring and the disordered structure of the condensing species is

effectively "frozen in". Minimisation of the total energy associated with the material structure to that of the crystalline state cannot therefore occur and the system is forced into a local metastable energy minimum. For covalently bonded amorphous materials the resulting interatomic bond lengths are found to be close to that of the crystalline material, but disorder is introduced into the bond angle (that between an atom and two of its nearest neighbours) and the dihedral angle (the angle measured between the plane of two neighbouring bonds) distribution [5]. Typically a bond angle variation of 10% from the corresponding crystalline materials occurs, and the dihedral angle moves from a single value (or a well defined set of values) in the crystalline case to a more uniform distribution.

Much work has been carried out on amorphous hydrogenated silicon, a-Si:H, due to its many possible electronic applications [3]. In this work a structural study of the analogous material amorphous hydrogenated carbon, a-C:H, is carried out. The variety of bonding configurations open to carbon are detailed in Chapter (2). As the number of bonding types available to this atom type is greater than for silicon, the number and complexity of possible a-C:H phases is greatly increased. In Chapter (2) a survey of the preparation and properties of amorphous carbons and amorphous hydrogenated carbons is presented. As part of this work, a fast atom source has been commissioned and a series of a-C:H samples produced, so that structural investigations into several phases of this family of materials could be carried out and the interplay between atomic composition and deposition conditions further elucidated. Details on the fast atom source used and the production technique for each of the a-C:H samples, is given in Chapter (3).

Both thin film and powder samples of a-C:H were deposited, and in Chapter (7) preliminary results on a novel glancing angle X-ray diffraction technique for the *in*

situ structural analysis of the thin film samples is described. The powder samples deposited have been studied using X-ray and neutron scattering techniques to provide complementary information on both the carbon and hydrogen network within these materials. Neutron scattering, carried out on the Rutherford Appleton Laboratory's pulsed neutron source, ISIS, is sensitive to both the carbon and hydrogen within the materials and provides information on the bonding environment of both. X-ray scattering, carried out at the Daresbury Laboratory synchrotron radiation source (SRS), provides structural information dominated by the carbon matrix. Chapter (4) details the theory of neutron and X-ray scattering techniques carried out in this work. In Chapter (5) the X-ray diffraction experimental techniques used are described and the Warren-Mavel fluorescence detection technique, used to remove the incoherent scattering contribution to the data, is introduced. Chapter (6) gives an account of the neutron scattering experimental techniques carried out, including efforts made to minimise the inelastic scattering contributions to the measured data. Such contributions to the neutron scattering data can be particularly problematic for hydrogenous systems and are discussed in detail.

In Chapter (8) the results obtained by neutron diffraction are presented and discussed in the context of present models for the system. In particular, details are given on the use of isotopically substituted samples, deposited in the fast atom source, to extract the partial correlation functions for both the carbon and hydrogen within the material, affording a structural insight into a-C:H of unique clarity.

In Chapter (9) the X-ray diffraction data collected on the fast atom source deposited a-C:H samples is presented. This data provides an enhanced structural picture of the carbon matrix within those samples studied using neutron diffraction techniques. Further X-ray diffraction data is presented on a series of other a-C:H

samples deposited in a different energy range to those detailed in Chapter (8). This has allowed the effect of this deposition parameter on the resultant material to be investigated.

Chapter 2

Amorphous Hydrogenated Carbon

Crystalline carbon can exist in several distinct allotropic forms e.g. diamond, graphite, or as the more recently discovered Buckminster fullerenes. These allotropes are noticeable by their widely differing optical, electrical and mechanical properties which reflect their varying crystal structure. Carbon can also exist in a huge variety of amorphous phases, the properties of which represent a continuum between those displayed by graphite and those displayed by diamond. The exact properties displayed by a given amorphous carbon material are intimately linked to their production process and its controlling parameters through the bonding and structures imposed upon the carbon atoms during the material's growth.

Many studies have revealed that amorphous carbon films can contain significant amounts of hydrogen [6]. Amorphous hydrogenated carbon (a-C:H) represents a family of non-crystalline materials displaying properties intermediate between diamond, graphite and polymeric hydrocarbons. Under appropriate deposition conditions a-C:H can be produced in a form displaying a density, hardness and resistance to chemical attack greater than any other hydrocarbon. This so-called "diamond-like" carbon

phase was first observed by Schellenmeier [7] in 1953. The diamond-like hydrocarbons provide the limiting values of atom number density and cross-linking that are possible in a hydrocarbon structure. This material has the added advantage that its exact properties can be varied by adjusting the conditions under which it is deposited. For example, diamond-like carbon anti-reflection coatings with precisely controlled refractive index and thickness have been deposited on germanium infra-red optics by Koidl et al [8].

The extreme chemical inertness and nanometre scale smoothness displayed by some a-C:H films has led to investigations into their application as protective coatings for optical and magnetic disks [9]. Their high differential etch selectivity and clean laser ablation in reactive gases also makes diamond-like carbon suitable for advanced photolithography applications [10]. However the usefulness of these diamond-like materials may be limited by their concomitant high intrinsic stress which limits the maximum film thickness which can be achieved before "bubbling" of the deposited film occurs followed by its detachment from the substrate. A reduction in this internal stress would be necessary for applications such as corrosion resistance coatings. Most a-C:H films also absorb too much light for many optical applications and require a greater thermal stability for many tribological applications.

In order to fully understand the macroscopic properties displayed by amorphous hydrogenated carbon phases a clear picture of the microscopic structure and its relationship to deposition conditions is needed. In this way, optimisation of the properties of a-C:H materials can be achieved through a knowledge of the required growth conditions. The work presented here has involved the production of a series of amorphous hydrogenated carbon samples using a fast atom source (see Section (3.1)) and their subsequent study using X-ray and neutron diffraction techniques. In this way the

effects of the deposition processes on the structure of the material has been investigated.

The following chapter begins with a description of the different types of bonding configurations displayed by carbon and the properties associated with such bonding types as displayed in crystalline graphite and diamond and the many forms of hydrocarbon structures that exist. This is followed by a survey of the preparation and associated properties of amorphous carbons and amorphous hydrogenated carbons. The chapter is concluded with a discussion of hydrogen within the amorphous network. In Chapter (3) a description of the fast atom deposition technique used to produce the series of a-C:H(D) samples studied in this work is given.

2.1 Carbon bonding

The electronic configuration of carbon is known to be $1s^2 2s^2 2p^2$. To display a valency of four the carbon atom can promote one of its 2s electrons into the unoccupied 2p orbital, resulting in an outer configuration of $2s^1 2p^3$. The principle of superposition allows a linear combination of the wavefunctions of these 2s and 2p orbitals to be constructed which represents an equally valid description of the system. The carbon atom can therefore form four equivalent orbitals which may be optimised so as to have maximum extension. This ensures that, on bonding, maximum overlap of the carbon orbitals with the bonded atom orbital occurs, minimising the molecular energy. These four sp^3 hybrids, formed from the four outer occupied orbitals, are found to point towards the corners of a tetrahedron and are very stable as they allow the electron pairs to avoid one another to the maximum possible extent. Similarly the carbon atom can form a linear combination of the 2s orbital and two of the 2p orbitals resulting in three planar sp^2 hybrids that point towards the corners of an equilateral

triangle. This leaves one p orbital unchanged lying perpendicular to the plane of the sp^2 hybrids. Mixing of the 2s orbital and a single 2p orbital likewise produces two sp hybrid orbitals which lie diametrically opposite one another and leaves two unchanged p orbitals perpendicular to each other and to the plane of the sp orbitals.

2.1.1 Multiple bonds

Overlap of the orbitals on two carbon atoms may result in the formation of a molecular orbital. The latter can be approximated by a linear combination of the two contributing atomic orbitals concerned [11]. This linear combination results in the formation of an antibonding and a bonding orbital. Antibonding orbitals relate to a less stable, higher energy configuration for the molecular orbital than that of the two separate atoms. A bonding orbital corresponds to a molecular orbital more stable than that of the two individual atoms. If a single overlap occurs between the orbitals of two carbon atoms, a sigma (σ) bond is formed. σ bonds are directional and are symmetrical about the axis defined between the two atoms. Antibonded σ states are denoted σ^*.

Carbon double bonds may be described with reference to the molecule ethylene (C_2H_4). All six atoms in the ethylene molecule lie in the same plane with HCH and CCH bond angles of 120°. Each of the carbon atoms are sp^2 hybridised and are linked by a $C(sp^2)$- $C(sp^2)$ σ bond. The hydrogen atoms form $C(sp^2)$-H(1s) σ bonds with the remaining carbon sp^2 hybrids. Since the carbon atoms are sp^2 hybridised each has an unused 2p orbital perpendicular to the plane of the σ bond formed between them. Overlap of these two 2p orbitals may occur as they are close together leading to the formation of a charge cloud that consists of one region above and one below the plane of the molecule. The entire charge cloud, consisting of both regions, is known

as a pi bond (π). Therefore the -C=C- double bond consists of an electron pair in a σ bond plus a second electron pair in a π bond. Both bonding (π) and antibonding (π^*) pi states can be formed in a similar manner to sigma bonding (σ) and antibonding (σ^*) states. However the gap between π and π^* states is smaller than that between σ and σ^* states [12]. -C=C- double bonds are stronger than a -C-C- single bond but weaker than two -C-C- single bonds. Pi bonds in carbon are approximately 84kJ/mol weaker than sigma bonds because their electrons lie in a less favourable location for pulling the atoms together.

The triple bonded sp configuration is found in acetylene (C_2H_2). Two valence electrons on each carbon in C_2H_2 are assigned to linearly directed σ bonds between a second carbon atom and a hydrogen atom. The remaining two electrons on each carbon are placed in one of two π orbitals which lie perpendicular to each other about the axis of the sigma bond.

The presence of double bonds in carbon compounds inhibits the rotation of one part of a carbon molecule relative to the other, as rotation results in a reduction of the overlap region between the π orbitals, increasing the energy of the molecule. Double bonds in carbon therefore always favour a planar arrangement of atoms.

Multiple bonds between elements of period higher than two are rare: this results from the very small overlap that occurs between the pi orbitals on neighbouring large atoms. Thus -Si=Si- double bonds are very rare. The ability of carbon to form double and triple bonds therefore results in amorphous hydrogenated carbon phases displaying a more complex structural arrangement than the corresponding system a-Si:H.

2.1.2 Bonding in diamond and graphite

Graphite consists of sp^2 bonded carbon atoms arranged in a planar hexagonal network as shown in Figure (2.1). Sigma bonds between the carbon atoms within the planes result in an intraplanar bond length of $1.42\mathring{A}$. Bonding between the layers is by weaker pi bonds resulting in an interplanar bond length of $3.34\mathring{A}$. In normal α (or hexagonal) graphite the atoms are arranged in an ABAB... sequence such that atoms in alternate layers lie above each other. In β (or rhombohedral) graphite the stacking sequence is ABCABC... The two forms are interconvertible by grinding ($\alpha \rightarrow \beta$) or heating above 1025°C ($\beta \rightarrow \alpha$).

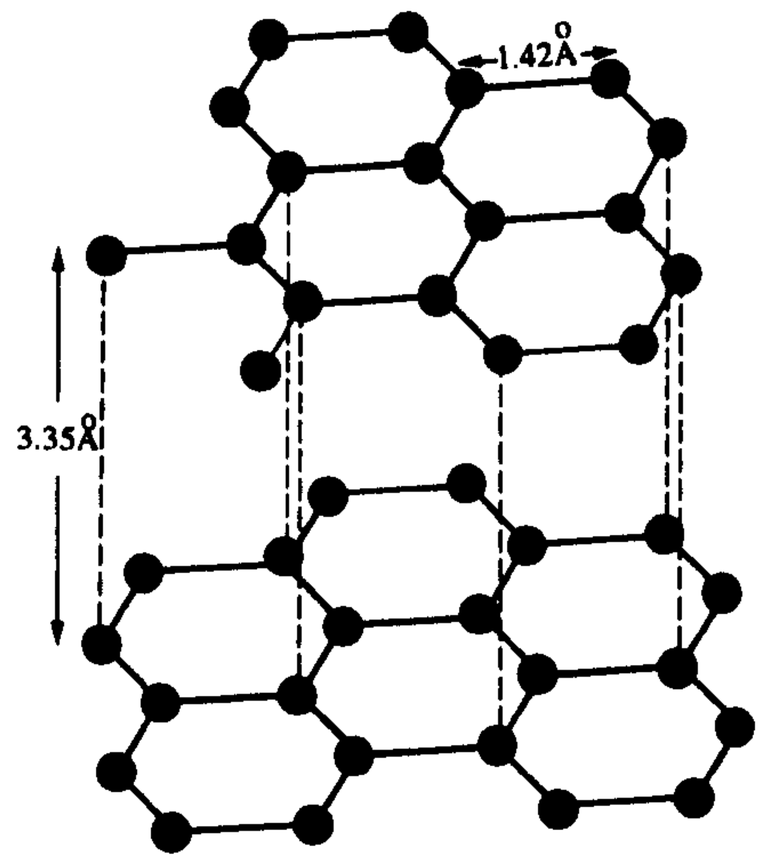

Figure 2.1: Atomic structure of graphite

As to be expected from the bonding observed in graphite, many of its physical and electronic properties are highly anisotropic. It is easily cleaved parallel to the basal plane due to the weaker pi bonding in this direction, leading to its softness and common use as a lubricant. However bonding within the layers is very strong. Delocalised electrons in the pi bonds in graphite can move easily between the layers

hence graphite is a black, electrically conducting solid with zero band gap. In contrast, electrons can move much less readily from one sheet to another. Graphite therefore has an electrical conductivity which is much higher parallel to the basal plane than in a direction perpendicular to this plane.

In diamond each carbon atom is linked to its four neighbours in a three dimensional tetrahedral structure with all bonding electrons localised in -C-C- sp^3 hybrid σ bonds. The bond angle for the structure is 109.5° as shown in Figure (2.2). It is very difficult to distort the crystal as this involves breaking covalent bonds between the carbon atoms and thus diamond is hard and brittle. The rigidity of the arrangement is such that diamond is the hardest known substance. Localisation of the electrons within covalent bonds prevents their moving freely in an applied field and thus diamond is a very poor electrical conductor. It is, however, one of the best known conductors of heat. This thermal conductivity is a result of the crystal structure which rapidly transmits the vigorous vibration of an atom in a hot part of the crystal to distant cooler parts. The bonding in diamond therefore results in a rigid, transparent, electrically insulating substance with a bandgap of 5.5eV and a much higher density than graphite (c.f. density for diamond of 3.51gcm^{-3} and that for graphite of 2.26gcm^{-3}). In contrast to graphite, diamond provides an ideal abrasive material as it is able to wear down all other substances yet the heat generated by friction is rapidly conducted away.

Thermodynamically diamond is slightly unstable with respect to graphite at standard temperatures and pressures, the free energy difference being 0.03eV per atom (only slightly greater than kT). However, there is a large activation energy barrier between the two phases.

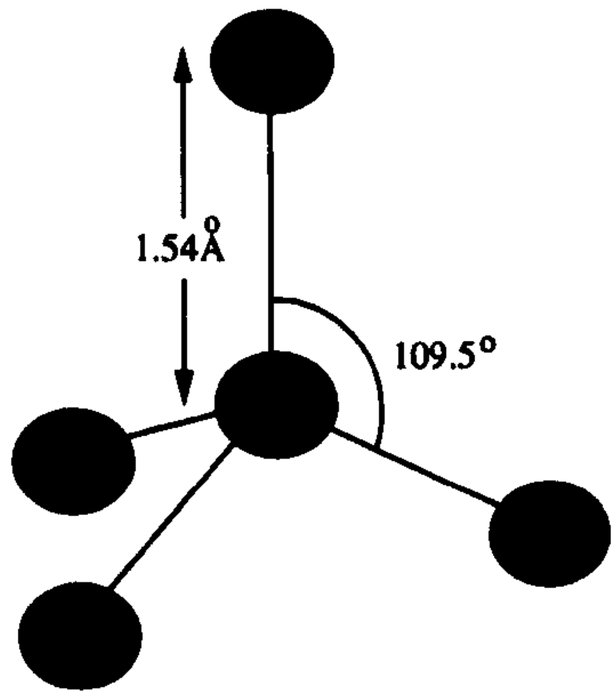

Figure 2.2: Tetrahedral arrangement of carbon atoms in diamond

2.1.3 Hydrocarbons

The many possible bonding types displayed by carbon atoms result in a wide range of structures being displayed by binary compounds of hydrogen and carbon. Hydrocarbon compounds can be divided into two families: saturated hydrocarbons are those with no multiple carbon-carbon bonds; unsaturated hydrocarbons are those with at least one carbon-carbon double or triple bond. Figure (2.3) shows schematically the classification of hydrocarbons.

Aromatic hydrocarbons are those based on the benzene ring structure. The benzene molecule (C_6H_6) consists of a hexagonal ring of six carbon atoms with a hydrogen atom attached to each carbon (see Figure (2.4)). The carbon atoms forming the benzene ring are bonded to one another and to their respective hydrogen atoms by sp^2 hybridised σ bonds. This leaves one unused p orbital on each carbon atom containing a single electron lying perpendicular to the plane of the carbon ring with one lobe above and below this plane. Each p orbital is able to overlap sideways with its two neighbouring p orbitals to form a single pi bond that extends as a ring of charge

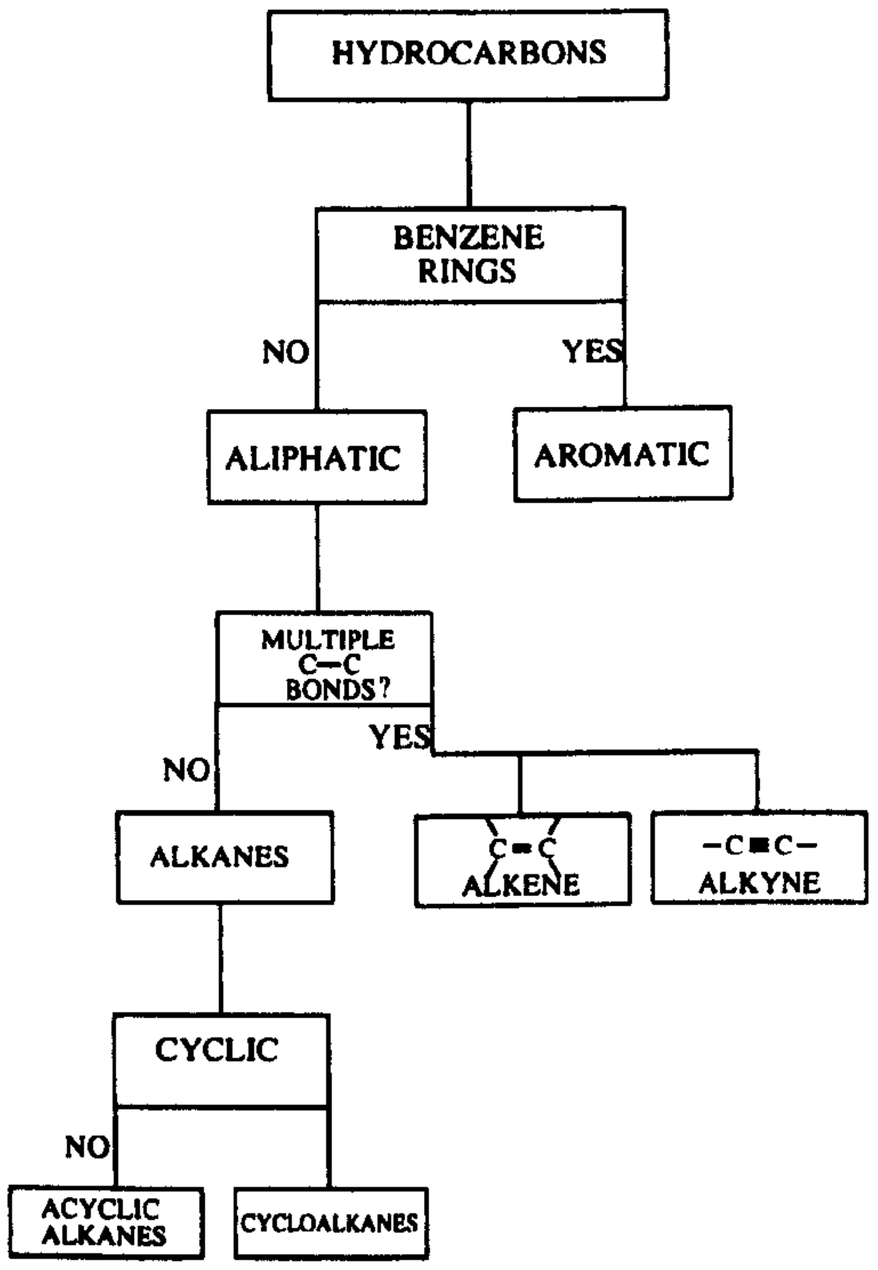

Figure 2.3: Classification of hydrocarbon compounds

above and below the plane of the molecule. The electrons in the pi bond are free to move throughout the entire pi system and are said to be delocalised. It is this delocalisation that leads to the high stability of the benzene molecule as electrons in the pi bond, which naturally repel one another, are free to move as far apart from one another as possible. The word aromatic is therefore used to describe any system which is stabilised by a ring of delocalised pi electrons.

The structure described for benzene leads to a planar, symmetrical molecule in which all -C-C- bond lengths are equal at $1.39\mathring{A}$ (c.f. carbon-carbon single bond length $1.54\mathring{A}$ and the carbon-carbon double bond length ($1.34\mathring{A}$).

Organic molecules that do not include benzene rings in their structure are known as aliphatic compounds. Saturated aliphatic compounds are known as alkanes and

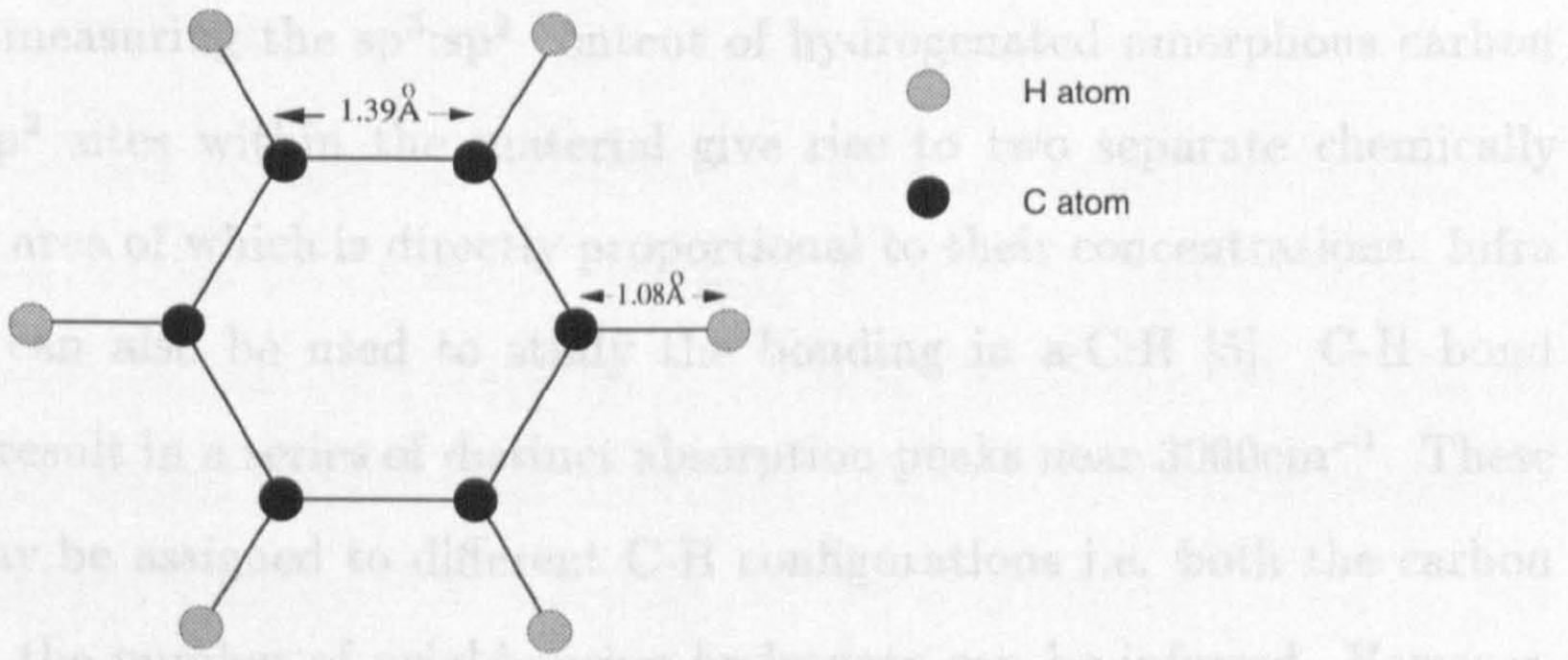

Figure 2.4: Atomic structure of benzene

may be described by the molecular formula C_nH_{2n+2}. The simplest of these is methane (CH_4). Ringlike saturated hydrocarbons are known as cycloalkanes e.g. cyclohexane (C_6H_{12}).

Unsaturated aliphatic hydrocarbons containing double bonds are known as alkenes or olefins and have the general formula C_nH_{2n}. As previously described, the four atoms attached to the carbon atoms forming the -C=C- double bond in an alkene will lie in the same plane. Unsaturated aliphatic hydrocarbons containing triple bonds are known as alkynes and have the general formula C_nH_{2n-2}. The two carbons and their attached groups in an alkyne form a linear structure.

2.2 Preparation and properties of a-C and a-C:H

As well as carbon's many crystalline allotropes, a large range of non-crystalline forms of carbon exist. The structure and properties of a-C and a-C:H are determined by the bonding types present in the material, in particular the proportion of sp^3 and sp^2 bonding is an important parameter. Many methods may be used to study the distribution of bonding types within the material. ^{13}C NMR studies provide a

direct method of measuring the sp^3:sp^2 content of hydrogenated amorphous carbon as the sp^3 and sp^2 sites within the material give rise to two separate chemically shifted peaks, the area of which is directly proportional to their concentrations. Infra red spectroscopy can also be used to study the bonding in a-C:H [5]. C-H bond stretching modes result in a series of distinct absorption peaks near 3000cm^{-1}. These peak positions may be assigned to different C-H configurations i.e. both the carbon hybridisation and the number of neighbouring hydrogens can be inferred. However, infra red studies require a uniform distribution of hydrogen over the sp^3 and sp^2 sites to give reliable sp^3:sp^2 bond ratio values. This assumption is not backed up by recent NMR studies of a-C:H [13]. Raman scattering also allows the phonon modes of a-C and a-C:H to be investigated and related to the material's structure.

X-ray, neutron and electron diffraction can be used to study the microscopic structure of a-C and a-C:H [14–16]. Both bond distances and the number of nearest neighbours can be inferred and related to the bonding types present. Although X-ray studies will only reveal the structure of the carbon matrix, neutron diffraction can provide complementary information on both the hydrogen and carbon network. As the scattering factor of electrons is relatively high, electron diffraction studies provide structural information from a smaller sample volume and therefore provide a good surface-sensitive, small area technique.

The following sections detail the properties of a-C and a-C:H materials prepared by a number of different techniques and their relationship to the imposed growth conditions.

2.2.1 Glassy carbon

Glassy carbon is formed by the heat treatment of complex hydrocarbon polymer resins. This thermal degradation, known as pyrolysis, results in a structure consisting of a convoluted ribbon-like network of sp^2 bonded carbon cross-linked by sp^3 bonded carbons [17]. Glassy carbons retain their disordered structure up to heat treatment temperatures of 3200°C and are thus classified as non-graphitizing carbons. The amorphous structure of glassy carbon is highly porous ($\sim$ 40%) displaying many unconnected 10-20$\mathring{A}$ voids [18]. Glassy carbon is found to be very hard and chemically inert. It is a good electrical conductor, the conductivity increasing dramatically with the heat treatment temperature applied, corresponding to an increased loss of hydrogen from the material. The structure of glassy carbon is such that it displays a significant degree of medium range order and in practice is difficult to treat as a truly amorphous material.

2.2.2 Evaporated carbon

Evaporated carbon is produced by low pressure resistive, laser beam or electron beam heating of solid carbon. In the first case a high current is passed between graphite electrodes, held in contact under vacuum, such that the ends of the electrodes become sufficiently heated to cause evaporation. Electron or laser beam evaporation may be used to produce similar results in a more controlled manner. The resultant material is found to be a very hard, amorphous substance. Raman, electron spin resonance and electron energy loss spectroscopy studies of the material have shown evaporated carbon to consist of trigonal, sp^2 bonded carbon [19]. Wada et al [19] suggested a model for evaporated carbon in which 3-fold coordinated atoms form a random network of planar clusters of the order of 20$\mathring{A}$ in size, having dangling bonds around

the cluster edges. As graphite is known to display a hardness along the basal plane greater than that of diamond, due to the presence of strong co-planar bonds, the observed hardness of evaporated carbon may be accounted for by a random orientation of graphite islands. The lack of long range order associated with such a structure is further suggested to explain the presence of a band gap (not observed in graphite) and the semitransparency and relatively high resistivity ($10^{-1} - 10^{3}\Omega$cm) observed in evaporated carbon. The latter two properties would normally be associated with diamond-like sp^3 bonding.

2.2.3 Sputtered carbon

Sputtering involves the bombardment of a target material by energetic ions (usually from a low pressure plasma), causing erosion of material, either atom by atom or as clusters of atoms, and the subsequent deposition of a film on a substrate [2] (see Figure (2.5)). This process results in a Maxwellian energy distribution for the film forming particles arriving at the substrate [3]. Carbon is known to have a particularly low sputtering yield (0.12 atoms per incident argon atom for a 500eV argon beam), but viable deposition rates can be achieved by use of a magnetron in which a magnetic field is used to confine the plasma electrons and reduce losses to the walls of the deposition chamber. This leads to increased ionisation, dissociation and sputtering, and has produced deposition rates of 450$\mathring{A}$ per minute. Spectroscopic studies of the emission products of the sputtering process have shown the resultant species to be thermal in energy (typically 10-40eV) [20] and therefore result in a structure very similar to that of thermally evaporated amorphous carbon. As sputtering is generally a slow process (i.e. deposition rates are generally below 0.1$\mathring{A}$/ sec), sputtered carbon films are susceptible to contamination from residual impurity gases in the deposition

chamber or the sputtering gas (e.g. argon).

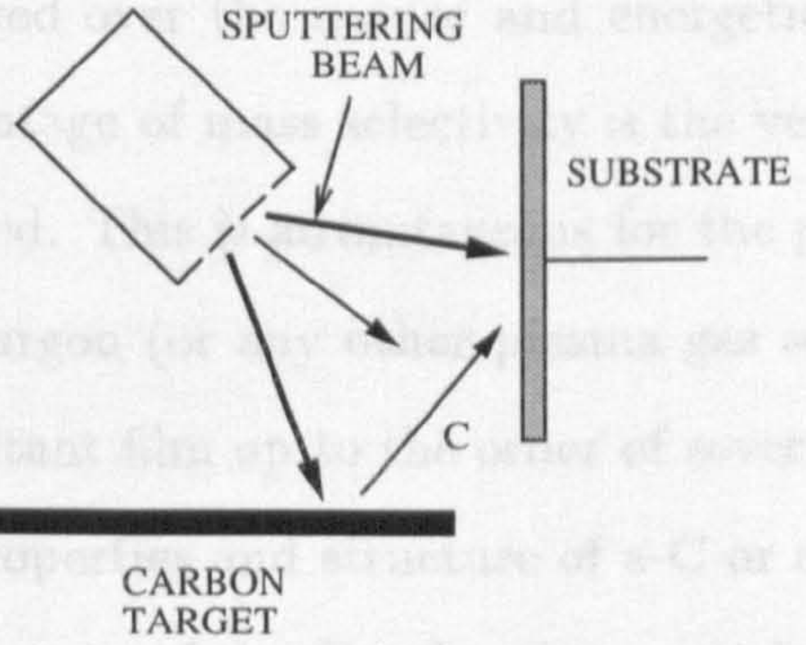

Figure 2.5: Schematic diagram of sputtering process

Although an inert gas such as argon is often used in the sputtering process, when amorphous carbon films are being produced, species which react with the material being sputtered may also be used. If hydrogen is mixed with argon gas during the sputtering process, it may be incorporated into the growing film allowing amorphous hydrogenated carbon to be produced.

2.2.4 Ion beam deposited a-C and a-C:H

Ion beam deposition of amorphous carbon has received increasing attention since Aisenberg and Chabot published their findings in the early seventies on the formation of "diamond-like" carbon by the condensation of energetic ions onto a number of different substrates [21]. This method of production involves the extraction of ions from a plasma source and their direct deposition onto a substrate external to the plasma. For amorphous carbon, a carbon arc source may be used, in which a plasma is maintained between carbon electrodes using a gas such as argon. For a-C:H a hydrocarbon gas may be injected into a Kaufman-type ion gun [22] producing ions and ionised molecular fragments. The extracted ions in each case may be accelerated

to a desired energy and/or mass selected using a magnetic field. In this way a high degree of control is achieved over the nature and energetic state of the impacting species. A particular advantage of mass selectivity is the very pure source of carbon ions which may be produced. This is advantageous for the production of a-C from a carbon arc plasma where argon (or any other plasma gas source employed) may be incorporated into the resultant film up to the order of several atomic percent [3].

A critical role in the properties and structure of a-C or a-C:H has been shown to be played by the impact energy of the film forming particles (e.g. [23]). Ishikawa et al [24] studied a series of thin films produced by mass selected negative-carbon-ion-beam deposition for a series of carbon ion energies ranging between 25eV and 1000eV. They observed a peak in the optical gap (0.96eV), electrical resistivity ($1.5 \times 10^{8} \Omega$cm) and atomic density (1.7×10^{23} cm $^{-3}$) in the energy range 100eV to 200eV indicating a high degree of diamond-like sp^3 bonding. They explained their observations in terms of the fact that ions impacting on the growing film surface above 100eV will have sufficient energy to sputter the depositing film (see Table (2.1)) and thus preferentially remove atoms with weaker bonds. Above this impact energy there will therefore be a predominance of atoms with stronger bonds within the resultant film. At low energies (i.e. below 100eV) graphitic, sp^2 bonded structures are observed, whilst above 100eV a gradual transformation occurs to dense sp^3 bonded carbon films. As the ion energy increases still further the deposited film will suffer damage from impinging ions and a degradation to a graphitic structure is observed. This structural change is accompanied by a reduction in the band gap of the carbon films, the atomic density and the electrical resistivity.

Weissmantel [30] carried out a study of a series of a-C:H films produced using benzene as a precursor plasma gas and an accelerating voltage in the range 20V to

Item (Reference)	Energy(eV)
Displacement energy of carbon atoms in diamond [25]	80
Displacement energy of carbon ions in graphite [26]	25
Threshold energy for graphite sputtering [26]	15
Intraplanar bond energy in graphite [27]	7.43
Interplanar bond energy of graphite [28]	0.86
Bond energy of diamond [28]	7.41
C-H bond energy [29]	3.5

Table 2.1: Energies for various carbon processes.

3kV. a-C:H films produced with ion impact energies below 100eV were found to be soft and polymeric in nature. Films deposited from ions impacting on the substrate at energies between 100eV and 1keV kere found to exhibit diamond-like properties being extremely inert to chemical attack by acids, alkalis and organic solvents. These films were transparent in the infra red and displayed a hardness that peaked in the impact energy range between 0.8keV and 1.0keV. Subsequent studies [31] were carried out by Weismantel involving a dual ion beam technique in which additional energy and momentum is supplied to the growing film from a second beam of energetic, ionised species directed towards the substrate. These studies led Weissmantal to suggest that intense and rapidly collapsing thermal and pressure spikes, brought about in the film by decelerating impacting ions, may explain the formation of unusual metastable diamond-like structures, resembling high pressure diamond synthesis on an atomic scale.

The impact energy at which a maximum in the sp^3 bonding occurs, and a predominance of diamond-like properties are observed in the a-C:H films, may be related to the precursor gas species used during ion beam deposition. This relationship arises from the fact that the impact energy of the impinging ions will be distributed equally

amongst the atoms of the impacting species. When a precursor gas such as benzene (C_6H_6) is used, the average fragment size arriving at the film surface will be greater than that for a system using methane (CH_4) as the precursor. Thus for a constant acceleration voltage the average energy of the carbon atoms penetrating the film surface will be greater when a benzene plasma is employed rather than a methane plasma.

2.2.5 Vacuum arc deposition

This deposition mechanism for amorphous carbon involves the striking of an arc between a planar graphite cathode separated from an anode under vacuum conditions. The cathode spot of such an arc is a very hot plasma which provides a source of both singly and doubly ionised carbon atoms. A curved magnetic filter may be used to remove any neutral carbon and macroscopic graphite particles and provide a beam of ionised carbon atoms (as opposed to the ionised atoms and molecular fragments used in ion beam deposition) [17]. The ion beams produced have been used to form a highly tetrahedrally bonded form of amorphous carbon displaying up to 90% sp^3 bonding [16, 32, 33] commonly known as mass selected ion beam (MSIB) carbon. Recently, attempts have been made to produce a-C:H samples from this system by introducing hydrogen gas into the vacuum system whilst the arc is being struck [34]. Although the degree of hydrogenation achieved is small ($< 10\%$) structural and electronic changes have been observed. The sp^3 content has been found to increase slightly upon initial hydrogen incorporation, but fall with further hydrogenation. This fall in the sp^3 content is contrary to the commonly held belief that hydrogen acts to stabilise sp^3 sites within a-C:H phases.

2.2.6 R.F. plasma deposition of amorphous hydrogenated carbon

One of the most commonly employed methods of production of a-C:H involves the plasma (or glow-discharge) deposition of thin films from hydrocarbon gases. Unlike sputtering, glow discharge techniques do not involve the removal of material from a solid target source, but the decomposition of the precursor gas itself to produce condensable species. The glow discharge plasma is generally produced using an r.f. power source which may be inductively or capacitively coupled to the plasma gas [2] (see Figure (2.6)). Within the plasma, electron bombardment leads to excitation, ionisation and dissociation of the gas molecules. In general the energy required to cause dissociation of molecules is lower than that required to cause ionisation so that molecular fragments (or radicals) are the predominantly formed discharge species rather than ions. It is therefore radicals, which diffuse towards the electrodes and the chamber walls, that chiefly contribute to the growth of the deposited material.

In the glow discharge technique the substrate employed may be mounted on either electrode and the source most commonly runs at a frequency of 13.56MHz. Above frequencies of $\sim$ 100kHz ions cannot follow the alternating electric field but electrons are able to because of their much lower mass. The variance in the mobilities of the two species causes an electrode capacitively coupled to the r.f. source to develop a negative bias, V_B, if its area is smaller than the grounded area of the system. As the higher mobility electrons are more readily removed from the plasma in each cycle, the plasma develops a positive potential with respect to the electrodes and chamber walls. This process occurs until such time as the number of ions leaving the plasma in each cycle equals the number of electrons. This results in ion bombardment of the electrodes,

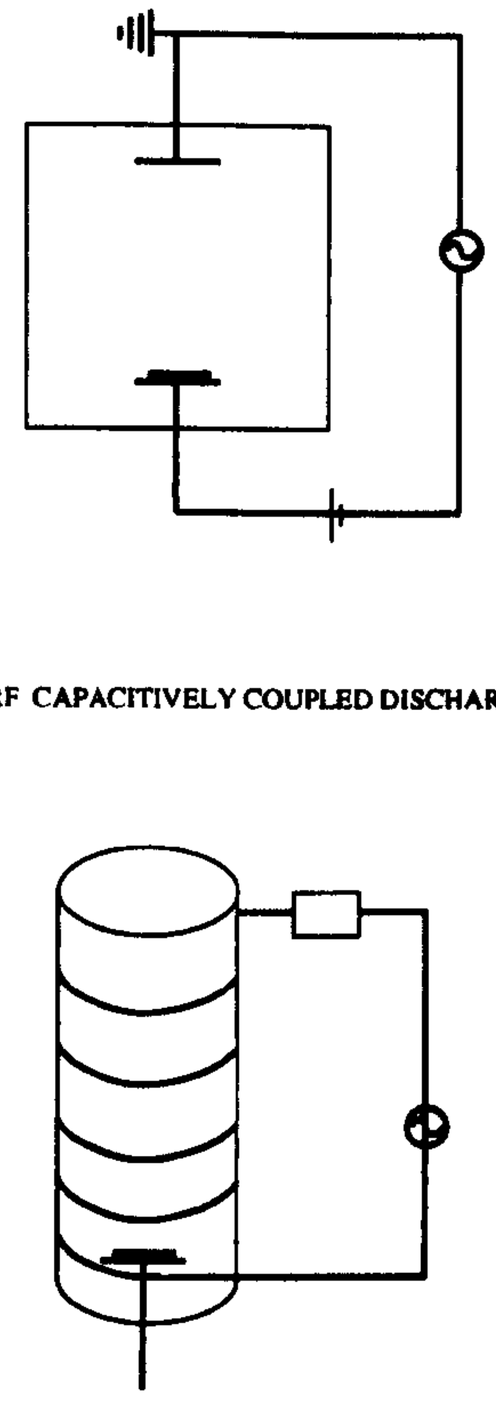

Figure 2.6: Inductively and capacitively coupled glow discharge deposition processes

primarily on the negative cathode. This ion bombardment of the growing a-C:H film will affect the kinetics of the growth process (as in dual ion beam deposition) and ultimately the properties and composition of the deposited films. Pronounced ion bombardment of a-C:H films growing on the cathode leads to an observably lower hydrogen content for cathodic films as opposed to anodic films. This lower hydrogen content leads to a lower band gap in those films formed on the cathode.

By varying the growth parameters, such as power density, gas pressure, self bias potential, a wide spectrum of a-C:H phases can be formed displaying a range of physical and electronic properties. Zou et al [35] studied a series of a-C:H films

deposited on the water-cooled cathode of a methane gas glow discharge. A number of samples were produced at different negative self bias potentials in the range $|V_B|$=50 to 1400V and the pressure range 1.3×10^{-3} to 1.3×10^{-1} mbar. Films deposited in the range 0V< $|V_B|$ <100V were found to be soft and polymeric in nature containing a high hydrogen content. In the range 100V< $|V_B|$ <600V much harder films were obtained, having a reduced hydrogen content; these films were also found to possess high internal compressive stress. As $|V_B|$ increased still further, those films deposited in the range 600V < $|V_B|$ < 1300V were found to be more graphite-like, soft and display low internal mechanical stress levels.

As $|V_B|$ increased within the region 100V< $|V_B|$ <600V the hardness of the a-C:H films was found to rise to a peak at 500V and subsequently fall off. Infra red spectroscopy studies of the films showed this fall off to correlate with a reduction in the sp^3:sp^2 bonding ratio within the samples. The measured proportion of sp^3 bonding was found to relate to the hydrogen content of the films. As the microhardness of the films was observed to fall so too were the internal compressive stress levels within the material. Similar studies by Prince and Romach on glow discharge a-C:H films [36] showed the compressive stress levels in such films to be proportional to $\frac{P^{0.5}}{V_B}$ where P is the gas pressure in the discharge.

A fall in the internal stress levels of a-C:H with increasing hydrogen content correlates with computer-generated Monte Carlo models of the system as carried out by Tersoff [37]. These simulations indicate that hydrogen acts to relieve local strain in amorphous carbon, facilitating sp^3 bonding by reducing the energetic cost of such bonding. This promotion of sp^3 sites initially leads to an increase in the hardness of the a-C:H system. However a tradeoff occurs with the reduction in hardness brought about by the reduced cross-linking caused by hydrogen incorporation. Thus the

hardness of a-C:H is found to peak at intermediate levels. The fall in the hydrogen content of the films with increasing $|V_B|$ is thought to be due to ion bombardment of the growing film causing preferential sputtering of weakly bonded hydrogen.

Electrical and optical properties

The electrical and optical properties of r.f. plasma deposited a-C:H are found to vary with the self bias potential and the deposition gas pressure. Rowher [38] measured the conductivity as a function of $|V_B|$ and found that the films became more electrically conducting as $|V_B|$ increased. Jiang [39] studied films deposited in the range $|V_B|$=100V to 600V and found that the optical bandgap of the films fell from values in the region of 2-3eV for low $|V_B|$ polymeric films to 1 to 1.5eV for high $|V_B|$ hard, dense films. At $|V_B|$=200V he found the most "diamond-like" films and observed the sp^3:sp^2 ratio to decrease monotonically with increasing $|V_B|$ above this value. NMR studies of these films showed each of the sp^3 hybridised carbons to be bonded to at least one hydrogen atom. Thus hydrogen appears to stabilise sp^3 hybridisation. This is born out by the transformation of sp^3 sites to sp^2 sites as hydrogen is driven out of the films on heating. The effect of substrate temperature on the optical gap of a-C:H films was studied by Anderson who found a drop from $\sim$ 2.5eV to $\sim$ 1.5 eV to occur as the temperature rose from 400K to 650K [40].

The electronic properties of a-C:H are controlled by the π states of the sp^2 sites as these lie closer to the Fermi level [12]. sp^3 hybridisation leads to a wide band gap between a valence band of bonding σ states and a conduction band of antibonding states, σ^*. It is the σ states that appear to provide the rigid network of the a-C:H and therefore define the mechanical properties of the system.

Energetically, π bonding favours aromatic rings over olefinic chains and clustering

of these rings into graphitic sheets. Robertson therefore has suggested that any concentration of sp^2 sites will have a tendency to cluster. As clustering achieves no energetic gains for sp^3 sites, Robertson proposed a model for a-C:H involving two phases: the first phase consisting of π bonded graphitic clusters embedded in a second phase of sp^3 bonded material which forms the link between the sp^2 clusters. The sp^3 phase in this model may be highly cross-linked (as in hard a-C:H) or polymeric (as in soft a-C:H). The model is, however, contradictory to recent NMR studies on hard a-C:H samples [41] (prepared by plasma deposition from a fast atom source, see Section (3.1)). These studies indicate the presence of two distinct matrices within the carbon network: one consisting of chains of alternately doubly and singly bonded carbon having statistically distributed hydrogen and a second of polymeric sp^3 bonded carbon terminated by hydrogen atoms. These two environments are separated by regions of non-hydrogenated olefinic sp^2 hybridised carbon.

2.3 Hydrogen within a-C:H

The bonding of hydrogen in a-C:H films has been shown to be weak by thermal effusion measurements [35] such as those carried out by Rowher [38], which indicate that all the hydrogen has left such films after annealing at 600°C. Thermal effusion studies on films deposited in an r.f. plasma at $|V_B|$=400V carried out by Jiang [39] showed decomposition to begin at 300°C. Above 400°C he observed chemically bonded hydrogen and -CH_3 to desorb and effuse.

Wild [42] carried out a study of the effusion products of a-C:H as a function of the self bias voltage, $|V_B|$, at which they were deposited. As $|V_B|$ increased he found the temperature range over which effusion occurred to narrow and the threshold temperature for effusion to begin to increase. These results have been related to

the porous nature of the films. At higher values of $|V_B|$, as the hydrogen content of a given film decreases, the amorphous network becomes more cross-linked. This causes a reduction in the size of the pores within the network. Thus films deposited at low $|V_B|$ are found to evolve hydrogen molecules and hydrocarbons whereas those deposited at higher $|V_B|$ evolve hydrogen only. This occurs because hydrocarbons are unable to diffuse through the tighter network structure of those films deposited at higher self bias potentials. Thus the thermal stability of the films is found to increase with the self bias potential.

Isotopically substituted samples of a-C:H have been used by Wild [42] to determine that the molecules effusing out of the system are produced in the bulk of the sample and diffuse to the surface as opposed to atomic diffusion followed by molecular formation at the surface. The a-C:H films studied by thermal effusion again show a structural transition towards a disordered graphitic structure as the annealing temperature is increased.

Studies carried out on the hydrogen environment in a-C:H using infra red spectroscopy [43,5] and NMR [44,41] indicate the hydrogen to be predominantly bonded to sp^3 hybridised carbons. This is supported by inelastic neutron scattering data on these materials [45], which also provides evidence for the presence of a small ($< 10\%$) proportion of molecular hydrogen trapped within cages in the material. Hydrogen bonded to the carbon matrix has been shown to be mainly in the form of CH and CH_2 groups with the CH_3 concentration being very small or negligible.

In the previous sections details have been given on the many forms of a-C and a-C:H possible. The relationship between the deposition conditions chosen and the

resultant materials have been discussed. In summary, it appears that the deposition energy is the most critical parameter in determining the properties of the deposited material. This energy determines the structural configuration and, in the case of a-C:H, the hydrogen content of the materials. These in turn determine the electronic, optical and mechanical properties. In Chapter (3) the fast atom source deposition technique used to deposit the a-C:H materials studied in this work will be detailed.

Chapter 3

Plasma Deposition Involving a Saddle Field Fast Atom Source

Each of the a-C:H(D) samples studied in this work was deposited in a saddle field fast atom source. This chapter describes the configuration and use of such sources. The deposition parameters used for each sample are given and the resultant compositions discussed.

3.1 Deposition technique

Figure (3.1) shows a schematic diagram of the deposition system commissioned, as part of this work, for the production of the amorphous hydrogenated carbon samples studied in this work. The system incorporates an Ion Tech Fab104-2 fast atom source mounted onto a $0.5 \times 0.5 m^2$ vacuum chamber. This chamber may be pumped to a base pressure of 1×10^{-7} mbar using a Leybold Turbovac 1000C turbomolecular pump backed by a Leybold D65BCS rotary pump. The latter pump was also employed to rough out the vacuum chamber to a pressure of $\sim 10^{-3}$mbar. Roughing was

carried out through the rotary pump, using a slow start valve to prevent a-C:H debris from previous deposition runs being drawn through the turbomolecular pump; hard a-C:H powders can cause considerable damage if allowed into the region of the turbomolecular pump bearings due to their abrasive properties.

Within the vacuum chamber, substrates were fixed to an aluminium, motor-driven mount which could be used to drive them up and down in a plane normal to the beam and/or rotate them about an axis perpendicular to that plane. In this way they could be moved continuously through the beam from the fast atom source to achieve an even coating of a substrate extending beyond the size of the central beam.

Gases were admitted to the Fab104-2 source through a series of dedicated Tylan 280A mass flow controllers as shown in Figure (3.1). The gas composition in the deposition chamber could be monitored using a Spectrametrics Spectra Vacscan 100 quadrupole mass spectrometer and the chamber pressure measured using either a pirani or cold cathode gauge.

3.1.1 Substrates

Both copper and silicon substrates were used for deposition of the a-C:H(D) samples studied. The thin film samples of a-C:H(D) produced using the fast atom source were deposited onto silicon substrates. Both randomly cut 3in silicon wafers and 2in oriented wafers were used (see Section 7.3.1). Silicon was used as a substrate for the thin film samples as a-C:H adheres well to the silicon surface due to the formation of a silicon carbide layer at the thin film/substrate interface. The powder samples of a-C:H(D) were produced by deposition onto a copper substrate. As carbon cannot form a carbide at the thin film/substrate interface in this case, the films formed adhere poorly to the copper and the inherent compressive stress in the deposited

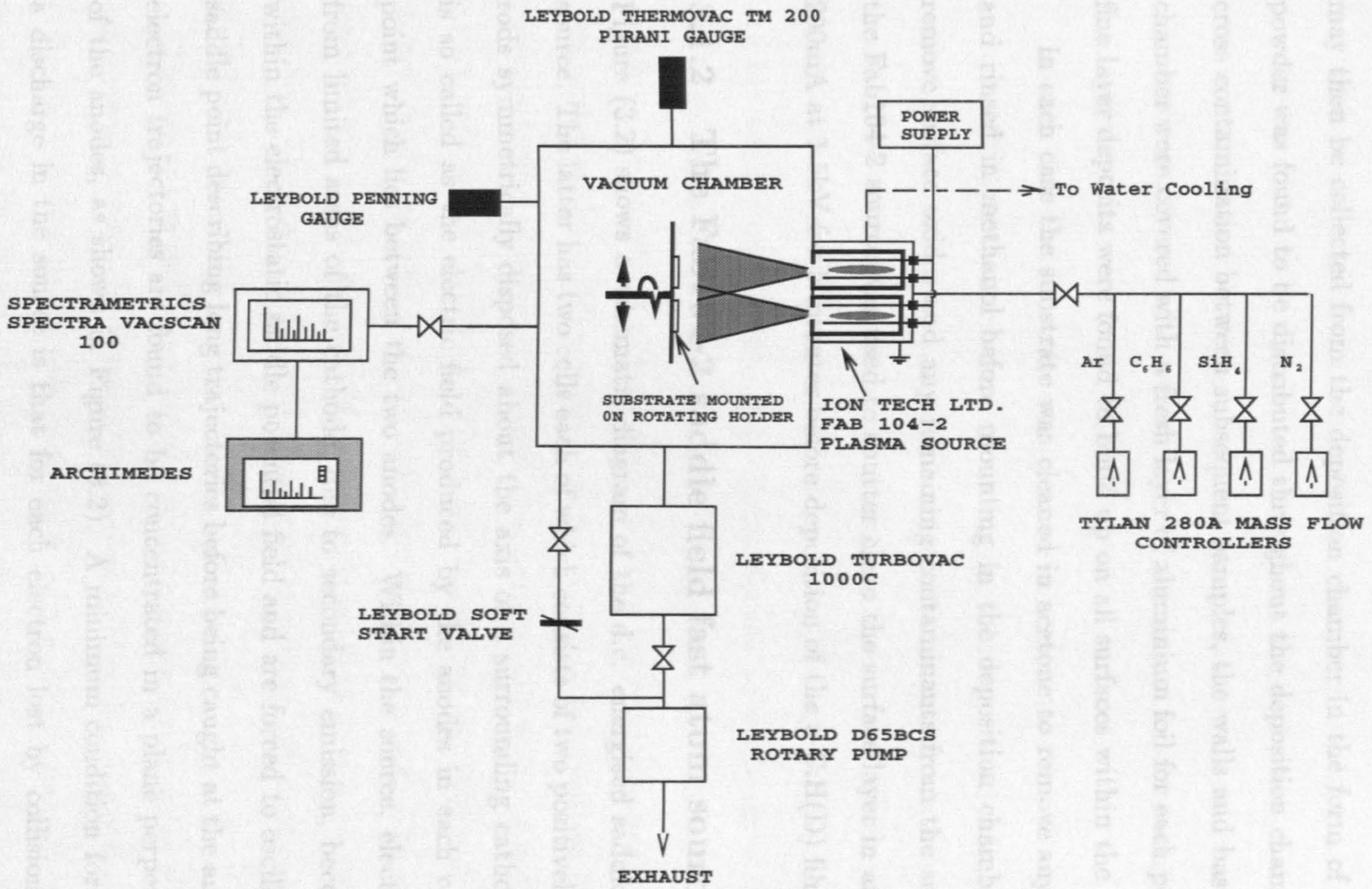

Figure 3.1: Schematic Diagram of Plasma Deposition System Incorporating Saddle Field Fast Atom Source

films causes the a-C:H to violently splinter from the substrate. The a-C:H(D) sample may then be collected from the deposition chamber in the form of a powder. This powder was found to be distributed throughout the deposition chamber. To prevent cross contamination between subsequent samples, the walls and base of the vacuum chamber were covered with a fresh layer of aluminium foil for each powder sample as fine layer deposits were found to build up on all surfaces within the chamber.

In each case the substrate was cleaned in acetone to remove any surface greases and rinsed in methanol before mounting in the deposition chamber. In order to remove surface oxides and any remaining contaminants from the substrate surface, the Fab104-2 source was used to sputter clean the surface layer in an argon beam of 200mA at 1.5kV for 5 minutes before deposition of the a-C:H(D) films.

3.1.2 The Fab104-2 saddle field fast atom source

Figure (3.2) shows a schematic diagram of the d.c. energised saddle field fast atom source. The latter has two cells each of which consists of two positively charged anode rods symmetrically disposed about the axis of a surrounding cathode. The source is so called as the electric field produced by the anodes in each cell has a saddle point which lies between the two anodes. Within the source, electrons originating from limited areas of the cathode, due to secondary emission, become constrained within the electrostatic saddle potential field and are forced to oscillate through the saddle point describing long trajectories before being caught at the anode [46]. Stable electron trajectories are found to be concentrated in a plane perpendicular to that of the anodes, as shown in Figure (3.2). A minimum condition for maintenance of a discharge in the source is that for each electron lost by collision at the anodes, one secondary electron should appear due to ion collisions at the cathode. With the

long electron paths produced in such a source the probability of ionisation of the gas molecules is much greater and therefore a discharge can be maintained at a lower pressure (5×10^{-4} to 10^{-3}mbar) relative to conventional cold cathode tubes (usually 10^{-1} to 10^{-2}mbar) without the use of a magnet. This therefore increases the efficiency of the source and minimises scattering of the ions and thus the energy distribution of the resultant beam.

Within the discharge the positive ions formed travel out towards the cathode. In each cell those ions incident on an aperture in a grid defined on one wall of the cathode continue on and emerge as a beam in the deposition chamber. The beam produced by such an arrangement contains a high degree of energetic neutrals and may be fully neutralised (as in this case) by optimising the geometry of the source and the applied electric field [47]. Neutralisation of the beam is thought to occur due to recombination of slow secondary electrons at the cathode aperture [48]. The energy of the ions which go on to form the beam has been measured using a retarding field energy analyser [47] and has been found to be approximately 85% of the anode potential over a wide range of potentials (with a half width of 200V at 5kV) for a source such as the Fab104-2. The beam formed by the Fab104-2 source is wedge shaped producing a rectangular foot print at the substrate. The sample/substrate distance was set at 15cm giving a minor axis beam span of 2.5cm with a uniformity of ±20%. The major axis beam span provides a beam coverage uniformity as given in Table (3.1).

The use of a neutral beam has the advantage that insulators as well as conductors can be used as substrates without the need for electron flooding of the growing sample.

In the Fab104-2 source used both the anodes and cathode walls were constructed from graphite therefore reducing the risk of contamination of the samples produced.

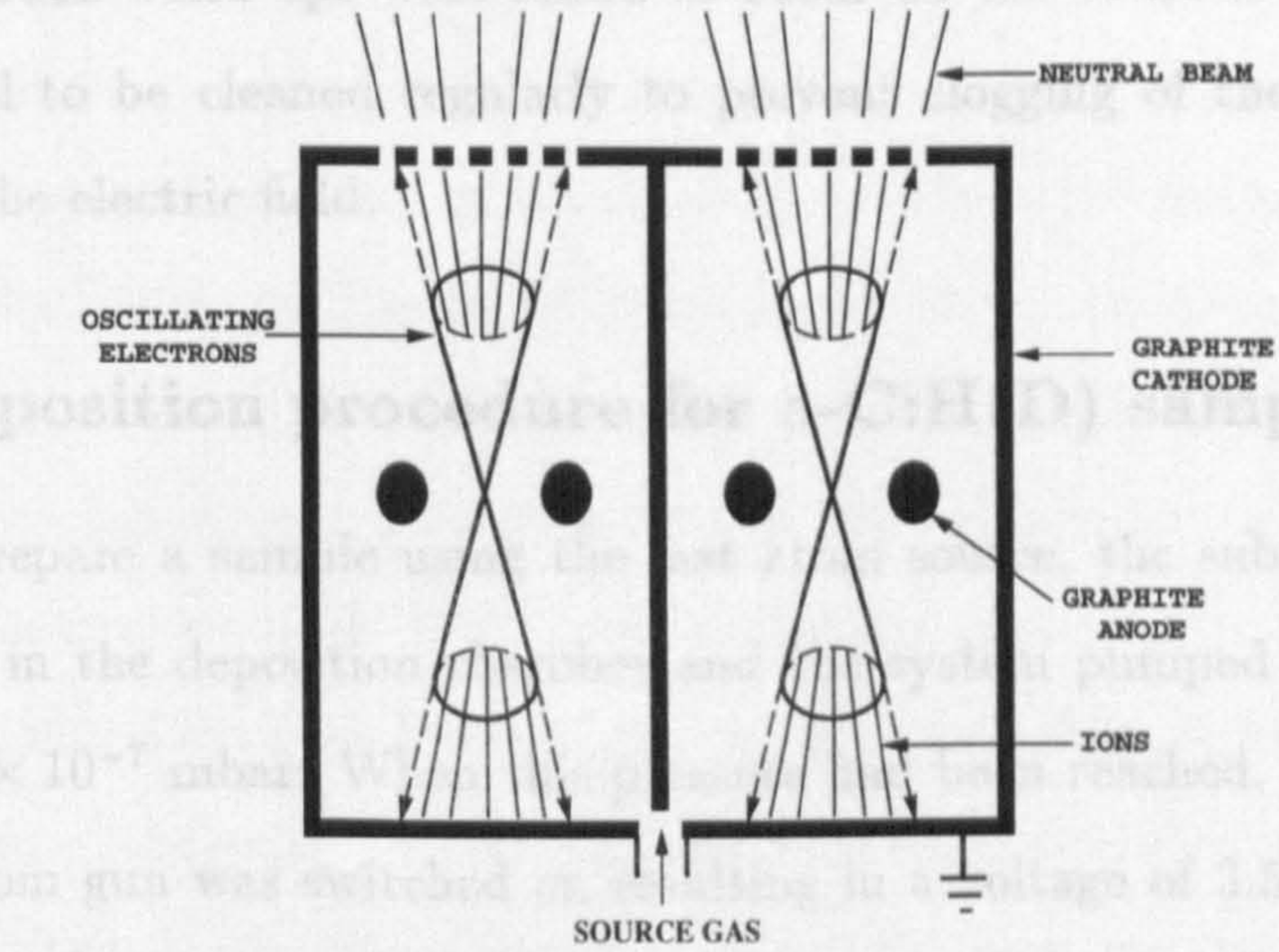

CROSS–SECTIONAL VIEW OF FAB104 SADDLE FIELD SOURCE INCLUDING SCHEMATIC OF ELECTRON TRAJECTORIES, REGIONS OF ION FORMATION AND NEUTRAL BEAM.

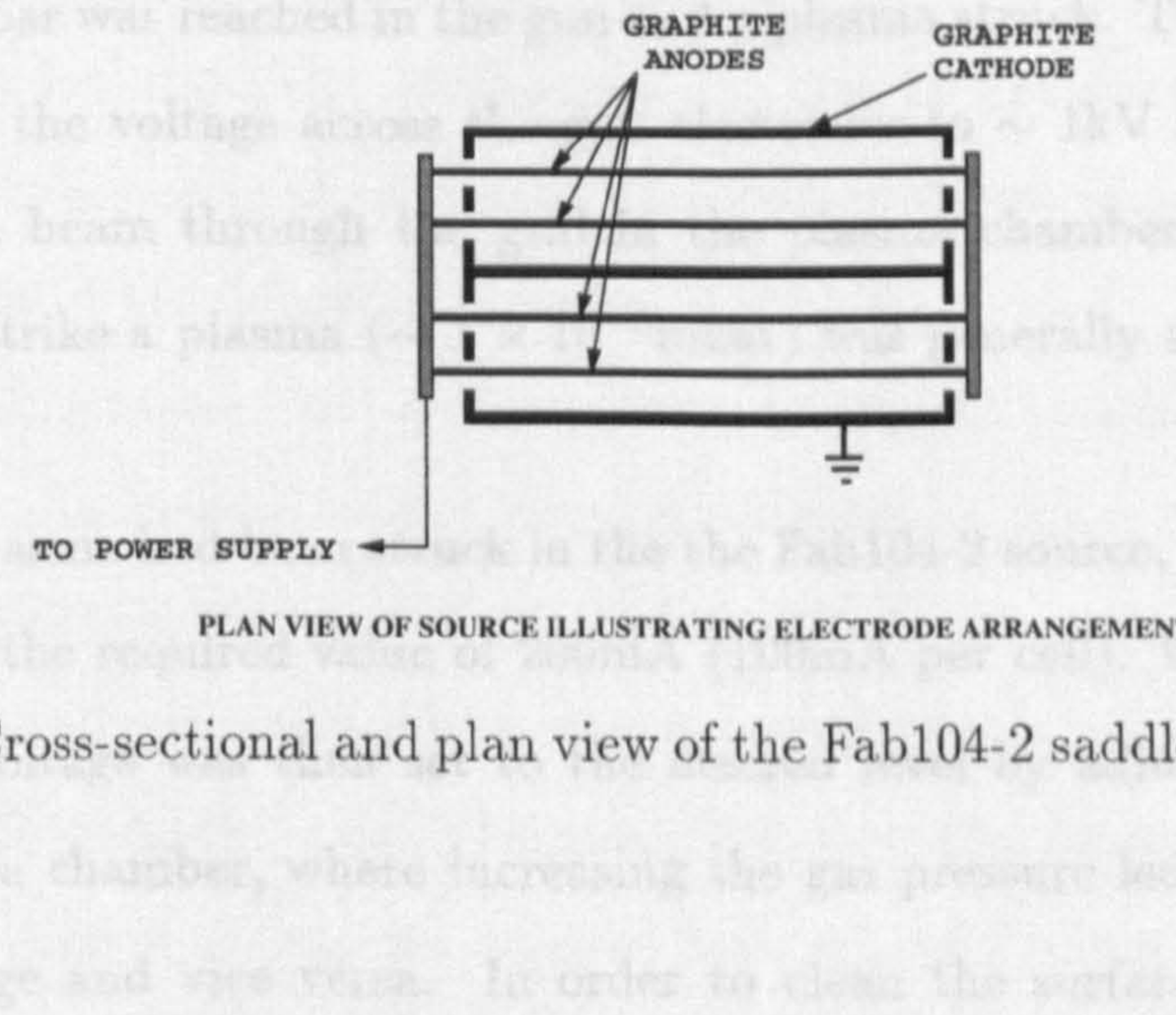

PLAN VIEW OF SOURCE ILLUSTRATING ELECTRODE ARRANGEMENT

Figure 3.2: Cross-sectional and plan view of the Fab104-2 saddle field fast atom source

Beam Span	Flux Uniformity
7cm	±10%
10cm	±20%
12cm	±25%

Table 3.1: Beam coverage of Fab104-2 Fast Atom Source

Over time, carbon build ups were found to occur on the cathode walls so that the latter required to be cleaned regularly to prevent clogging of the cathode grid or distortion of the electric field.

3.1.3 Deposition procedure for a-C:H(D) samples

In order to prepare a sample using the fast atom source, the substrate to be used was mounted in the deposition chamber and the system pumped down to its base pressure of 1×10^{-7} mbar. When this pressure had been reached, the power supply to the fast atom gun was switched on resulting in a voltage of 3.5kV being applied to the anodes. Argon was then admitted to the gun through a dedicated mass flow controller. The flow rate of gas into the system was increased until an argon pressure of $\sim 1 \times 10^{-3}$mbar was reached in the gun and a plasma struck. The latter was indicated by a drop in the voltage across the gun electrodes to $\sim$ 1kV and the appearance of a blue argon beam through the grid in the plasma chamber. The argon pressure required to strike a plasma ($\sim 1 \times 10^{-3}$mbar) was generally achieved at a flow rate of $\sim 32 sccm$.

Once a plasma had been struck in the the Fab104-2 source, the source current was increased to the required value of 200mA (100mA per cell). With the current fixed, the source voltage was then set to the desired level by adjusting the gas pressure in the plasma chamber, where increasing the gas pressure led to a reduction in the source voltage and vice versa. In order to clean the surface of the substrate the source voltage was set to 1.5kV and the latter sputtered clean in the argon beam for a period of approximately five minutes. After cleaning, the power supply to the gun was switched off and the argon gas line closed. The pressure in the deposition chamber was then allowed to drop back to 1×10^{-7}mbar to ensure that any remaining

argon had been pumped out of the system.

For the samples produced from an acetylene precursor, a gas source was used whilst for those produced from cyclohexane and deuterocyclohexane a liquid source was used. In the latter case the liquid source was held in a stainless steel cylinder (of 110ml capacity) connected to the Fab104-2 source via a mass flow controller. Before admitting the cyclohexane to the fast atom gun, the cylinder was first placed in ice so as to solidify the cyclohexane (melting point C_6H_{12}/C_6D_{12} =6.5°). In this way the air in the cylinder above the cyclohexane could be drawn off through the vacuum system via the mass flow controller without drawing through a significant proportion of the cyclohexane. This process was monitored using the mass spectrometer attached to the vacuum chamber. When the latter indicated only traces of C_6H_{12}, the mass flow controller was closed so that any residual gases from the cylinder could be pumped out of the system whilst the cyclohexane was allowed to return to room temperature Removal of the air from the cylinder prior to deposition was carried out to prevent contamination of the deposited samples. (An a-C:H sample produced without this procedure being carried out was found to contain 0.2 atomic percent of nitrogen whereas no measurable traces of nitrogen were found to be present in any samples produced after the removal of the air in the cylinder.)

Once the vacuum system had returned to its base pressure power, was again supplied to the Fab104-2 gun. The mass flow controller on the cyclohexane line was then used to allow the vacuum system to draw off cyclohexane vapour from the liquid in a controlled manner. The vapour pressure of cyclohexane at room temperature was found to be suitable to produce the required gas flow into the system to allow a plasma to be struck.

In the case of the samples prepared from an acetylene precursor, the source gas

could be admitted directly into the Fab 104-2 source, via a mass flow controller, without any preparation procedures. For the samples prepared from an acetylene precursor and those produced from either cyclohexane or deuterocyclohexane the deposition source current and voltage were set to the required value as described for argon.

Samples deposited using the fast atom source

Table (3.2) gives the deposition parameters for each of the samples deposited using the fast atom source including precursor composition, source current and deposition voltage. The source current quoted relates to that measured at the walls of the plasma chamber, I_s, as shown in Figure (3.2). The corresponding neutral flux at the sample is determined by the fraction of ions that are incident on the cathode at a position on the grid in the cathode walls and hence travel on and through to the sample substrate. The flux at the substrate is therefore found to be proportional to the measured source current [48].

The Fab104-2 source is capable of delivering a maximum beam output of 100mA equivalent ion current per cell. However, the sample deposition rate at the substrate is also a function of the source gas as the species arriving at the substrate are in general larger for a larger precursor gas molecule. For the thin film samples deposited from an acetylene precursor, detailed in Table (3.2), a deposition rate of $\sim 0.5\mu$m per hour was obtained. For the powder samples deposited from cyclohexane a sample of $\sim$ 0.3g would be deposited from a continuous 24 hour run of the fast atom source. The materials efficiency of the system was generally found to be approximately 1% (i.e. 1g of material was deposited for every 100g equivalent of precursor gas consumed).

The compositional measurements given in Table (3.2) for powder samples 1 and

Sample	Precursor Gas	C_6H_{12}/C_6D_{12} Gas Ratio	Source Voltage (kV)	Source Current(mA)	Particle Impact Energy(keV)	Composition
Powder 1	cyclohexane (C_6H_{12})	1:0	1.2	200	1.02	a-$C_{0.75}$:$H_{0.25}$
Powder 2	deuterocyclohexane (C_6D_{12})	0:1	1.1	200	0.94	a-$C_{0.73}$:$D_{0.27}$
Powder 3	cyclohexane/ deuterocyclohexane	0.56:1	1.1	200	0.94	a-$C_{0.74}$:$D_{0.09}$:$H_{0.17}$
Powder 4	acetylene (C_2H_2)	-	1.0	160	0.85	a-$C_{0.78}H_{0.22}$
Film 1	acetylene (C_2H_2)	-	1.3	400	1.11	-
Film 2	acetylene (C_2H_2)	-	1.5	380	1.28	-

Table 3.2: Deposition parameters for a-C:H(D) fast atom source samples

2 were determined using a Carlo-Erba CHN combustion analyser. This work was carried out at the Dept. of Chemistry, University of Kent. This analysis technique involves burning a small sample of the material in pure oxygen at $\sim 900°C$. The diffusion rates of the oxide vapours produced may be related to their mass, allowing a measurement of the C:H ratio of the original sample to be determined. In each case three measurements were made per sample and an average composition determined. The compositional variation between the three measurements made was within 1% for each of the materials analysed.

It can be seen from Table (3.2) that three samples of a-C:H having varying degrees of isotopic substitution were produced using very similar deposition parameters from a combination of cyclohexane and deuterocyclohexane precursors. If the deposition process for the samples is determined purely by the relevant parameters set for the plasma, i.e. gas flow, source current and voltage, then the atomic structure of the three samples would be expected to correspond to one another. If this is the case then neutron scattering studies on these three samples may be used to provide a measure of the partial structure factors for this particular phase of amorphous hydrogenated carbon. Thus these samples were deposited partly to test whether isotopically substituted, structurally equivalent a-C:H samples could be deposited in a fast atom source, and then, if so, to allow a more detailed investigation of the a-C:H phase produced.

The deuterated cyclohexane (C_6D_{12}) used in the production of Samples 2 and 3 was purchased sealed in 10ml ampoules to prevent its conversion to C_6H_{12}, which occurs on contact with air. To avoid such a conversion when the C_6D_{12} was introduced into the stainless steel cylinder, the residual air above the liquid C_6D_{12} was immediately drawn off through the vacuum system (as described for C_6H_{12}). To prevent contamination of Samples 2 and 3 from previous sample depositions involving C_6H_{12}

care was taken to pump out all traces of the latter from the cylinder and the pipework to the vacuum system. This process was monitored using the mass spectrometer.

Null mixture sample

As described in Chapter 4, a "null mixture" sample of a-C:H is one in which the degree of isotopic substitution is such that the neutron scattering length for the hydrogen matrix is zero. If b_H and b_D represent the coherent neutron scattering cross-sections for hydrogen and deuterium, then such a sample would be required to contain a hydrogen to deuterium atomic ratio such that:

$$c_H b_H + c_D b_D = 0 \tag{3.1}$$

where c_H and c_D are the atomic concentrations of hydrogen and deuterium respectively. As b_H=-3.7423fm and b_D=6.674fm [49], the required hydrogen to deuterium atomic ratio for a "null mixture" sample is:

$$\frac{c_D}{c_H} = 0.5067 \tag{3.2}$$

To allow suitable statistics on the neutron diffraction data to be achieved in a viable time, a sample mass of approximately 0.5g is required. As the materials efficiency of the Fab104-2 source is approximately 1%, to produce such a sample $\sim$ 50g of a liquid C_6H_{12}/C_6D_{12} mixture is required. As the atomic mass of C_6H_{12}=84.16g and that of C_6D_{12}=96.16g a liquid mixture containing 20g of C_6D_{12} and 31.22g of C_6H_{12} was prepared, placed immediately in the stainless steel cylinder and the previously described preparation and deposition processes carried out. Such a mixture was prepared on the assumption that the deposited material's composition would be identical to that of the precursor liquid mixture. The independently measured composition for the material given in Table (3.2) is very close to that required for a "null" sample, the

ratio $\frac{c_D}{c_H}$ being 0.4999±0.0025. This compositional measurement was made by Drs A. Morse and S. Russell of the Planetary Science Unit, Dept. of Earth Sciences, Open University, by analysis of the combustion products of a sample of this material. This has been confirmed by Rutherford back scattering analysis by Dr. C Jeynes, Dept. of Electronic and Electrical Engineering, University of Surrey. The resultant effective scattering length for hydrogen in this material is discussed in Section (8.1.3).

From the powder sample compositions given in Table (3.2) it can be seen that it has been possible to deposit a series of a-C:H materials with a controlled level of isotopic substitution. In Chapters (8) and (9) these samples are used in neutron and X-ray diffraction experiments to study the structural configuration of this phase of a-C:H. In Chapter (7) the thin film samples listed in Table (3.2) are examined *in situ* using glancing angle X-ray diffraction techniques.

Chapter 4

Thermal Neutron and X-ray Scattering Theory

Since the advent of the first nuclear reactor in 1945 at the Argonne National Laboratory, U.S.A., thermal neutrons have become a valuable tool for the study of condensed matter. The de Broglie wavelength, λ, of a neutron of mass m and velocity v is given by

$$\lambda = \frac{h}{mv} = \frac{0.286}{\sqrt{E}} \mathring{A} \tag{4.1}$$

where h is the Planck constant and E is the energy of the neutron in eV. The value of the mass of the neutron is such that the corresponding neutron wavelength at thermal energies is of the order of the interatomic distances in a solid ($\sim 1\mathring{A}$). Thus interference effects occur when thermal neutrons are scattered by a target which may be related to the structure of the scattering system. As neutrons are uncharged they can penetrate deeply into a target (no Coulomb barrier) and are thus scattered by nuclear forces. X-rays, likewise in the wavelength region around $1\mathring{A}$, may similarly be used to investigate the structure of a material but, in contrast to neutrons, are scattered

by the electrons in a target. Used in conjunction, neutron and X-ray scattering can contribute complementary information on the structural characteristics of a material which combined can provide a clearer picture of the structure being probed.

4.1 Neutron Scattering Theory

The theory of neutron scattering may be found in several texts. Most notably it is covered in detail in [50] and [51] and more briefly in [52], [53] and [54].

4.1.1 The first Born Approximation and the Fermi Pseudo-Potential

The geometry of the scattering problem is shown in Figure (4.1). Consider an incident neutron which has the state ψ_k. The scattered neutron has a state $\psi_{k'}$ and propagates at a polar angle θ and an azimuthal angle ϕ to the incident neutron. If the number of neutrons incident on the target sample per unit area per unit time is N then the number scattered per unit time into unit solid angle $\mathrm{d}\Omega = sin\theta d\theta d\phi$ is

$$N(\frac{d\sigma}{d\Omega})\sigma \tag{4.2}$$

where $\frac{d\sigma}{d\Omega}$ is the differential cross-section of the sample. σ is the total cross-section and has the dimensions of area.

In order to calculate $\frac{d\sigma}{d\Omega}$ for this case it is necessary to know the probability for a change of neutron state from that defined by the plane wave **k** to that defined by **k'**, both having the energy

$$E = \frac{\hbar^2 k^2}{2m} \tag{4.3}$$

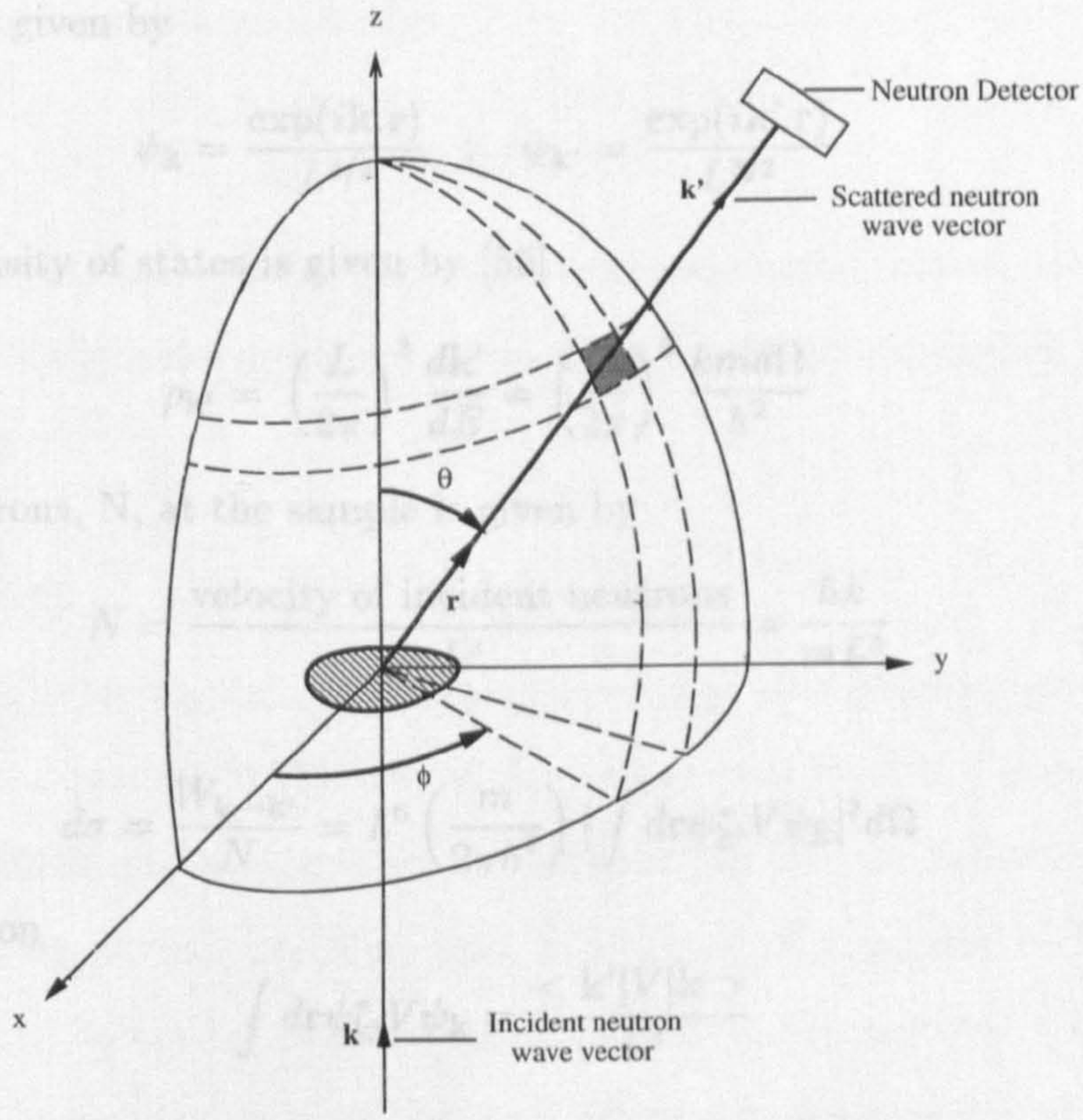

Figure 4.1: Scattering Geometry

As the neutron scattering is a weak process and the sample response linear, it may be described using first-order perturbation theory. Thus the probability for this change of state is given by Fermi's golden rule

$$W_{\mathbf{k}\to\mathbf{k}'} = \frac{2\pi|\int d\mathbf{r}\psi_{\mathbf{k}'}V\psi_{\mathbf{k}}|^2\rho_{\mathbf{k}'}(E)}{\hbar} \tag{4.4}$$

where V is the interaction potential causing the state transition i.e. that between the incident neutron and the target sample, and $\rho_{\mathbf{k}'}(E)$ is the density of final scattering states per unit energy range.

The normalized forms of the wave functions $\psi_{\mathbf{k}}$ and $\psi_{\mathbf{k}'}$ for the case of a large box

of volume L_3 are given by

$$\psi_{\mathbf{k}} = \frac{\exp(i\mathbf{k}.\mathbf{r})}{L^{3/2}} \quad , \quad \psi_{\mathbf{k}'} = \frac{\exp(i\mathbf{k}'.\mathbf{r})}{L^{3/2}} \tag{4.5}$$

and the final density of states is given by [55]

$$\rho_{\mathbf{k}'} = \left(\frac{L}{2\pi}\right)^3 \frac{d\mathbf{k}'}{dE} = \left(\frac{L}{2\pi}\right)^3 \frac{km d\Omega}{\hbar^2} \tag{4.6}$$

The flux of neutrons, N, at the sample is given by

$$N = \frac{\text{velocity of incident neutrons}}{L^3} = \frac{\hbar k}{mL^3} \tag{4.7}$$

Therefore

$$d\sigma = \frac{W_{\mathbf{k}\to\mathbf{k}'}}{N} = L^6 \left(\frac{m}{2\pi\hbar^2}\right) |\int d\mathbf{r}\psi^*_{\mathbf{k}'} V \psi_{\mathbf{k}}|^2 d\Omega \tag{4.8}$$

Using the notation

$$\int d\mathbf{r}\psi^*_{\mathbf{k}'} V \psi_{\mathbf{k}} = \frac{< \mathbf{k}'|V|\mathbf{k} >}{L^3} \tag{4.9}$$

then

$$\frac{d\sigma}{d\Omega} = \left(\frac{m}{2\pi\hbar^2}\right) | < \mathbf{k}'|V|\mathbf{k} > |^2 \tag{4.10}$$

The scattering amplitude may now be defined such that

$$\frac{d\sigma}{d\Omega} = |f(\mathbf{k}, \mathbf{k}')|^2 \tag{4.11}$$

where

$$f\,|(\mathbf{k}, \mathbf{k}')|^2 = \frac{-m}{2\pi\hbar^2} < \mathbf{k}'|V|\mathbf{k} > \tag{4.12}$$

If the scattering process is inelastic (i.e. one in which the scattered neutron energy varies from that of the incident neutron) and involves a change of neutron state from its initial state α to its final one α' combined with a target energy change from E_α to $E_{\alpha'}$ then we may define the cross-section as follows

$$\left(\frac{d\sigma}{d\Omega}\right)_{\substack{\mathbf{k},\alpha \\ \mathbf{k}',\alpha'}} = \frac{\mathbf{k}'}{\mathbf{k}} \left(\frac{m}{2\pi\hbar^2}\right)^2 |< \mathbf{k}'\alpha'|V|\mathbf{k}\alpha >|^2 \tag{4.13}$$

From the laws of conservation of energy

$$\frac{\hbar^2 k^2}{2m} + E_\alpha = E_{\alpha'} + \frac{\hbar^2 k'^2}{2m} \tag{4.14}$$

Incorporating this into the cross-section we may define a partial cross-section involving a change of state of the incident neutron from $\mathbf{k}$ to $\mathbf{k}'$ and a corresponding target state change from α to α'

$$\left(\frac{d^2\sigma}{d\Omega dE'}\right)_{\substack{\mathbf{k},\alpha \\ \mathbf{k}',\alpha'}} = \frac{\mathbf{k}'}{\mathbf{k}}\left(\frac{m}{2\pi\hbar^2}\right)^2 |< \mathbf{k}'\alpha'|V|\mathbf{k}\alpha >|^2 \delta(\hbar\omega + E_\alpha - E_{\alpha'}) \tag{4.15}$$

To obtain the total partial cross-section involving all scattering processes it is necessary to sum Equation (4.15) over all final target states α' and average over all initial states α taking into account isotopic distributions over the target, nuclear spin orientations, precise nuclear positions and, in the case of magnetic nuclei, electron spin orientations. Also taking into account initial and final spin states of the neutron, β and β' respectively with corresponding probability distributions p_β and $p_{\beta'}$ we have

$$\left(\frac{d^2\sigma}{d\Omega dE'}\right) = \frac{\mathbf{k}'}{\mathbf{k}}\left(\frac{m}{2\pi\hbar^2}\right)^2 \sum_{\alpha,\beta} p_\alpha p_\beta \sum |< \mathbf{k}'\beta'\alpha'|V|\mathbf{k}\beta\alpha >|^2 \delta(\hbar\omega + E_\alpha - E_{\alpha'}) \tag{4.16}$$

where p_α is the probability of initial target state α. Since the transition probability was derived from perturbation theory this expression for the cross-section is an approximation and Equation (4.16) is thus denoted the first Born approximation.

As the wavelength of incident neutrons at thermal energies ($\sim 10^{10}m$) is much greater than both the mean nuclear radius and the interaction range of the incident neutron-nucleus force (the latter has been experimentally determined to be $1.5\times^{-15m}$) then the resultant scattering contains only s-wave components. Thus the scattering process is isotropic and can be defined by a single parameter, the scattering length, b, which may be complex. The imaginary part of b represents absorption, which at thermal energies mainly involves radiative capture, and in most cases is quite small.

In general b varies between atom types and also between isotopes of the same atom. b also depends upon the relative orientation of the neutron and nuclear spin (assuming the latter exists).

The only form of the interaction potential V that leads to isotropic scattering when using the first Born approximation is the Fermi pseudo-potential, given as follows

$$V(\mathbf{r}) = \frac{2\pi\hbar b}{m}\delta(\mathbf{r} - \mathbf{R}) \tag{4.17}$$

where **R** defines the position of the nucleus. Substituting for V in equation 1.15 and taking **R**=0 then f, the scattering amplitude, becomes

$$f = -\left(\frac{m}{2\pi\hbar^2}\right)\frac{2\pi\hbar^2 b}{m}\int d\mathbf{r}\exp(-i\mathbf{k}'.\mathbf{r})\delta(\mathbf{r})\exp(i\mathbf{k}.\mathbf{r}) = -b \tag{4.18}$$

Thus from Equation (4.12)

$$\frac{d\sigma}{d\Omega} = |b|^2 \tag{4.19}$$

and therefore the total cross-section is

$$\sigma = 4\pi\,|b|^2 \tag{4.20}$$

4.1.2 The Van Hove Scattering Law

The Van Hove scattering law [56] relates the partial scattering cross-section per unit energy range to the dynamic structure function $S(\mathbf{Q},\omega)$ where $\mathbf{Q} = \mathbf{k}'$ - $\mathbf{k}$ is the wavevector transfer vector for the scattering process as shown in Figure (4.2) and the energy transfer $E = \hbar\omega$. It can be seen from Figure (4.2) that Q is given in this case as

$$Q = \frac{4\pi}{\lambda}sin(\theta) \tag{4.21}$$

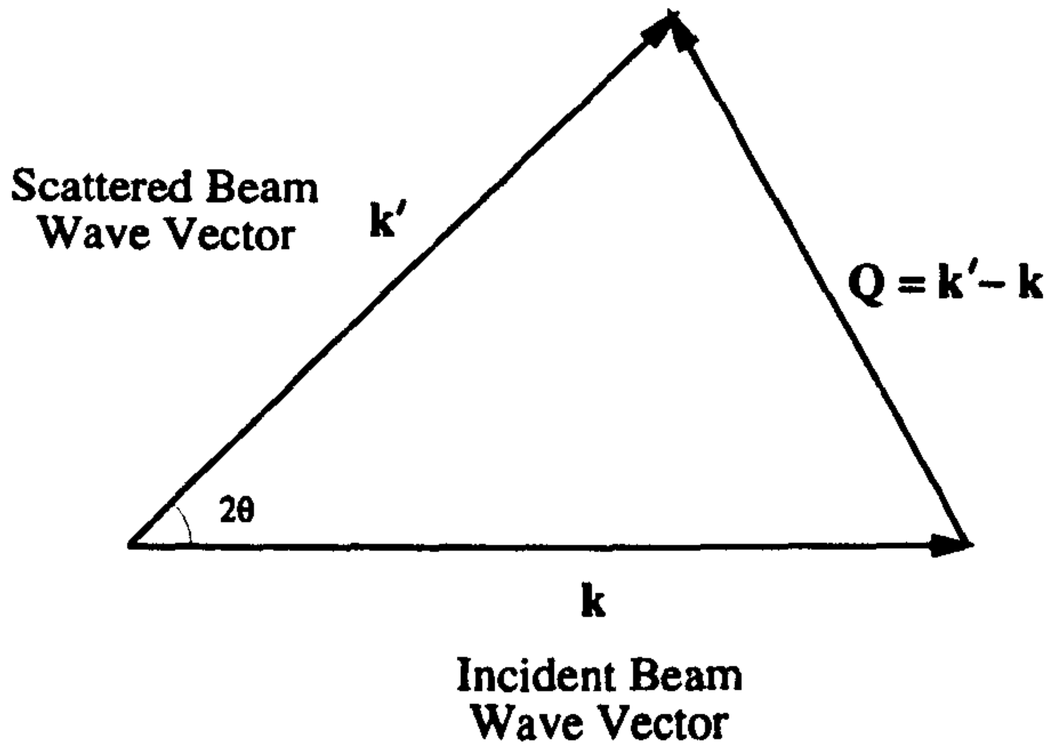

Figure 4.2: Scattering vector Q

where 2θ is the angle between the incident and scattered beam.

For an assembly of N independent atoms

$$\frac{d^2\sigma}{d\Omega d\omega} = Nb^2 \left|\frac{\mathbf{k}'}{\mathbf{k}}\right| S(\mathbf{Q},\omega) \tag{4.22}$$

where

$$S(\mathbf{Q},\omega) = \frac{1}{2\pi}\int_{-\infty}^{\infty} \exp(-i\omega t)\int_{0}^{\infty} \exp(i\mathbf{Q}.\mathbf{r})G(\mathbf{r},t)d\mathbf{r}dt \tag{4.23}$$

$S(\mathbf{Q},\omega)$ represents the probability of the neutron exchanging an energy $\hbar\omega$ and a momentum $\mathbf{Q}$ with the system and $G(\mathbf{r},t)$, the Van Hove pair correlation function, is the probability of finding an atom at $\mathbf{r}$ at a time t when at $t = 0$ there is an atom at $\mathbf{r} = 0$.

4.1.3 The Static Approximation

If the assumption is made that the nucleus does not recoil during the scattering process, and therefore that the energy transfer that takes place is small compared to the incident neutron energy, then the scattering can be taken to be elastic to a good approximation. If this is the case we can sum over all final states of the target system

at constant $\mathbf{Q}$ in Equation (4.16) and put $\mathbf{k}' = \mathbf{k}$ so that Equation (4.22) becomes

$$\frac{d^2\sigma}{d\Omega d\omega} = Nb^2 \int_{-\infty\, const Q}^{\frac{E}{\hbar}} d\omega S(\mathbf{Q},\omega) \tag{4.24}$$

$$\frac{d\sigma}{d\Omega} = Nb^2 S(\mathbf{Q}) \tag{4.25}$$

This is known as the static approximation and $S(\mathbf{Q})$ is the static structure factor. Although the static approximation reduces the cross-section to elastic scattering it is distinct from purely elastic scattering. The former, by definition, includes all possible final states whereas elastic scattering involves only states for which $\alpha = \alpha'$ in Equation (4.16). Assuming the static approximation, the differential cross-section may be written as [50]

$$\frac{d\sigma}{d\Omega} = < \left| \sum_{i=1}^{N} b_i \exp(i\mathbf{Q}.\mathbf{r}_i) \right|^2 > \tag{4.26}$$

where b_i and $\mathbf{r}_i$ are the scattering length and vector position of the i^{th} atom respectively. $S(\mathbf{Q})$ is defined as follows [57]

$$S(\mathbf{Q}) = \frac{1}{N} < \sum_{i=1}^{N}\sum_{j=1}^{N} \exp(-i\mathbf{Q}.\mathbf{r}_i) \exp(i\mathbf{Q}.\mathbf{r}_j) > \tag{4.27}$$

$$= 1 + < \sum_{i\neq j}^{N} \int\int \exp[-i\mathbf{Q}.(\mathbf{r}-\mathbf{r}')]\delta(\mathbf{r}-\mathbf{r}_i)\delta(\mathbf{r}'-\mathbf{r}_j)d\mathbf{r}d\mathbf{r}' > \tag{4.28}$$

where $< >$ denotes an ensemble average for all atoms i,j and $\mathbf{r}_i$ is the position vector for the i^{th} atom. The second term in Equation (4.28) is related [57] to the pair distribution function $g(\mathbf{r})$ which is defined such that if the sample volume is V and therefore the average number density $\rho_0 = N/V$ then $\rho_0 g(\mathbf{r})d\mathbf{r}$ gives the probability of finding a particle at $\mathbf{r}$ to $\mathbf{r} + d\mathbf{r}$ from an atom at the origin. Thus $S(\mathbf{Q})$ may be given as

$$S(\mathbf{Q}) = 1 + \rho \int \exp(-i\mathbf{Q}.\mathbf{r}) g(\mathbf{r}) d\mathbf{r} \tag{4.29}$$

$$= 1 + (2\pi)^3 \delta(\mathbf{Q}) + \rho \int \exp(-i\mathbf{Q}.\mathbf{r})[g(\mathbf{r}) - 1]d\mathbf{r} \tag{4.30}$$

The delta function in Equation (4.30) corresponds experimentally to forward scattering and can be neglected. Thus

$$S(\mathbf{Q}) = 1 + \rho \int \exp(-i\mathbf{Q}.\mathbf{r})[g(\mathbf{r}) - 1]d\mathbf{r} \tag{4.31}$$

and hence

$$g(\mathbf{r}) = 1 + \frac{1}{(2\pi)^3\rho} \int \exp(i\mathbf{Q}.\mathbf{r})[S(\mathbf{Q}) - 1]d\mathbf{Q} \tag{4.32}$$

Thus it is possible to access the real space pair distribution function for a sample, and its corresponding information on the atomic positions, through Fourier inversion of the experimentally available structure factor. In practice the range of the integral in Equation (4.32) is limited to the experimentally accessible $\mathbf{Q}$ range.

4.1.4 Incoherent and Coherent scattering

For a monatomic system the value of b in Equation (4.25) will vary from atom to atom due to isotopic and spin effects. Assuming there is no correlation between b_l and $b_{l'}$ where l and l' refer to different atomic sites then

$$\overline{b^*_{l'} b_l} = \overline{b^*_{l'}}\,\overline{b_l} = |\bar{b}|^2 \qquad \text{if } l \neq l' \tag{4.33}$$

$$\overline{b^*_{l'} b_l} = \overline{|b_l|^2} = \overline{|b|^2} \qquad \text{if } l = l' \tag{4.34}$$

so that in general

$$\overline{b^*_{l'} b_l} = |\bar{b}|^2 + \delta_{l,l'}(\overline{|b|^2} - |\bar{b}|^2) \tag{4.35}$$

Thus Equation (4.25) may be written as follows

$$\begin{aligned} \frac{d\sigma}{d\Omega} &= N(\overline{|b|^2} - |\bar{b}|^2) + |\bar{b}|^2 N S_{coh}(\mathbf{Q}) \\ \frac{d\sigma}{d\Omega} &= \frac{d\sigma}{d\Omega}_{inc} + \frac{d\sigma}{d\Omega}_{coh} \end{aligned} \tag{4.36}$$

where $\frac{d\sigma}{d\Omega}_{inc}$ and $\frac{d\sigma}{d\Omega}_{coh}$ are the incoherent and coherent cross-sections respectively. Thus the scattering from the target may be considered as the sum of that from an

assembly of N atoms having the average scattering length $\bar{b}$ and a second contribution which is the sum of the scattering from individual nuclei which depends on the spread in scattering lengths. An incoming neutron sees a system in which the scattering potential varies from one point to the next. It is only the average potential that can give interference effects and the coherent scattering contribution. As the average scattering potential is proportional to $\bar{b}$ then the coherent scattering cross-section is proportional to $|\bar{b}|^2$. The deviations from the average potential are randomly distributed and therefore cannot produce interference effects. Thus the incoherent scattering is proportional to the mean-square deviation, i.e. to $\overline{|b-\bar{b}|^2} = \overline{|b|^2} - |\bar{b}|^2$.

4.1.5 Corrections to the Static Approximation

An atom may be considered bound and the static approximation to hold if the mass of the atom is very large compared to the mass of the neutron. If this does not hold and any energy transfer to the target system cannot be considered small compared to the initial neutron energy then corrections must be made to the static structure factor to compensate for the divergence from the static approximation. Placzek [58] gave a method of calculating these corrections involving expanding $S(Q,\omega)$ in powers of $\frac{\hbar\omega}{E}$ also taking into account the change in detector efficiency with scattered neutron energy. In general these corrections are not suitable for very low mass atoms such as hydrogen and deuterium as higher order mass dependent terms in the expansion become more significant and the expansion does not converge. These corrections are discussed in more detail in Section (6.3.6).

4.1.6 Multicomponent Systems

For a multicomponent system it is often more convenient to use the Faber-Ziman formalism for the total cross-section [59] in which the latter is separated into self and distinct components rather than coherent and incoherent. For a diatomic system containing atom types α and β Equation (4.26) becomes

$$\frac{d\sigma}{d\Omega} = < \sum_{\alpha} \sum_{\beta} b_{\alpha} b_{\beta} \exp(-i\mathbf{Q}.\mathbf{R}_{\alpha}) \exp(i\mathbf{Q}.\mathbf{R}_{\beta}) > \quad (4.37)$$

$$= < \sum_{\alpha} \sum_{\beta} b_{\alpha} b_{\beta} \delta_{\alpha\beta} + \sum_{\alpha} \sum_{\alpha \neq \beta} b_{\alpha} b_{\beta} \exp(-i\mathbf{Q}.(\mathbf{R}_{\alpha} - \mathbf{R}_{\beta})) > \quad (4.38)$$

where $\mathbf{R}_{\alpha}$ and $\mathbf{R}_{\beta}$ are used to label *sets* of position vectors for atoms of the α and β species respectively. It is useful to introduce a function $g_{\alpha\beta}(\mathbf{r})$ analogous to that of $g(\mathbf{r})$ given in Equation (4.32) which defines the probability of finding an atom β at a distance $\mathbf{r}$ from an α type atom at the origin. By analogy with Equation (4.32)

$$g_{\alpha\beta}(\mathbf{r}) = 1 + \frac{1}{(2\pi)^3 \rho} \int \exp(i\mathbf{Q}.\mathbf{r})[S_{\alpha\beta}(\mathbf{Q}) - 1] d\mathbf{Q} \quad (4.39)$$

and

$$S_{\alpha\beta}(\mathbf{Q}) = 1 + \rho \int \exp(-i\mathbf{Q}.\mathbf{r})[g_{\alpha\beta}(\mathbf{r}) - 1] d\mathbf{r} \quad (4.40)$$

$g_{\alpha\beta}(\mathbf{r})$ and $S_{\alpha\beta}$ are known as partial pair distribution and partial structure functions respectively. If c_{α} and c_{β} are the concentrations of the two species in the system and the second term in Equation (4.38) is replaced by its relation to $g_{\alpha\beta}(\mathbf{r})$ then

$$\frac{d\sigma}{d\Omega} = \sum_{\alpha} \sum_{\beta} b_{\alpha} b_{\beta} (N c_{\alpha} \delta_{\alpha\beta} + N c_{\alpha} c_{\beta} \rho \int \exp(i\mathbf{Q}.\mathbf{r})[g_{\alpha\beta}(\mathbf{r}) - 1] d\mathbf{r}) \quad (4.41)$$

$$= \sum_{\alpha} \sum_{\beta} b_{\alpha} b_{\beta} \left(N c_{\alpha} \delta_{\alpha\beta} + N c_{\alpha} c_{\beta} (S(\mathbf{Q}) - 1)\right) \quad (4.42)$$

$$= \sum_{\alpha} N c_{\alpha} b_{\alpha}^2 + \sum_{\alpha} \sum_{\beta} N c_{\alpha} c_{\beta} b_{\alpha} b_{\beta} (S_{\alpha\beta}(\mathbf{Q}) - 1) \quad (4.43)$$

$$= \frac{d\sigma}{d\Omega}_{self} + \frac{d\sigma}{d\Omega}_{dist} \quad (4.44)$$

In general for an M component system there will be $M(M+1)/2$ partial structure factors e.g. for an a-C:H sample there will be three; $S(\mathbf{Q})_{\mathbf{C-H}}$, $S(\mathbf{Q})_{\mathbf{C-C}}$ and $S(\mathbf{Q})_{\mathbf{H-H}}$.

4.2 X-ray Scattering

Scattering of X-rays by a target occurs when an X-ray photon interacts with one electron of the target atom. If the scattering is elastic (i.e. no energy lost during the collision) then the scattering is said to be coherent and is known as Rayleigh scattering. The coherence occurs because the scattered radiation has the same wavelength as the incident radiation and a definite phase relationship exists between the incident and scattered beam. If the collision process is inelastic then fluorescence or Compton scattering may occur. Fluorescence occurs when the energy of the incident X-rays is great enough to eject an electron from an inner shell of the target atom. The resultant electron cascade from higher energy shells to fill the empty inner shell results in the emission of radiation at wavelengths characteristic of the atom type involved. Compton scattering occurs when the incident X-ray transfers a small amount of its energy to a loosely bound electron. As a consequence the scattered radiation will be of a wavelength slightly longer than the incident one.

X-ray scattering theory is covered in several texts [60], [61], [62] and the use of X-ray and neutron scattering techniques for the study of amorphous solids and/or liquids has been reviewed by many authors [63], [64] , [65].

4.2.1 Coherent Scattering

Consider the scattering of X-rays by a single, free electron according to classical theory. In Figure (4.3) an unpolarized X-ray beam propagating along the y-axis is

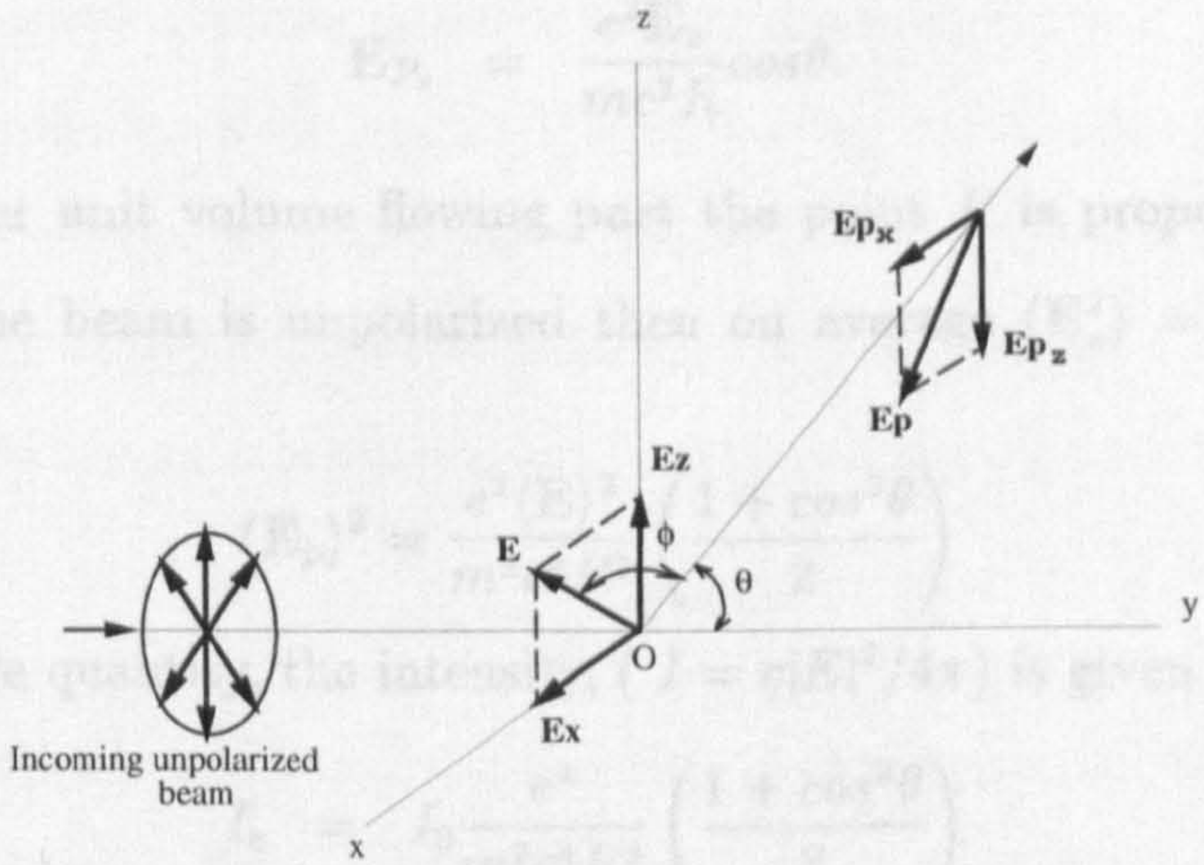

Figure 4.3: X-ray Scattering of Unpolarized Beam By a Single Electron

incident upon an electron at O. Let $E = E_0 \exp(i\omega t)$ be the electric field vector at time t. Assuming the electron has a small velocity compared to c then it will receive an acceleration $\mathbf{a}$ such that $\mathbf{a} = e\mathbf{E}/m$ where e and m are the charge and mass of the electron respectively. This accelerated electron will in turn become a source of radiation having the same frequency ω.

This interaction will thus produce a scattered beam at the point P and the same time t of the form

$$\mathbf{E}_P = \mathbf{E}\frac{e^2}{mc^2R}sin\theta \tag{4.45}$$

where

$$\mathbf{E} = \mathbf{E}_0 e^{i\omega(t-\frac{r}{c})} \tag{4.46}$$

R is the distance OP and θ is the angle between the scattering direction and the direction of acceleration of the electron. The negative sign simply indicates that the forward scattered beam has the opposite phase to the incident beam. If P is taken to lie in the yz plane then the components of $\mathbf{E}_p$ along the x and z directions are

$$\mathbf{E}_{P_x} = \frac{e^2\mathbf{E}_x}{mc^2R} \tag{4.47}$$

$$\mathbf{E}_{P_z} = \frac{e^2\mathbf{E}_z}{mc^2R}cos\theta. \tag{4.48}$$

The energy per unit volume flowing past the point P is proportional to $\mathbf{E}_P^2 = \mathbf{E}_{P_x}^2 + \mathbf{E}_{P_z}^2$. If the beam is unpolarized then on average $\langle\mathbf{E}_x^2\rangle = \langle\mathbf{E}_z^2\rangle = \langle\mathbf{E}^2\rangle/2$. Therefore

$$\langle\mathbf{E}_p\rangle^2 = \frac{e^2\langle\mathbf{E}\rangle^2}{m^2c^4R^2}\left(\frac{1+cos^2\theta}{2}\right) \tag{4.49}$$

and the observable quantity, the intensity, ($I = c|E|^2/4\pi$) is given by

$$I_e = I_0\frac{e^4}{m^2c^4R^2}\left(\frac{1+cos^2\theta}{2}\right) \tag{4.50}$$

$$= I_0\frac{{r_e}^2}{R^2}\left(\frac{1+cos^2\theta}{2}\right) \tag{4.51}$$

where r_e is the classical electron radius. Equation (4.51) is known as the Thomson scattering equation and gives the intensity of classical scattering by a single free electron. The factor in parenthesis is the polarization factor for an unpolarized primary beam.

The classical differential scattering cross-section per electron for Thomson scattering is given by [61]

$$\left(\frac{d\sigma_e}{d\Omega}\right)_{Thom} = \frac{\text{Energy radiated / unit time / unit solid angle}}{\text{Incident energy flux in energy /unit area/ unit time}} \tag{4.52}$$

$$= \frac{I_e}{I_0}R^2 \tag{4.53}$$

$$= r_e^2\left(\frac{1+cos^2\theta}{2}\right) \tag{4.54}$$

The classical scattering cross-section per electron is [61]

$$\sigma_e = \int\left(\frac{d\sigma_e}{d\Omega}\right)2\pi sin\theta d\theta = \frac{8\pi}{3}r_e^2 = 6.66\times10^{25}cm^2 \tag{4.55}$$

Now consider the cooperative effect of all the electrons in an atom (Rayleigh scattering). Each electron will be forced into vibration at the frequency of the incident

X-ray beam and, assuming this is much greater than its natural frequency, will be in anti-phase with the incident beam. The scattering amplitudes produced by each electron at the point of observation are added and then squared to obtain the intensity of coherent scattering so that the cross-section per electron is now non-additive. We may now introduce an atomic scattering cross-section σ_a such that

$$\sigma_a = \frac{8\pi}{3} r_e^2 f^2(\theta) \tag{4.56}$$

where $f(\theta)$ is the atomic scattering factor which gives the ratio of the amplitude of the radiation scattered by the atom to the amplitude which would be scattered by a single electron according to classical theory. If we assume the sample to have an electron density $\rho_e(\mathbf{r})$ which interacts with the incident beam, we may define a scattering amplitude per atom in electron units i.e. in terms of the amplitude scattered by a classical free electron in the same situation as the sample, by

$$A_{eu}(\mathbf{Q}) = \int \rho_e(\mathbf{r}) e^{-i\mathbf{Q}.\mathbf{r}} d\mathbf{r} \tag{4.57}$$

where $\mathbf{Q}$ is again the scattering vector (see Figure (4.2)).

To gain information on the atomic positions in the sample it is useful to express the total electron density of the sample as a superposition of electron densities centred at the atomic sites i.e.

$$\rho_e(\mathbf{r}) = \sum_n (\mathbf{r} - \mathbf{r}_n) \tag{4.58}$$

So that the amplitude becomes

$$A_{eu}(\mathbf{Q}) = \int \sum_n \rho_n(\mathbf{r} - \mathbf{r}_n) e^{-i\mathbf{Q}.\mathbf{r}} d\mathbf{r} \tag{4.59}$$

$$= \sum_n e^{-i\mathbf{Q}.\mathbf{r}_n} \int \rho_n(\mathbf{r} - \mathbf{r}_n) e^{-i\mathbf{Q}.(\mathbf{r}-\mathbf{r}_n)} d(\mathbf{r} - \mathbf{r}_n) \tag{4.60}$$

$$= \sum_n f_n(\mathbf{Q}) e^{-i\mathbf{Q}.\mathbf{r}_n} \tag{4.61}$$

where f_n, the scattering factor of atom n, is

$$f_n(\mathbf{Q}) = \int \rho_n e^{-i\mathbf{Q}.\mathbf{r}} d\mathbf{r} \tag{4.62}$$

i.e. it is the Fourier transform of the electron density of the atom.

Scattering factors can be calculated from the electronic wave functions of the atoms and may be found in tabulated form e.g. [66]. Calculations are usually made for free atoms and ions assumed to be spherically symmetric. In this case the scattering factor depends only on the modulus of the scattering vector and not on its direction. Although this assumption is incorrect for atoms with incomplete electron shells or those involved in covalent bonding, the scattering factors are not in general particularly sensitive to distortions in electron density. However it can become more of a problem for low Z atoms where the fraction of the total atom electron number involved in chemical bonding may become significant. Hydrogen, for example is unique in that its 1s electron serves as both core and valence electron resulting in a substantial distortion of the atom electron density function in the presence of molecular binding. For application to terminally bonded hydrogen (e.g. in C-H) Stewart et al [67], [68] have calculated the atomic scattering factor over the range 0 to 1.72Å.

The intensity measured during a diffraction experiment is proportional to the square of the scattering amplitude such that

$$I_{eu}^{coh}(\mathbf{Q}) = \left| \sum_n f_n e^{-i\mathbf{Q}.r_n} \right|^2 \tag{4.63}$$

$$= \sum_n \sum_m f_n f_m e^{i} Q.r_{nm} \tag{4.64}$$

which gives the coherent scattered intensity in electron units. For an isotropic system such as an amorphous material, where each vector $\mathbf{r}_{nm}$ takes all possible orientations with equal probability, each term of the double summation in Equation (4.64) can be

averaged over all directions for a fixed interatomic vector modulus i.e.

$$I_{eu}^{coh}(Q) = \sum_n \sum_m f_n f_m \frac{1}{4\pi} \int_0^{\pi} \int_0^{2\pi} e^{-iQ.r} cos\alpha sin\alpha d\alpha d\phi \tag{4.65}$$

$$= \sum_{n=1}^{N_a} \sum_{m=1} N_a f_n f_m sin\left(\frac{sinQ.r_{nm}}{Q.r_{nm}}\right) \tag{4.66}$$

where N_a is the total number of atoms in the scattering volume. The intensity now depends on the modulus of **Q**. Equation (4.66) is called the Debye scattering equation.

4.2.2 Multicomponent Systems

Consider a system containing M different atomic species. If x_i is the fractional concentration of atomic type i in the system and N is the total number of atoms then using Equation (4.66)

$$\frac{I_{eu}^{coh}}{N} = \sum_{i=1}^{M} x_i f_i^2 + \sum_{i=1}^{M} x_i f_i \sum_{m=1}^{N_a} f_m \left(\frac{sinQ.r_{nm}}{Q.r_{nm}}\right) \tag{4.67}$$

where the sums are taken over all the atomic species for i and over all atoms for m. The first term in Equation (4.67) represents the coherent independent scattering i.e. the elastic scattering that would result if all atoms scattered independently without interference effects. The second term contains the structural information on the scattering system. Let

$$i(Q) = \sum_{i=1}^{M} x_i f_i \sum_{m=1}^{N_a} f_m \left(\frac{sinQ.r_{nm}}{Q.r_{nm}}\right) \tag{4.68}$$

If the number of j type atoms at a distance r to $r + dr$ is given by $4\pi r^2 \rho_{ij} dr$ and the sum in Equation (4.68) is replaced by an integral then

$$i(Q) = \sum_i \sum_j x_i f_i f_j \int_V 4\pi r^2 \rho_{ij}(r) \left(\frac{sinQ.r}{Q.r}\right) dr \tag{4.69}$$

where the integral is taken over the volume of the sample V. Equation (4.69) will contain a forward scattering contribution which falls rapidly to zero with Q and will be hidden in the primary beam. This forward scattering term is of the form

$$I^0 = \sum_i \sum_j x_i f_i f_j \int_V 4\pi r^2 \rho_{0j} \left(\frac{sinQ.r}{Q.r} \right) dr \tag{4.70}$$

$$= \left(\sum_i x_i f_i \right)^2 \int_V 4\pi r^2 \left(\frac{sinQ.r}{Q.r} \right) dr \tag{4.71}$$

where ρ_{0j} is the average number density for j type atoms in the sample and ρ_0 is the average number density for the sample including all atom types. Subtracting the forward scattering contribution from both sides of Equation (4.71) we get

$$i'(Q) = \sum_i \sum_j x_i f_i f_j \int_0^\infty 4\pi r^2 [\rho_{ij} - \rho_{0j}] \left(\frac{sinQ.r}{Q.r} \right) dr \tag{4.72}$$

$$= \sum_i \sum_j x_i x_j f_i f_j \int_0^\infty 4\pi \rho_0 r^2 [g_{ij}(r) - 1] \left(\frac{sinQ.r}{Q.r} \right) dr \tag{4.73}$$

$$= \sum_i \sum_j x_i x_j f_i f_j (S_{ij} - 1) \tag{4.74}$$

Substituting Equation (4.74) back into Equation (4.67) the total intensity observed for elastic scattering is given as

$$i(Q) = \sum_{i=1}^{M} x_i f_i^2 + \sum_i \sum_j x_i x_j f_i f_j (S_{ij} - 1) \tag{4.75}$$

which is analogous to the equation derived for neutron scattering from a multicomponent system, Equation (4.44).

4.2.3 Compton Scattering

Consider a photon with momentum **p** and energy hv incident upon a stationary electron of rest mass m. After collision, the photon has a momentum **p′** and the electron recoils with momentum **P**. The scattering angle 2θ is shown in Figure (4.4).

The scattering plane is defined by the incident and scattered photon paths. The initial photon momentum normal to this path is zero and therefore the path of the recoiling electron must lie in the scattering plane. For momentum to be conserved during the scattering process

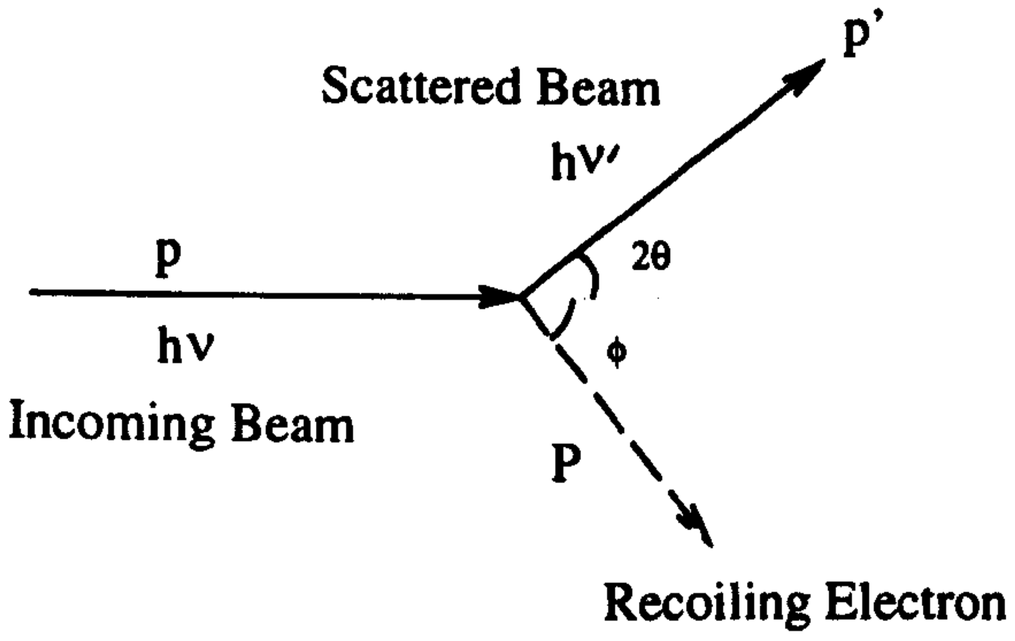

Figure 4.4: Schematic of Compton Scattering Process

$$p^2c^2 = (hv)^2 + (hv')^2 - 2(hv)(hv')cos2\theta \tag{4.76}$$

where v' is the frequency of the scattered photon. From conservation of energy considerations

$$p^2c^2 + m^2c^4 = (hv - hv')^2 + 2mc^2(hv - hv') + m^2c^4 \tag{4.77}$$

Combining Equations (4.76) and (4.77)

$$mc^2(vv') = hvv'(1 - cos2\theta) \tag{4.78}$$

or equivalently

$$\lambda' - \lambda = \frac{h}{mc}(1 - cos2\theta) \tag{4.79}$$

$$= 0.0243(1 - cos2\theta)\mathring{A} \tag{4.80}$$

This is the Compton effect equation and the term $\frac{h}{mc}$ is called the Compton wavelength of the electron. It can be seen from Equation (4.80) that $\lambda' > \lambda$ and that the increase

in wavelength of the incoherently scattered line depends only on the scattering angle 2θ.

In practise the unmodified line (λ) is observed to be broader than the modified line (λ'). This is because the electrons in the target are not initially at rest, as assumed above, but have a range of momenta and energies.

Both the modified and unmodified line are observed at the same time. This is because for part of the time the electron behaves as a free particle at rest and for part of the time it behaves as though it is bound to the rest of the atom. In the latter case the collision is between the whole atom of mass M_a where $M_a \gg m$. Thus $\frac{h}{mc}$ in Equation (4.80) goes over to $\frac{h}{M_a c}$. As the latter is approximately equal to zero then $\lambda' = \lambda$ for this case.

Chapter 5

X-Ray Diffraction Experimental Method and Data Reduction

Each of the X-ray diffraction experiments detailed in this work was carried out on beamline 9 at the Daresbury Laboratory Synchrotron Radiation Source, Warrington, U.K. Five samples of a-C:H(D) were studied having a carbon content ranging from 65% to 75%. As X-rays scatter from the electrons in a sample, the data collected is dominated by contributions from the carbon matrix. The following chapter details the experimental method used for the collection of the X-ray scattering data and the subsequent data reduction steps carried out to access the structure factor, S(Q), for each of the materials studied.

Measurements were taken for each of the samples using two X-ray scattering techniques: conventional transmission geometry X-ray scattering was used to measure the total scattering profile, including both coherent and incoherent scattering contributions, and the Warren-Mavel fluorescence detection technique was used to measure the coherent scattering profile only.

5.1 Daresbury Laboratory Synchrotron Radiation Source (SRS)

Synchrotron radiation is the name used to describe the electromagnetic radiation emitted by electrons (or positrons) moving at relativistic velocities along a curved orbit. In synchrotrons and storage rings these particles are maintained in this orbit by dipole magnets. As the particles pass through the dipole magnets and an acceleration is imparted to them they emit a continual spectrum of radiation, the range of which depends upon the energy of the particles and the magnetic fields applied. The radiation produced is highly collimated, linearly polarized in the plane of the particle orbit and significantly more intense than that available from conventional laboratory sources. The Daresbury Laboratory SRS has a wavelength range from hard X-rays to far into the infra-red (or from ~100keV to ~ 10^{-4}eV) and a typical vertical beam divergence of 1 milliradian.

A schematic diagram of the source, which consists of three accelerators, is shown in Figure (5.1). The first of these, a 12MeV linear accelerator (linac), injects electrons into a booster synchrotron which further accelerates them to 600MeV. The electrons are then extracted from the synchrotron and injected into the storage ring. The process of injection would continue until a design current of 300mA is achieved but in practice other factors tend to reduce this somewhat. Within the storage ring, a klystron, coupled to the electron beam via radio frequency cavities, acts on the beam both to increase its energy to 2GeV and to replenish any energy lost as synchrotron radiation. The action of the klystron causes bunching of the electron beam so that the source is not continuous but pulsed, having a typical pulse width of 180ps.

The storage ring uses sixteen 1.2T dipole magnets and thirty-two focusing quadrupoles

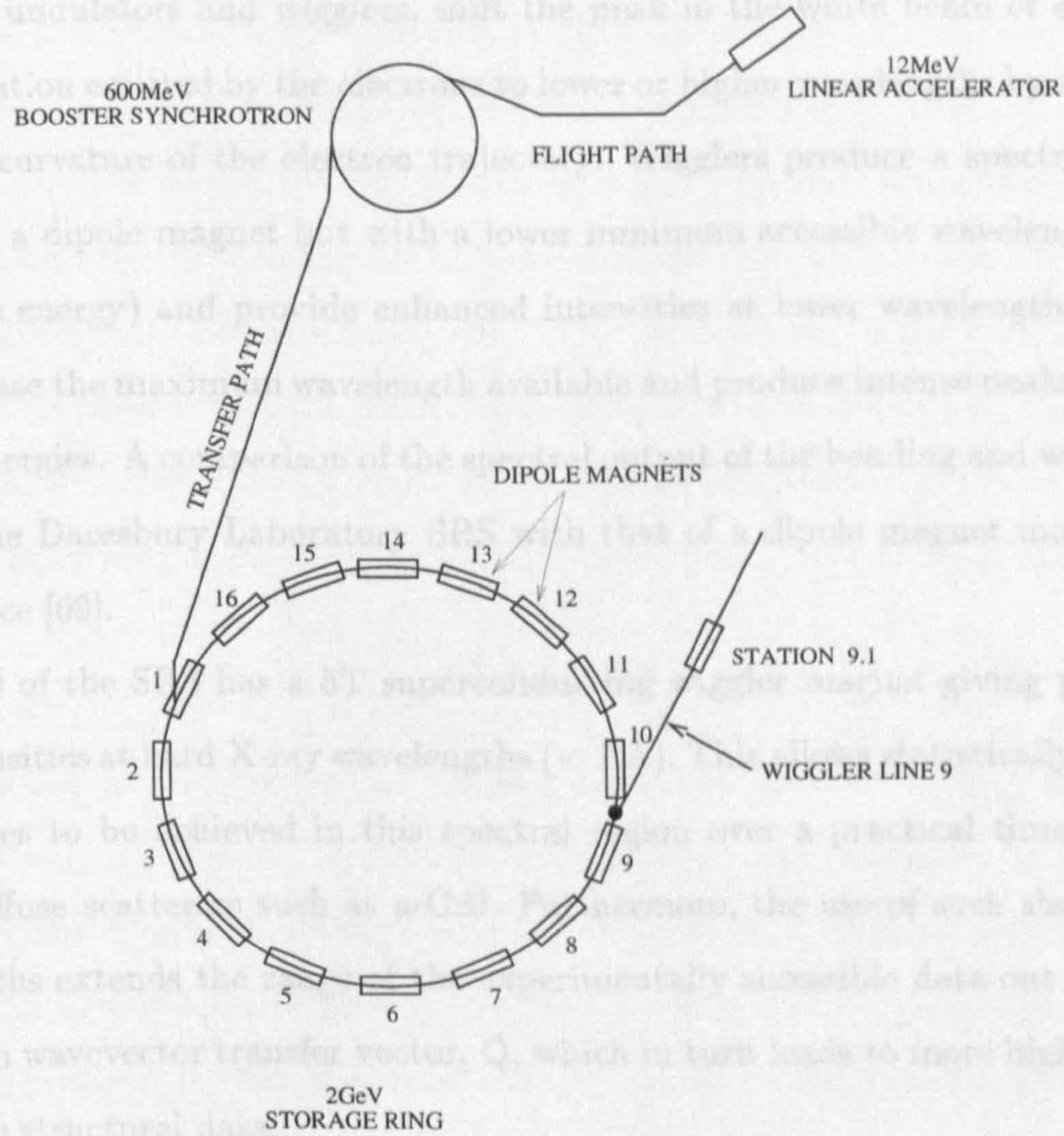

Figure 5.1: Schematic diagram of the Daresbury Laboratory SRS including Station 9.1.

and sextupoles to maintain the circular orbit of the beam. Between certain of the dipole magnets, additional multipole magnets are inserted which force the beam to oscillate in a periodic manner (without a net deflection). These insertion devices, known as undulators and wigglers, shift the peak in the white beam of electromagnetic radiation emitted by the electrons to lower or higher wavelengths by altering the radius of curvature of the electron trajectory. Wigglers produce a spectrum similar to that of a dipole magnet but with a lower minimum accessible wavelength (higher maximum energy) and provide enhanced intensities at lower wavelengths. Undulators increase the maximum wavelength available and produce intense peaks at specific photon energies. A comparison of the spectral output of the bending and wiggler magnets at the Daresbury Laboratory SRS with that of a dipole magnet may be found in reference [69].

Line 9 of the SRS has a 5T superconducting wiggler magnet giving particularly high intensities at hard X-ray wavelengths (< 1 Å). This allows statistically significant count rates to be achieved in this spectral region over a practical time period for low Z, diffuse scatterers such as a-C:H. Furthermore, the use of such short incident wavelengths extends the range of the experimentally accessible data out to a higher maximum wavevector transfer vector, Q, which in turn leads to more highly resolved real space structural data.

Although the synchrotron is maintained at a vacuum of $\sim 10^{-9}$ mbar in order to minimise scattering of the electrons from their orbit, the beam decays over a period of time due to scattering from residual gaseous molecules and also partly due to electron-electron interactions. Consequently it is necessary to refill the storage ring at least every twenty-four hours.

5.1.1 Station 9.1

Station 9.1 lies 15m from the tangent point of the superconducting wiggler magnet described in the previous section. A schematic diagram of the instrumental configuration for this station is given in Figure (5.2). The white, unfocussed beam from the synchrotron source enters the monochromator vessel shown, held at a pressure of $\sim 10^{-2}$mbar, via a Be window and is reduced in size by a fixed water-cooled aperture. The resultant beam is then further reduced to a suitable size for the monochromator by a set of vertical and horizontal jaws. The required wavelength for the scattering experiment is chosen from the white beam using a channel cut Si(111) monochromator. The latter is tunable to a given wavelength by altering the angle of incidence of the beam relative to the scattering plane of the crystal. According to Bragg's law

$$n\lambda = 2dsin\theta \tag{5.1}$$

where θ is the angle between the incident beam and the scattering plane, d is the plane spacing and n is the order of the reflection. The resultant beam therefore consists of the chosen wavelength plus higher order contributions (such as the 333 reflection). To avoid contributions from the latter being included in the measured scattering profiles, an energy window may be set up at the detector such that only the fundamental wavelength contributions are accepted in the counting register.

After passing through the monochromator, the resultant beam enters a set of vertical and horizontal slits which define the beam profile at the sample. A variety of slits, mounted on a removable carriage, may be chosen according to the incident beam size required. For the experiments carried out on the a-C:H(D) samples, a 5mm horizontal and 0.8mm vertical slit width was typically used. The choice of these dimensions is detailed in Section (5.2). The monochromator beam emerges from the

front end of the vacuum system via a second Be window. The beam is then incident on the sample which is mounted on the θ axis of a two circle diffractometer.

5.2 Conventional X-ray scattering profile measurement

The conventional transmission X-ray diffraction experiments carried out at the SRS were done so in angular dispersive mode i.e. in order to scan the sample scattering in Q space the wavelength, λ, in Equation (4.21) was fixed and the scattering angle 2θ varied. A schematic diagram of the experimental arrangement used is given in Figure (5.3). The sample and detector circles of the diffractometer shown may be driven individually, allowing the incident beam angle at the sample to be set independently of, or coupled to the scattering angle at which data is collected.

The incident angle, θ, is measured between the sample normal and the incident beam as shown in Figure (5.3). The (θ : 2θ) method was used to scan the sample scattering for all the powder samples studied. In this technique, the detector is set at a scattering angle 2θ to the transmitted beam. By rotating the sample position through a range of θ values (generally from 1° to 65°) and scanning the detector in the vertical plane through the corresponding 2θ range a scattering profile is measured. This method allows a large angular diffraction range to be sampled in a single scan and also maintains the pathlength of the X-rays to the detector at a constant value, thus simplifying any absorption corrections.

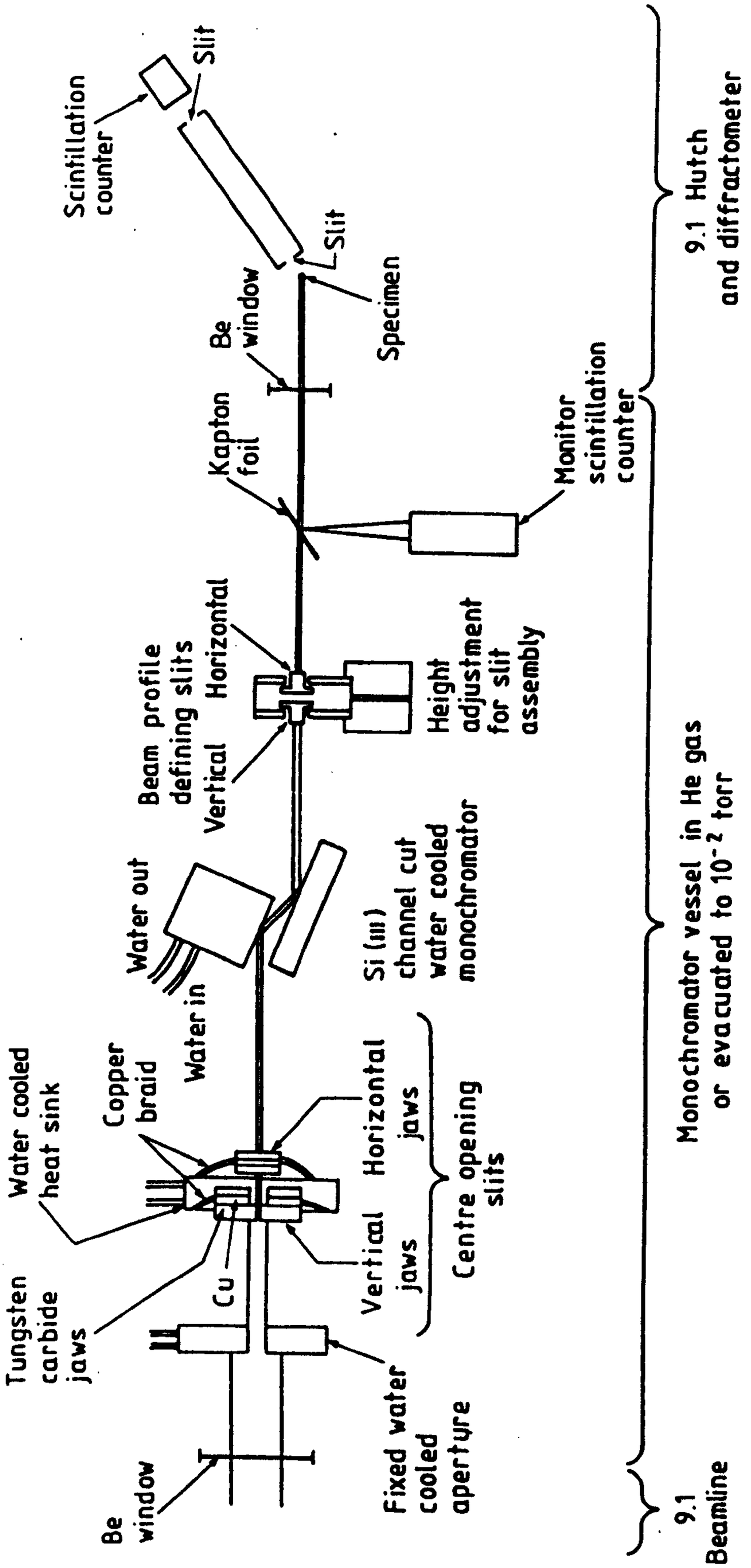

Figure 5.2: Schematic Diagram of the Instrumental Configuration For Beamline 9.1 at the Daresbury Laboratory SRS.

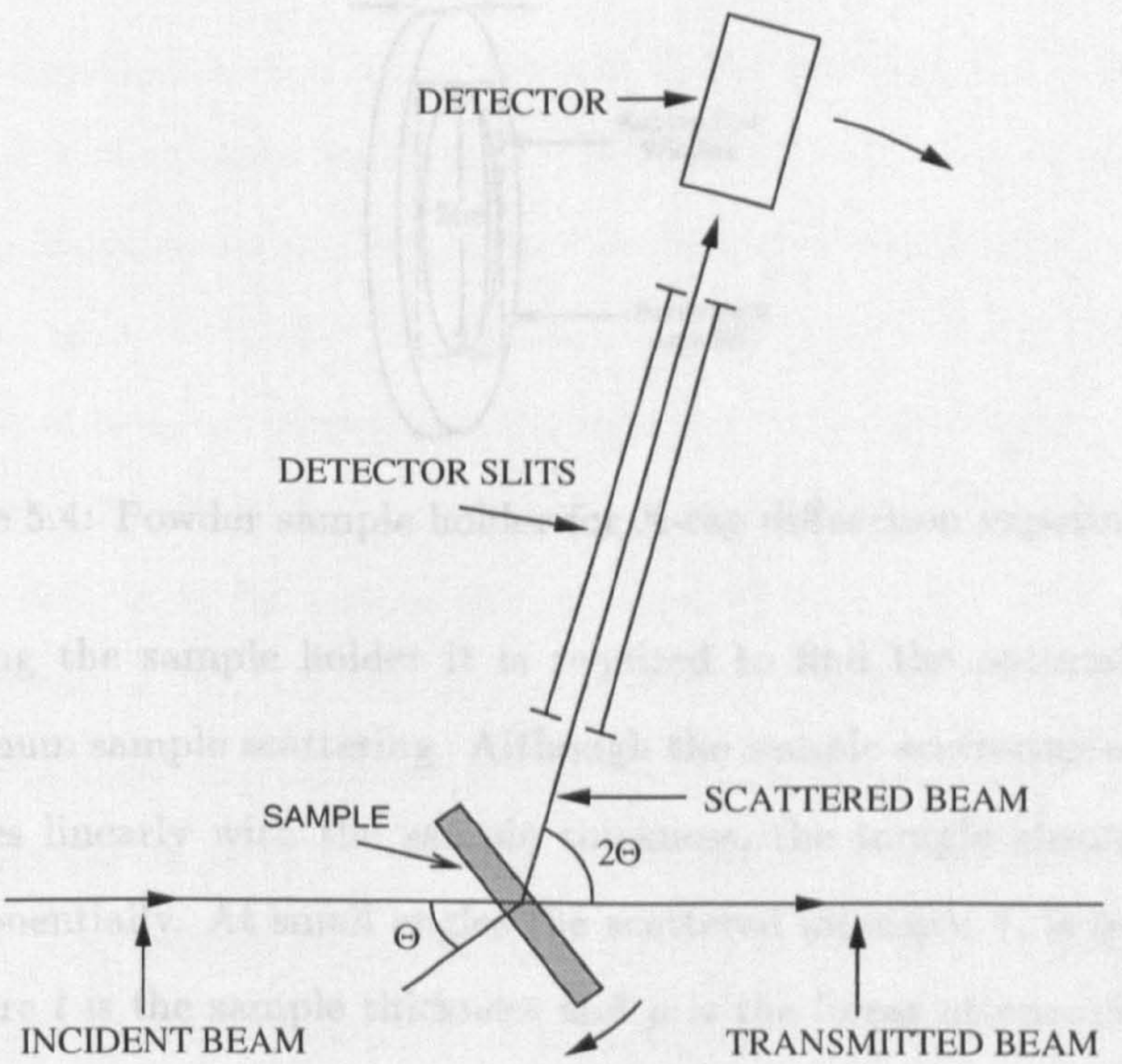

Figure 5.3: Schematic Diagram of $(\theta : 2\theta)$ Scattering Geometry.

5.2.1 Sample holder

For the powder samples analysed, the sample holder used was of the form of an aluminium annulus (see Figure (5.4)). The sample was held in place by 60μm kapton foil windows. Kapton was chosen for the windows as it has very low absorption and shows very little structure over the Q range to be investigated.

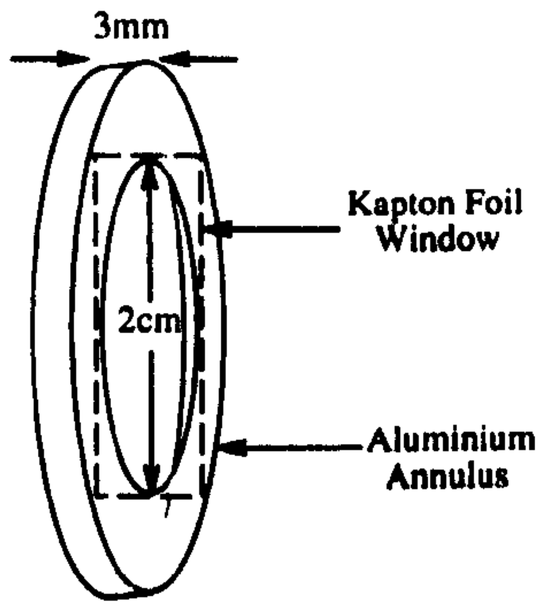

Figure 5.4: Powder sample holder for X-ray diffraction experiments.

In designing the sample holder it is required to find the optimal thickness to achieve maximum sample scattering. Although the sample scattering of the incident beam increases linearly with the sample thickness, the sample absorption likewise increases exponentially. At small angles the scattered intensity, I, is proportional to $te^{-\mu t}$ [70] where t is the sample thickness and μ is the linear attenuation coefficient. Differentiating I with respect to t and setting the differential to zero to find the maximum intensity obtainable gives the optimal value for t as

$$t = \frac{1}{\mu} \tag{5.2}$$

For larger scattering angles, where the path length of the X-rays through the sample increases, optimisation of the scattered intensity requires that $\mu t < 1$ [70]. As μ for the a-C:H samples studied is in the region of 0.8 cm^{-1} for the incident

wavelength used, two sample holders of thickness 1.5mm and 2mm respectively were used. The 1.5mm cell was used when the size of the available sample dictated.

A second advantage of choosing the sample thickness such that $\mu t < 1$ is a reduction in multiple scattering effects in the sample (see Section (5.4.8)).

5.2.2 Detector slits

To limit the angular range of the scattered X-rays entering the detector, a set of horizontal and vertical slits was used. The volume of sample illuminated by the incident X-ray beam, and thus the height of the scattered beam, varies with scattering angle 2θ (see Figure (5.11) Section (5.4.4)). In the case of weak, diffuse scatterers such as a-C:H it is advantageous for the detector to accept X-rays scattered from the whole of the illuminated volume at every detector angle. This also removes the need for any corrections for the angular variation in "effective" scattering volume as seen by the detector. To achieve this, the vertical dimensions of the slits must be greater than the maximum scattered beam height. As the height of the slits increases, the angular resolution of the scattering profile collected decreases. For crystalline samples, where sharp Bragg peaks may occur in close proximity, the angular resolution of the measured data is paramount. For amorphous materials, where the peaks in the scattering profile are broad and often merge together continuously, resolution constraints may be relaxed, to some extent, in favour of increased scattered intensity at the detector. Some increase in the scattered intensity may be gained, without loss of resolution, by increasing the dimensions of the incident beam normal to the scattering plane. The extent to which the beam dimensions can be increased in this direction is limited only by the corresponding detector dimensions. To allow a viable count rate to be achieved at the detector, whilst maintaining a suitable angular

resolution, a rectangular incident beam profile having a width of 5mm and height of 0.8mm was used for the samples studied. Using standard geometry, the maximum scattered beam height, d, was calculated for each of the sample cell thicknesses used and a suitable vertical height of 2mm was chosen for the detector slits.

5.2.3 The scintillation detector

Scattering profiles for each of the samples were collected using a NaI scintillation detector. NaI with a trace of thallium iodide impurity is found to produce an exceptionally large scintillation output [71]. This output may be coupled to a photomultiplier tube where the light is converted to an electrical pulse. As NaI is hygroscopic, it will deteriorate due to water absorption if exposed to the atmosphere for any length of time. The crystal is therefore held under vacuum with the incident X-rays passing through a beryllium window into the evacuated detector body. The energy resolution of the NaI detector used on Station 9.1 at the SRS is approximately 30% [72].

As previously stated, for each of the samples studied two techniques for scanning the scattering profile were used. Standard transmission geometry, detailed in the preceding sections, was used to obtain the total scattering profile including both coherent and incoherent contributions. To remove the incoherent Compton scattered contribution from the scattering profile experimentally, the Warren-Mavel fluorescence detection technique was used. This technique, used to determine the coherent scattering contribution to the data only, is described in Section (5.3). Under some circumstances, it is necessary to combine the conventional and Warren-Mavel data to access a fully coherent scattering profile for samples (see Section (9.2.1)). Resolution and geometrical effects on the data due to the experimental arrangement should

remain constant between the two data collection methods in order to allow the incoherent scattering to be fully removed from the data. The Warren-Mavel data was, therefore, measured using the same ($\theta : 2\theta$) scattering geometry, sample containers and detector slits as those used for the collection of the conventional scattering data.

5.3 Warren-Mavel fluorescence detection technique

The use of a synchrotron radiation source for the study of amorphous materials overcomes a particular problem experienced by traditional laboratory sources. The high intensity beam available from such sources allows suitable statistics to be gathered, in a reasonable time period, on the scattering intensity at high Q values, where the scattering is much weaker due to the X-ray atomic form factor. Particularly high Q values are accessible on the instrument on Station 9.1 at the SRS ($\sim 18\mathring{A}^{-1}$) due to the high incident beam intensities available at short wavelengths. The quality and extent of this high Q data directly affects the real-space structural information obtained on the samples. However, as Q increases so too does the Compton scattering contribution to the measured total scattering. Thus removal of this contribution from the collected scattering profiles becomes necessary.

The inelastically scattered Compton photons have no definite phase relationship between themselves and the incoming beam and thus between each other. Therefore no interference effects can occur between these outgoing waves and the Compton scattered radiation is incoherent. It does not contain any structural information on the samples and simply contributes to the background on an X-ray diffraction scan. Compton scattering contributions to the total measured scattering will be present not only from the sample, but also from the container windows.

The shift in the wavelength of the modified Compton radiation increases with

scattering angle as given by Equation (4.80). This is the basic Compton equation. If the motion of the scattering electrons is considered, then a second term, dependent on the electron momentum, p_e, along the scattering vector occurs, so that $\Delta\lambda$ is more accurately given by [61]

$$\Delta\lambda = 0.0243(1 - cos(2\theta)) + 2\sqrt{\lambda\lambda'}\left(\frac{p_e}{mc}\right) sin\theta \tag{5.3}$$

where 2θ is the scattering angle, m the rest mass of the electron and c the speed of light. The result of this is a broadening of the modified radiation wavelength line resulting from the momentum distribution of the electrons in the scattering atoms. The wavelength distribution of the Compton scattered radiation at a given scattering angle, 2θ, is centred about a wavelength given by the first term in Equation (5.3). The second term in Equation (5.3) defines the wavelength spread around the central value and is seen to be angularly dependent. Thus the wavelength profile of the incoherent radiation is found to broaden as the scattering angle increases.

Compton scattering only occurs if the incident energy transferred to the scattering electron is greater than its binding energy and the electron may behave as a free particle [61]. The Compton effect is, therefore, more pronounced in low Z atoms where the binding energies are lower. Compton scattered radiation provides a significantly large contribution to the total measured scattering from the a-C:H samples studied here. A theoretical calculation of this contribution would require a knowledge of the exact Compton profile for the sample at every scattering angle. This would then have to be convoluted with the detector energy window function and the relevant absorption corrections applied to each Compton scattered radiation wavelength contribution observed by the detector. A more practical approach involves the removal of the wavelength modified radiation before it reaches the detector.

A method for the experimental elimination of the Compton component of the X-ray scattering from amorphous materials was given by Warren and Mavel [73] in 1965, for use on standard laboratory sources. This technique exploits the energy difference between the elastically scattered radiation and the wavelength-shifted Compton component of the scattered beam. A foil with an absorption edge slightly below the incident radiation energy is placed in the scattered beam between the sample and the detector. The elastically scattered radiation has sufficient energy to excite fluorescence in the foil; the majority of the energy shifted radiation cannot. A scan of the fluorescent radiation will then effectively give the coherent elastic scattering component. A schematic diagram of the experimental layout for the Warren-Mavel experimental technique is given in Figure (5.5).

As the wavelength of the Compton scattered radiation is a continuum from the elastically scattered value, a percentage of the incoherent radiation will be included in the measured scattering profile. In particular, at small scattering angles, where the wavelength shift is small, the incoherently scattered radiation may still excite fluorescence in the foil. Some incoherent radiation will also reach the detector through scattering processes in the foil and from air scattering of the transmitted beam as it passes close to the detector. Warren and Mavel used a Rh K_α incident beam ($\lambda = 0.615\mathring{A}$) and a molybdenum foil (Mo K edge $0.620\mathring{A}$) in their work and considered the incoherent scattering contribution to their measured profiles to be of the order of 10% of the Mo K fluorescent radiation. In order to minimise this contribution to the total measured scattering, they placed a Zr filter in front of the detector window. Since Zr has a K edge at $\lambda = 0.689\mathring{A}$ almost all of the modified scattering occurs on the short wavelength side of the absorption edge and is highly absorbed. The unmodified radiation passes through the filter with little absorption. However this results in a

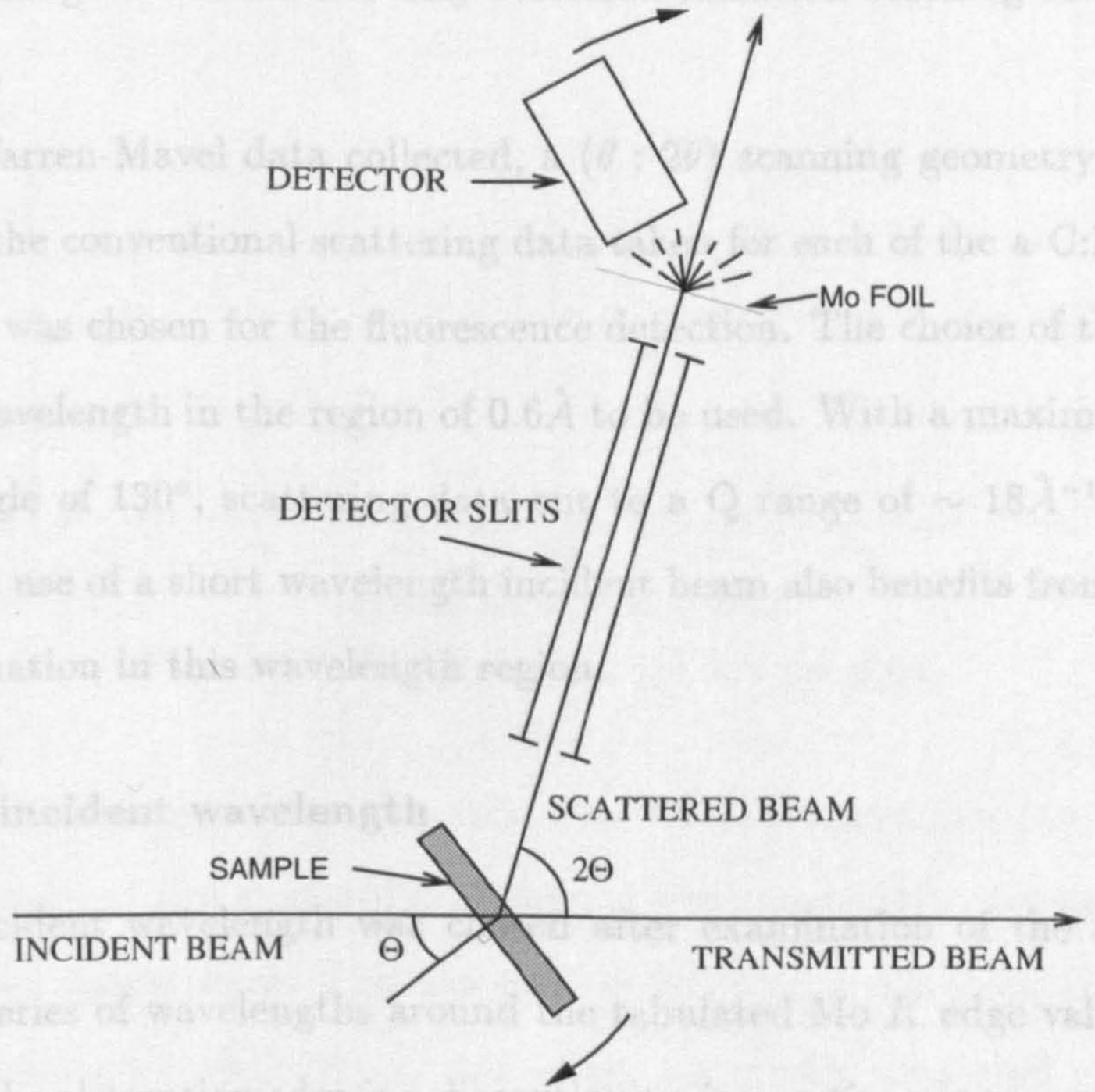

Figure 5.5: Schematic diagram of the experimental arrangement used by the Warren-Mavel fluorescence detection technique.

reduction in the fluorescent beam of the order of $\sim$ 30%. In the work carried out by Warren and Mavel, the proximity of the incident X-ray wavelength to the foil edge was limited by the available laboratory source targets and corresponding foils. The continuum of radiation available from the Daresbury SRS allows the incident wavelength to be set at a value very close to that of a chosen fluorescence foil. In this way the percentage of the incoherently scattered radiation reaching the detector can be minimised.

For the Warren-Mavel data collected, a $(\theta : 2\theta)$ scanning geometry was used, in parallel with the conventional scattering data taken for each of the a-C:H samples. A 20μm Mo foil was chosen for the fluorescence detection. The choice of this foil allows an incident wavelength in the region of 0.6$\mathring{A}$ to be used. With a maximum accessible scattering angle of 130^o, scattering data out to a Q range of $\sim 18\mathring{A}^{-1}$ can then be accessed. The use of a short wavelength incident beam also benefits from the reduced sample attenuation in this wavelength region.

Setting the incident wavelength

The exact incident wavelength was chosen after examination of the absorption of the foil at a series of wavelengths around the tabulated Mo K edge value. Although theoretically the absorption edge is a discontinuity, in practice a more gradual increase in the absorption occurs. To examine the form of the edge, the foil was placed in the sample position normal to the incident beam. An ion chamber on the far side of the foil was then used to measure the transmission in the region of the edge as a function of the monochromator angle. The scan taken is shown in Figure (5.6). The monochromator angle chosen was $-5.649°$ as this position is far enough above the edge to prevent synchrotron source movements causing changes in conversion

efficiency as the incident radiation energy falls down the edge. It is not, however, so far above the edge to allow a significant proportion of the modified beam to cause fluorescence in the foil.

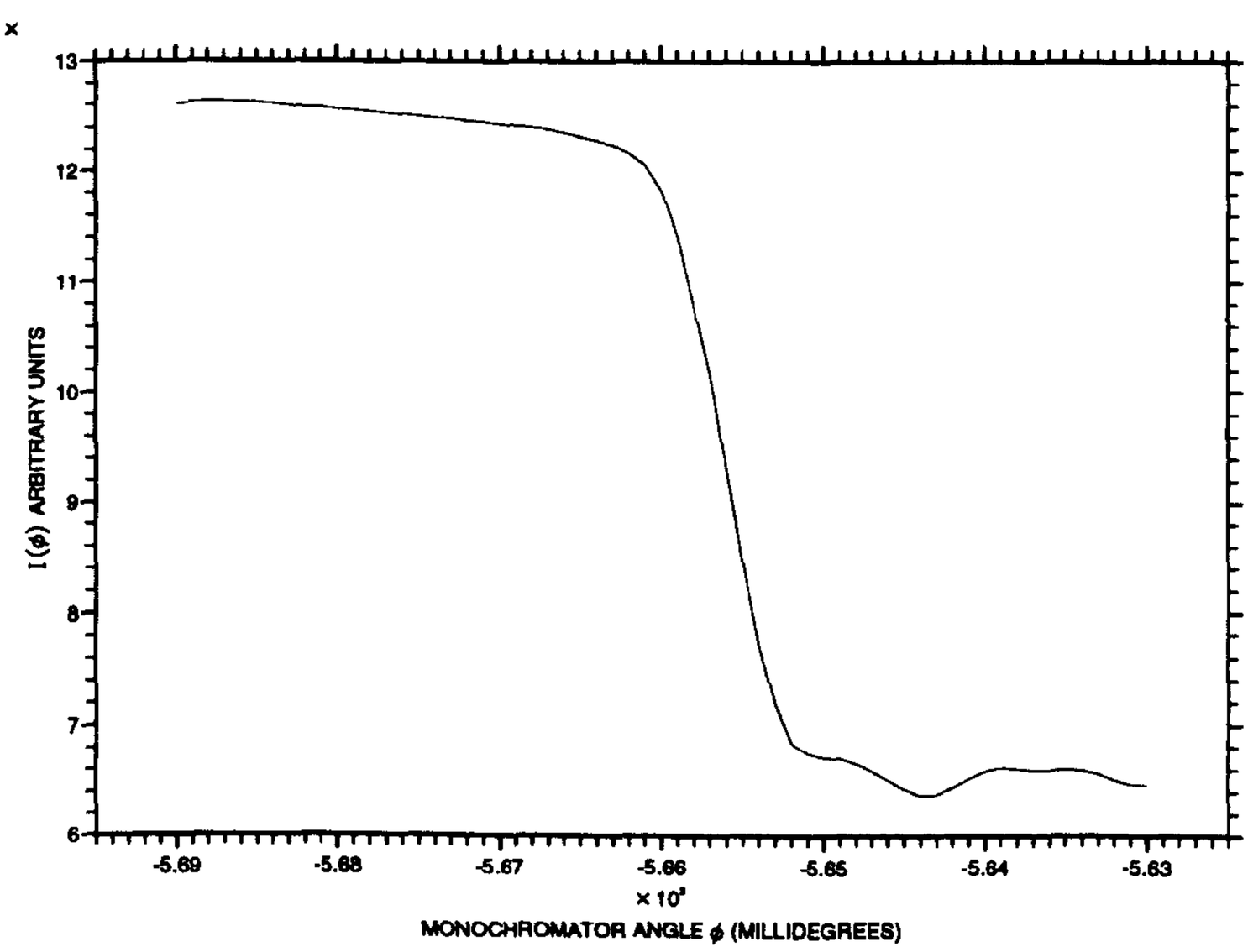

Figure 5.6: Molybdenum foil K edge scan.

Backlash on the monochromator driver motor can sometimes result in the real angle of incidence of the synchrotron beam at the monochromator crystal varying slightly from the chosen value. The incident wavelength corresponding to a monochromator angle setting of $-5.649°$ was, therefore, accurately measured using a silicon standard powder (S.M.R. 640b) and found to be $0.6185 \pm 0.0001 \mathring{A}$. This silicon standard measurement also provides a check on the zero angle set for the 2θ arm of the diffractometer which may typically be offset by a few millidegrees. The measured value for the incident wavelength corresponds to an incident radiation energy 49eV above the Mo K edge. The shift in energy, ΔE, of the Compton component of the

X-ray scattering data is given by [61]

$$\Delta E = \frac{hc(\lambda_i - \lambda_s)}{\lambda_i \lambda_s} \tag{5.4}$$

where h is Planck's constant, c the speed of light, and λ_i and λ_s are the incident and scattered radiation wavelengths respectively. As previously stated, the wavelength distribution of the incoherently scattered radiation at a given scattering angle, 2θ, is centred around a value defined by the first term in Equation (5.3). This can be converted to an energy distribution using Equation (5.4). It can then be calculated that at a scattering angle of approximately 20° the energy spread of the incoherent radiation will be centred around 49eV. Thus, above a scattering angle of 20° the majority of the incoherent radiation will fall below the K edge of the Mo foil and will not contribute to the fluorescent signal at the detector.

The NaI scintillation detector used to collect the conventional scattering data was also used for the collection of the Warren-Mavel data. However, in the latter case the detector was placed 13mm from the Mo foil, set at an angle of 45° to the scattered beam (see Figure (5.5)). These values were chosen following optimisation of the system by previous workers to maximise the fluorescence to background ratio [74]. The angle between the detector and foil was held constant throughout a scan.

A small proportion of the X-rays arriving at the detector will do so as the result of diffraction of the *scattered beam* by the Mo foil. As the scattering angle, 2θ, increases the wavelength distribution of the Compton scattered component of the radiation incident at the foil will change and move to longer wavelengths. Each wavelength incident at the Mo foil will produce a diffraction pattern that the detector will sample at a scattering angle *relative to the foil*, ϕ, of 45°. The intensity of the diffraction pattern at this angle will be determined by the the wavelength of the X-rays concerned. Thus as the wavelength distribution at the foil changes, so too will

the intensity at the detector due to diffraction in the foil. This may lead to some structure in the Warren-Mavel data due to scattering in the foil and not in the sample. This structure will contribute to the difference profile between the conventional X-ray scattering data and that taken using the Warren-Mavel technique.

5.4 Data analysis

Real space structural information on the samples studied can be accessed by extracting the structure factor, $S(Q)$, for the sample concerned from the collected scattering profile. $S(Q)$ is defined as follows

$$\begin{aligned} S(Q) = 1 \quad &+ \quad \frac{1}{(\sum_{i=1}^{M} x_i f_i)^2}(x_i^2 f_i^2(Q)[S_{ii}(Q) - 1] + x_j^2 f_j^2(Q)[S_{jj}(Q) - 1] \\ &+ \quad 2x_i x_j f_i(Q) f_j(Q)[S_{ij}(Q) - 1]) \end{aligned} \tag{5.5}$$

where x_i and x_j are the atomic concentrations of atom type i and j in the sample respectively. f_i and f_j are the corresponding X-ray scattering factors, in electron units, for the given atom types. In order to obtain this function from the measured scattering profile a number of data reduction steps must be carried out. These steps are detailed in the following paragraphs.

5.4.1 Detector dead time

The dead time , τ, of a detector is defined as the minimum time within which two counting events may be resolved. If a photon, p_2, arrives at the detector within a time τ of a photon, p_1, the detector will not have returned to a state in which it may record the second event. Thus only one event will be registered and the detector count will not give a true representation of the incident photon flux. The value of τ may be determined by the detector itself and/or the associated electronics.

A detector may show a) paralyzable or b) non-paralyzable dead time behaviour. A schematic diagram of the two cases is shown in Figure (5.7). In case a) although a photon such as p_2 incident on the detector within τ of p_1 is not recorded by the detector, it will still contribute to the detector dead time. For non-paralyzable detectors, case b), only those events recorded by the detector contribute to the dead time. The NaI detector used on Station 9.1 was found to show non-paralyzable dead time behaviour with $\tau = 6.5\mu s$. For the case of such a non-paralyzable detector the true incident photon intensity at the detector, I_{inc}, may be related to the the intensity registered by the detector, I_{det}, as follows [71]

$$I_{inc} = \frac{I_{det}}{1 - \tau I_{det}} \tag{5.6}$$

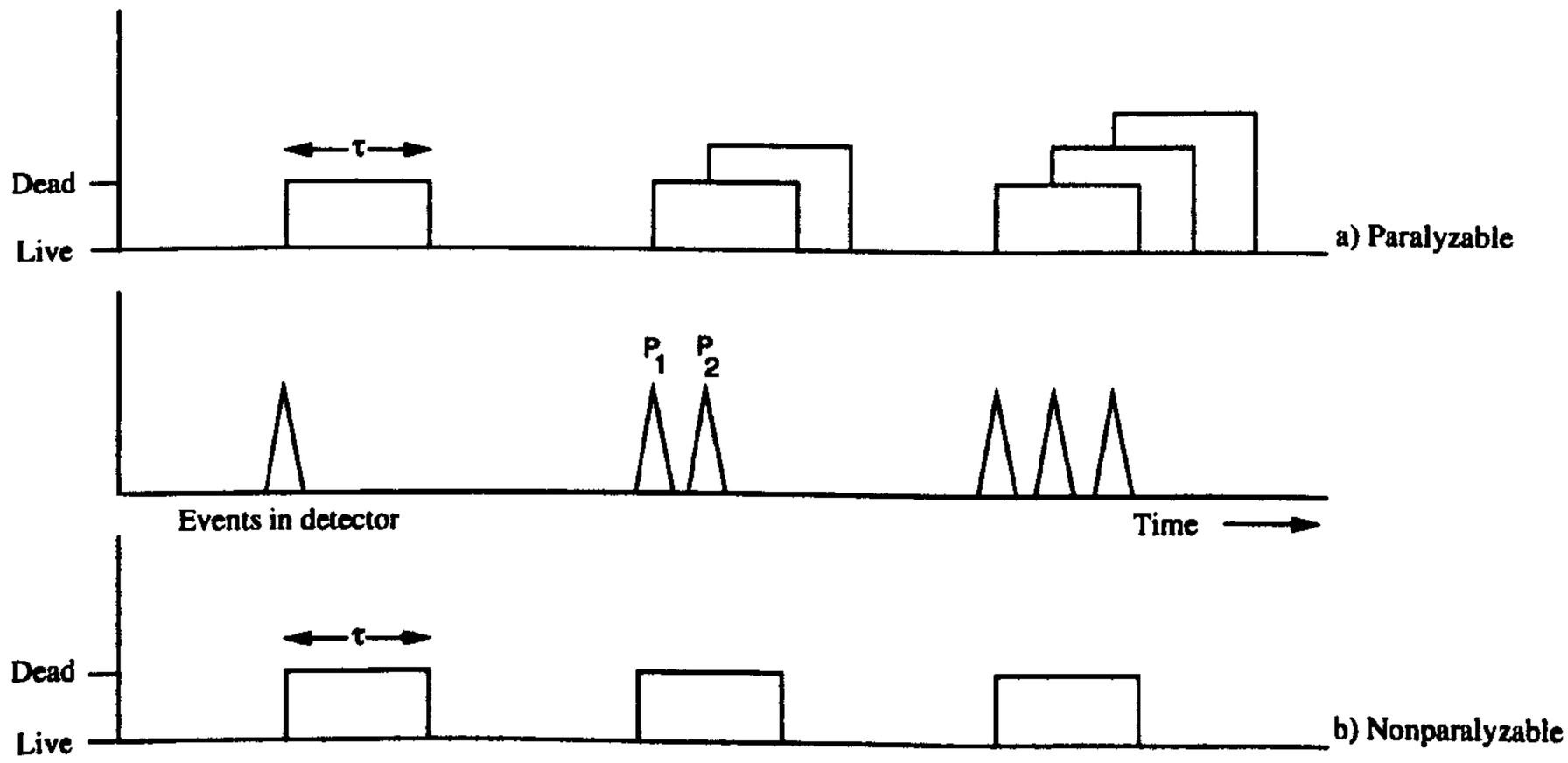

Figure 5.7: Illustration of paralyzable and non-paralyzable dead time: if 6 events occur at the detector, 3 events are registered in the paralyzable detector and 4 events are registered in the non-paralyzable detector.

It should be noted that although the energy window set on the detector prevents contributions to the scattering data from monochromator harmonics, such as the

silicon 333 reflection, from being registered by the electronics, these events may still contribute to the detector dead time (providing that they do not arrive at the detector within τ of a previous event). Figure (5.8) shows the collected scattering profile for the a-$C_{0.74}$:$D_{0.09}$:$H_{0.17}$ sample, normalised to the incident beam intensity, with and without dead time corrections applied. This shows that the effect of detector dead time on the collected data is most significant at lower scattering angles where the X-ray photon flux incident on the detector is greatest.

If dead time corrections are not applied to the data, subtraction of the container background scattering from the total scattering profile leads to errors, most significantly at small scattering angles. In this region the sample scattering data may be greatly affected by detector dead time whereas the lower count rate, container only, scan is affected less so. The discrepancy in the relevant scattering intensities and the resultant effect are shown in Figure (5.9).

5.4.2 Normalisation to the incoming beam

As previously stated, the synchrotron beam has a finite lifetime of the order of ~ 24 hours. The major lifetime limiting effects result from a) scattering of the electrons out of orbit by residual gas particles in the synchrotron ring or b) the Touschek effect [75]. Minimisation of a) requires optimisation of the synchrotron vacuum. Difficulties occur in achieving this, however, as the synchrotron radiation emitted by the electrons causes desorption of atoms and molecules from the walls of the chamber.

Effect b) is caused by electron-electron scattering events within a single bunch. These cause a fraction of the electrons' transverse momentum to be converted to longitudinal momentum, which in turn leads to a time delay in some electrons reaching the r.f. cavities. If this time delay is great enough then electrons may be lost from

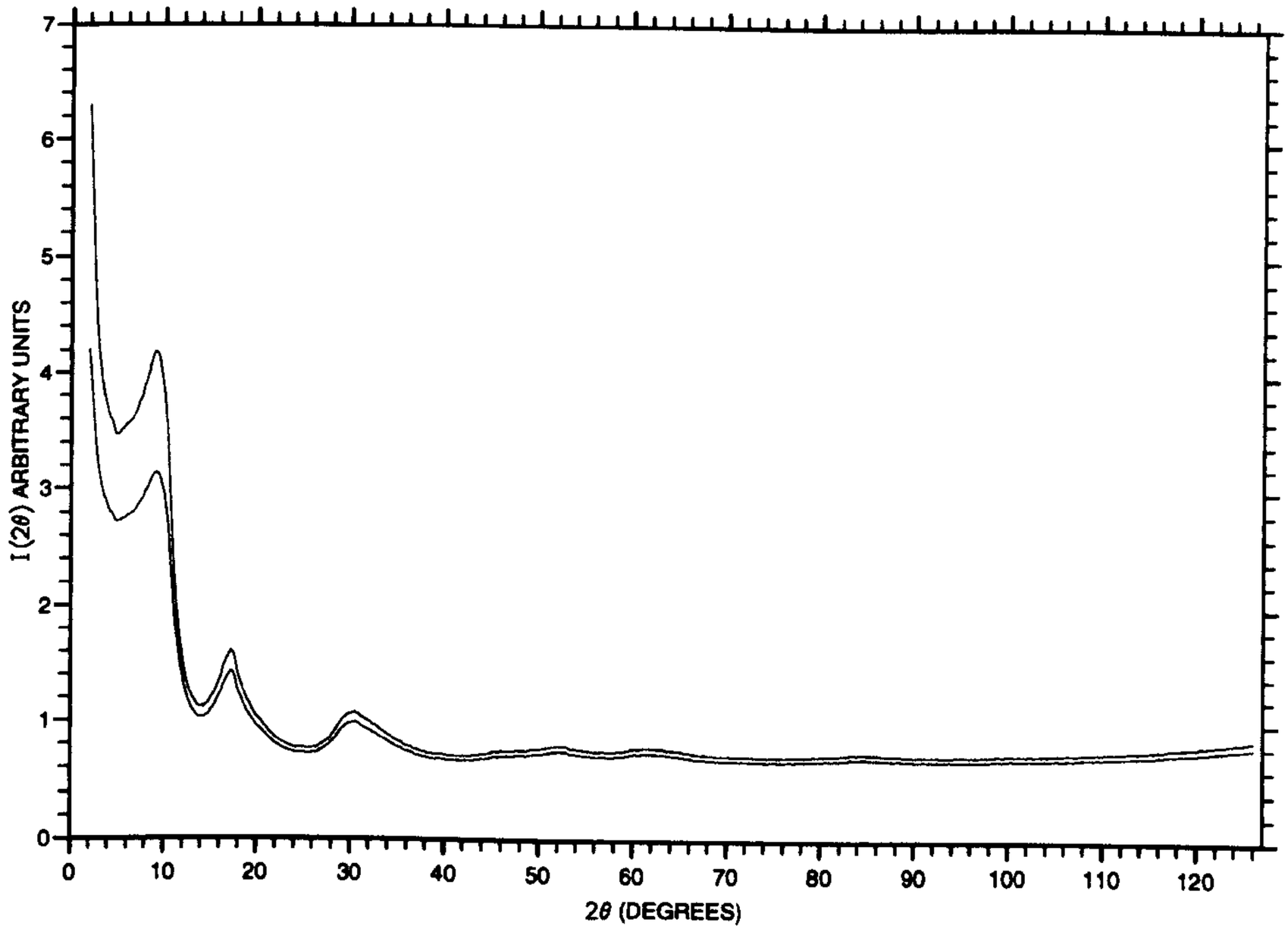

Figure 5.8: Scattering profile for a-$C_{0.74}$:$D_{0.09}$:$H_{0.17}$ showing effect of dead time corrections: top curve dead time corrected data; bottom curve uncorrected data.

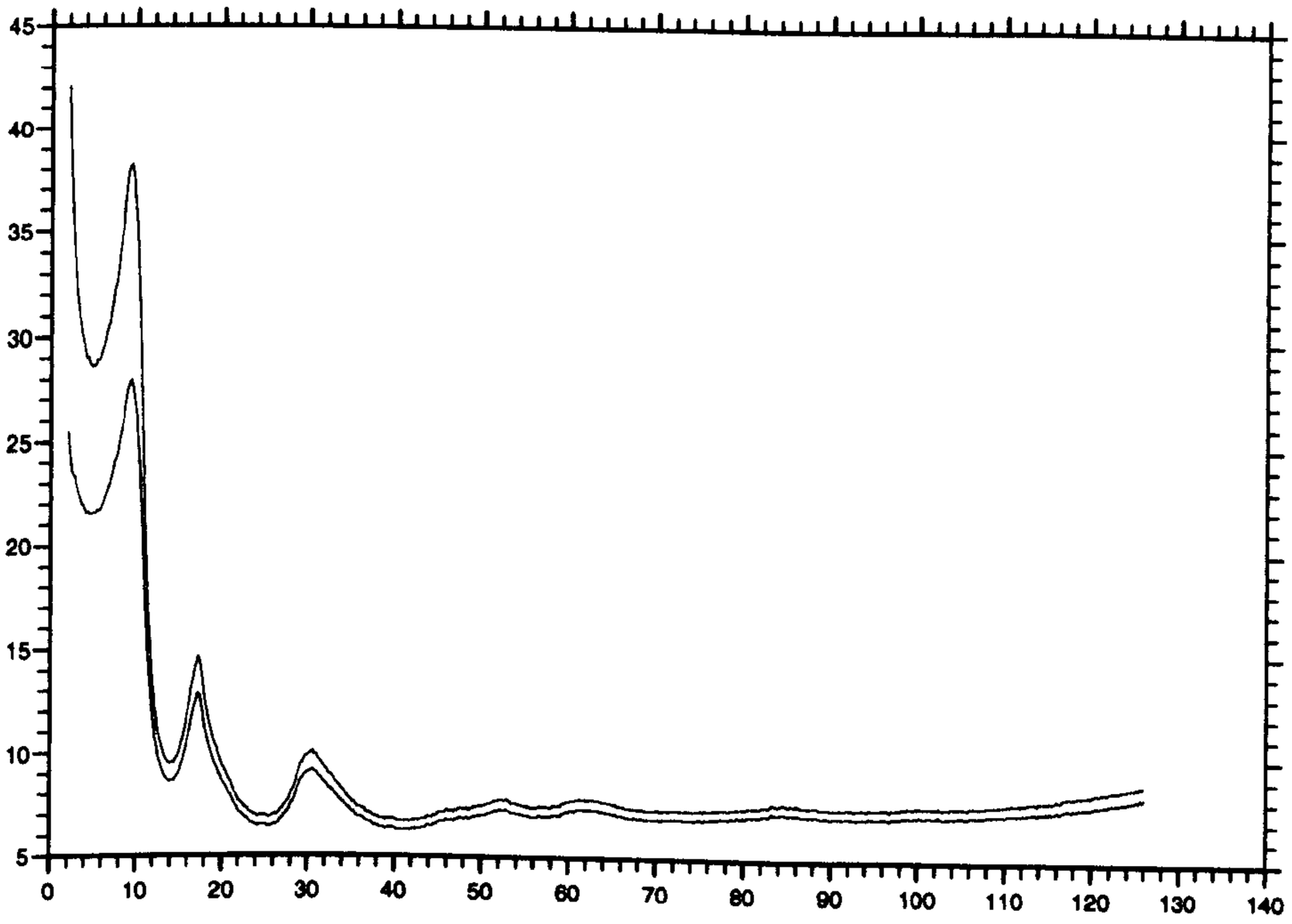

Figure 5.9: Comparison of scattering profile for a-$C_{0.74}$:$D_{0.09}$:$H_{0.17}$ after subtraction of sample container scattering: (top curve) with and (bottom curve) without detector dead time corrections.

the beam.

The net result of these two effects is a reduction in the intensity of radiation incident at the sample over time. Thus it is necessary to monitor the incident flux during a diffraction scan. To achieve this a kapton foil is placed before the sample, inclined at 45^0 to the incident beam as shown in Figure (5.2). The intensity scattered by the foil is measured by a second NaI detector as a function of time and in this way the incident photon flux may be monitored. The monitor count recorded during a scan is then used to normalise the scattered count rate to a constant incident flux. The normalised count rate obtained is still in arbitrary units however. Normalisation of the data to electron units is carried out as described in Section (5.5) after further data correction.

Dead time corrections must also be applied to the monitor count rate. With the high photon flux expected upstream of the sample, a detector having a relatively small dead time is used at this point. The beam monitor on Station 9.1 has a measured dead time of 1.2μs.

A single X-ray scattering scan taken on Station 9.1 was typically collected over a period of 2-6 hours (the lower detector count rate obtained for those scans involving use of the Warren-Mavel fluorescence detection technique requires a longer counting period at each sampled scattering angle to obtain suitable statistics). During this time a significant drop in the incident photon flux occurs. Since the scattering cross-section for X-rays falls as the scattering angle increases, due to the effect of the atomic form factor, the scattering profile was collected by scanning from high to low scattering angle 2θ. In this way the statistical error on the data in the high scattering angle region may be improved relative to that in the low scattering angle region.

Each scattering profile was collected up to a minimum of 10,000 detector counts

per sampled scattering angle so as to give a maximum statistical error on the scattered beam incident on the detector of 1%.

5.4.3 Polarization factor

For an incident X-ray beam with its electric vector, **E**, polarized perpendicular to the scattering plane there will be no angularly dependent effect on the scattered intensity observed. For a beam having **E** parallel to the scattering plane a $cos^2\theta$ angular dependence on the observed intensity results. This can be seen from Equation (4.51). Thus

$$I_{det} \propto I_o[p_\perp + p_{||}cos^2\theta] \tag{5.7}$$

where I_{det} is the scattered intensity recorded by the detector (corrected for dead time) and I_o is the incident beam intensity at the the sample. $p_{||}$ and $p_\perp$ are the fraction of the incident beam polarized parallel and perpendicular to the scattering plane respectively.

Radiation emitted in the orbital plane of the synchrotron is linearly polarized with its electric vector in the plane of the electron orbit. However the effect of the beamline optics on Station 9.1 is such that the incident beam at the sample is only 90% polarized in the plane of the synchrotron ring. Thus for a scan taken in the vertical plane on Station 9.1 a correction factor must be applied to the collected data to account for this such that

$$I_{PC} = \frac{I_{det}}{0.9 + 0.1cos^2\theta} \tag{5.8}$$

where I_{PC} is the polarization factor corrected intensity. The effect of the polarization factor correction on the scattering profile for the a-$C_{0.74}$:$D_{0.09}$:$H_{0.17}$ sample is shown in Figure (5.10).

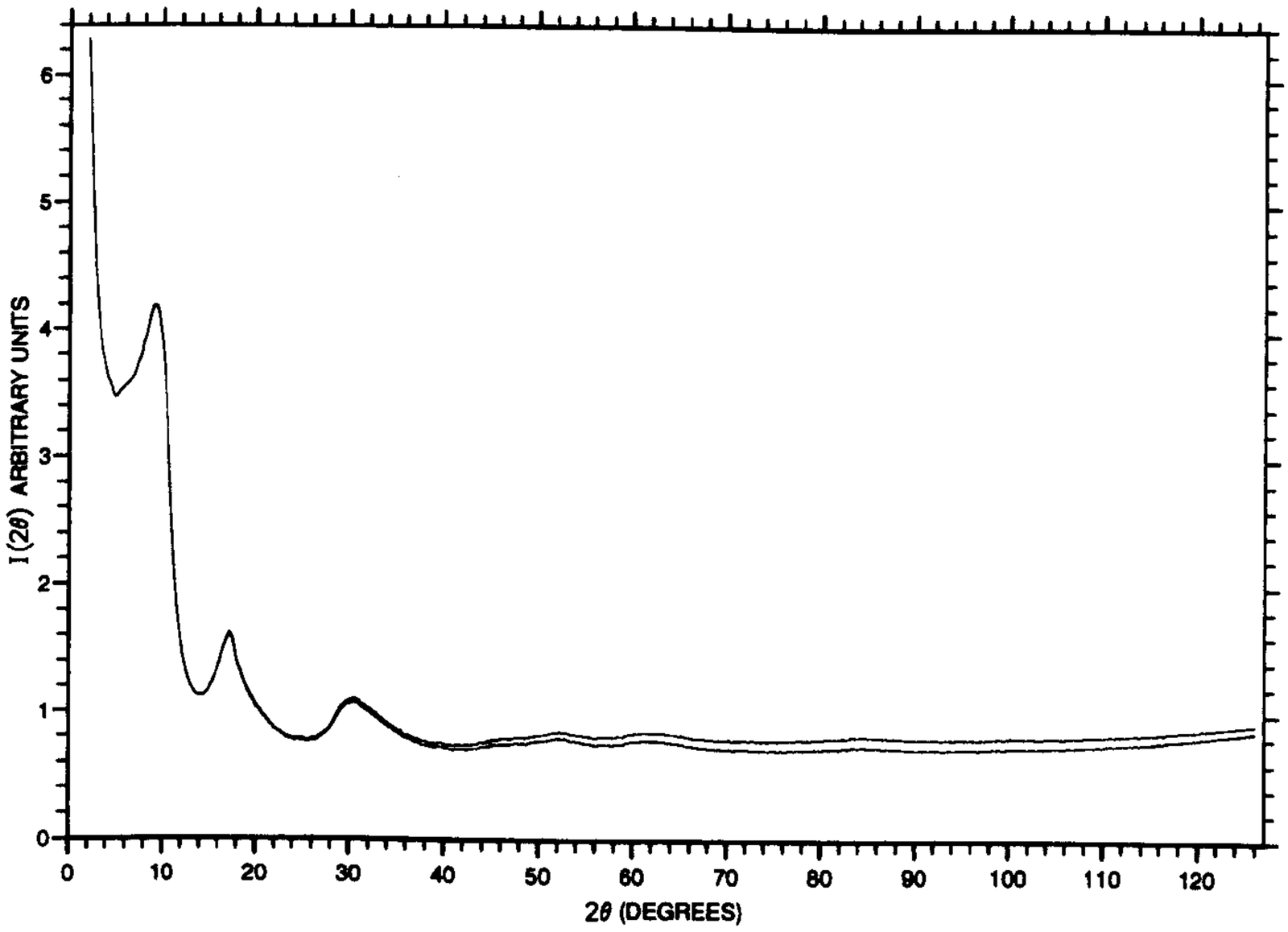

Figure 5.10: Effect of polarization factor correction on the scattering profile for a-$C_{0.74}$:$D_{0.09}$:$H_{0.17}$: bottom curve data before correction has been applied; top curve after correction.

5.4.4 Sample scattering volume

As previously stated (see Section (5.2.2)), the sample volume illuminated by the synchrotron beam and thus the total scattering cross-section presented by the sample to the beam is angularly dependent for a $(\theta : 2\theta)$ scan (see Figure (5.11)). The volume illuminated is given by

$$\text{Scattering Volume} = hw\frac{t}{cos\theta} \tag{5.9}$$

where h is the beam height, w the beam width (normal to the page in Figure (5.11)) and t the sample thickness. The collected data can thus be normalised to a constant scattering volume as follows

$$I_{CV} = I_{PC}\frac{cos\theta}{t} \tag{5.10}$$

where I_{CV} is the intensity that would be observed for a constant volume sample and I_{PC} is the measured scattered intensity corrected for dead time and polarization effects. The effect of the scattering volume correction on the X-ray scattering data collected for the a-$C_{0.74}$:$D_{0.09}$:$H_{0.17}$ sample is shown in Figure (5.12).

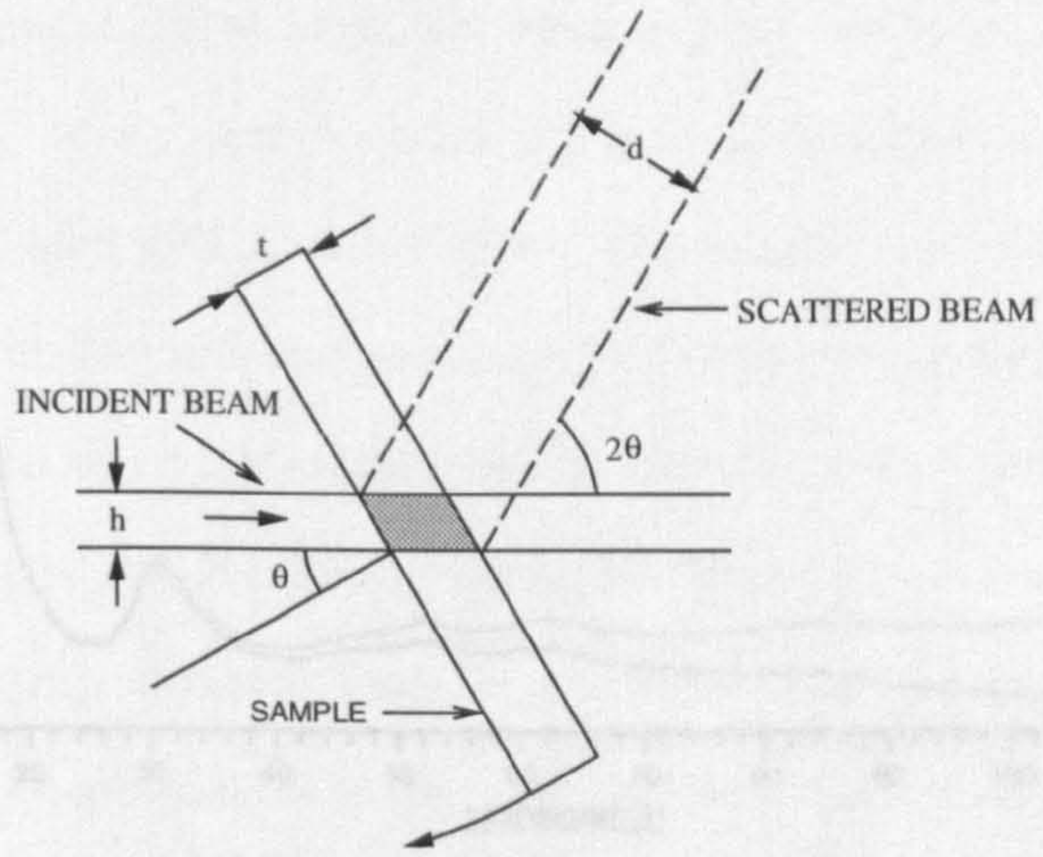

Figure 5.11: Schematic diagram of sample volume illuminated by incident X-ray beam.

5.4.5 Background and air scattering

The scattering profile collected by the detector, I_{s+c+b}, contains not only contributions from sample scattering but also those due to scattering from the container, the volume of air in the vicinity of the sample and noise in the detector electronics. Figure (5.13) shows a cross-sectional view of the air scattering volume as seen by the detector where S is the width of the detector slits. The latter two effects determine the background scattering, I_b. A measure of the background scattering contribution to the data may be gained by scanning with neither sample nor container in the beam. The container scattering and background contributions to the data must be subtracted from the scattering profile to obtain the required sample only scattering.

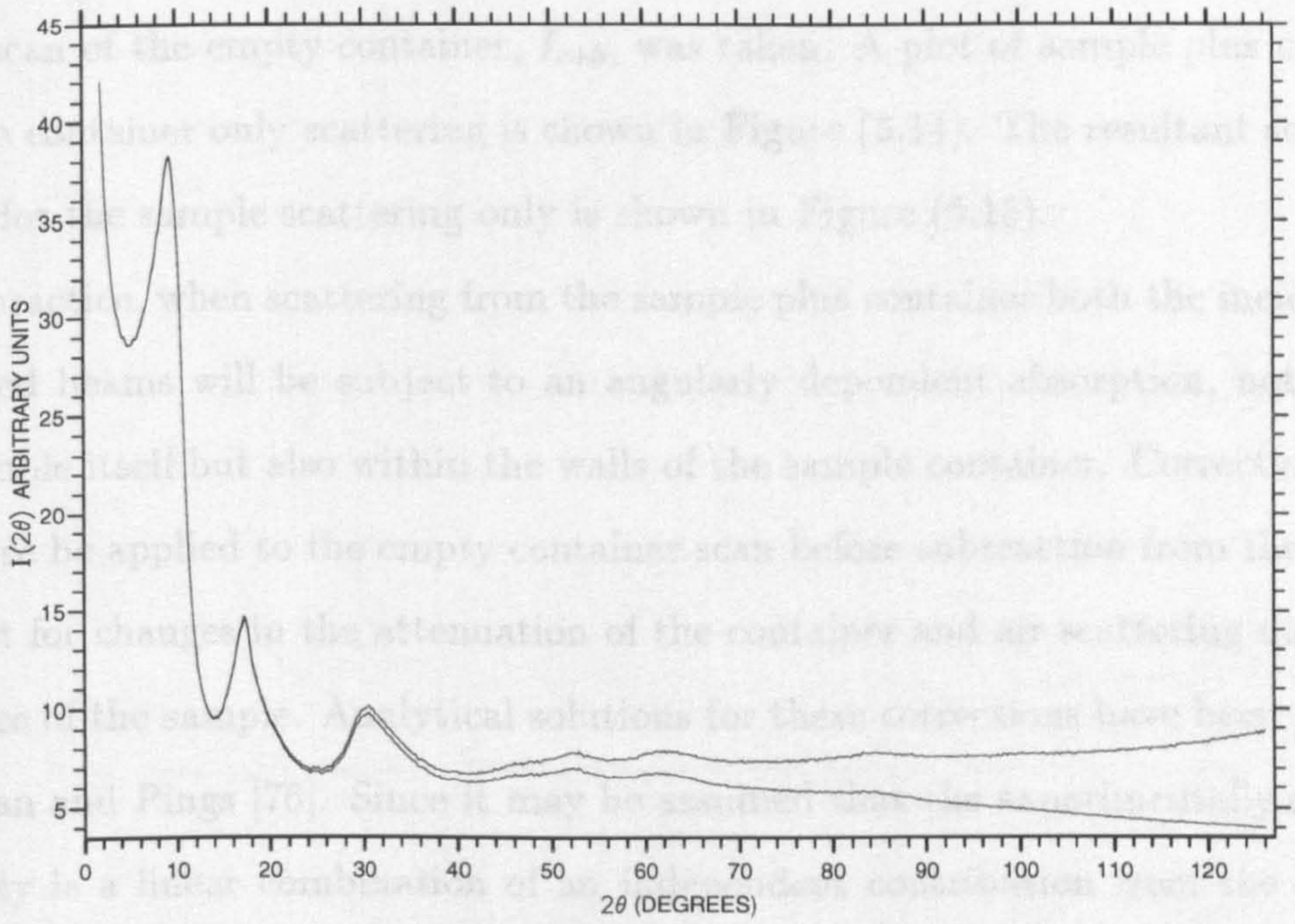

Figure 5.12: Effect of the scattering volume correction on the scattering profile for a-$C_{0.74}$:$D_{0.09}$:$H_{0.17}$: top curve collected data before correction; bottom curve corrected data.

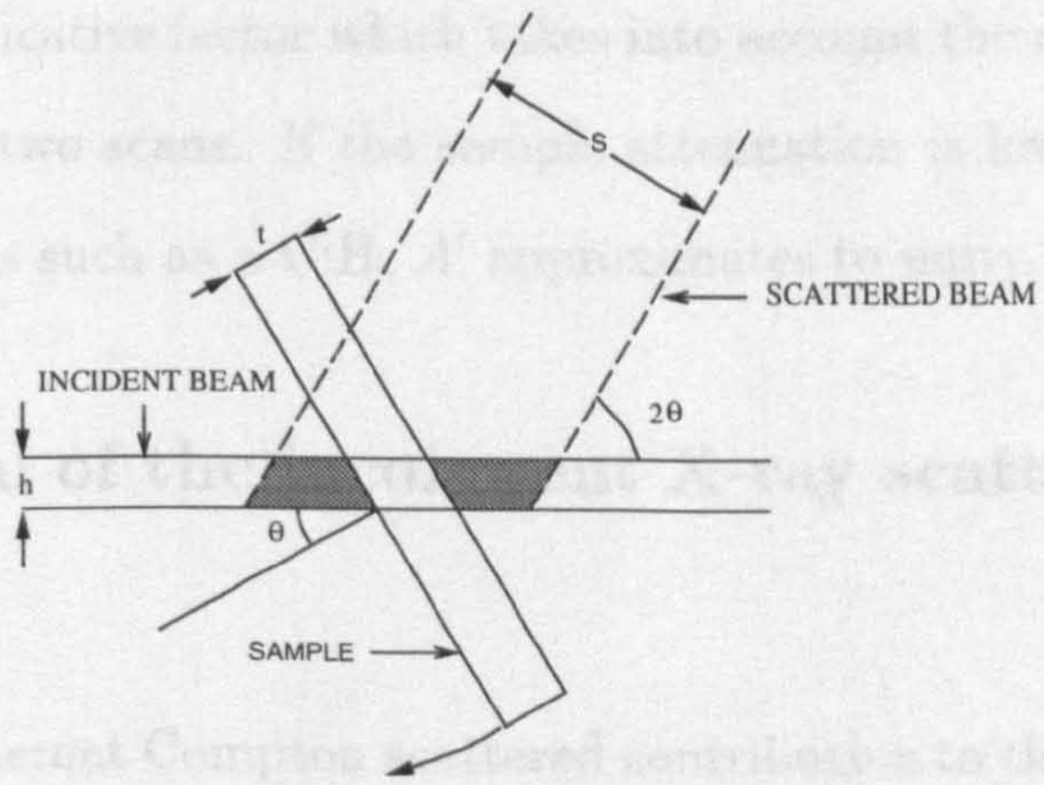

Figure 5.13: Cross-section of the scattering air volume for a $(\theta : 2\theta)$ geometry.

To determine the container scattering contribution to the collected scattering profile, a scan of the empty container, I_{c+b}, was taken. A plot of sample plus container and the container only scattering is shown in Figure (5.14). The resultant scattering profile for the sample scattering only is shown in Figure (5.15).

In practice, when scattering from the sample plus container both the incident and scattered beams will be subject to an angularly dependent absorption, not only in the sample itself but also within the walls of the sample container. Corrections must therefore be applied to the empty container scan before subtraction from the data to account for changes in the attenuation of the container and air scattering due to the presence of the sample. Analytical solutions for these corrections have been given by Paalman and Pings [76]. Since it may be assumed that the experimentally observed intensity is a linear combination of an independent contribution from the confined sample and a component from the sample cell, the required sample only scattering may be expressed as follows

$$I_s = (I_{s+c+b} - I_b) - A'(I_{c+b} - I_b) \tag{5.11}$$

where A' is a multiplicative factor which takes into account the change in attenuation factors between the two scans. If the sample attenuation is low, for example in the case of low Z systems such as a-C:H, A' approximates to unity.

5.4.6 Removal of the incoherent X-ray scattering contribution

Removal of the incoherent Compton scattered contribution to the collected data must be carried out before the data can be converted from a scattered intensity profile measured as a function of angle, $I(2\theta)$, to an intensity profile as a function of momentum

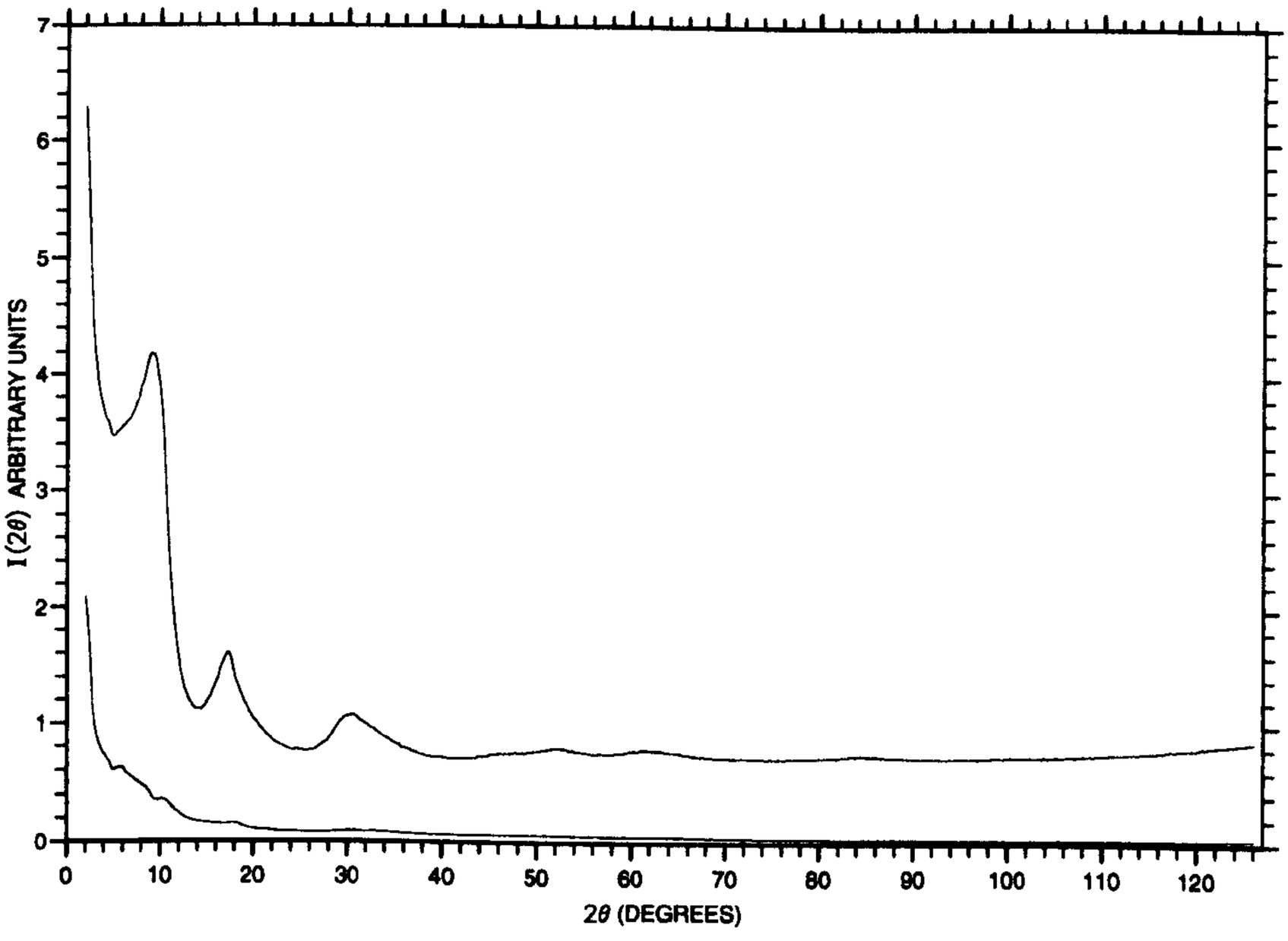

Figure 5.14: Sample plus container scattering (top curve) and container only scattering (bottom curve) for a-$C_{0.74}$:$D_{0.09}$:$H_{0.17}$.

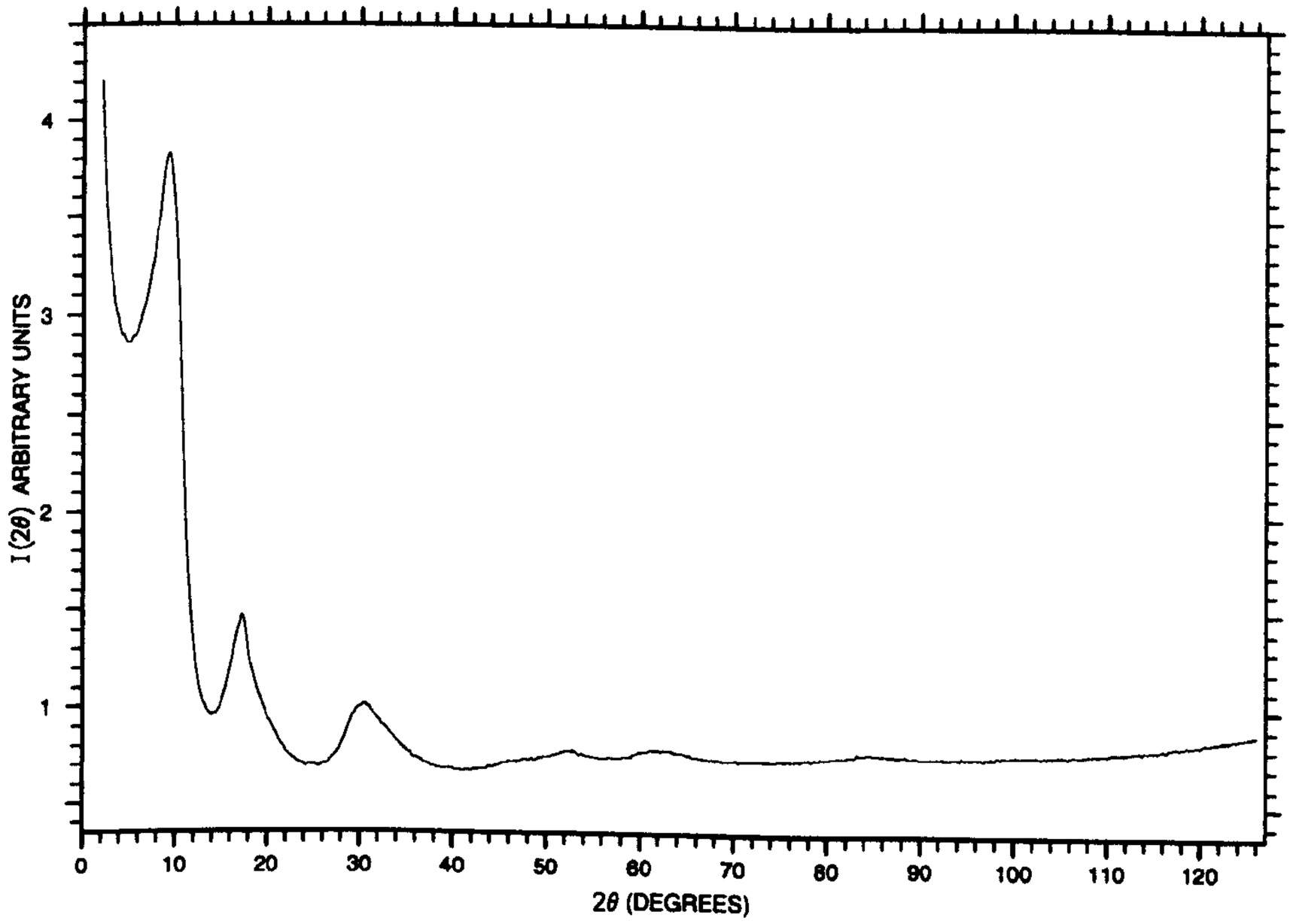

Figure 5.15: Sample only scattering profile for a-$C_{0.74}$:$D_{0.09}$:$H_{0.17}$.

transfer vector, $I(Q)$. If $I(2\theta)$ is converted to $I(Q)$ and account is not taken of the change in wavelength of the Compton scattered radiation from the elastically scattered value, this contribution to the data will be assigned to the wrong Q value. This results in a smearing of the data in Q space. As the absorption corrections to the data are wavelength dependent, these must also be carried out after removal of any incoherent scattering contributions to the data.

Once the data has been corrected for the sample independent factors detailed in the previous subsections, a difference profile may be obtained between the conventional scattering data and that obtained using the Warren-Mavel technique. This difference profile should correspond to the Compton scattered component in the conventional scattering data. There may also be a small contribution to the difference profile from the diffraction pattern of the Mo foil used as a filter in the Warren-Mavel technique. At small scattering angles (i.e. $< 5°$) the incoherent contribution to the conventional scattering profile should approach zero. Thus to obtain a difference profile, the conventional scattering data was scaled to approximately the same scattering intensity level as the Warren-Mavel data in the region of the smallest scattering angle measured ($\sim 2°$). The level of the conventional data was then adjusted until the Compton profile tended to zero at $2\theta = 0°$ and any residual structure in the profile was removed. Figure (5.16) shows the Warren-Mavel data for the a-$C_{0.74}$:$D_{0.09}$:$H_{0.17}$ sample and the scaled conventional scattering profile. In Figure (5.17) the Compton profile obtained for this sample is given. Also shown in Figure (5.17) is the fit made to the profile using a smoothing function. This function uses a fast Fourier transform to filter the noise from the data and is detailed in [77]. The measured Compton profile will include noise contributions from both the standard and the Warren-Mavel data. To avoid introducing this noise into the final structure factor, the smoothed Compton

profile is removed from the scattering profiles.

5.4.7 Absorption corrections

When a parallel, monochromatic beam of X-rays with intensity I_o is incident normally upon a flat plate sample of thickness t and cross-section greater than the incident beam, the transmitted beam, I_t, is given by

$$I_t = I_o exp(-\mu t) \tag{5.12}$$

where μ is the total linear attenuation coefficient for the sample. For X-rays, μ varies with the incident wavelength and the nature of the scattering material. As the reduction in the beam is determined by the amount of matter traversed, the absorber thickness is generally expressed in terms of the mass attenuation coefficient $\frac{\mu}{\rho}$ where ρ is the sample density. Values of the coefficient for the elements can be found in tabulated form [66]. For a multicomponent system the mass attenuation coefficient is given by a weighted sum over those for the constituent elements i.e.

$$\frac{\mu}{\rho} = \sum_i g_i (\frac{\mu}{\rho})_i \tag{5.13}$$

where g_i is the mass fraction of element i whose mass absorption coefficient is $(\frac{\mu}{\rho})_i$. The two main processes contributing to μ are a) photoelectric absorption where the absorbed radiation is used for ejection of a lower-level electron from the atom or excitation to a higher level or b) scattering.

Absorption corrections for $(\theta : 2\theta)$ geometry

Consider a beam of intensity I_o incident on a sample as shown in Figure (5.18). The beam arriving at X is given by $\rho\sigma_s dL$ where ρ is the sample number density and σ_s

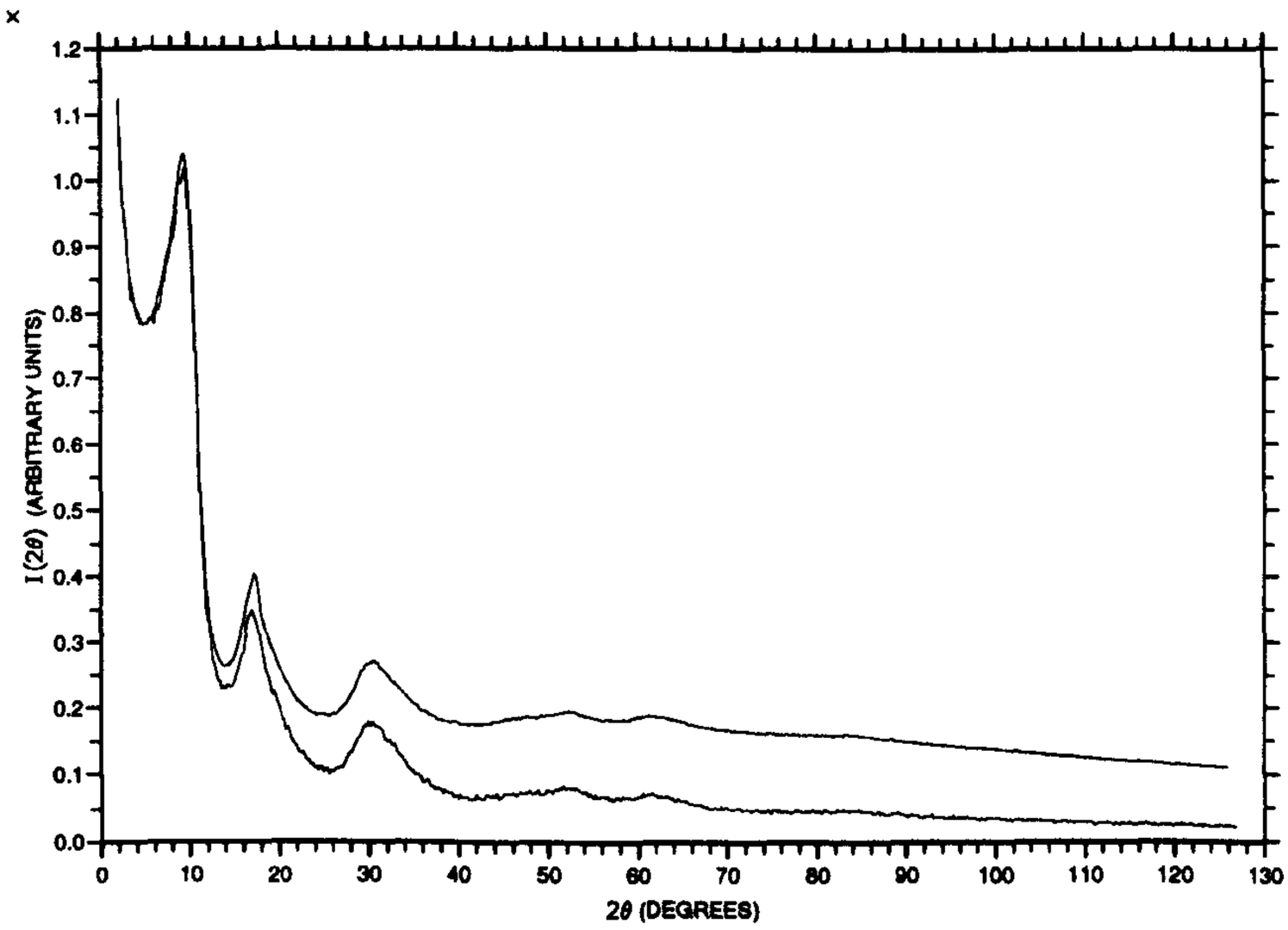

Figure 5.16: Warren-Mavel scattering profile and scaled conventional data for sample a-$C_{0.74}$:$D_{0.09}$:$H_{0.17}$.

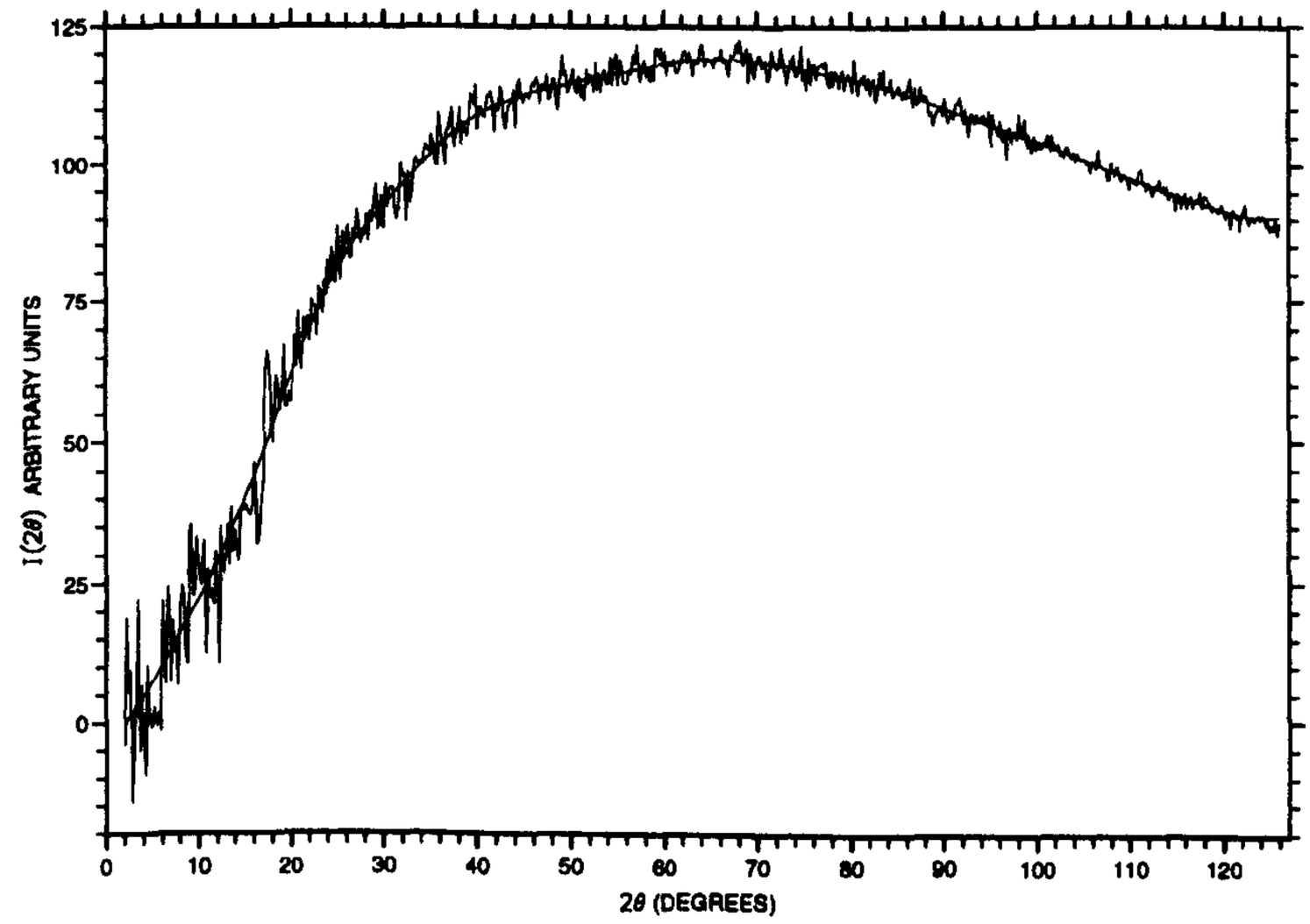

Figure 5.17: Compton scattering profile for a-$C_{0.74}$:$D_{0.09}$:$H_{0.17}$.

is the scattering cross-section. The beam incident at the detector of intensity, I_θ, scattered through β, is given by

$$I_\theta = I_o \rho \sigma_s dl exp[-\mu(l + l')] \tag{5.14}$$

If the absorption coefficient , A, is defined such that

$$\begin{aligned} A &= \frac{\text{absorbed beam intensity}}{\text{Unabsorbed beam intensity}} \\ &= \frac{\int_0^{\frac{t}{cos\alpha}} I_o \rho \sigma_s dl exp[-\mu(l + l')]}{\int_0^{\frac{t}{cos\alpha}} I_o \rho \sigma_s dl} \end{aligned} \tag{5.15}$$

Using a change of variable to x, where $l = \frac{x}{cos\alpha}$ and $l' = \frac{t-x}{cos(\alpha-\beta)}$

$$A = \frac{\int_0^t exp[-\mu\left(\frac{x}{cos\alpha} + \frac{t-x}{cos(\beta-\alpha)}\right)]dx}{\int_0^t dx} \tag{5.16}$$

For a $(\theta : 2\theta)$ geometry where $\alpha = \theta$ and $\beta = 2\theta$

$$\begin{aligned} A &= \frac{\int_0^t exp[-\mu\left(\frac{x}{cos\theta} + \frac{t-x}{cos\theta}\right)]dx}{\int_0^t dx} \\ &= exp\left(\frac{-\mu t}{cos\theta}\right) \end{aligned} \tag{5.17}$$

Therefore

$$I_{corr} = I_o exp\left(\frac{\mu t}{cos\theta}\right) \tag{5.18}$$

where I_{corr} is the absorption corrected intensity. Figure (5.19) shows the effect of absorption corrections when applied to the sample a-$C_{0.74}$:$D_{0.09}$:$H_{0.17}$.

5.4.8 Multiple scattering

The previous data analysis has assumed that X-rays reaching the detector at a scattering angle 2θ have done so as the result of a single scattering event. In practice

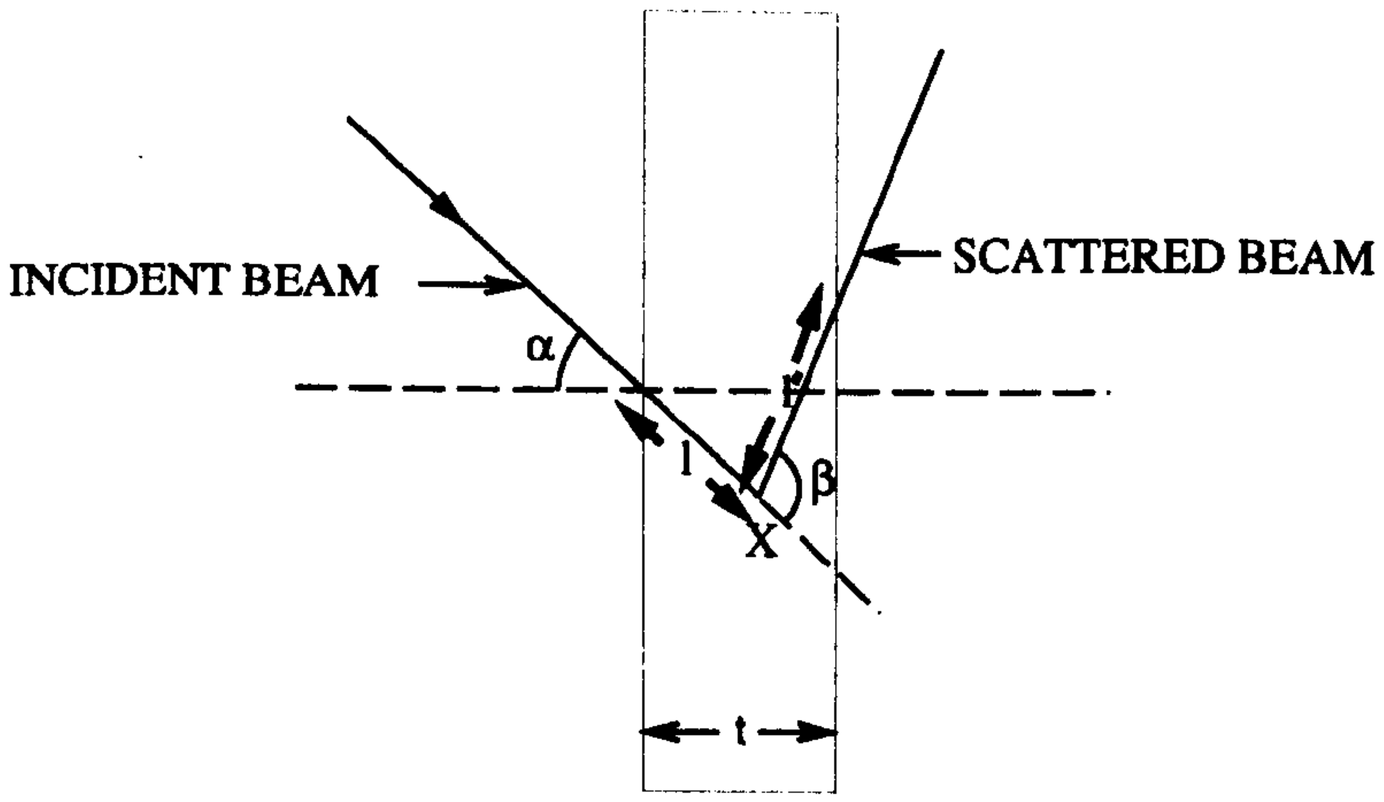

Figure 5.18: Absorption of X-rays in the sample.

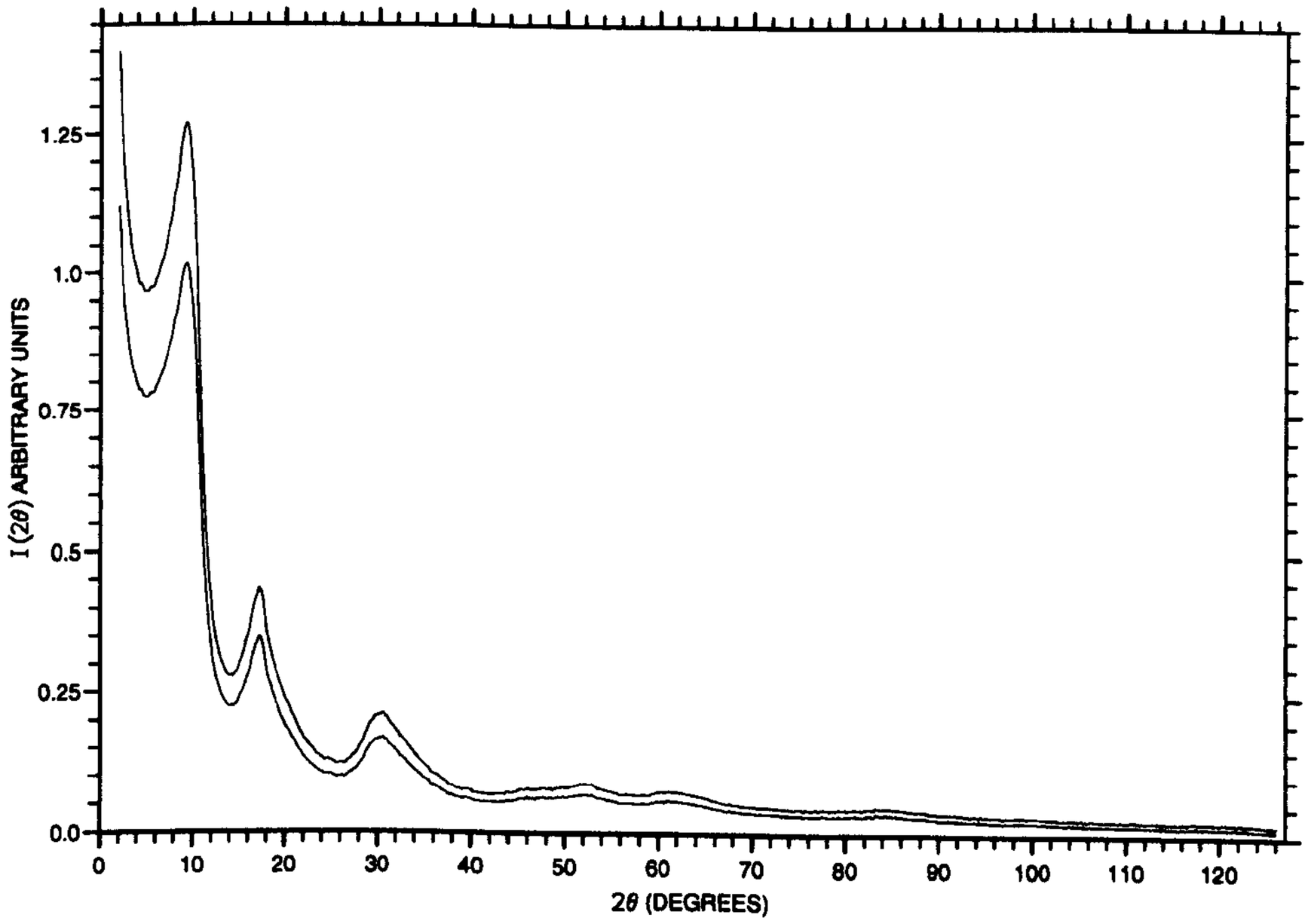

Figure 5.19: Scattering profile for a-$C_{0.74}$:$D_{0.09}$:$H_{0.17}$: before (bottom curve) and after (top curve) absorption correction.

X-rays may be scattered into a given angle as the result of one or more scattering events. Photons scattered into a 2θ angle as a result of more than one scattering process lose their phase relationship to those scattered into the same angle as the result of one interaction only. Only first order scattering is required to investigate the structure of a material and thus contributions resulting from multiple scattering events should be removed from the data.

The ratio of the scattered intensity resulting from second order scattering processes to those resulting from a single scattering process has been evaluated by Warren [60] for the case of an amorphous sample of infinite thickness in reflection geometry. Analytical functions for the secondary scattering of X-rays from non-crystalline materials of finite thickness, in reflection geometry, have been calculated by Dwiggins [78]. In general the multiple scattering component of the data may be reduced by using thinner samples. However the samples are required to be thick enough to produce a statistically significant scattering profile in a practical time period. This problem is reduced by the use of a high intensity source such as the Daresbury Laboratory, SRS. Dwiggins calculated that for a system containing mainly hydrocarbons with μt values ranging from 0.3 to 1, the ratio of secondary to first-order scattering varied correspondingly from 1% to 10%. The value of μt for the a-C:H samples studied was in each case in the region of 0.2. Multiple scattering processes should therefore not contribute significantly to the data collected on these samples and corrections for such have not been applied.

Vineyard [79] has calculated the second order correction for neutron and X-ray scattering from a slab sample. This work shows the ratio of secondary to first order scattering to be proportional to the ratio of the scattering cross-section for the sample to that for scattering plus absorption. Thus multiple scattering provides a greater

contribution to neutron scattering data where this ratio is in general much higher.

5.5 Scaling to absolute units

When all of the above corrections have been applied to the raw data, the resultant scattering curve should represent the function, I_{coh}, where

$$I_{coh} = K[\sum_{i=1}^{M} x_i f_i^2 \quad + \quad (x_i^2 f_i^2(Q)[S_{ii}(Q)-1] + x_j^2 f_j^2(Q)[S_{jj}(Q)-1] \\ + \quad 2x_i x_j f_i(Q) f_j(Q)[S_{ij}(Q)-1])] \tag{5.19}$$

$$= K I_{coh}^{eu} \tag{5.20}$$

K is an arbitrary scaling factor and I_{coh}^{eu} is the coherent scattering curve in electron units. x_i and f_i are the atomic concentration and scattering factor (in electron units) of atom type i respectively. To normalise the scattering curve to electron units it is necessary to determine the value of K. It can be seen from Equation (5.20) that the normalised function, I_{coh}^{eu}, should oscillate about $x_i f_i^2$. At high scattering angles, where the oscillations in the structure factor are very small, I_{coh}^{eu} will approximate to $x_i f_i^2$. For every point, n, in this region the scaling factor K_n is given by

$$K_n(2\theta) = \frac{I_{coh}(2\theta)}{\sum_{i=1}^{M} x_i f_i^2(2\theta)} \tag{5.21}$$

The scaling constant K is then given by the average value over the N points included in the chosen scaling region such that

$$K = \frac{(\sum_{n=1}^{N} K_n)}{N} \tag{5.22}$$

The function $x_i f_i^2$ can be determined for each atom type in the sample from theoretical scattering factor curves (see Section (4.2.1)). The analytical approximations of Stewart, Davidson and Simpson [67,66] have been used to calculate the atomic form

factors for carbon and hydrogen in this case. Stewart et al have calculated theoretical curves specifically for the case of hydrogen terminally bonded to carbon, taking into account the distortion in the electron density function of the hydrogen atom. In their calculations, Stewart et al assume a spherical density for the bound H-atom but "float" this spherical distribution $0.07\mathring{A}$ off the proton into the bond. The curves, for both carbon and hydrogen, are of the form

$$f_i = \left(\sum_{l=1}^{4} A_{l_i} exp[-B_{l_i}\frac{sin^2\theta}{\lambda}]\right) + C_i \tag{5.23}$$

and Table (5.1) gives the coefficients A_l and B_l used.

	Carbon C_i=0.2156		Hydrogen C_i=0.003038	
l	A_l	B_l	A_l	B_l
1	2.31	20.8439	0.493002	10.5109
2	1.02	10.2075	0.322912	26.1257
3	1.5886	0.5687	0.140191	3.14236
4	0.865	51.6512	0.040810	57.7997

Table 5.1: Coefficients A_l and B_l from Stewart et al.

The results of the scaling procedure for sample a-$C_{0.74}$:$H_{0.17}$:$D_{0.09}$ are given in Figure (5.20). Once this procedure has been carried out, the self scattering contribution can be removed from the data and the average scattering factor for the sample divided out to give the total structure factor S(Q), where S(Q) represents a weighted function of the partial C-C, C-H and H-H structure factors i.e.

$$S(Q) = W_{CC}S(Q)_{CC} + W_{CH}S(Q)_{CH} + W_{HH}S(Q)_{HH} \tag{5.24}$$

In practice the weighting factor W_{HH} is negligible and W_{CH} is small i.e. S(Q) is dominated by scattering from the carbon matrix. The structure factor determined for the a-$C_{0.74}$:$H_{0.17}$:$D_{0.09}$ sample is given in Figure (5.21).

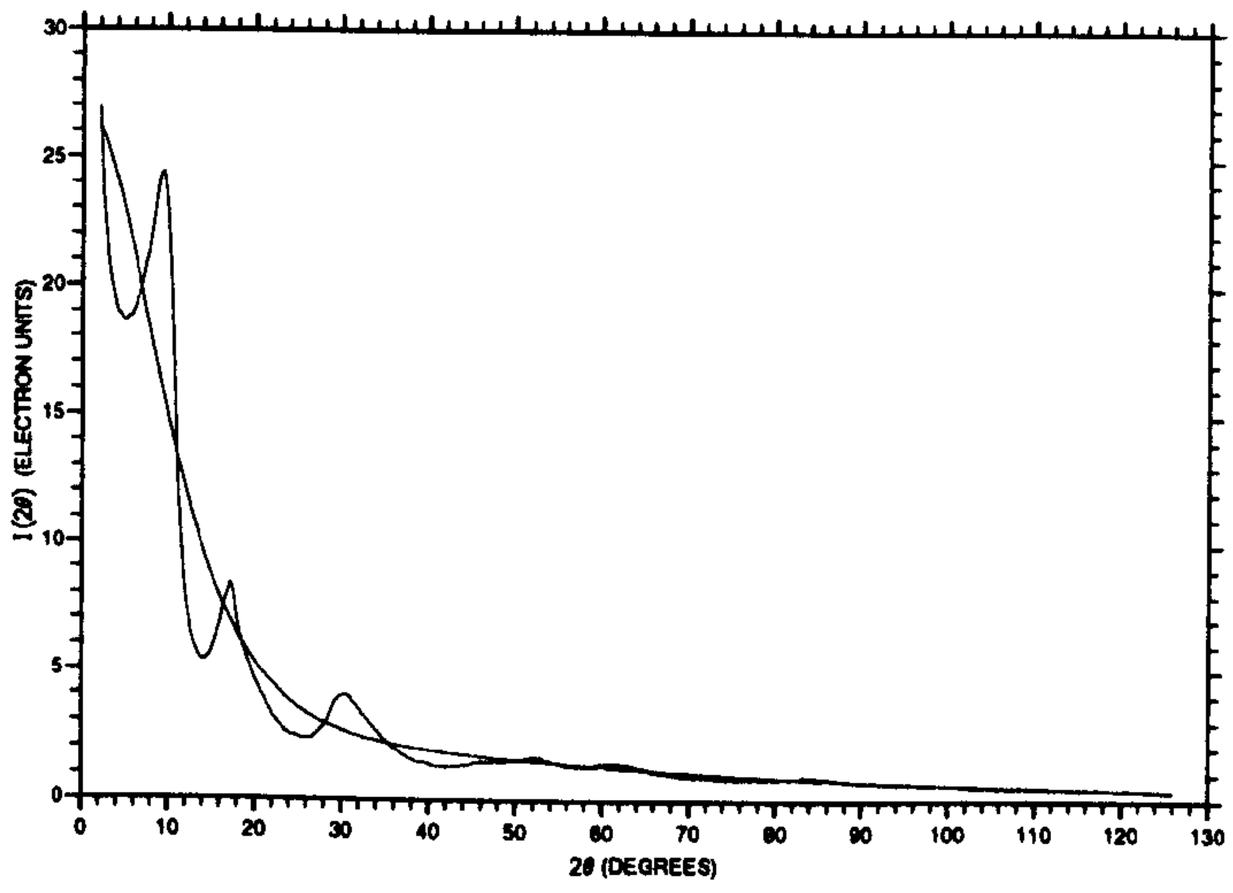

Figure 5.20: Theoretical self-scattering curve and scaled experimental coherent scattering data for sample a-$C_{0.74}$:$H_{0.17}$:$D_{0.09}$.

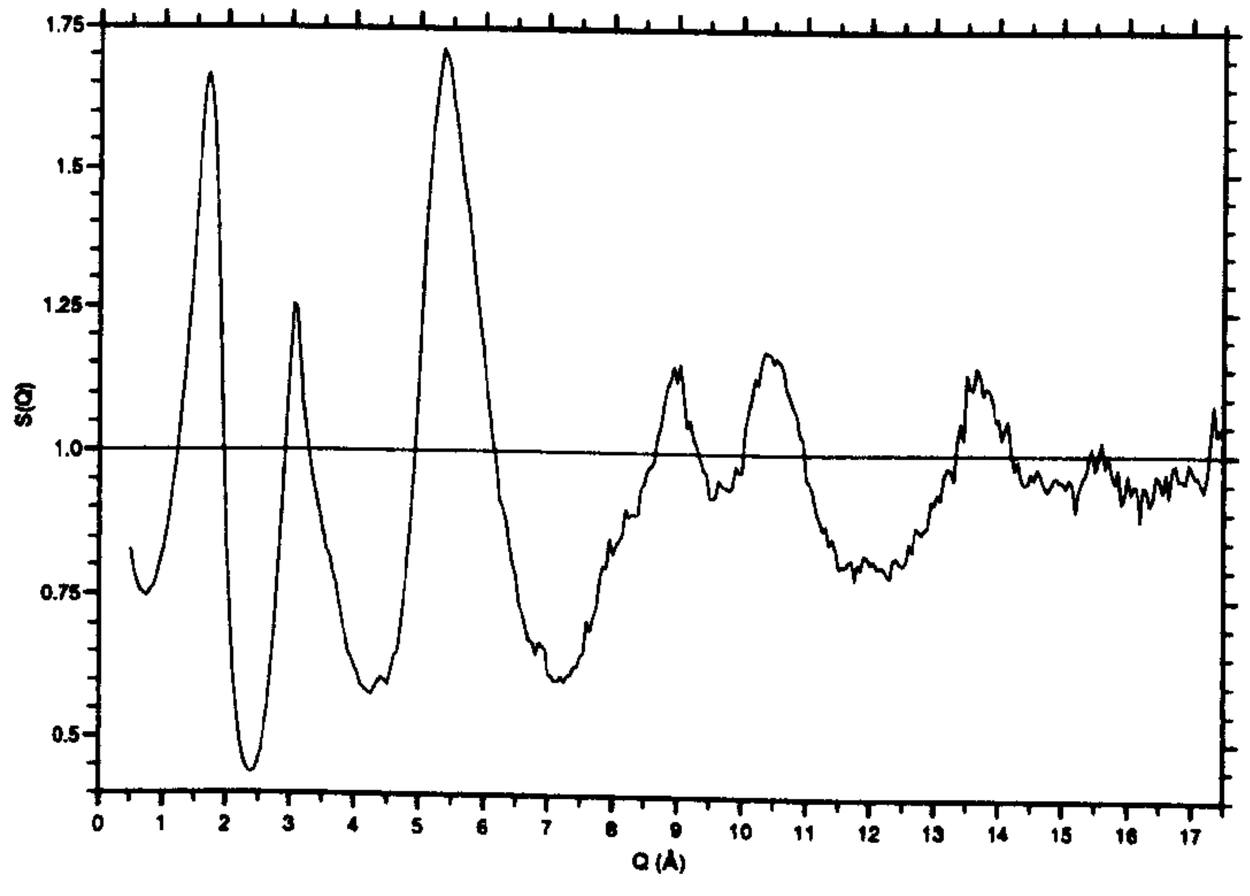

Figure 5.21: Measured structure factor for sample a-$C_{0.74}$:$H_{0.17}$:$D_{0.09}$.

In Chapter (9), the total structure factor obtained by carrying out the data reduction procedures detailed in this chapter are presented for each of the a-C:H(D) samples. Direct comparison of the structure factors measured is made and the real space structural information accessed discussed.

Chapter 6

Experimental Considerations For Neutron Scattering

Neutron scattering studies have been carried out on three samples of a-C:H, having varying degrees of isotopic substitution, at the Rutherford Appleton Laboratory's pulsed neutron source, ISIS, Didcot, Oxon, U.K.

Unlike X-rays, which scatter from the electrons in an atom, neutrons scatter from the nucleus. As the nucleus is a point scatterer, there is no fall off in the scattering factor (or length) with increasing scattering angle, as occurs in X-ray scattering. This is advantageous for the collection of scattering data for amorphous materials at high Q values where the oscillations in the structure factor become much smaller. The quality of the data collected in this region directly affects the resolution of the real space structural information obtained.

Neutrons diffraction studies may be used to probe both the hydrogen and the carbon atomic distribution within the samples. This is in contrast to corresponding X-ray diffraction techniques, where the measured scattering profiles are dominated

by contributions from the carbon matrix. Diffraction data have been collected for these hydrogenous samples on the SANDALS diffractomter at ISIS so as to minimise experimentally inelastic scattering contributions to the measured profiles. The latter can be particularly problematic in the analysis of neutron diffraction data for light elements. Details on the SANDALS diffractometer are given in Section (6.2.1).

Neutron scattering lengths are found to be isotope dependent. Such isotopes will scatter X-rays identically as, by definition, they have the same electronic structure. The technique of isotopic substitution exploits the difference in neutron scattering profiles between chemically identical, isotopically substituted samples to access the partial pair correlation functions for a system (see Section (8.2.1)). The following chapter describes the experimental methods used to collect the neutron scattering data on the three a-C:H(D) samples and the subsequent data analysis required to access the required structure factor, S(Q), from which the structural information on the materials can be inferred.

6.1 Rutherford Appleton Laboratory Pulsed Neutron Source

Neutron scattering experiments are generally carried out on either a pulsed or reactor neutron source. Reactors produce a steady source of fission neutrons in thermal equilibrium with a moderator, the latter being used to slow these neutrons to thermal energies. The neutrons produced by a reactor source therefore have a Maxwellian distribution of energies appropriate to the moderator temperature. The reactor neutron beam is usually then monochromated and neutron scattering data collected at a single wavelength.

A schematic diagram of the main components of a typical pulsed neutron source is given in Figure (6.1). The pulsed accelerator source, ISIS, at the Rutherford Appleton Laboratory produces neutrons by proton spallation. This process involves the bombardment of heavy target nucei by high energy ($\sim$ 800 MeV) protons producing highly excited target nuclear states which decay, either immediately or after a delay, resulting in the release of neutrons (as well as α and β particles, γ rays etc.). At such high energies the proton range is long, tens of centimetres, so many nuclei are affected and the neutron yield is high ($\sim$ 30 neutrons per proton). Nuclear decay process which occur immediately result in so-called "prompt" neutrons and it is these that are used for time-of-flight analysis. "Delayed" neutrons produce a low level, time independent background in the diffractometer; in general the fraction of delayed neutrons is of the order of 0.1%.

There are six main components to ISIS which are: a) an ion source, b) a linear accelerator (linac), c)a fast cycling, high intensity proton synchrotron d) a ^{238}U spallation target e)four neutron moderators at different spectral temperatures and f) a set of neutron scattering instruments.

Protons, injected into the synchrotron from the linac, are forced into a circular orbit by a series of bending and focusing magnets. A radio frequency electric field acting periodically on the proton beam causes both acceleration and bunching of the latter. Single bunches are extracted from the synchrotron by a further magnet and are guided to a depleted uranium target, producing a pulse of neutrons. The design intensity of the proton synchrotron is 2.5×10^{13} protons per pulse at a pulse rate of 50Hz (200μA mean current).

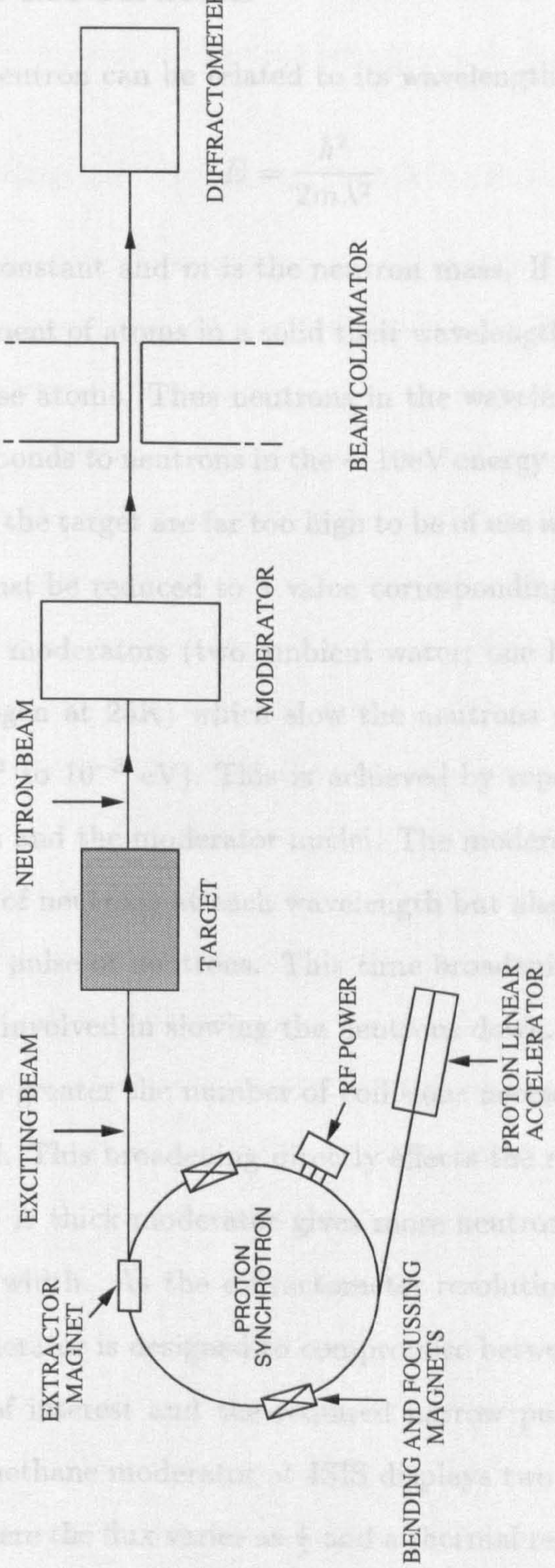

Figure 6.1: Schematic diagram of the main c

6.1.1 Neutron Moderation

The energy, E, of a neutron can be related to its wavelength, λ, as follows

$$E = \frac{h^2}{2m\lambda^2} \tag{6.1}$$

where h is Planck's constant and m is the neutron mass. If neutrons are to be used to study the arrangement of atoms in a solid their wavelength must be of the order of the separation of these atoms. Thus neutrons in the wavelength region of $\sim 1\mathring{A}$ are required. This corresponds to neutrons in the $\sim$ 10eV energy range. The energy of the neutrons produced in the target are far too high to be of use in diffraction experiments and their velocity must be reduced to a value corresponding to the required energy range. ISIS has four moderators (two ambient water; one liquid methane at 100K, and one liquid hydrogen at 25K) which slow the neutrons down to epithermal and thermal energies (10^2 to 10^{-3} eV). This is achieved by repeated inelastic collisions between the neutrons and the moderator nuclei. The moderation process determines not only the number of neutrons at each wavelength but also the broadening in time of the initially sharp pulse of neutrons. This time broadening, Δt, results from the inevitable time scale involved in slowing the neutrons down. The slower the neutron velocity required, the greater the number of collisions necessary and the greater the resultant time spread. This broadening directly effects the resolution of the time-of-flight data collected. A thick moderator gives more neutrons at longer wavelengths but a broader pulse width. As the diffractometer resolution is proportional to the pulse width, the moderator is designed to compromise between the neutron intensity at the wavelengths of interest and the required narrow pulse width. The neutron spectrum from the methane moderator at ISIS displays two distinct regions [80]: an epithermal region where the flux varies as $\frac{1}{\lambda}$ and a thermal region where a Maxwellian

distribution is observed. In the epithermal region $\Delta t \propto \lambda$. At thermal energies this breaks down and the associated extra broadening is undesirable.

6.1.2 Collimation of the Neutron Beam

As the neutrons emerge in all directions from the moderator, they must be collimated before use in a diffraction experiment. In deciding upon the beam collimation a trade-off must be made between incident intensity at the sample and resolution. For the case of neutron scattering from an amorphous sample the demands on resolution are less restrictive due to the diffuse nature of the scattering profile. The total cross-section for neutron scattering from carbon, hydrogen and deuterium is sufficiently large that the incident neutron intensity for the a-C:H(D) samples is not required to be particularly high, in contrast to the case for X-ray scattering from these low Z samples. However, where isotopic substitution experiments are being carried out, the counting error on the individual time-of flight scans collected is required to be suitably small such that when the data sets are combined a statistically significant profile for the individual partial pair correlation functions may be obtained. Thus, when carrying out isotopic substitution experiments, the incident intensity is required to be such that these statistical requirements can be met in a reasonable time period.

In a time-of-flight experiment a full wavelength spectrum from the maximum neutron energy ($\sim$ 800 MeV) downwards is incident upon the sample. Therefore materials such as cadmium, which are often used in the case of a reactor where the beam is monochromated, are not suitable (particularly because of the high energy γ rays produced by neutron capture in this material). Thus boron is used as a primary component in the construction of the collimators at ISIS as it has a neutron capture cross-section inversely proportional to the neutron velocity over a wide energy range.

These collimators are further surrounded by a shielding of materials such as iron and borated wax to minimise any radiation reaching workers at the diffractometers.

6.1.3 The Time-of-Flight Diffraction Method

For elastic scattering, the momentum transfer vector, Q, is related to the scattering angle, 2θ, and the incident wavelength, λ, as follows (see Section (4.1.2)

$$Q = \frac{4\pi}{\lambda} \sin\theta \tag{6.2}$$

In the case of a time-of-flight experiment, a white beam is incident at the sample. Scattered neutrons are collected by a series of detectors at fixed angles to the transmitted beam, as a function of the elapsed time after a trigger signal just prior to firing of the pulsed source. Assuming the scattering to be elastic, the wavelength of a neutron incident at the detector may be related to its recorded flight time, t, over the distance from the moderator to the detector, $L_o + L_1$, as follows [81]

$$\lambda(\mathring{A}) = 0.03956 \frac{t(\mu s)}{L_o(\text{mm}) + L_1(\text{mm})} \tag{6.3}$$

where L_o and L_1 are the incident and scattered flight paths as shown in Figure (6.2). Each detector therefore scans the neutron scattering profile for the sample over a Q range determined by its total flight path distance from the moderator. The Q space resolution of the collected data is determined by several factors including contributions due to uncertainties in the scattering angle and flight time of the detected neutrons and from the effect of the pulse width at the moderator. The latter is determined by the moderator characteristics and has been discussed in the previous section. The flight path and angular uncertainty arise because of the finite size of the moderator, sample and detector and are therefore determined by the particular instrument geometry. For an instrument such as SANDALS, where the maximum

detector angle is 21°, the uncertainty in the scattering angle dominates the resolution function [80].

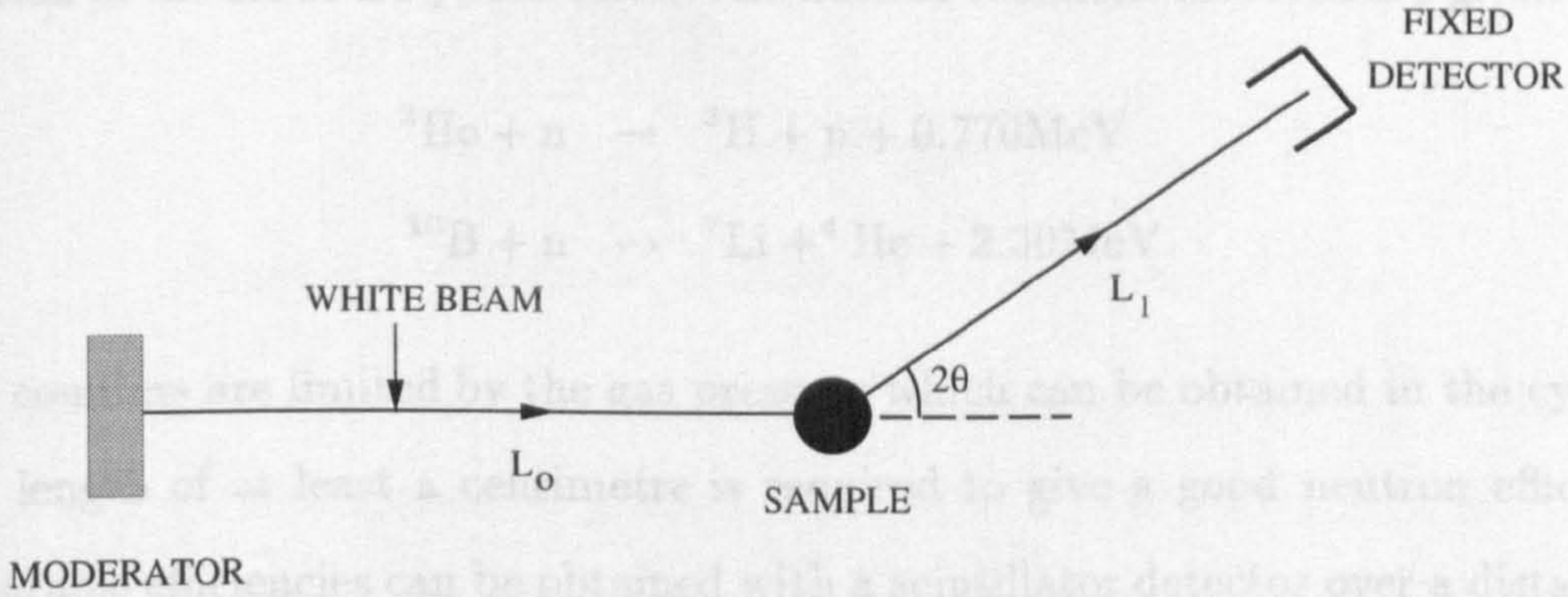

Figure 6.2: Schematic diagram of the time-of-flight diffraction method

6.2 Neutron Detection

An ideal neutron detector would record the incidence of all thermal and epithermal neutrons whilst being insensitive to any background radiation such as γ rays, fast neutrons and cosmic rays. It should also recover quickly from the process of recording one neutron event and rapidly return to a state in which it is able to record subsequent events i.e. it should have a short dead time (see Section (5.4.1)). For time-of-flight data collection, a further requirement is that neutron detection should take place over over a short distance so as to minimise the uncertainty in the neutron flight path.

As neutrons are uncharged they cannot be detected by direct ionisation of the detector medium. However they can induce nuclear reactions in some media which result in the release of ions and a considerable amount of energy. These ions subsequently cause a strong degree of ionisation which can be detected. ^{3}He or BF_3 gas

counters are commonly used as detectors. These detectors consist of a stainless steel or copper cylinder, in which the gas is held, and a thin wire anode which runs through the cylinder. The positively charged anode collects the electrons resulting from the ionisation of the He or BF_3 molecules. The nuclear reactions involved are given below

$$\begin{aligned} {}^{3}\mathrm{He} + \mathrm{n} &\rightarrow {}^{3}\mathrm{H} + \mathrm{p} + 0.770\mathrm{MeV} \\ {}^{10}\mathrm{B} + \mathrm{n} &\rightarrow {}^{7}\mathrm{Li} + {}^{4}\mathrm{He} + 2.30\mathrm{MeV} \end{aligned} \tag{6.4}$$

These counters are limited by the gas pressure which can be obtained in the cylinder and a length of at least a centimetre is required to give a good neutron efficiency. Comparable efficiencies can be obtained with a scintillator detector over a distance of a few millimetres by using a much denser neutron absorber. Typically the absorber used is ^{6}Li and the nuclear reaction involved is

$${}^{6}\mathrm{Li} + \mathrm{n} \rightarrow {}^{4}\mathrm{He} + {}^{3}\mathrm{He} + 4.79\mathrm{MeV} \tag{6.5}$$

The reaction products are detected by a crystal phosphor, such as ZnS, which may be mixed with the absorber. The phosphor emits a flash of light as the ionising particle passes through the mixture and the light emitted is coupled, via a light guide, to a photomultiplier tube. A schematic diagram of the detector is given in Figure (6.3). A particular problem with scintillator detectors is their response to γ rays which may also be produced as a result of the nuclear reactions. However this can be overcome by pulse shape analysis [81].

6.2.1 SANDALS Diffractometer

Neutron scattering studies of the a-C:H(D) samples were carried out on the SANDALS (Small Angle Diffraction for Amorphous and Liquid Samples) diffractometer

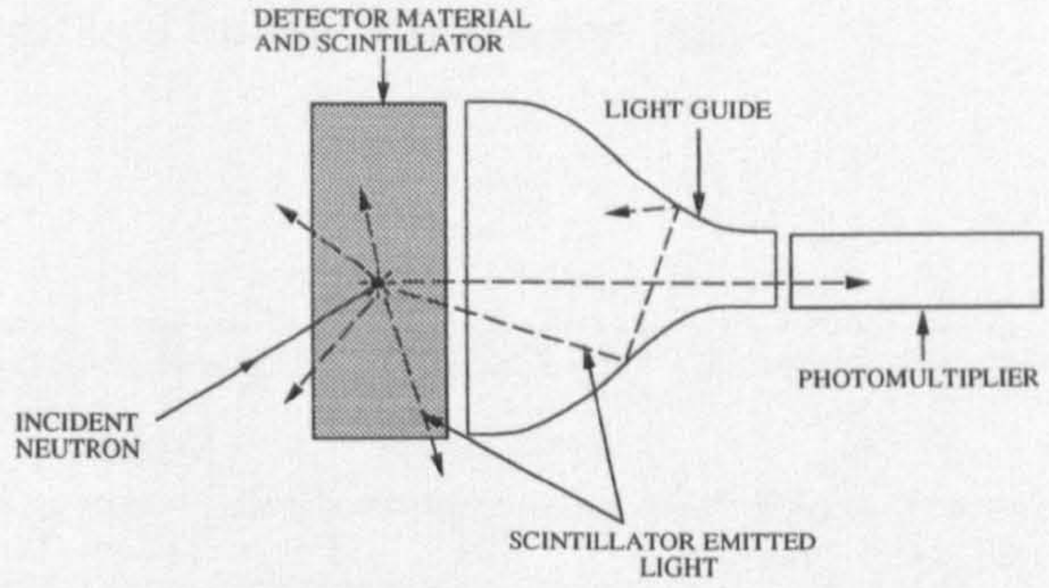

Figure 6.3: Schematic diagram of a scintillator detector

at the Rutherford Appleton Laboratory's pulsed neutron source, ISIS. A schematic diagram of the diffractometer is given in Figure (6.4). This instrument has a series of detectors biased towards smaller scattering angles (i.e. $< 22°$) and an incident wavelength spectrum in the high energy neutron range. Both of these factors help to minimise inelasticity effects in the collected data. Such effects can be difficult to correct effectively for in some cases and are particularly problematic for systems such as amorphous hydrogenated carbon which contain light elements (see Section (6.3.6)). The SANDALS diffractometer was chosen for the neutron scattering studies of the a-C:H(D) samples specifically so as to minimise this problem. The use of small detector angles also allows access to the small Q scattering region which draws its structure from longer range correlations in the scatterer. The wavelength spectrum incident at the sample on the SANDALS diffractometer typically covers a range from 0.05 to 4.0$\mathring{A}$.

Scattered neutrons are detected on the SANDALS diffractometer by a series of ZnS detectors. These detectors are typically 10mm wide x 200mm tall and are arranged in two groups which cover the scattering range from 3° to 21° in a continuous span. Each group is divided into modules of twenty detectors. Table (6.1) gives the angular range; the number of detectors; the corresponding Q range sampled, and the resolution for

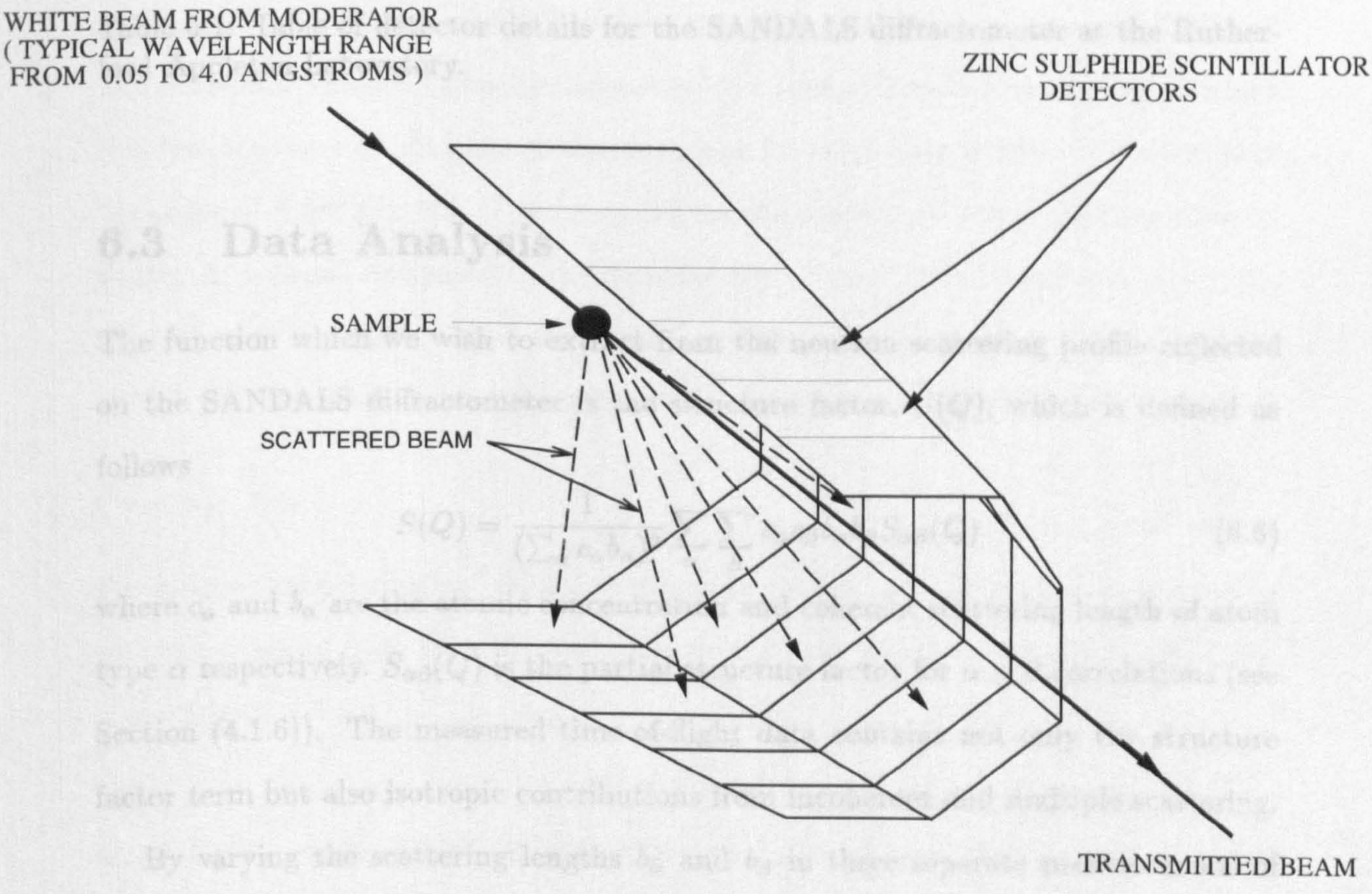

Figure 6.4: Schematic diagram of the SANDALS diffractometer at the Rutherford Appleton Laboratory Pulsed Neutron Source

each of the detector groups on the instrument [82].

Detector Group	Angular Range Covered	Number of Detectors	Q range sampled ($\AA^{-1}$)	Resolution $\frac{\Delta Q}{Q}$
1	$3° - 11°$	100	$0.08 - 24.09$	$0.03 - 0.16$
2	$11° - 21°$	360	$0.30 - 45.80$	0.03

Table 6.1: Table of detector details for the SANDALS diffractometer at the Rutherford Appleton Laboratory.

6.3 Data Analysis

The function which we wish to extract from the neutron scattering profile collected on the SANDALS diffractometer is the structure factor, $S(Q)$, which is defined as follows

$$S(Q) = \frac{1}{(\sum_\alpha c_\alpha b_\alpha)^2} \sum_\alpha \sum_\beta c_\alpha c_\beta b_\alpha b_\beta S_{\alpha\beta}(Q) \tag{6.6}$$

where c_α and b_α are the atomic concentration and coherent scattering length of atom type α respectively. $S_{\alpha\beta}(Q)$ is the partial structure factor for $\alpha - \beta$ correlations (see Section (4.1.6)). The measured time-of-flight data contains not only the structure factor term but also isotropic contributions from incoherent and multiple scattering.

By varying the scattering lengths b_α and b_β in three separate measurements of S(Q), three independent equations in the partial structure factors can be obtained, from which the functions $S_{\alpha\alpha}$, $S_{\beta\beta}$ and $S_{\alpha\beta}$ can be determined. This is the basis of the isotopic substitution technique which is described in Section (8.2.1).

6.3.1 Dead Time Correction

Regardless of the quality of the detector, there will always be a finite time after a neutron event has occurred before the detector has returned to a state in which it is able to record a subsequent neutron event. If the occurrence rate of neutron events exceeds a certain value, a fraction of these will not be recorded by the detector. The period of time during which a detector is unable to record neutron events is known as its dead time. For a ZnS detector, such as those used on the SANDALS diffractometer, the dead time lies between 2 and 10μs, depending on the way in which the detector is set up. In general the correction for dead time on this instrument is of the order of a few percent. Two cases can be considered: a) where the time channel width, Δ, is broad compared to the detector dead time, τ, and b) the case where the time channel is narrower than the dead time. Here the time channel represents the time "bin" into which a neutron event at the detector is assigned.

Case a): $\Delta > \tau$

For a time channel width of Δ, a detector dead time τ and a recorded count rate, in counts per μs, of C_{rec}, then the period of time during which the channel is dead, D, is given by

$$D = \Delta C_{rec} \tau \tag{6.7}$$

where both Δ and τ are in μs. Thus the actual neutron event rate, C, which would have been measured if the detector dead time was zero, is greater than that recorded and is given by

$$\begin{aligned} C &= \frac{\Delta}{(\Delta - D)} C_{rec} \\ &= \frac{1}{(1 - \frac{D}{\Delta})} C_{rec} \end{aligned}$$

$$= \frac{C_{rec}}{(1 - C_{rec}\tau)} \tag{6.8}$$

Case b): $\Delta < \tau$

If the channel width, Δ, is narrower than the detector dead time, τ, then the dead time for a given channel, m, may have contributions from previous channels. The length of time during which this channel is dead is then given by

$$D_m = \tau \sum_{j=n,m} \Delta_j C_j \tag{6.9}$$

assuming channels n to m contribute to the dead time in channel m. Δ_j and C_j are the width and count rate in channel j respectively. The dead time is then calculated in the same manner as for case a), with D in Equation (6.7) replaced by D_m.

In practice, when a large number of detectors are in use on a diffractometer, it is not practical to have a separate input to the data acquisition electronics for each detector. Instead, an encoder is used which produces a binary address describing which detector has fired. If the dead time of the encoder, τ_e, is greater than that of the detector, then τ_e will determine the detector dead time. Further, as the encoder can only process one event at a time, when one detector fires all the detectors in the group connected to that encoder will effectively become "dead" for the period of time required to process the event. Account should therefore be taken of the encoder dead time when calculating the corrections. A sum should therefore be taken over all the detector channels, k, feeding into the encode such that the detector dead time in Equation (6.9) becomes

$$D_m = \tau \sum_{j=n,m} \sum_{k} \Delta_j C_{j,k} \tag{6.10}$$

where $C_{j,k}$ is the count rate in time channel j and encoder channel, k. Δ_j in Equation (6.10) now corresponds to the encoder dead time. Although the dead time for the

individual detectors may be small, when they are grouped into a single encoder, the effective count rate increases in proportion to the number of detectors grouped together. Thus the dead time correction factor will be greater than the apparent value from the count rate at an individual detector.

6.3.2 Normalisation To the Incident Beam

The neutron spectrum incident at the sample may vary over time due to slight changes in the moderator temperature or the proton beam steering. In order to monitor the flux incident at the sample a detector is placed in the incident beam. This detector is required to be of low efficiency so as not to reduce significantly the incident intensity at the sample. The monitor count recorded is used to normalise each scan to the incident spectrum. Assuming that dead time corrections have been made, the monitor count rate will depend on the incident spectrum, I_{in^M}, and the monitor efficiency, $E_M(k)$. Similarly the detector count rate will be determined by the flux incident at the detector, I_{in^D} and the detector efficiency E_D. The efficiency for both will vary with the wavevector of the incident neutrons, k, and therefore

$$I_{mon}(k) = I_{in^M}(k)E_M(k) \tag{6.11}$$

and

$$I(k) = I_{in^D}(k)E_D k \tag{6.12}$$

where I represents the raw data and I_{mon} the monitor count rate. If N_u is the number of scattering units in the beam and $\Delta\Omega$ is the detector solid angle, then the normalised data, I_{norm} is given by

$$\begin{aligned} I_{norm} &= \frac{I(k)}{I_{mon}(k)} \\ &= N_u \frac{d\Omega}{d\sigma} \frac{E_D}{E_M} \Delta\Omega \end{aligned} \tag{6.13}$$

$\frac{d\Omega}{d\sigma}$ is the differential scattering cross-section which defines the number of neutrons scattered per unit time into unit solid angle per scattering unit (see Section (4.1.1)). The normalised data for the a-$C_{0.75}$:$H_{0.25}$ sample is shown in Figure (6.5). Also shown is a scan of the sample independent background. This background results from neutrons, and other forms of radiation, which arise from the neutron source but not from the beam, as well as noise in the detector electronics, and both must be subtracted from all of the measured scattering profiles.

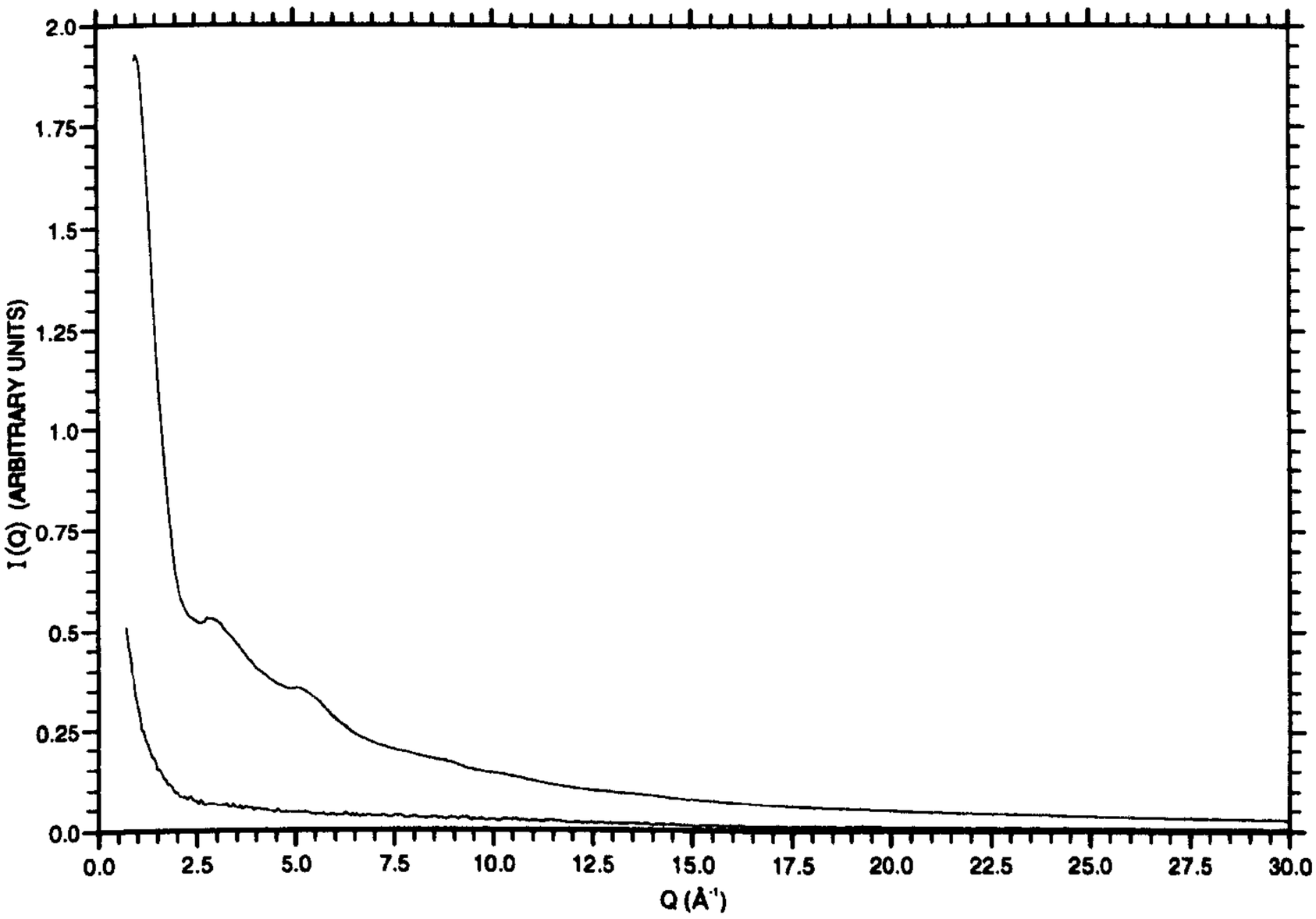

Figure 6.5: Neutron scattering profile for the a-$C_{0.75}$:$H_{0.25}$ sample normalised to the incident neutron spectrum (top curve). Also shown is the measured sample independent background (lower curve)

6.3.3 Vanadium Standard Calibration

It can be seen from Equation (6.13) that in order to obtain the differential scattering cross-section, $\frac{d\Omega}{d\sigma}$, and hence the structure factor, $S(Q)$, for the samples studied the

function

$$F_{cal} = \frac{E_D}{E_M}\Delta\Omega \tag{6.14}$$

must be determined where $\Delta\Omega$ is the detector solid angle. E_D and E_M are the monitor and detector efficiencies respectively and will be energy dependent. The function, F_{cal}, may be determined using the scattering from a vanadium calibration rod of identical dimensions to the sample. Vanadium is chosen as a calibrant as its cross section is almost all incoherent (i.e. smooth in Q space) and well determined. The normalised scattering from the vanadium rod is given by

$$\begin{aligned} I^{van}_{norm} &= F_{cal}[N_v \Sigma_{van} A_{v,v} + M^{van}] \\ &= F_{cal}\left(\frac{d\sigma}{d\Omega}\right)^{van} \end{aligned} \tag{6.15}$$

where Σ_{van} is the time-of-flight differential scattering cross-section (see Section (6.3.6)) and M^{van} the multiple scattering contribution for the vanadium respectively. N_v is the number of vanadium atoms in the beam. As the terms in square brackets are well defined, F_{cal}, can therefore be determined from I^{van}_{norm}. Figure (6.6) shows the vanadium rod calibration scan measured immediately before the sample scattering scans were taken.

To prevent contributions from statistical noise and the small, (311), Bragg peak in I^{van}_{norm} at Q=2.57$\mathring{A}$ (and other, smaller peaks) from contributing to F_{cal}, the former is smoothed using a spline fit and F_{cal} determined from the smoothed function.

6.3.4 Beam Transmission

Attenuation of the incident neutron beam occurs through scattering and capture processes in the sample. Except for a few elements which have resonances below 0.5eV (0.4$\mathring{A}$), all the elements have a capture cross section proportional to the neutron

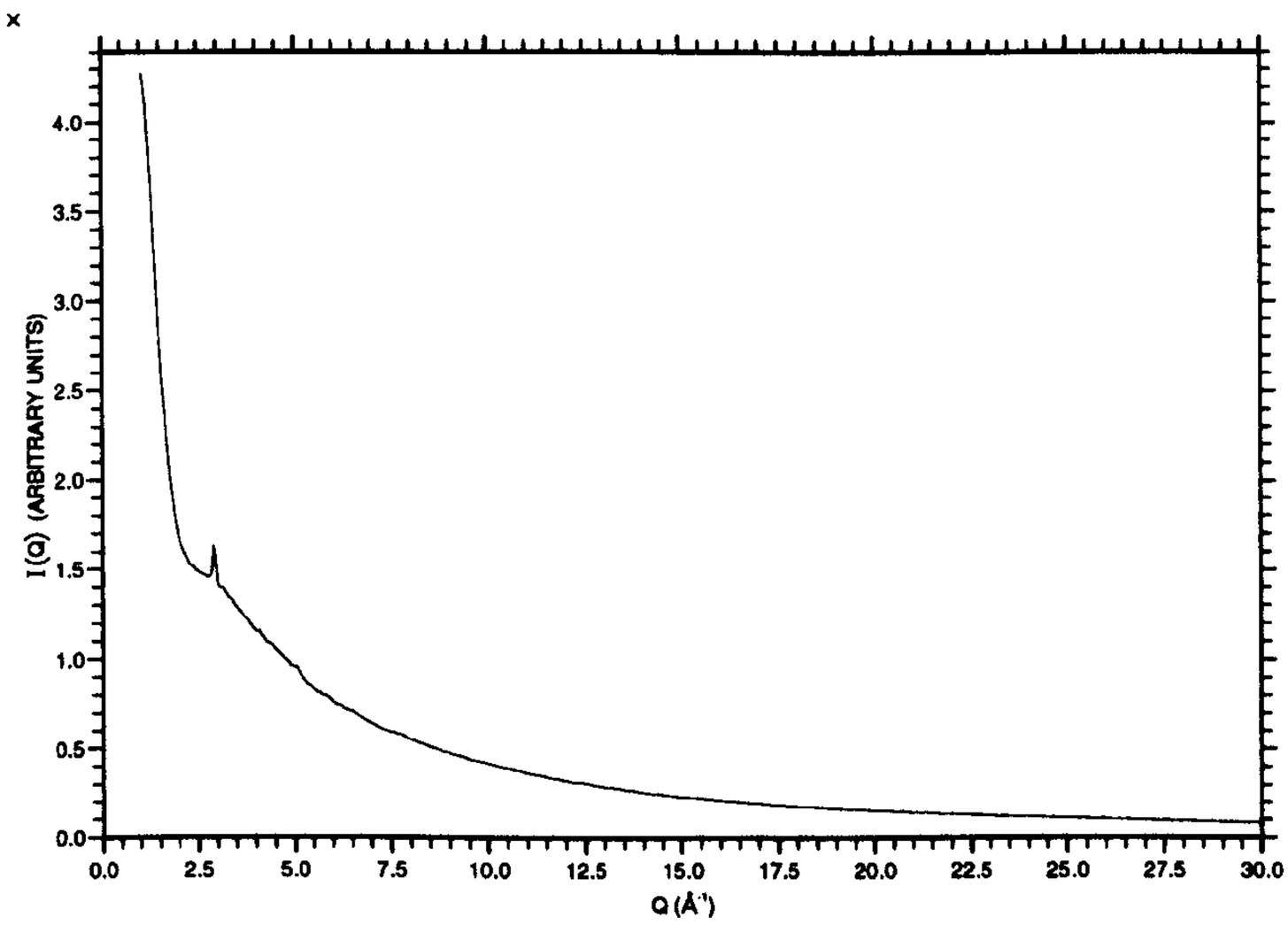

Figure 6.6: Scattering profile for 5mm diameter vanadium rod

wavelength. The constant of proportionality, usually tabulated at $\lambda = 2200ms^{-1}$, is the capture cross-section, σ_a. The scattering cross-section, σ_s, for the elements represents the sum over all angles of the differential cross-section, $\frac{d\sigma}{d\Omega}(\lambda)$, at wavelength λ, where

$$\frac{d\sigma}{d\Omega}(\lambda) = N_u b^2 S(Q) \tag{6.16}$$

If the assumption is made that the nucleus is fixed during the scattering process, then b, in Equation (6.16), represents the bound scattering length, b_{bound}, which is the value generally quoted in tables. In practice, the nucleus may recoil and the scattering should be considered in a centre-of-mass system. The mass of the nucleus, M, is then exchanged for the the reduced mass, $m_{reduced}$, where

$$m_{reduced} = \frac{mM}{m+M} \tag{6.17}$$

and M is the mass of the neutron. The corresponding "free" values for the scattering length, b_{free}, which occurs at higher incident neutron energies is given as follows

$$b_{free} = \left(\frac{M}{M+1}\right)^2 b_{bound} \tag{6.18}$$

It is obvious from Equation (6.18) that this effect is most significant in low mass nuclei. For light atoms, such as hydrogen and deuterium, the differential scattering cross-section falls dramatically with scattering angle at all but the longest wavelengths. The shape of the fall depends upon the exact form of $S(Q,\omega)$ for the sample (defined in Section (4.1.2)) and is energy dependent. At low energies the incident neutrons can excite only vibrational motions in the sample whereas at high energies they can excite all possible modes including molecular dissociation. As there is no transmission monitor on the SANDALS diffractometer, previously measured transmission profiles, taken as a function of wavelength, were used for the samples studied. The sample transmission profile was determined by summing the profiles for carbon and hydrogen(deuterium) in proportion to the atomic concentrations of the elements in the sample.

The total neutron cross-section for each of the three a-C:H(D) samples studied is given in Figure (6.7). The large incoherent scattering cross-section for hydrogen accounts for the generally higher level of the total cross-section for the a-$C_{0.75}$:$H_{0.25}$ sample. The fall in the scattering cross-section from a bound to a free value with decreasing wavelength causes a steeper drop to occur in the total cross-section for the hydrogenated sample than in the deuterated sample. The level and the gradient of the fall off in the total scattering cross-section for the a-$C_{0.74}$:$D_{0.09}$:$H_{0.17}$ sample lies somewhere between that of the deuterated and hydrogenated sample as expected.

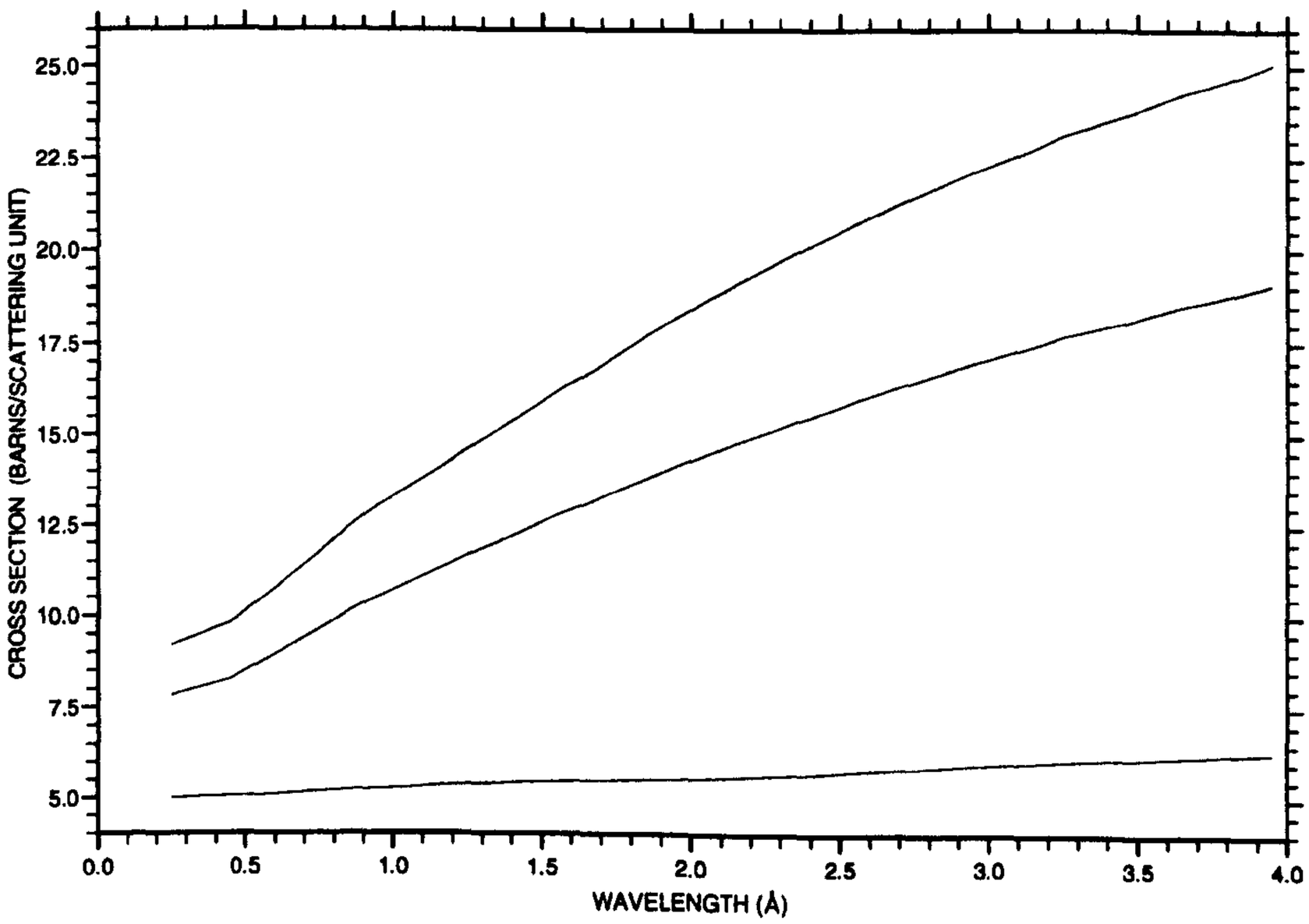

Figure 6.7: Total neutron cross-section for the a-$C_{0.75}$:$H_{0.25}$ (top), a-$C_{0.74}$:$D_{0.09}$:$H_{0.17}$ (middle) and a-$C_{0.73}$:$D_{0.27}$ (bottom) samples.

6.3.5 Attenuation and Multiple Scattering Corrections

For the neutron scattering experiments carried out at ISIS, each of the powder samples of a-C:H(D) was held in a 5mm diameter sample can made from vanadium. Vanadium is often used for the container material as it scatters almost completely incoherently ($\sigma_{inc}^{van} = 4.98$ barns/atom, $\sigma_{coh}^{van} = 0.02$ barns/atom). The sample container therefore gives a scattering profile which is almost isotropic but includes some weak Bragg reflections due to the small coherent scattering amplitude. Contributions to the collected data from neutrons scattered by the container and the effects of attenuation, by the container, of neutrons scattered at the sample must be corrected for before the required sample-only scattering can be obtained. In order that the scattering due only to the sample may be accessed, measurements were taken of the scattering profile for a) the sample plus vanadium can, and b) the can only. Figure (6.8) shows scans a) and b) for the a-$C_{0.75}$:$H_{0.25}$ sample. Before subtracting the container scattering profile from the sample plus container profile, the former must first be corrected for the change in the attenuation factors between cases a) and b). The method described by Paalman and Pings [76] was used to determine the attenuation factors in this case. This method uses the following equation relating the experimental sample plus container intensity, I_{s+c}, and the experimental empty container scattering, I_c, to the sample only scattering intensity:

$$I_s = \frac{I_{s+c}}{A_{s,sc}} - \frac{I_c A_{c,sc}}{A_{s,sc} A_{c,c}} \tag{6.19}$$

where $A_{i,j}$ are the absorption coefficients for the processes defined by subscripts i and j. i defines the point of scattering (e.g. s=sample, c=container) and j the point of absorption (e.g. sc=sample plus container). The three processes defined in Equation (6.19) are illustrated in Figure (6.3.5). The attenuation factors are defined by the sample geometry and can be determined exactly. I_{s+c} and I_c in Equation

(6.19) are assumed to have been normalised to the incident flux and corrected for any background effects.

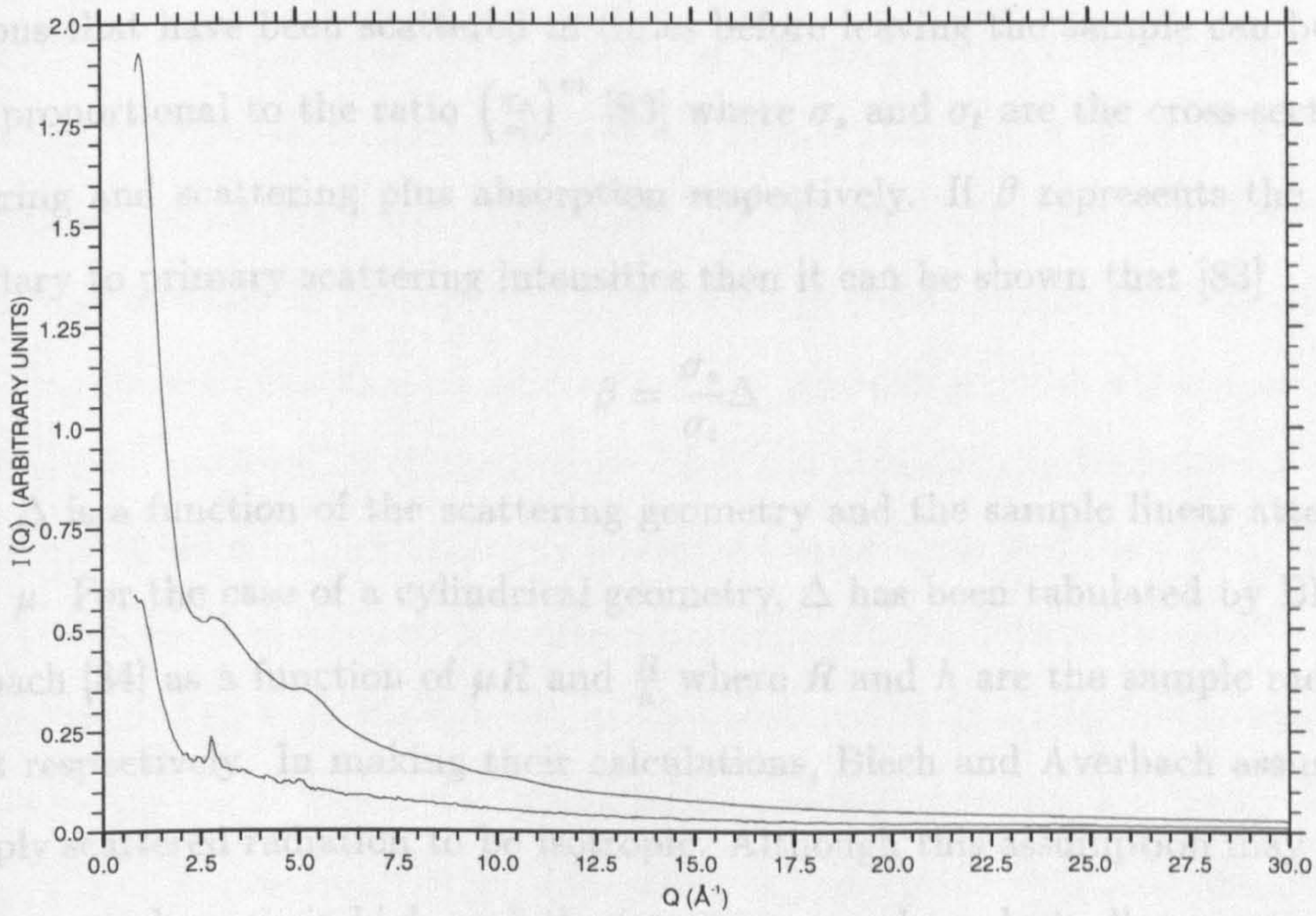

Figure 6.8: Sample plus vanadium can scattering profile for the a-$C_{0.75}$:$H_{0.25}$ sample (top) and the can-only scattering profile (bottom).

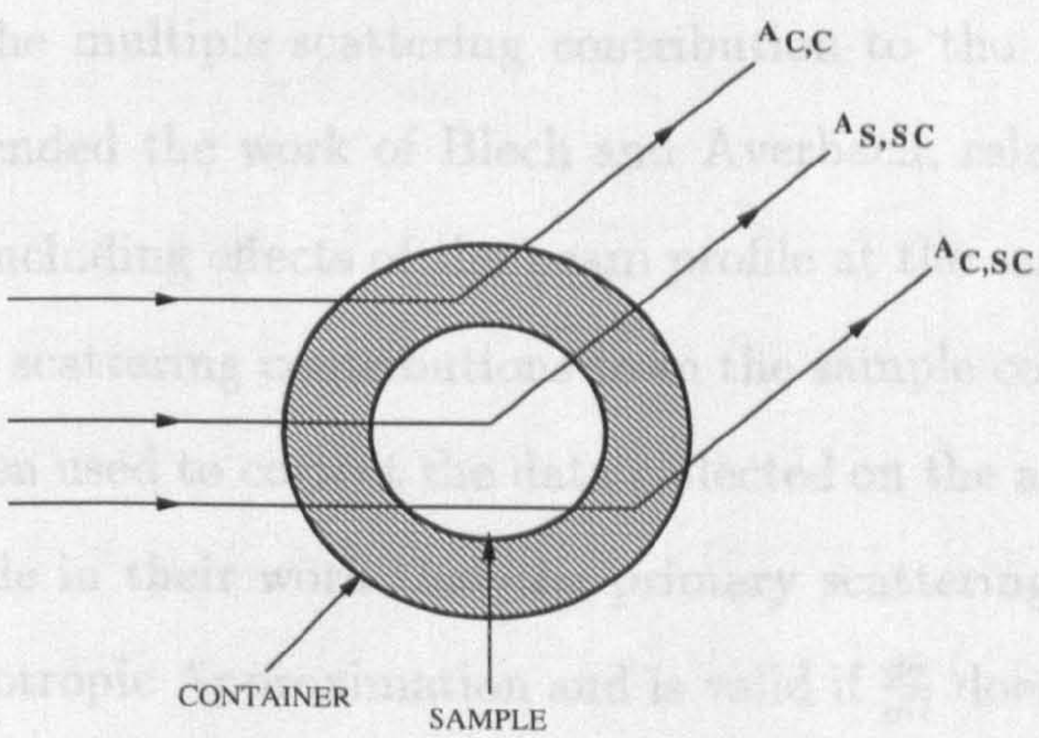

Figure 6.9: Illustration of Paalman and Pings absorption coefficients.

The Paalman and Pings attenuation correction factors apply strictly only to singly

scattered neutrons and thus the data must be corrected for multiple scattering events before these corrections can be applied. The contribution to the collected data from neutrons that have been scattered m times before leaving the sample can be shown to be proportional to the ratio $\left(\frac{\sigma_s}{\sigma_t}\right)^m$ [83] where σ_s and σ_t are the cross-sections for scattering and scattering plus absorption respectively. If β represents the ratio of secondary to primary scattering intensities then it can be shown that [83]

$$\beta = \frac{\sigma_s}{\sigma_t}\Delta \tag{6.20}$$

where Δ is a function of the scattering geometry and the sample linear attenuation factor μ. For the case of a cylindrical geometry, Δ has been tabulated by Blech and Averbach [84] as a function of μR and $\frac{R}{h}$ where R and h are the sample radius and height respectively. In making their calculations, Blech and Averbach assumed the multiply scattered radiation to be isotropic. Although this assumption may be valid in the case where m is high and the neutrons may have lost all memory of their incident direction, it is not clear, however, that this argument will hold for neutrons which have been scattered only two or three times. It is such neutrons that will, in general, dominate the multiple scattering contribution to the data. Soper and Egelstaff [85] have extended the work of Blech and Averbach, relaxing some of the restrictions made and including effects of the beam profile at the sample. Their work also allows for multiple scattering contributions from the sample container as well as the sample, and has been used to correct the data collected on the a-C:H(D) samples. The assumption is made in their work that the primary scattering is isotropic [85]. This is known as the Isotropic Approximation and is valid if $\frac{d\sigma}{d\Omega}$ does not vary rapidly with scattering angle or the sample is very narrow compared with its distance from the detector. Soper and Egelstaff's method uses the transmission cross-section for the sample to obtain the scattering cross-section, at each neutron wavelength, from

the relation

$$\sigma_s(\lambda) = \sigma_t(\lambda) - \sigma_a(\lambda) \tag{6.21}$$

Here $\sigma_a(\lambda)$ is the absorption cross-section of the sample. An alternative method for estimating multiple scattering contributions involves the use of Monte Carlo simulations. These require the sample dimensions, the scattering geometry and an estimate of the cross-sections to be supplied. Monte Carlo codes simulate an experiment by generating neutron events, such as scattering or absorption, with a frequency proportional to their probability of occurrence. Neutron histories can be followed individually so that those which are multiply scattered can be separated from those which are singly scattered. The fraction of multiple scattering in the detected intensity can then be calculated. Although the approximations required by analytical techniques can be avoided by the use of Monte Carlo simulations, such simulations are highly computer intensive [86]. In practice, the ideal situation is to keep the total scattering from the sample sufficiently low that multiple scattering constitutes only a small fraction of the total measured scattering profile.

6.3.6 Inelasticity Corrections

In the case of a real system, where the nuclei have a finite mass, the latter are not fixed in position at the atomic sites, but execute limited motion due to their thermal energy. The motion of each atom is correlated with those of others in the system due to the forces which exist between atoms in close proximity. The energy associated with these vibrations is quantised , the quantum of energy being known as a phonon. An incoming neutron (or X-ray) can transfer some of its energy to these vibrations or take up energy from them. In the two cases the outgoing neutron will have a wavelength longer or shorter than than its incident value respectively.

The energy of a neutron of mass m and velocity v is given by $E = \frac{1}{2}mv^2$ and for thermal neutrons ($\lambda \sim 1\mathring{A}$) will be of the order of 0.01 to 0.1 eV. The energy of a photon of wavelength λ is given by $E = \frac{hc}{\lambda}$ where h is Planck's constant and c is the speed of light. X-ray photons, having $\lambda \sim 1\mathring{A}$, will therefore have a corresponding energy of the order of 10,000eV. Creation or annihilation of a phonon by a thermal neutron will thus result in a significant change in the neutron's energy whereas the corresponding change in energy in the case of X-ray photons is negligible.

So far in this chapter the static approximation has been assumed to hold i.e. the energy exchange between the neutron and the nucleus has been taken to be small or negligible. In practice this is not generally the case. The total neutron scattering cross-section measured using thermal neutrons is always an integration over an inelastic cross-section. For the case of a reactor experiment this integral is simply taken over all scattered energies. In the case of a time-of-flight experiment each time channel sums over a series of incident and scattered neutron wavelengths which result in an equal total flight time i.e.

$$\frac{L_o}{k_o} + \frac{L_1}{k_1} = \frac{L_o + L_1}{k_e} \tag{6.22}$$

where k_o and k_1 are the incident and scattered neutron wavevectors respectively. k_e is the neutron wavevector for elastic scattering corresponding to the time channel. L_o and L_1 are the incident and scattered flight paths as shown in Figure (6.2).

The kinematic equations for the scattering process defined by the laws of conservation of momentum and energy give

$$Q^2 = k_o^2 + k_1^2 - 2k_o k_1 cos2\theta \tag{6.23}$$

and

$$2m\hbar w = \hbar^2 k_o^2 - \hbar^2 k_1^2 \tag{6.24}$$

where 2θ is the scattering angle and h is Planck's constant. Equation (6.22) may be combined with Equations (6.23) and (6.24) to define a path in (Q, w) space over which the time-of-flight experiment integrates.

Thus, in practice, what is measured on the SANDALS diffractometer is not $\frac{d\sigma}{d\Omega}$, but the differential time-of-flight scattering cross-section, $\sum_{TOF}$. For a detector at an angle 2θ to the incident beam the differential cross-section measured for a given Q value is given by [87]

$$\sum_{TOF}(Q,\theta) = \int_{-\infty}^{\frac{E}{\hbar}} \frac{k_1}{k_o} S(Q,w) \frac{I(k_o)}{I(k_e)} \left(\frac{\partial k_o}{\partial k_e}\right) \frac{E_D(k_1)}{E_M(k_e)} dw \tag{6.25}$$

where $I(k_o)$ is the incident spectrum. E_M and E_D are the monitor and detector efficiencies respectively.

The most commonly used method for correcting for these inelasticity effects is that of Placzek [58]. Placzek's method involves expanding the scattering law $S(Q, w)$ in Equation (6.25) in powers of $Q^2 - Q_e^2$ about the elastic scattering vector Q_e such that

$$S(Q,w) = S(Q_e,w) + \left(\frac{\partial S}{\partial Q^2}\right)_{Q_e} (Q^2 - Q_e^2) + \frac{1}{2!}\left(\frac{\partial^2 S}{\partial (Q^2)^2}\right)(Q^2 - Q_e^2) + \cdots \tag{6.26}$$

$Q^2 - Q_e^2$ is then converted to a function of the energy variable $\frac{\hbar w}{E_o}$ such that

$$Q^2 - Q_e^2 = -\frac{1}{2}(1-2f)Q_e^2\left(\frac{\hbar w}{E_o}\right) + \frac{1}{8}[2k_e^2 - (1-2f)Q_e^2 + 2f^2Q_e^2]\left(\frac{\hbar w}{E_o}\right)^2 + \ldots \tag{6.27}$$

where $f = \frac{L_0}{L_0+L_1}$, the ratio of incident to total flight paths (see Figure (6.2)). All the remaining factors in Equation (6.25) are also expanded in the variable $\left(\frac{\hbar w}{E_o}\right)$. The result is that the time-of-flight differential cross-section given by Equation (6.25) is expressed as a series of terms in the moments of $S(Q, w)$ (evaluated at $Q = Q_e$) where the n^{th} order moment is given by

$$\int_{-\infty}^{\frac{E}{\hbar}} w^n S(Q,w) dw \tag{6.28}$$

The zeroth order term gives the elastic scattering structure factor, $S(Q_e)$, and the higher order terms the corrections to this elastic scattering term due to inelasticity effects.

$S(Q,w)$ may be split into self, $S^{self}(Q,w)$, and distinct, $S^{dist}(Q,w)$, terms in the same manner as $S(Q)$ (see Section (4.1.6). Placzek showed that for a classical system, the first order correction term for the "self" contribution to the scattering law is given by

$$S_1^{self} = \int_{-\infty}^{\frac{E}{\hbar}} wS(Q,w)dw = \frac{\hbar^2 Q^2}{2M} = \frac{8\pi^2\hbar^2 sin^2\theta}{M\lambda^2} \tag{6.29}$$

where M is the effective mass of the nucleus. Thus it can be seen that the corrections to the self term due to inelasticity effects decrease with the scattering angle and the incident wavelength, and increase for lower mass nuclei. Difficulty arises in the definition of M for a solid as it may lie anywhere between the nuclear mass and the mass of the entire sample. The first order correction to the distinct term was shown, by Placzek, to be zero i.e.

$$S_1^{dist}(Q) = \int_{-\infty}^{\frac{E}{\hbar}} wS(Q,w)dw = 0 \tag{6.30}$$

For nuclei much more massive than the neutron the corrections to the elastic scattering term may be taken to first order only, since the effective mass dependency of the higher order terms leads to a rapid convergence of the expansion.

Powles has extended Placzek's method to the case of the time-of-flight experimental method [87] and found that to first order the correction term to the self scattering is given by

$$S_{1_{TOF}}^{self}(Q) = 2\left(\frac{m}{M}\right) sin^2\theta \times C \tag{6.31}$$

where C is given by

$$C = \left(\frac{2L_o + 3L_1}{L_o + L_1}\right) + \left(\frac{L_1}{L_o + L_1}\right) \frac{d(\ln I)}{d(\ln \lambda}\bigg|_{\lambda=\lambda_e} + \left(\frac{L_o}{L_o + L_1}\right) \frac{d(\ln E_D)}{d(\ln k)}\bigg|_{k=k_e} \tag{6.32}$$

For light atoms, such as hydrogen and deuterium, it is not sufficient to approximate the inelasticity corrections to first order terms only as higher order, mass dependent terms are more significant. To allow an accurate inelasticity correction to be applied to such low mass systems, a precise model describing their structure *and* dynamics is required. However, the purpose of the neutron scattering experiments carried out on the a-C:H(D) samples studied is to investigate the static structure of these complex systems only and therefore it is not possible to provide such a model.

As previously stated, the SANDALS diffractometer at ISIS was chosen for neutron scattering experiments on the a-C:H(D) samples as it has been designed in such a way as to minimise the inelasticity effects in the data collected. The measured scattering profiles for the a-C:H(D) samples are presented in Chapter (8). In Section (8.1.1) the inelastic scattering contribution to the collected data is detailed and discussed, and in Section (8.1.2) the empirical method used to remove these contributions from the data is described.

6.3.7 Differential Scattering Cross-section

After normalising the raw data to the incident flux, correcting for detector and moderator efficiencies, absorption and multiple scattering, the time of flight differential scattering cross-sections was obtained for the data. The detectors on the SANDALS diffractometer are grouped into ten banks and the average angle for each bank is given in Table (6.2). Each detector bank provides a single profile for the differential scattering cross-section. The Q range measured by each bank is determined by the spread in wavelengths detected.

Figure (6.10) shows the differential scattering cross-section for the a-$C_{0.75}$:$H_{0.25}$ sample measured by the ten detector banks. It can be seen that the data from

Detector Bank	Average Angle
1	20.13°
2	18.11°
3	16.23°
4	14.61°
5	13.07°
6	11.79°
7	9.34°
8	6.75°
9	5.02°
10	2.88°

Table 6.2: Average angle for the ten detector banks on the SANDALS diffractometer.

the different detector banks corresponding to the same Q value does not always overlap. In particular the two lowest angle scattering banks can be seen to deviate strongly from the the remainder of the detector banks. This effect results from a background contribution to the data due to scattering from an aluminium pipe on the "downstream" end of the diffractometer, which carries the transmitted beam [88]. The unscattered transmitted beam passes cleanly down this pipe without coming into contact with the walls. However, neutrons scattered by the sample at very small angles to the incident beam may be intercepted by the pipe. These neutrons may subsequently be scattered by the pipe into the detectors. The contribution to the detector count rate from this secondary scattering will obviously be greater for the smaller angle detectors. As the neutron intensity hitting the pipe is a function of the original scatterer, the background due to scattering by the aluminium is sample dependent.

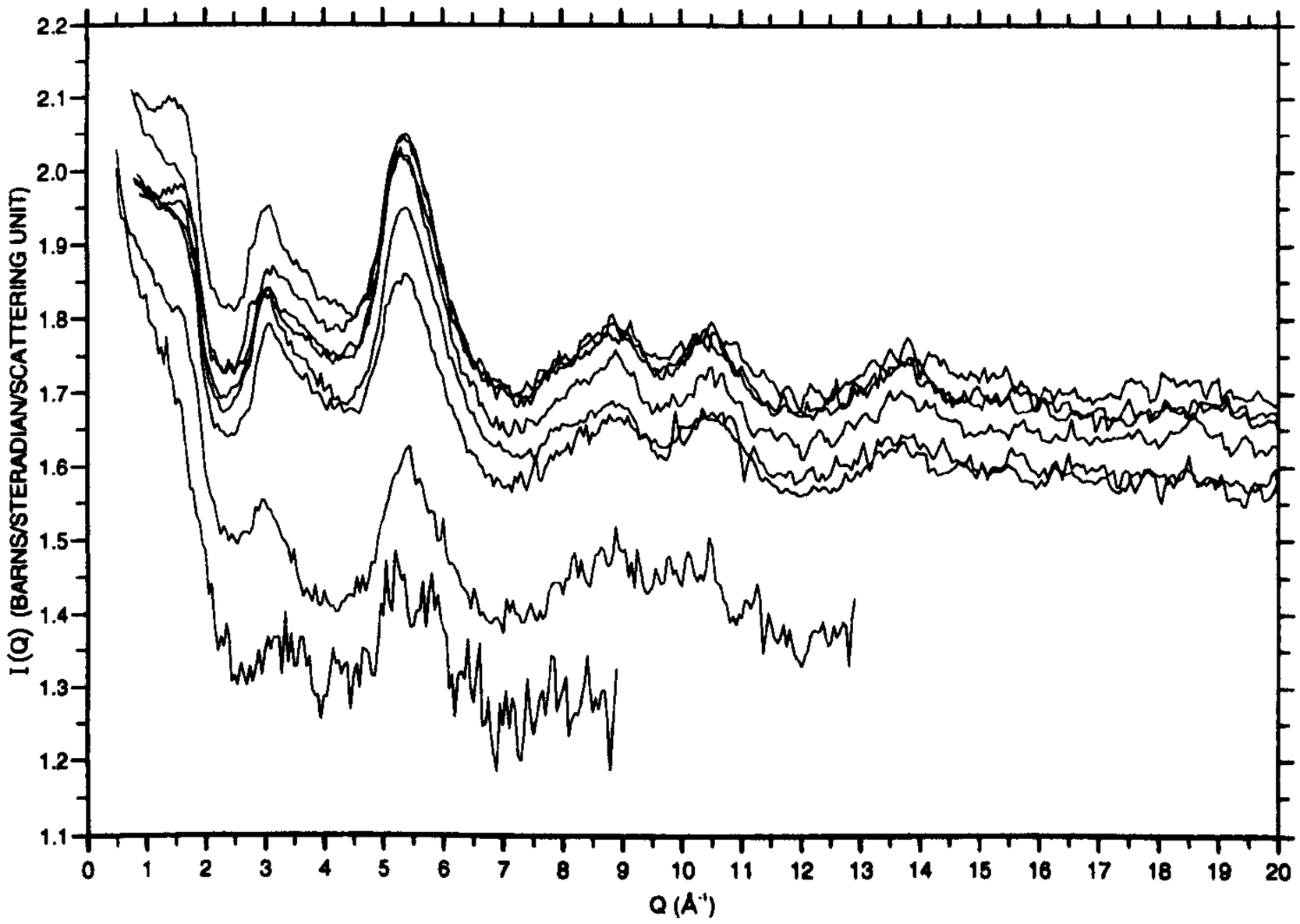

Figure 6.10: Differential scattering cross-section for a-$C_{0.75}$:$H_{0.25}$ measured by the ten detector banks on the SANDALS diffractometer.

A routine has been devised by Soper [88] to correct for this background. This routine uses the measured scattering for the vanadium rod to determine the contribution to the detector count rate from the aluminium pipe scattering. The calibration factor F_{cal} (see Section (6.3.3)) may be determined from the highest angle detector bank, where the effect of the aluminium pipe is negligible. Once F_{cal} is known, the scattering in the lower angle detectors due to the vanadium rod may be calculated. From the count rate measured for the vanadium rod scan at each detector bank, a measure of the aluminium pipe background scattering can then be obtained. The contribution of the secondary scattering from the aluminium pipe to each of the sample runs may be determined by scaling the values obtained for vanadium to the appropriate scattering cross-section for the sample. Figure (6.11) shows the differential scattering profile for the ten detector banks after correction for the aluminium pipe scattering.

Although some variation in the scattering level between different detector banks remains, the effect of the scattering from the aluminium pipe appears to have been largely removed.

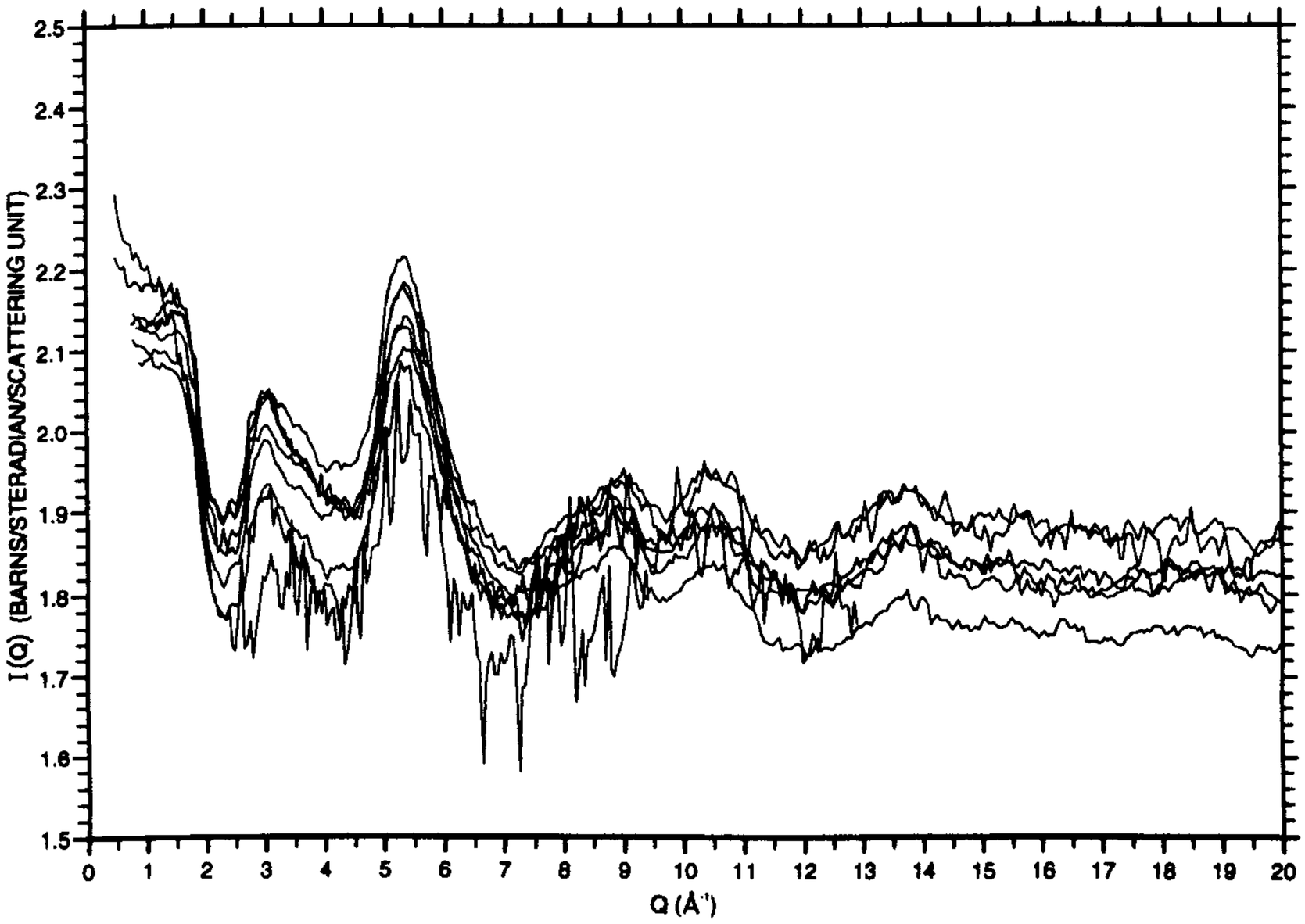

Figure 6.11: Differential scattering cross-section data as in Figure (6.10) corrected for scattering from aluminium pipe.

Figure (6.12) shows the corrected differential scattering cross-section measured by each of the detector banks for the a-$C_{0.75}$:$H_{0.25}$ sample plotted sequentially.

The self scattering contributions were removed from the differential scattering cross-section data by fitting a Chebyshev polynomial [89] to the profile for each detector bank and subsequently subtracting this polynomial to give the interference function $I(Q)$ where

$$I(Q) = \Sigma_{\alpha,\beta} c_\alpha b_\alpha c_\beta b_\beta [S_{\alpha\beta}(Q) - 1] \tag{6.33}$$

In this way the need to correct the self scattering component of the data for inelasticity effects was removed (more details are given on this in Section (8.1.2)). Total structure

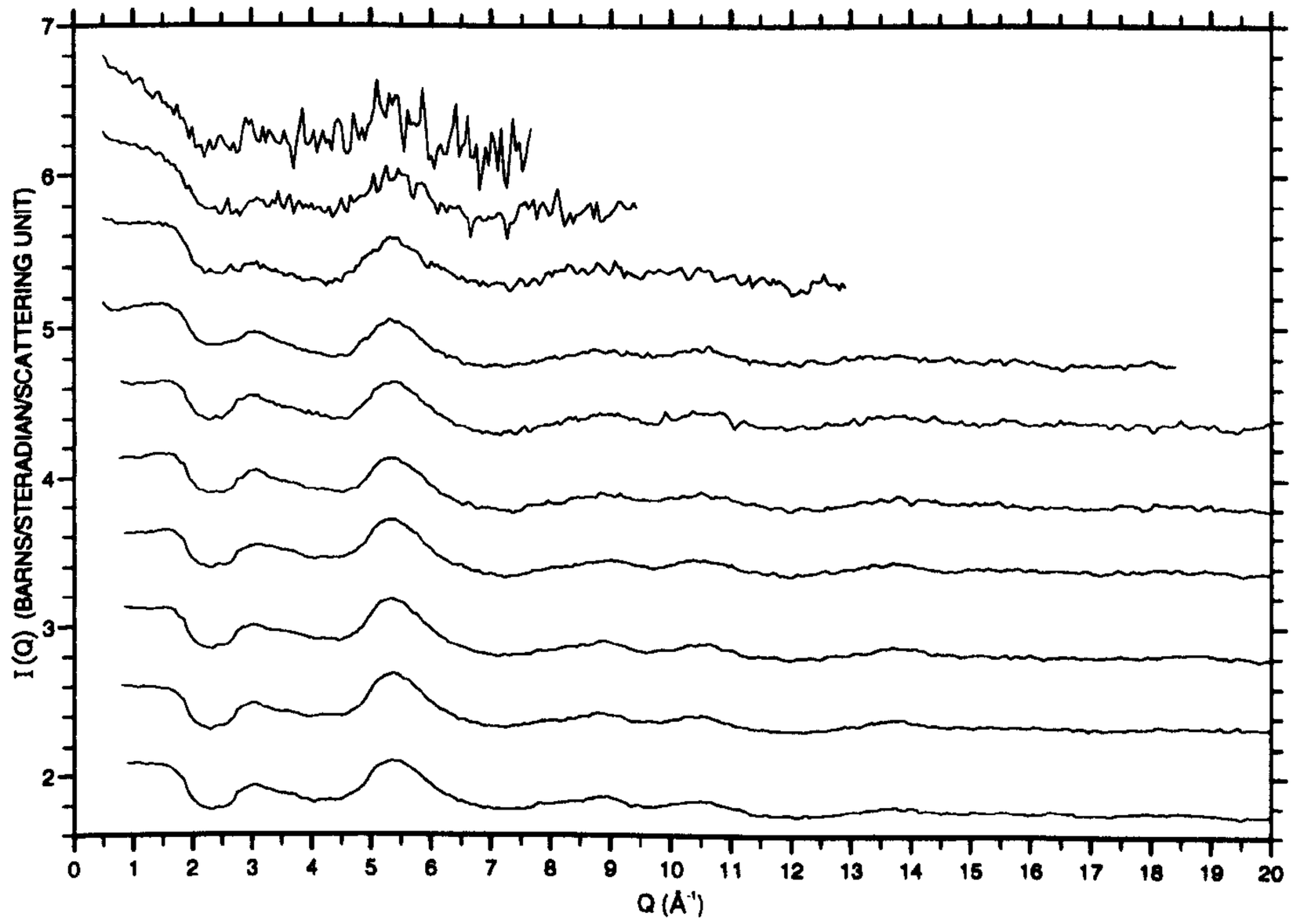

Figure 6.12: Differential scattering cross-section data from Figure (6.11) plotted sequentially and offset for clarity.

factors, $S(Q)$, for the three samples were obtained by dividing $I(Q)$ by the coherent scattering cross-section for the sample and setting the resultant function to oscillate about unity. This gives a suitably normalised structure factor

$$S(Q)_{total} = \frac{1}{(\Sigma c_\alpha b_\alpha)^2} \Sigma c_\alpha b_\alpha c_\beta b_\beta S_{\alpha\beta}(Q) \tag{6.34}$$

where c and b represent the atomic concentrations and coherent scattering lengths of elements α and β respectively. Details of the polynomials fitted to the data and the structure factors obtained for the samples are given in Chapter (8). The structural information on the phase of a-C:H studied, derived from these structure factors is discussed in the context of presently accepted models for this material.

Chapter 7

Grazing Angle X-ray Diffraction Studies of Amorphous Hydrogenated Carbon

As previously stated in Chapter (2) many of the potential applications of amorphous hydrogenated carbon involve the use of the material in the form of a thin film (i.e. $\sim$ 1μm thick) for example as wear resistant coatings for machine tools or as a protective surface layer on magnetic disks [4]. It would therefore be useful to be able to study the as-deposited material mounted on a substrate. The central characteristics of the grazing angle X-ray diffraction technique, in relation to the study of crystalline iron oxide layers on glass substrates, have been detailed by Lim et al [90]. The following chapter details some exploratory studies carried out on the use of the technique as a method for the *in situ* study of carbon-based amorphous thin films on crystalline substrates.

7.1 Grazing Angle X-ray Diffraction Theory

For an electromagnetic wave of frequency ν in a medium with resonances ν_i (of oscillator strength f_i) the refractive index, n, is given by [91]

$$n = 1 - \frac{(\bar{\rho}_e e^2)}{(2\pi m_e)\Sigma_i \frac{f_i}{\nu_i^2 - \nu^2}} \tag{7.1}$$

where m_e and e are the electron mass and charge respectively and ρ_e is the mean electron density. For the case of X-rays, where ν is generally much greater than any resonance, then the index of refraction may be given by

$$\begin{aligned} n &= 1 - \lambda^2 \frac{\bar{\rho}_e r_e}{2\pi} \\ &= 1 - \delta \end{aligned} \tag{7.2}$$

where $r_e = \frac{e^2}{m_e c^2} = 2.82 \times 10^{-5} \mathring{A}$ is the classical electron radius. It can be seen from Equations (7.1) and (7.2) that the refractive index for materials at X-ray wavelengths is less than unity. It was pointed out by Compton in 1922 [92] that as a consequence of this, X-rays having a wavevector $k_i = \frac{2\pi}{\lambda}$ incident on a surface at an angle, α_i, less than a critical angle, α_c, will experience total external reflection. α_c is given by

$$\begin{aligned} \alpha_c &= \lambda \left(\frac{r_e \bar{\rho}_e}{\pi} \right)^{\frac{1}{2}} \\ &= (2\delta)^{\frac{1}{2}} \end{aligned} \tag{7.3}$$

The incident angle, in this case, is measured from the tangent to the sample surface as shown in Figure (7.1). For a material of density ρ in gcm^{-3} and an incident wavelength λ in $\mathring{A}$, α_c may be expressed as

$$\alpha_c = 1.6 \times 10^{-3} \rho^{\frac{1}{2}} \lambda \tag{7.4}$$

where α_c is given in radians. For X-ray wavelengths ($\lambda \sim 1\mathring{A}$), α_c is in general in the region of 3 to 5mrad.

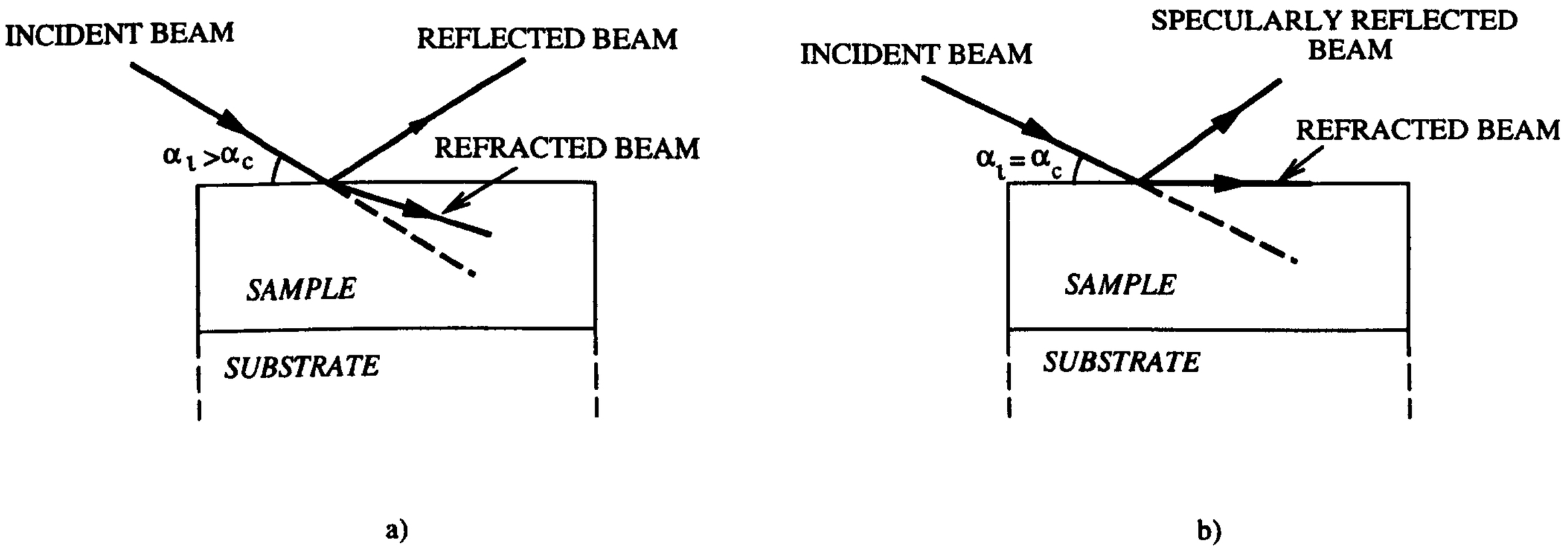

Figure 7.1: Schematic diagram to illustrate total external reflection of X-rays at the critical angle: a) $\alpha_i > \alpha_c$, b) $\alpha_i = \alpha_c$.

In the regime of total external reflection, a specularly reflected beam occurs whilst within the material the refracted wave propagates parallel to the interface and is exponentially damped with distance below the interface. The latter is then described as the evanescent wave.

The near-surface region of the material will be illuminated by this evanescent wave to a characteristic depth, t, at which the field has fallen by a factor of e^{-1} where t is given by

$$t_{\alpha_i<\alpha_c} = \frac{\lambda}{[2\pi(\alpha_c^2 - \alpha_i^2)^{\frac{1}{2}}]} \tag{7.5}$$

Above the critical angle penetration into the material increases rapidly with the incident angle and is limited by photoelectric absorption. If α_i is appreciably larger than α_c, but still small, we have [93]

$$t_{\alpha_i>\alpha_c} = \frac{2\alpha_i}{\mu} \tag{7.6}$$

where μ is the linear attenuation coefficient for the material (see Section (5.2.1)).

It is the diffraction profile of the evanescent mode that has been used to probe the

structure of the thin films studied in this work. It can be seen from Equation (7.5) that the penetration of the evanescent waves and thus the film depth sampled may be controlled by varying the incident wavelength and/or the incident angle so that in principle sampling depths of the order of $10\mathring{A}$ to $1000\mathring{A}$ may be achieved. Thus depth profiling of a material should be possible using the grazing incidence X-ray diffraction technique. Similarly, contributions to the scattering profile from the substrate may be eliminated by the choice of an incident angle such that the evanescent mode expires, in the context of experimentally measurable limits, within a depth shallower than the deposited film thickness.

7.1.1 Refraction Effects

In the case of diffraction data collected at grazing angles of incidence in the region of the critical angle, peak shifting in the scattering angle, 2θ, resulting from refraction of the evanescent mode by the material may become significant. As $n < 1$, a positive shift in the peak position as a function of scattering angle 2θ occurs. This shift, $\Delta 2\theta$, which represents the difference between the observed scattering angle and the real scattering angle, is shown in Figure (7.2) and may be calculated as follows

$$n = 1 - \delta = \frac{cos\alpha_i}{cos\phi} \tag{7.7}$$

therefore

$$\begin{aligned} cos\phi &= (1-\delta)^{-1} cos\alpha_i \\ &\approx (1+\delta) cos\alpha_i \end{aligned} \tag{7.8}$$

as δ is of the order of 1×10^{-6}.

Hence

$$cos\alpha_i - cos\phi \equiv \Delta(cos\alpha_i)$$

$$\equiv \quad -sin\alpha_i \Delta 2\theta$$

$$\equiv \quad -\delta cos\alpha_i \tag{7.9}$$

so that

$$\Delta 2\theta = \delta cot\alpha_i \tag{7.10}$$

It can be seen from Equation (7.10) that the effects of refraction become increasingly important as the incident angle gets smaller, and the disparity between the observed scattering angle and the real scattering angle likewise increases. This effect must be corrected for when analysing the collected grazing angle scattering profile.

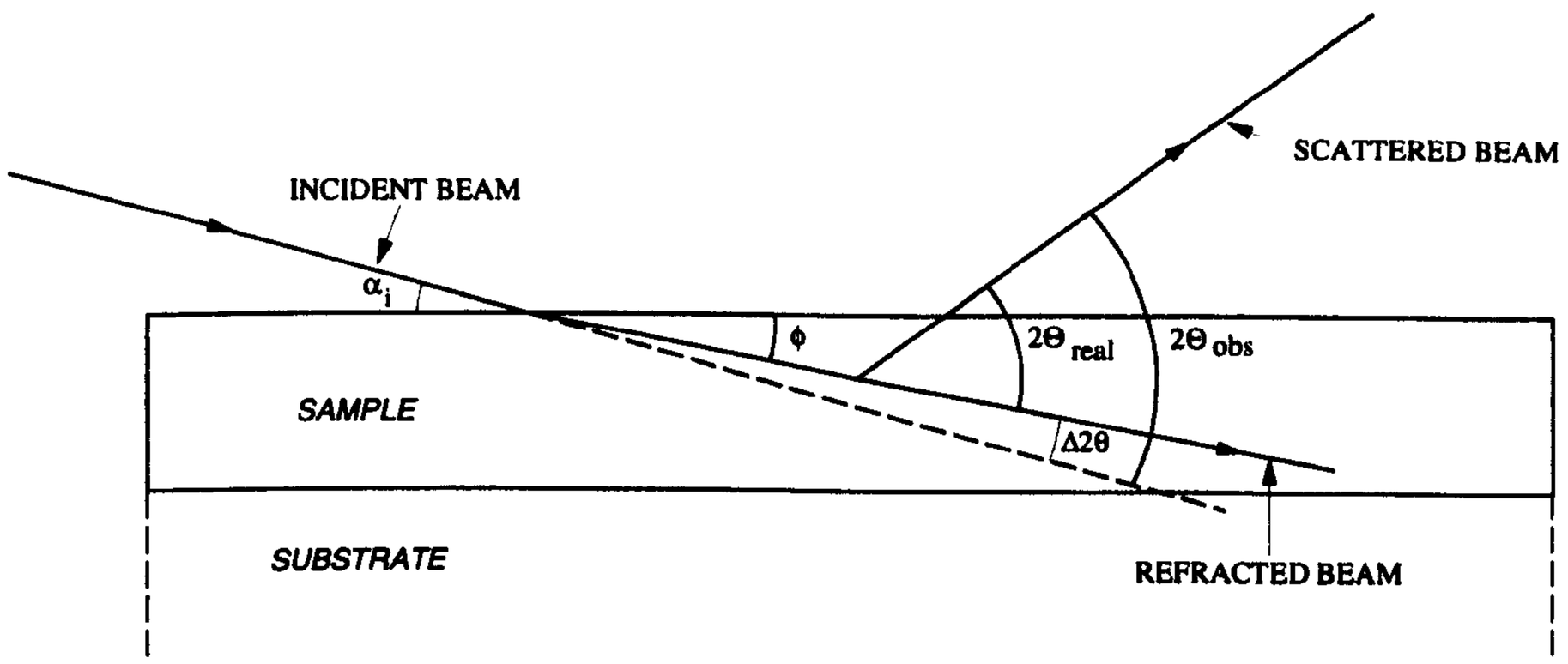

Figure 7.2: Diagram to illustrate shift in scattering angle due to refraction effects for grazing angle X-ray diffraction

7.2 Experimental Method

The technique of grazing angle incidence X-ray diffraction was originally used employing a divergent beam from a laboratory X-ray source in a focusing geometry [94].

However, this imposes a strict requirement on the coupling between the sample surface and the detector, which must maintain a (θ : 2θ) angular relation in order to avoid defocusing. The grazing incidence scattering studies detailed in this chapter were carried out on station 9.1 at the Daresbury Laboratory Synchrotron Radiation Source. Details of this experimental station are given in Chapter (5). Synchrotron radiation has a number of advantages over a laboratory source where the technique of grazing incidence X-ray diffraction is to be carried out. The high intensity available is an important factor in measuring the weak scattering from thin films caused by the very small scattering volumes involved. This is particularly problematic for studying the diffuse scattering from low Z amorphous systems such as a-C:H. As previously described (see Chapter (5)), the beam produced by a synchrotron radiation source is intrinsically highly parallel. This is particularly important when the incident angle of the beam relative to the sample is required to be well defined. The parallel beam produced by the SRS allowed for the use of an experimental method in which a 2θ detector, uncoupled from the sample axis, scans the diffracted intensity for a given fixed wavelength and scattering angle. The 2θ scan is measured in a vertical plane, the sample being offset from the horizontal by the incident angle.

A schematic diagram of the instrumentation used to collect the scattering profile for the samples studied is given in Figure (7.3). The incident wavelength is selected from the white beam spectrum produced by the 5 Tesla Wiggler insertion device on beamline 9 using a channel cut silicon (111) monochromator, CM [95]. A silicon standard powder (S.M.R 640b) was used to determine the incident wavelength and the zero angle of the diffractometer, D. The incident monochromatic beam intensity is constantly monitored during the experiment using the scattering from an inclined kapton foil in the beam, KF (see Section (5.4.2)).

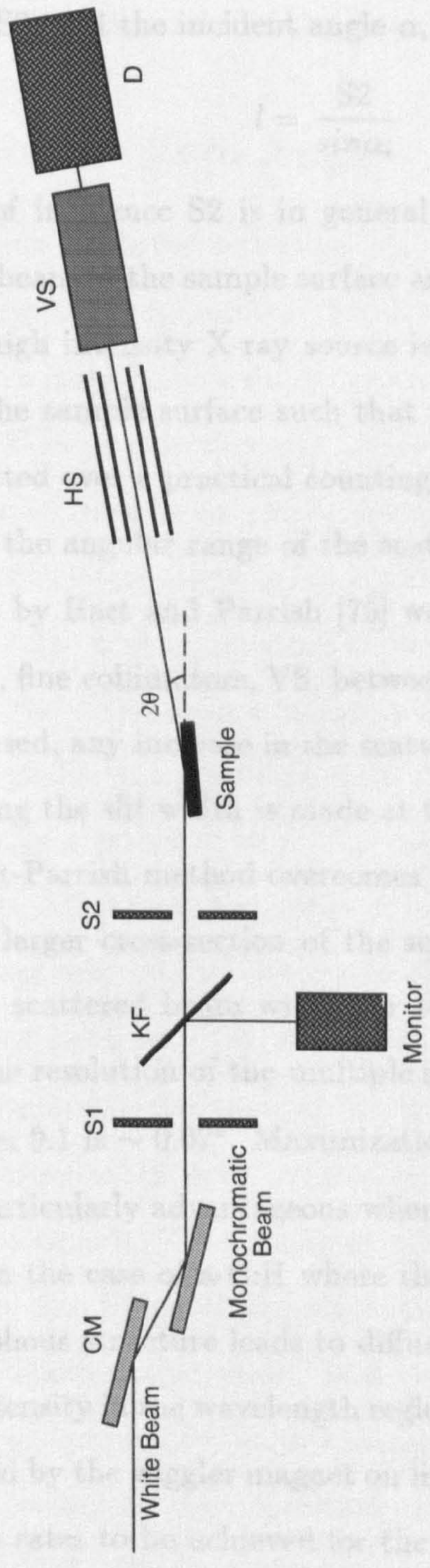

Figure 7.3: Schematic diagram of instrumentation for grazing angle X-ray diffraction.

The footprint, l, of the incident beam on the sample is determined by the width of the entrance slit, S2, and the incident angle α_i, where

$$l = \frac{\mathrm{S2}}{sin\alpha_i} \tag{7.11}$$

For grazing angles of incidence S2 is in general required to be small ($\sim 1\mu$m) to restrict the incident beam to the sample surface and avoid scattering from the sample mounting. Thus a high intensity X-ray source is required to ensure that a suitable flux is incident on the sample surface such that a statistically significant scattering profile may be collected over a practical counting period.

In order to limit the angular range of the scattered X-rays entering the detector, the system designed by Hart and Parrish [75] was used. This involves the use of a set of long (330mm), fine collimators, VS, between the sample and the detector. If a single set of slits is used, any increase in the scattered intensity reaching the detector achieved by increasing the slit width is made at the expense of the scattering profile resolution. The Hart-Parrish method overcomes this problem allowing scattering to be obtained from a larger cross-section of the scattered beam whilst maintaining a high resolution, the scattered beam width for this particular diffraction technique being very large. The resolution of the multiple slits used for the X-ray experiments carried out on station 9.1 is $\sim 0.07°$. Maximization of the scattering volume sampled by the detector is particularly advantageous when the sample depth illuminated is so small, particularly in the case of a-C:H where the electron density of the samples is low and their amorphous structure leads to diffuse scattering.

The increased intensity in the wavelength region of interest to this experiment (i.e. $0.5\mathring{A}$ to $1\mathring{A}$) produced by the wiggler magnet on line 9.1 at the SRS (see Section (5.1)) enables viable count rates to be achieved for the small scattering intensity involved. The use of hard X-rays available on this line (Section 5.1) is of advantage in the study

of amorphous materials as it provides access to an extended wavevector transfer range and thus increased real space resolution from the X-ray diffraction data.

7.2.1 Setting of the Zero Angle

For grazing angles of incidence the zero angle, α_0, determined for the sample mounted on the diffractometer is clearly important. The sample stage on station 9.1 is such that the latter is placed on a pair of motor-driven precision arcs which in turn are supported on a motor-driven XYZ-stage. In this way both the height and the inclination of the sample relative to the incident beam can be controlled from outside the experimental hutch. In determining this zero angle an ion chamber was used in place of the detector and slits in Figure (7.3). Having determined the ion chamber reading without the sample in the beam, the diffractometer stage, set at the nominal diffractometer zero angle, was raised normally into the beam until the sample in the beam reduced the ion chamber reading by a factor of two. The sample was then rocked about the α_i axis (i.e. that which determines the angle of inclination of the sample relative to the fixed incident beam position) to either side of the nominal α_0 and a transmission curve taken at the ion chamber. The zero angle of the diffractometer was then set to the angle at the centre of the peak in the transmission curve. Several iterative transmission curves were taken until a sharp peak occurred in the transmission at the zero angle of the sample. The accuracy of this value is eventually limited by any curvature of the thin film sample; curvature occurs as many thin films are in compressive stress. Studies have shown that the compressive stress in a-C:H thin films is found to peak around an impact energy for the film forming particles of 100eV to 600eV depending on the deposition method, the energy region leading to the formation of so-called "diamond-like carbon". The a-C:H samples studied using

the grazing angle X-ray diffraction technique were made at an impact energy in the region of 1KeV, an energy region in which the internal stress of the resultant a-C:H films would be generally be expected have dropped considerably. It is therefore hoped that curvature of the a-C:H thin films studied will not have a dramatic effect on the diffraction data collected.

7.3 Results

In order to prove that the experimental system used would allow grazing angle X-ray diffraction data to be collected for a series of incident angles around the critical angle for a sample, the system was first tested on a $\sim 1\mu$m sample of polycrystalline diamond deposited on a silicon substrate. This sample was prepared by a CVD process by a group at Heriot-Watt University, under Dr. J. Wilson. The critical angle for the sample was calculated to be 0.09° at the incident wavelength of 0.5$\mathring{A}$ used and the diffraction profiles measured were collected at a series of incident angles ranging from 2° to 0.1°. Due to the limitations on defining the exact angle of incidence of the X-ray beam at the sample surface, resulting from not only curvature of the sample surface but also backlash on the sample mount driver motors, it is possible that the beam may have entered the sample at an angle at or below the critical value for the polycrystalline diamond sample in the case of the 0.1° scan. Table (7.1) details the incident angles used and a nominal penetration depth calculated for an infinite diamond thin film for a corresponding incident angle and wavelength. It should be noted that the penetration depth, t, represents the distance over which the electric field decays by a factor of $\frac{1}{e}$, the distance over which the power deposited by the evanescent field falls by a corresponding factor is given by $\frac{t}{2}$. In practice that fraction of the refracted beam which penetrates as far as the silicon substrate will subsequently

be extinguished in a far shorter distance due to the higher attenuation coefficient for silicon.

Incident Angle α_i (degrees)	Penetration Depth t (μm)
2	1570
1	780
0.5	390
0.2	150
0.1	78

Table 7.1: Incident angles for which scattering profiles were collected and corresponding penetration depth for polycrystalline diamond thin film sample.

Figure (7.4) shows the scattering profiles collected for the five incident angles given in Table (7.1), the incident angle decreasing from 2° to 0.1° from the uppermost to the lowest curve. The raw data has been normalised to the incident beam intensity and corrected for refraction effects, no further corrections having been applied. Absorption corrections for the data will be minimal due to the scattering volumes involved and the low attenuation coefficients for the samples studied. Assuming the detector slits to be suitably large to accept the whole of the scattered beam for its maximum width, the scattering volume will be constant for a given incident angle.

A dramatic fall in the peaks corresponding to the silicon substrate, such as those at $Q = 9.75\mathring{A}^{-1}$ and $Q = 11.52\mathring{A}^{-1}$, can be seen in the data shown in Figure (7.4) as the incident angle decreases and the penetration depth correspondingly falls. Features believed to correspond to the polycrystalline diamond carbon surface film such as those at $Q = 5.03\mathring{A}^{-1}$ and $Q = 5.87\mathring{A}^{-1}$ can be clearly seen to increase in intensity as the incident angle decreases and the thin film/substrate signal to noise ratio increases.

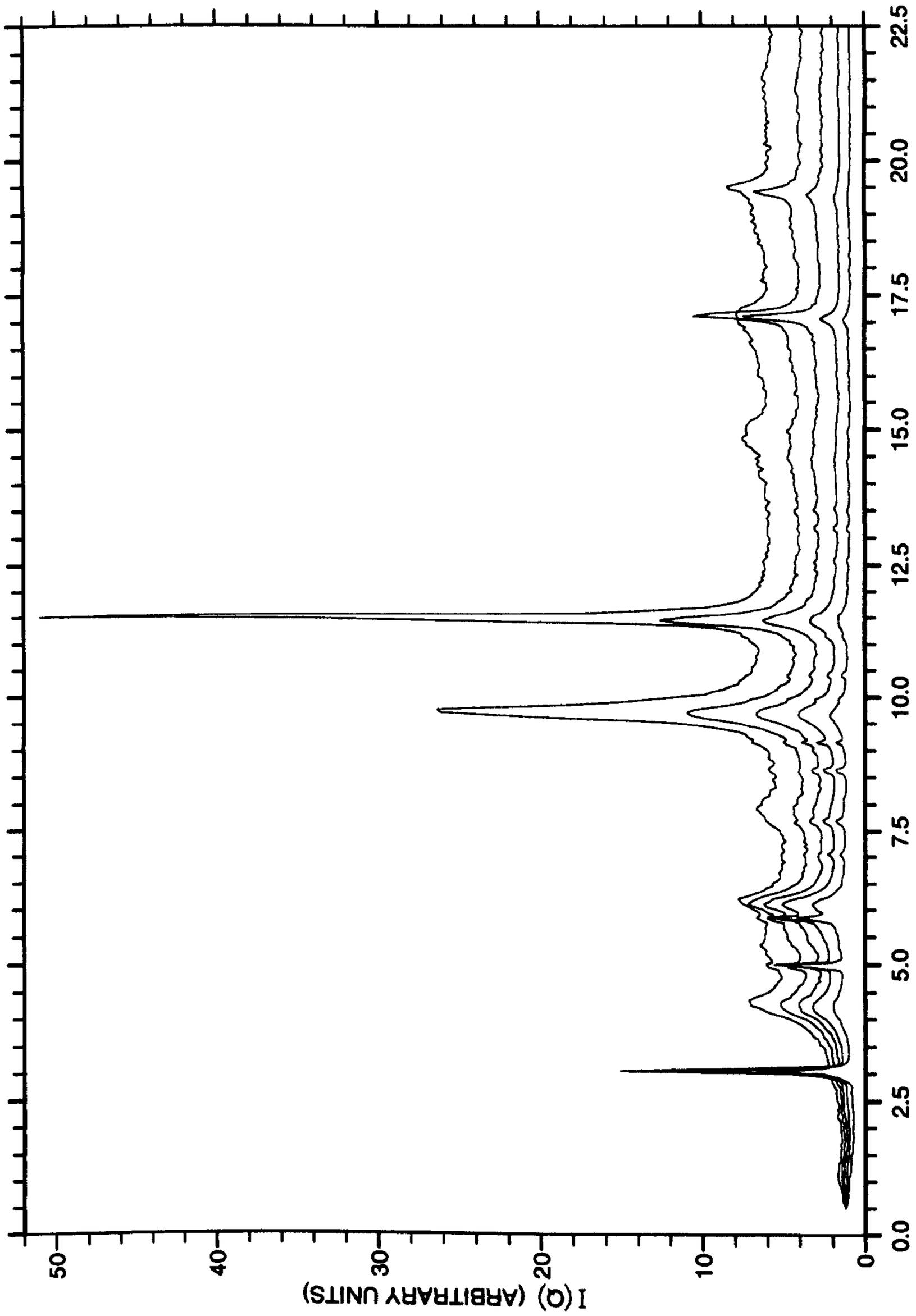

Figure 7.4: Grazing angle X-ray scattering profiles for a polycrystalline diamond thin film on a silicon substrate: uppermost to lowest curve corresponding to $\alpha_i = 2°, 1°, 0.5°, 0.2°, 0.1°$ respectively.

Figure (7.5) shows the same scattering profiles plotted over a smaller Q range and offset for clarity. Also plotted (lowest curve) is a corresponding Q-space scattering profile for a diamond powder sample collected using standard ($\theta : 2\theta$) diffraction on Station 9.1 at the Daresbury Laboratory SRS. Again the 2° incident angle scattering profile is plotted uppermost with consecutive profiles corresponding to decreasing α_i as given in Table (7.1). The features seen to grow in intensity as the incident angle decreases can be clearly seen to correspond to the reciprocal space peak positions observed in diamond. It can be concluded from the scattering profiles collected that by varying the incident angle at a fixed incident wavelength scattering from the surface film can be observed and depth profiling of the substrate/thin film structure can be achieved. Each of the scattering profiles will contain a weighted contribution of the silicon and carbon Compton scattering components which will vary with the incident angle as the ratio of substrate to surface film scattering changes. A knowledge of this ratio is required to accurately correct for these contributions. Further contributions to the data may occur from a SiC interface layer. This may be a possible explanation for the peaks observed in Figure (7.4) at 17.15$\mathring{A}^{-1}$ and 19.50$\mathring{A}^{-1}$ as these are seen to increase in intensity as the incident angle is decreased from 2° and subsequently to decrease in intensity again with a further decrease in the penetration depth.

7.3.1 Amorphous Hydrogenated Carbon Thin Film Samples

Two thin films of a-C:H approximately 1μm thick were produced using an Ion Tech FAB104 fast atom source as detailed in Chapter (3). The sample production parameters and the corresponding impact energy for the film forming particles are given in Table (7.2). Several studies of a-C:H thin film and powder samples produced by a variety of techniques [12,24,35,42] indicate that at such impact energies the resultant

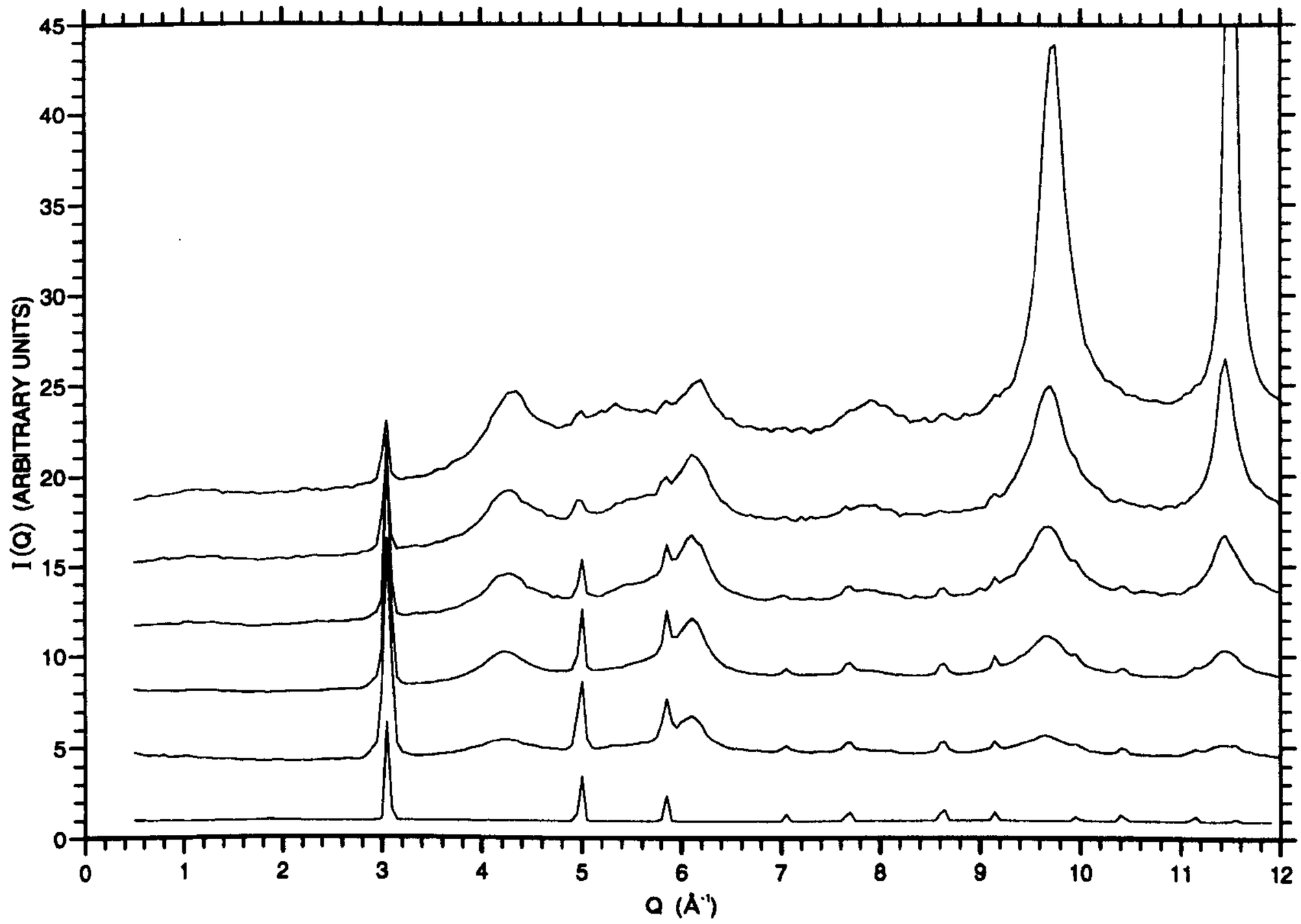

Figure 7.5: Grazing angle scattering profiles corresponding to Figure (7.4) offset for clarity. Also plotted (lowest curve) is the (θ : 2θ) scattering profile for a diamond powder sample.

materials would be expected to have a low hydrogen content and display a structure markedly more graphitic in nature.

Each of the two films detailed in Table (7.2) were deposited onto silicon substrates. In the case of Film 1 the orientation of the silicon planes relative to the substrate surface is unknown. After preliminary studies had been carried out on Film 1, it was decided to deposit Film 2 onto an oriented silicon wafer so that the Q-space contributions to the measured scattering profile to be expected from the substrate could be more accurately defined. The oriented wafer used had been cut so as to have the silicon (111) plane lying parallel to the silicon wafer surface.

An estimated critical angle for Films 1 and 2 was calculated assuming a density

Sample	Source Gas	Source Voltage (kV)	Source Current (mA)	Energy of Impacting Particles (keV)
Film 1	acetylene	1.3	400	1.11
Film 2	acetylene	1.5	380	1.28

Table 7.2: Production parameters for a-C:H thin films.

for both corresponding to that observed in graphite (i.e. $2.72 gcm^{-3}$). For the grazing angle studies carried out on the a-C:H thin films the incident wavelength was increased from the $0.5\mathring{A}$ value used for the polycrystalline diamond thin film to $1\mathring{A}$. This incident wavelength gives an estimated critical angle for both films of 0.15°. At an incident wavelength of $0.5\mathring{A}$ the estimated critical angle for the films would be 0.08°. Increasing the wavelength moves the incident angular range required to probe the surface film structure to higher values by reducing the penetration depth for a given incident angle and increasing the surface film/substrate signal to noise ratio. Furthermore, at higher incident wavelengths, the penetration into the film varies more slowly with the incident angle allowing increased control over any depth profiling carried out. A disadvantage of using a longer incident wavelength is the decreased maximum Q value accessible.

Table (7.3) details the incident angles at which scattering profiles were measured for Film 1 and the corresponding penetration depth for a graphitic film at the same incident angle and wavelength.

Figure (7.6) shows the scattering profiles for Film 1 measured at the scattering angles given in Table (7.3). The uppermost curve corresponds to an incident angle of 0.2°, at which angle the penetration depth into the thin film/substrate system would be such that the scattering profile collected would be expected to be dominated by

Incident Angle α_i (degrees)	Penetration Depth t
0.2	18 μm
0.1	79$\mathring{A}$
0.05	63$\mathring{A}$

Table 7.3: Incident angles used for Film 1 and corresponding penetration depth for graphite.

contributions from the silicon substrate. Sharp peaks can be seen in the scattering profile collected at this incident angle, the first two peak positions at $2.00\mathring{A}^{-1}$ and $5.73\mathring{A}^{-1}$ corresponding closely to the (111) ($2.00\mathring{A}^{-1}$) and (422) ($5.70\mathring{A}^{-1}$) reciprocal space peak positions observed in crystalline silicon. The middle curve in Figure (7.6) corresponds to an incident angle of 0.1°. Although this is below the estimated incident angle of 0.15° for this sample, sharp peaks corresponding to those observed in the 0.2° scan can still be clearly seen. The intensity of these peaks relative to the background level has however dropped. The result for the 0.1° scan implies that the penetration depth calculated in Table (7.3) is incorrect and that the the incident beam may have entered the sample above the critical angle. This is likely to be due to an overestimate of the sample density which would increase the estimated critical angle above that corresponding to the real sample density.

The lowest curve in Figure (7.6) gives the scattering profile collected at an incident angle of 0.05°. A distinct change can be seen to occur in the scattering profile collected at this incident angle, the sharp features observed in the 0.2° and the 0.1° scans being replaced by a more amorphous structure.

Figure (7.7) shows a grazing angle X-ray diffraction profile for Film 2 taken at an incident angle of 0.15°. Also shown (lower curve) is the corresponding grazing

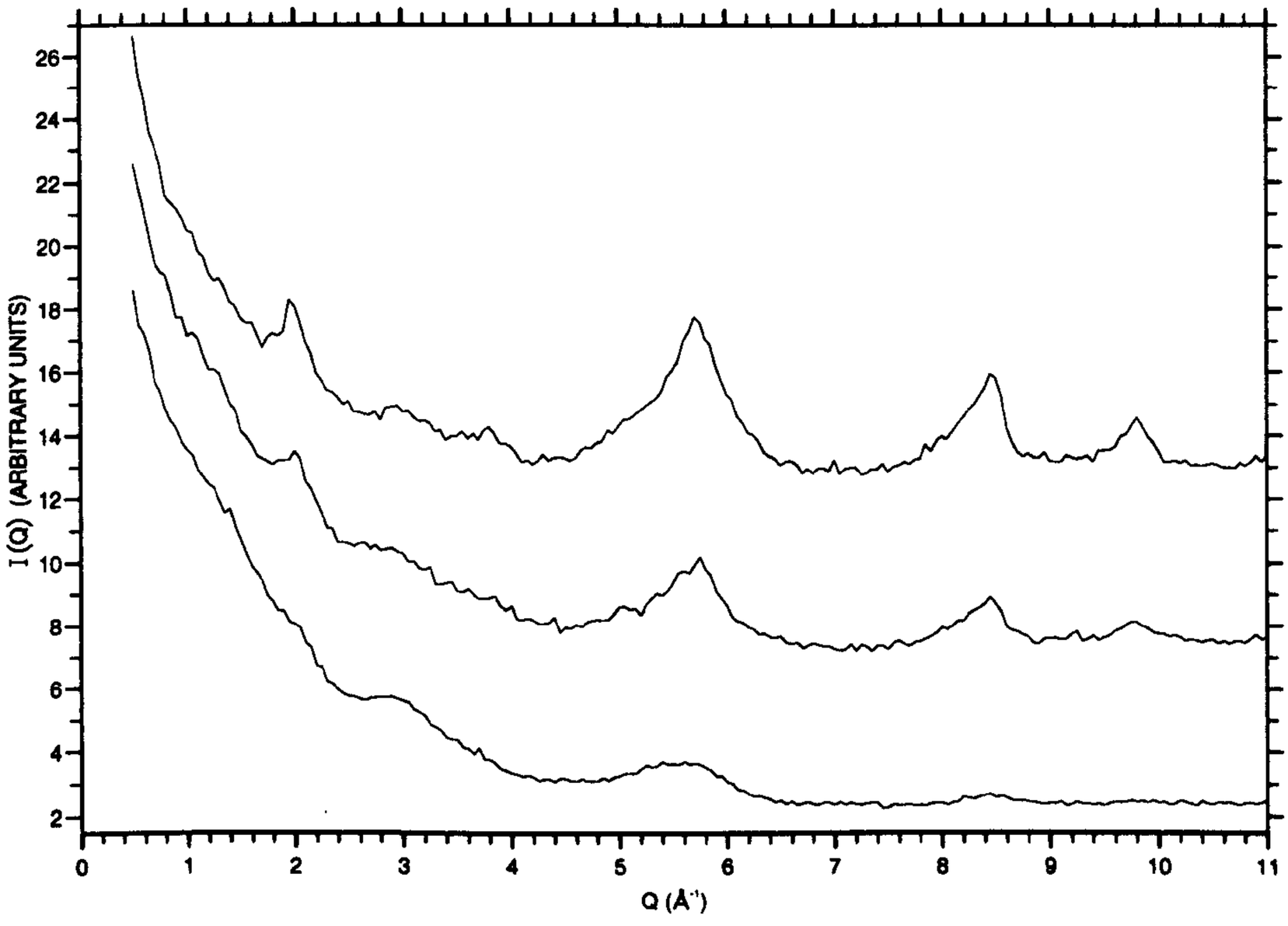

Figure 7.6: Grazing angle scattering profiles for Film 1 measured at an incident angle of 0.2° (uppermost curve), 0.1° (middle curve) and 0.05° (lowest curve).

incidence scattering profile for a (111) oriented silicon wafer measured at the same incident wavelength and angle. The silicon scan shows a single peak at $2.00\mathring{A}$ corresponding to the expected (111) peak position. The scan for Film 2 (upper curve) shows an amorphous structure and no obvious trace of a contribution from the substrate at $2.00\mathring{A}^{-1}$. Comparison of the silicon and thin film profiles implies that the structure observed in the scattering profile for the thin film originates from scattering in the surface film and not the substrate. In order to further examine the structure observed for the thin film a Chebyshev polynomial [96] was fitted to the measured scattering profile and subsequently subtracted from the scattering profile to reveal the interference function for the thin film sample. The interference function was then normalised to the intensity level of the structure factor obtained for a powder sample

of a-C:H produced using the same FAB104 fast atom source, a precursor gas of acetylene and a source voltage of 1keV. The structure factor for the powder a-C:H sample was measured using a combination of the Warren-Mavel fluorescence detection technique and standard ($\theta : 2\theta$) diffraction. The composition of the a-C:H powder sample was measured by combustion analysis to be a-$C_{0.78}$:$H_{0.22}$. The interference function corresponding to the grazing incidence scattering profile for Film 1 measured at 0.05° (shown in Figure 7.6) was obtained in a similar manner.

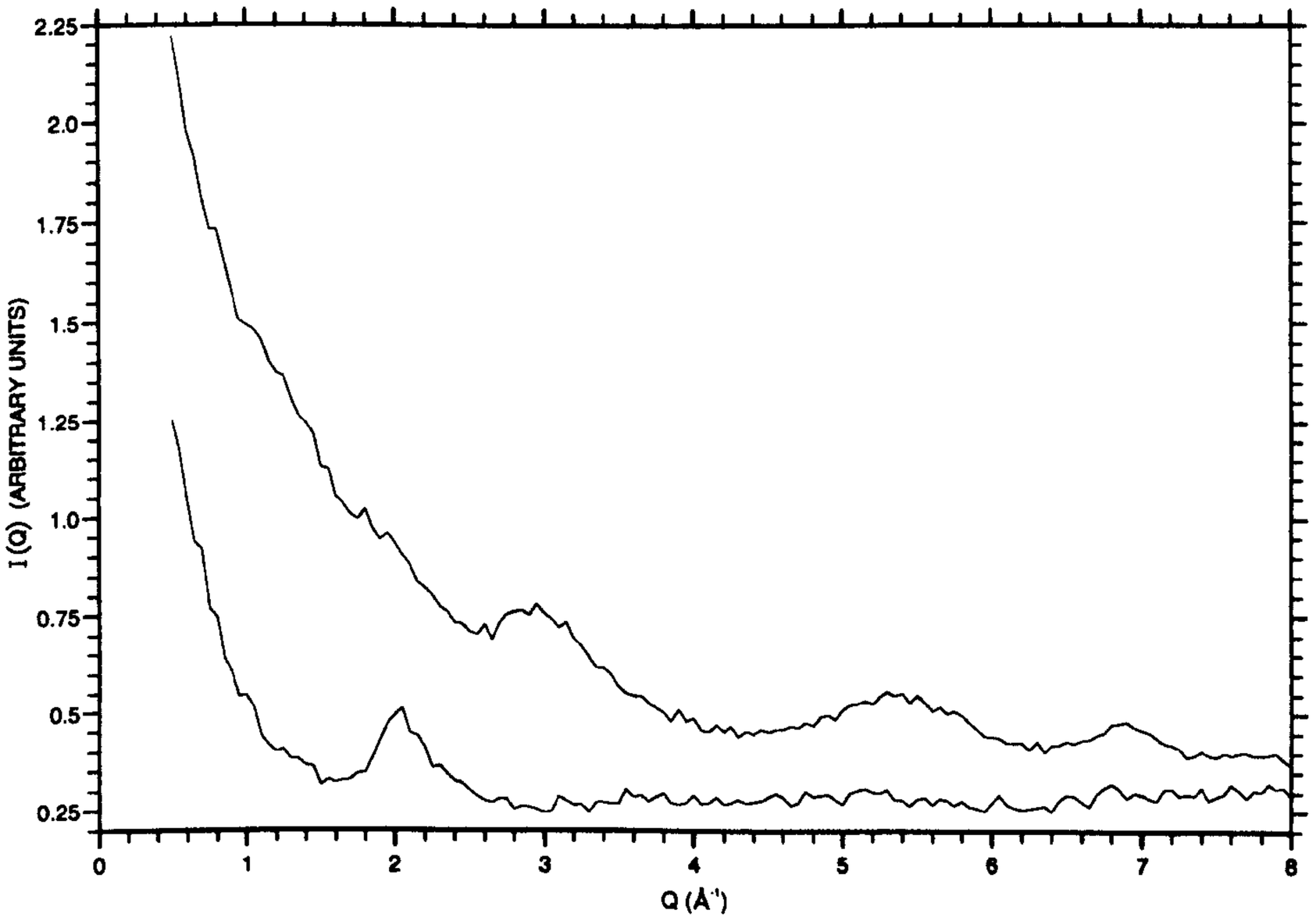

Figure 7.7: Grazing incidence scattering profile for Film 1 (top curve) and oriented silicon wafer (bottom curve) taken at $\alpha_i = 0.15°$.

Figure (7.8) shows the interference function for Film 2 (top curve), that for Film 1 (middle curve) and the structure factor for the 1keV powder sample of a-C:H (bottom curve). A distinct feature of the structure factor for the 1keV a-C:H sample is the peak at $Q = 1.89\mathring{A}^{-1}$ which occurs on the side of a broader peak which has its maximum at $1.53\mathring{A}^{-1}$. This feature is not observed in the structure factor for similar

a-C:H powder samples produced from a fast atom source from an acetylene precursor gas at an impact energy of 500eV. This feature corresponds to the interlayer distance observed in graphite and has been taken as an indication of the commonly observed transition of a-C:H to a graphitic structure for an impact energy in the region of 1keV or above. This feature can be seen in the interference functions for both Films 1 and 2. A peak can also be seen in both interference functions at around $1.42\mathring{A}^{-1}$ with that for Film 2 being more distinct from the peak at $1.89\mathring{A}^{-1}$ than that for Film 1. These features would correlate with an increased graphitic structuring of the samples with rising impact energy. The peak at $3.09\mathring{A}^{-1}$ in the structure factor for the 1keV sample can be clearly seen in the interference functions for Films 1 and 2. Film 2 shows a peak at $5.49\mathring{A}^{-1}$ corresponding to that observed in the 1keV a-C:H sample. However the interference function for Film 1 has a peak shifted to $5.72\mathring{A}^{-1}$ corresponding to that observed for the same sample at a grazing angle of 0.02°, which was assigned to silicon. The subsequent peak observed for Film 1 is again shifted from the corresponding peak in the structure factor for the 1keV sample and also corresponds to a silicon substrate peak observed in the scattering profile measured at higher angles of incidence. Therefore significant substrate scattering contributions to the measured total scattering profile for Film 1 are still apparent even at a grazing incidence of 0.05°.

In Film 2 a peak occurs at $Q = 6.91\mathring{A}^{-1}$ which cannot be assigned to a feature in the substrate scattering for this Film (see Figure (7.7)) although a peak does occur for crystalline silicon at $Q = 6.85\mathring{A}^{-1}$. Crystalline silicon carbide does however display a peak in its scattering profile at $Q = 7.0\mathring{A}^{-1}$. As the resolution of the detector slits used to collect the measured scattering profiles was 0.07° a tentative assignment of this peak to a SiC interface layer can then be made. As the energy of impact for

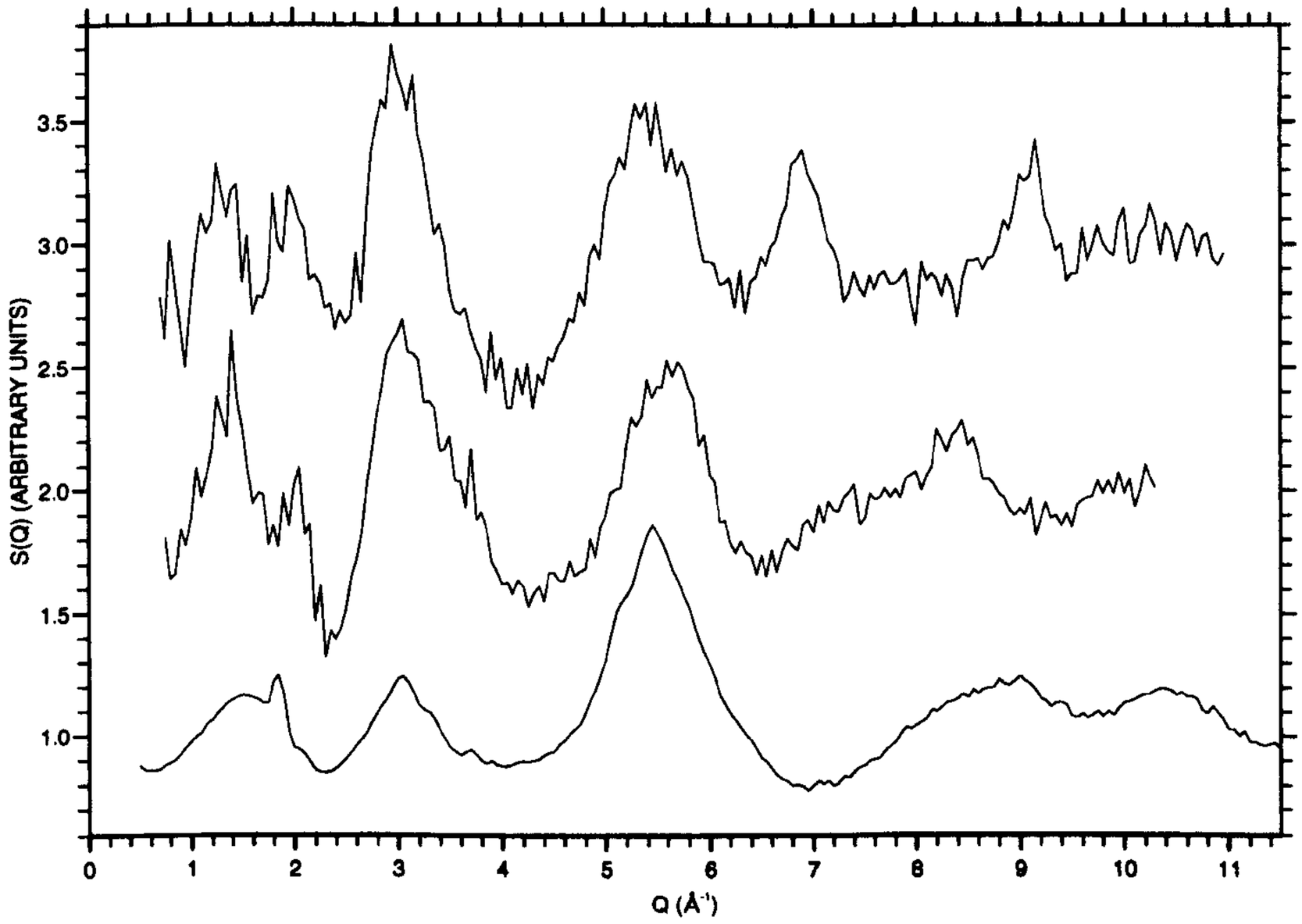

Figure 7.8: Interference function for Film 2 (top curve) and Film 1 (middle curve) measured using grazing angle X-ray diffraction. Also shown (bottom curve) is the structure factor for an a-C:H(acetylene) sample made at 1keV.

the carbon atoms impinging on the silicon substrate would have been greatest during the production of Film 2, the former would be expected to penetrate further into the substrate in this sample and therefore produce a larger interface layer than occurs in Film 1. This may be a possible explanation for the lack of a corresponding interface peak in the interference function for Film 1. Although the interference functions given for Films 1 and 2 should be treated with caution, as rigorous corrections to the data have not been applied, these preliminary results give an indication of the information that may be extracted from the data. Detailed corrections to the measured diffraction profiles would include evaluation and removal of residual substrate contributions including both elastic and Compton scattering components. Attenuation of the scattered beam within the substrate and the surface film could also be corrected

Chapter 8

Neutron Scattering From Amorphous Hydrogenated Carbon

Neutron scattering studies have been carried out on three samples of amorphous hydrogenated carbon having varying degrees of isotopic substitution namely: a-$C_{0.75}$:$H_{0.25}$, a-$C_{0.73}$:$D_{0.27}$ and a-$C_{0.74}$:$H_{0.17}$:$D_{0.09}$. The experimental data was collected on the SANDALS diffractometer at the Rutherford Appleton Laboratory (RAL), Didcot, Oxon where scattering profiles could be measured up to a maximum value of Q=35$\mathring{A}^{-1}$. In this way, well resolved real space structural information has been obtained on the named samples.

The isotope-dependent nature of the neutron scattering length has been exploited through these samples to provide a much improved definition of the structural origin of the observed features in the scattering profile of this amorphous phase. Moreover, the scattering profiles have been used to provide three linear equations from which the partial structure factors representing the C-C, C-H and H-H correlation functions may be extracted.

8.1 Neutron scattering profiles for a-C:H(D)

8.1.1 The differential scattering cross-section

Details of the neutron scattering technique carried out on the three samples have been given in Chapter (6). After normalising the raw data to the incident neutron flux, correcting for detector and moderator efficiencies, absorption and multiple scattering, the time of flight differential scattering cross-section, $\frac{d\sigma}{d\Omega}$, was obtained for each sample where the latter is defined as:

$$\frac{d\sigma}{d\Omega} = \frac{\text{No. neutrons scattered per unit time into solid angle } d\Omega \text{ at angle } 2\theta}{N\Psi(\lambda)d\Omega} \tag{8.1}$$

Here N represents the number of atoms in the sample and Ψ the incident flux at wavelength λ. As previously described, the detectors on the SANDALS diffractometer at the RAL are grouped into ten banks, each bank providing a single profile for $\frac{d\sigma}{d\Omega}$. Figures (8.1), (8.2) and (8.3) show the differential scattering cross-section profiles measured by the ten detector banks for each of the three isotopically substituted samples namely: a-$C_{0.75}$:$H_{0.25}$, a-$C_{0.73}$:$D_{0.27}$ and a-$C_{0.74}$:$H_{0.17}$:$D_{0.09}$. The average angle for each of the detector banks is given in Table (6.2) and the data is displayed with the scattering profile collected at the smallest angle detector bank uppermost.

From Figures (8.1), (8.2) and (8.3) it can be seen that those detector banks which are positioned at the smallest scattering angles and therefore allow the lowest Q values to be accessed, provide statistically poorer data. The total neutron scattering cross-sections for these samples are much smaller than the corresponding X-ray scattering cross-sections and therefore neutron scattering is at a disadvantage here in the time required to collect statistically viable data. However, as the nucleus acts as a point scatterer, the neutron scattering length does not fall off with scattering angle

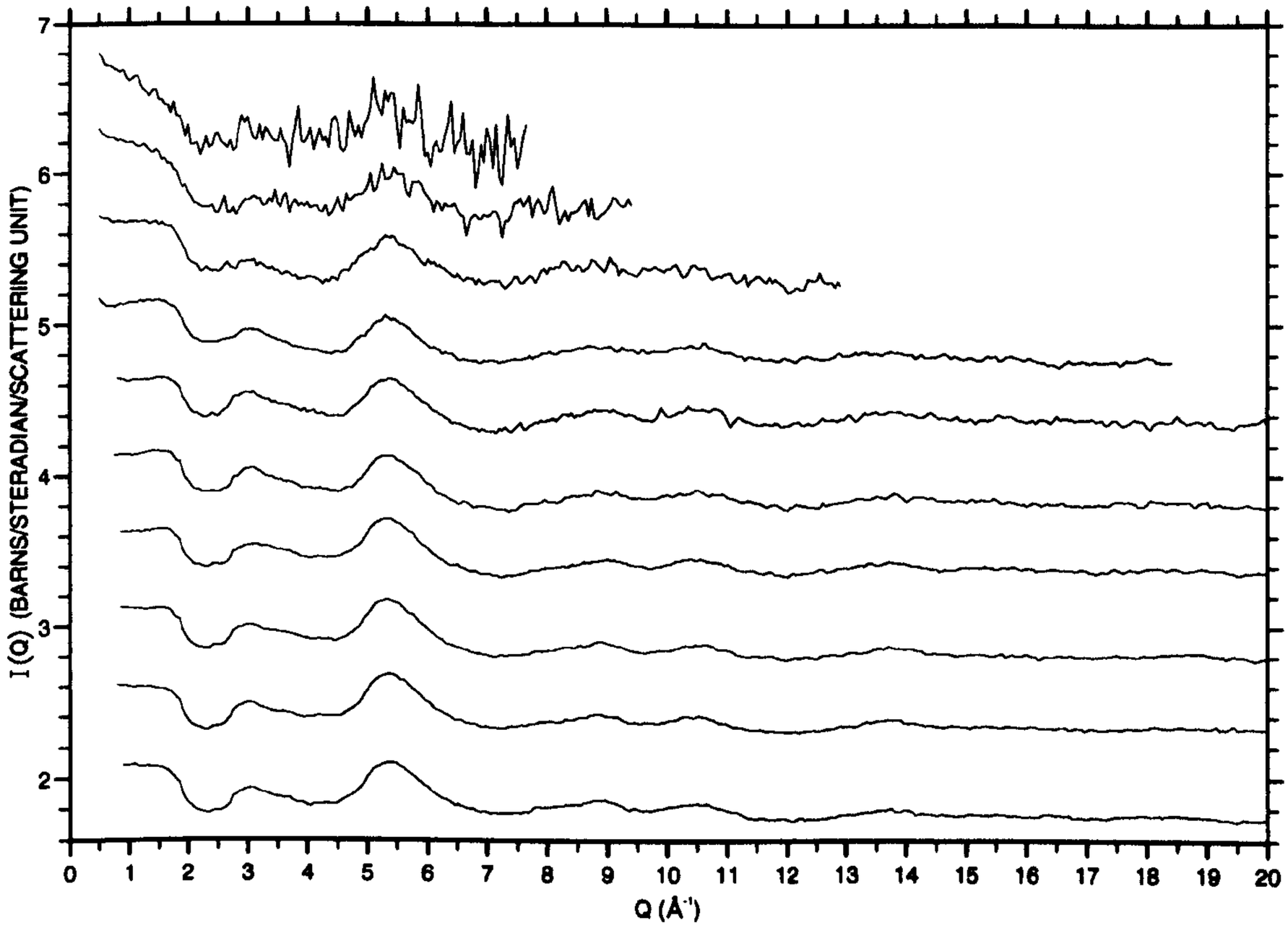

Figure 8.1: Differential scattering cross-section for a-$C_{0.75}$:$H_{0.25}$ as measured by each of the ten detector banks on the SANDALS diffractometer at the RAL. Data is offset for clarity.

(neglecting inelasticity effects) as is the case for X-rays. Therefore neutrons have an advantage over X-rays for accessing the small residual oscillations observed in amorphous materials at higher Q values. Further, neutron scattering experiments such as these allow both the hydrogen and the carbon environment to be investigated as the scattering cross-sections for both are of a similar magnitude. In contrast the X-ray scattering cross-section for carbon is far larger than that for hydrogen and thus X-ray scattering profiles for these samples are dominated by the carbon matrix.

For the fully deuterated sample, Figure (8.2), it can be seen that the data collected at the different detector banks show an analogous form across the corresponding Q ranges sampled. By contrast, for the fully hydrogenated sample, Figure (8.1), a

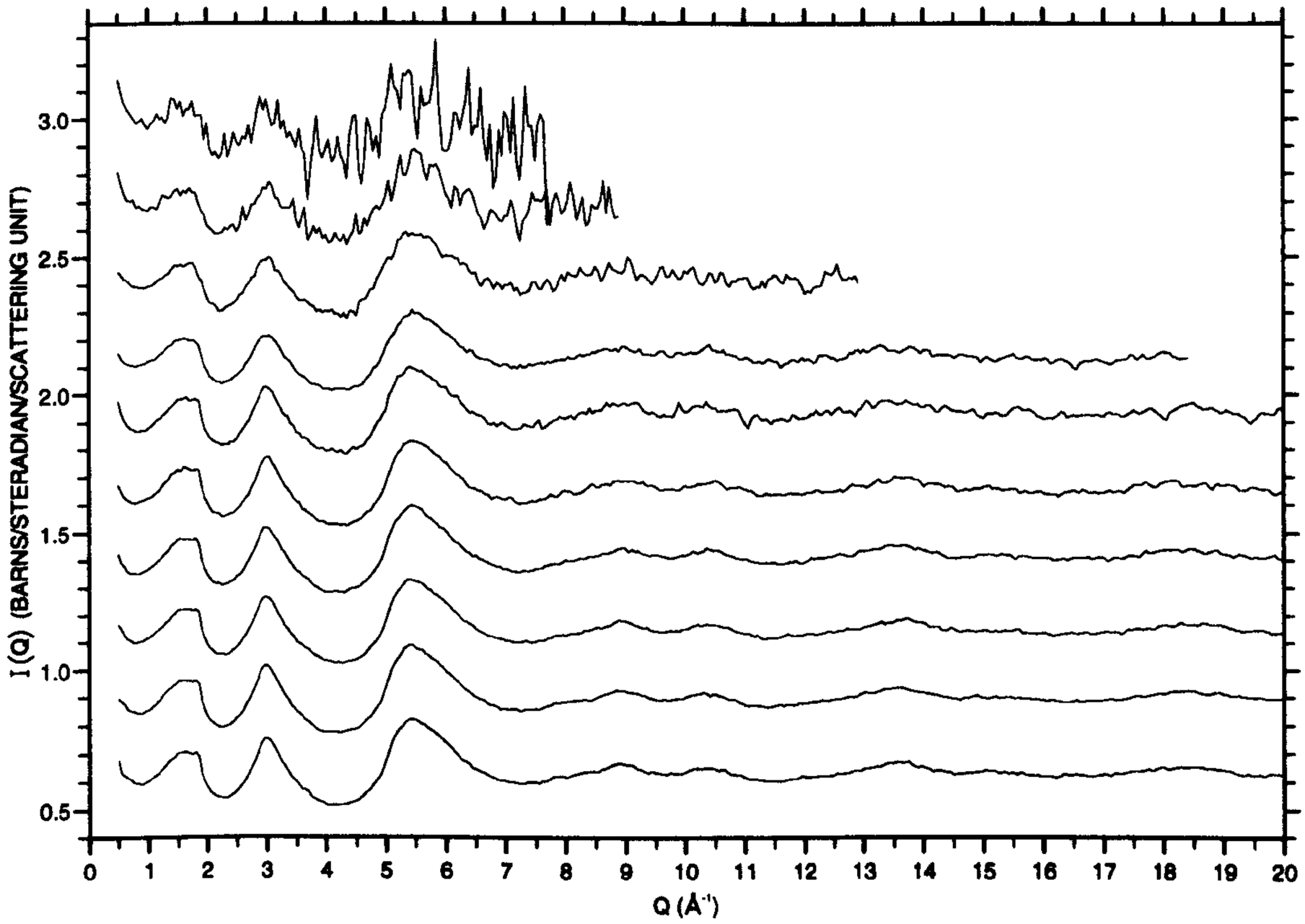

Figure 8.2: Differential scattering cross-section for a-$C_{0.73}$:$D_{0.27}$ as measured by each of the ten detector banks on the SANDALS diffractometer at the RAL. Data is offset for clarity.

variation in the form of the scattering profiles is found to occur as the average angle of the detector bank decreases. This change of form results from inelasticity effects associated with the scattering from the lighter hydrogen atoms in the sample. Such effects have been shown to cause a fall in the total scattering cross-section at higher Q values and are more pronounced in the scattering profile for lighter atoms and/or when longer incident wavelengths are used (see Section (6.3.6)). The SANDALS diffractometer at the RAL was chosen as the instrument on which to collect the neutron scattering data on these samples with the aim of experimentally minimising such inelastic scattering contributions to the collected data. This is achieved by the use of an incident wavelength range between $0.05\mathring{A}$ and $4.0\mathring{A}$ and the collection

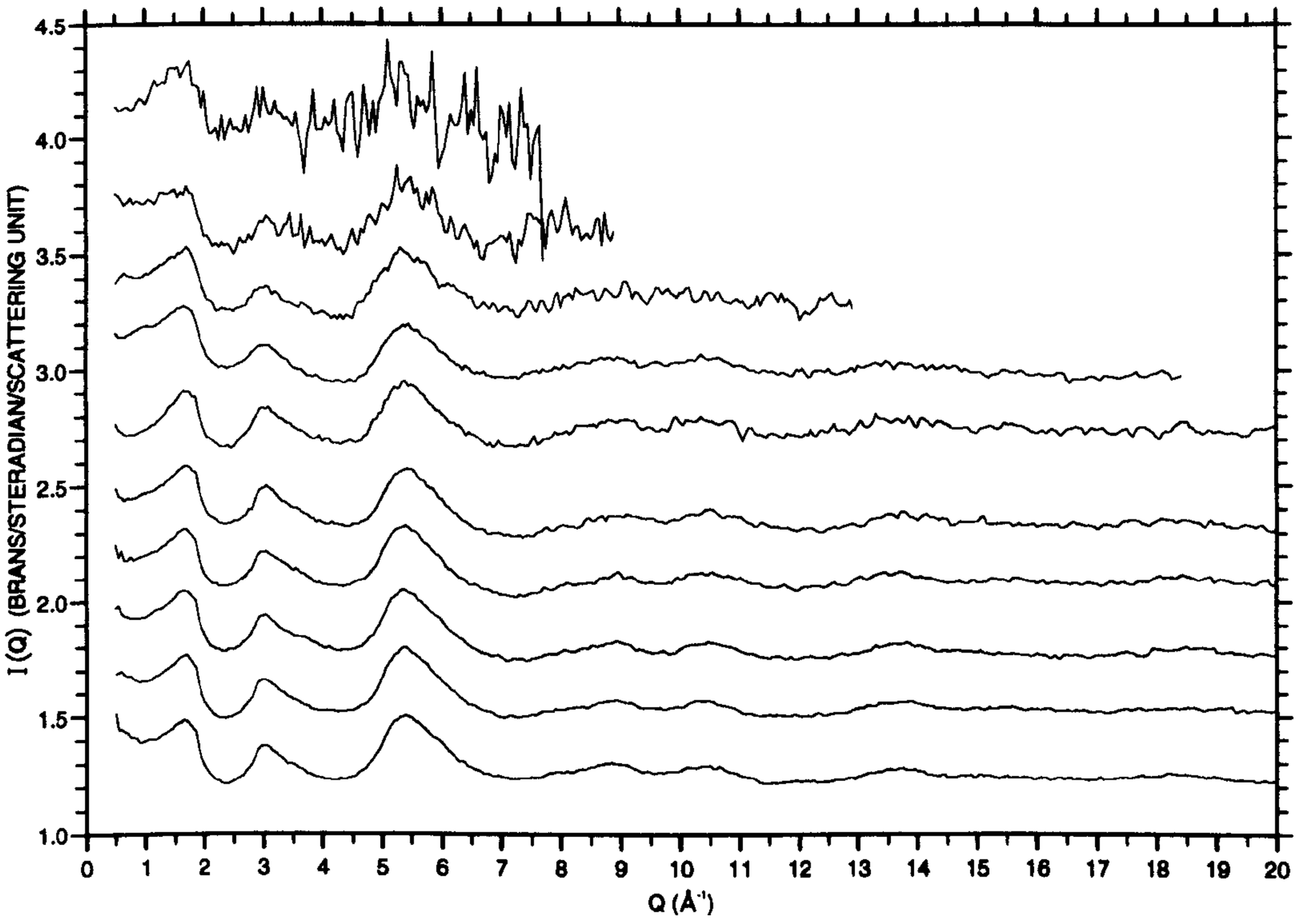

Figure 8.3: Differential scattering cross-section for a-$C_{0.74}$:$H_{0.17}$:$D_{0.09}$ as measured by each of the ten detector banks on the SANDALS diffractometer at the RAL. Data is offset for clarity.

of scattering profiles at or below a scattering angle of 21°. The form of the data collected on the fully deuterated sample appears to confirm that the contribution to the measured scattering profiles from such effects has been very much reduced. This can be seen as a minimal fall-off in the data is observed as Q increases for this sample which contains 25% of mass 2 a.m.u element.

Comparing the data collected for the three samples it can be seen that such inelastic scattering contributions appear to cause the most marked contrast between them in the form of their scattering profiles at lower Q values. The region below Q=2.5$\AA^{-1}$, as measured for the a-C:D sample, exhibits a clearly defined first peak at $\sim$ 1.5$\AA^{-1}$. For the a-C:H sample, although there is some evidence of a peak in

this region it appears to be strongly distorted. For the null mixture sample, a first diffraction peak is also evident at Q=$\sim 1.5\AA^{-1}$, as in the a-C:D sample. However a gradual rise in the leading edge of this peak can be seen to occur at the smaller angle detector banks. This results in a first diffraction peak shape intermittent between that observed for the a-C:H and the a-C:H:D samples.

Beyond Q=$2.5\AA^{-1}$, a second peak is observed for each of the samples at Q=$\sim 3\AA^{-1}$. Again the definition of the peak varies between the samples, with that for the fully deuterated sample being most pronounced and that for the fully hydrogenated sample being the least well defined. Beyond this second peak the scattering profiles for the three samples can be seen to compare more closely.

A more instructive investigation of the structural correlations between these samples can be obtained by comparison of the total structure factors for each of the three samples. The latter may be derived from the differential scattering cross-section as detailed in Section (6.3.7) and the following section.

8.1.2 Derivation of the total structure factor from the differential scattering cross-section.

To access the structurally sensitive contribution to the neutron scattering profiles measured for each of the three a-C:H(D) samples it is necessary to remove both the incoherent and the self scattering contributions to the measured differential scattering cross-section. Direct removal of these contributions to the data would require suitable corrections for the effect of inelastic scattering on the self and incoherent scattering cross-sections. As previously discussed (Section (6.3.6)), standard Placzek corrections are not suitable for samples which contain a significant concentration of small mass nuclei such as hydrogen or deuterium. Therefore to correct accurately for such effects

a suitable model of the system would be required. This would in turn demand prior knowledge of the sample structure. To overcome this problem, for the data presented in this work the incoherent and self scattering contributions were removed empirically by fitting a Chebyshev polynomial [96] to the differential scattering profile for each detector bank and subsequently subtracting this polynomial to give the interference function I(Q). In this way the need to attempt an analytical correction of the self and incoherent scattering components of the data for inelasticity effects was removed.

Although some residual inelastic scattering contributions may remain in the measured interference function, I(Q), to first order such contributions can be shown to be zero (Section (6.3.6)). Furthermore, higher order contributions should have been experimentally minimised by the use of short incident wavelengths and small detector angles. On this basis no further corrections have been made for these effects.

Merging of the interference functions

Having obtained the interference function at each of the ten detector banks, merging of these to form a single function was carried out. From the scattering profile for each detector a region was chosen within which the collected data correlated well with that collected at the consecutively lower angle bank. The interference data from each of the chosen regions was then weighted according to its statistical accuracy and summed to form a single function. The weighting function, W, in each case was obtained from the intensity data of a vanadium rod calibration scan which was carried out prior to data collection. From the latter scan a measure can be made of the variation with detector bank of the scattering intensity for an isotropic scatterer. Thus if $I_j(Q_e)$ is the measured interference function for the j^{th} detector bank, the

merged interference function is given as follows :

$$I_{merged}(Q_e) = \frac{\sum_j W_j(Q_e) \times F_j(Q_e)}{\sum_j W_j(Q_e)} \tag{8.2}$$

For the purpose of comparison of the structure factors of each of the a-C:H(D) samples, the region chosen from each of the detector bank profiles was held constant for each of the three samples. The chosen regions and the corresponding detector bank angle are given in Table (8.1).

Detector Group	Angle	Q_{min} ($\AA^{-1}$)	Q_{max} (A^{-1})
1	20.13°	6.40	35.00
2	18.11°	8.00	33.00
3	16.23°	6.40	25.00
4	14.61°	6.20	20.00
5	13.07°	6.15	20.00
6	11.79°	4.85	15.00
7	9.34°	0.60	15.00
8	6.25°	0.60	12.00

Table 8.1: Data regions from each detector bank chosen to contribute to the merged interference function for each of the isotopically substituted samples.

Contributions from detector banks nine and ten were considered too noisy to be included in the merged data for sample a-$C_{0.75}$:$H_{0.25}$. Thus for consistency they were not included in the merged data for the a-$C_{0.73}$:$D_{0.27}$ or the a-$C_{0.74}$:$H_{0.17}$:$D_{0.09}$ samples.

Having merged the data to form a single interference function for each sample, the latter was normalised by dividing out the scattering cross-section to obtain the structure factor.

8.1.3 Total structure factors for the isotopically substituted samples.

According to Faber-Ziman formalism [59], the total structure factor for each of the samples is given as follows:

$$\begin{aligned} S(Q)^{FZ} &= \frac{I_c(Q) - [< b^2 > - < b >^2]}{< b >^2} \\ &= \frac{I(Q)}{< b >^2} + 1 \end{aligned} \tag{8.3}$$

where I_c represents the coherent scattering contribution to the data. For a multi-component system containing elements a and b with atomic concentrations c_a and c_b respectively then

$$< b >= c_a b_a + c_b b_b \tag{8.4}$$

and

$$b^2 = c_a b_a^2 + c_b b_b^2 \tag{8.5}$$

where b_a and b_b are the coherent neutron scattering cross-sections for elements a and b respectively.

Figure (8.4) shows the total structure factor for the a-$C_{0.75}$:$H_{0.25}$, a-$C_{0.73}$:$D_{0.27}$ and a-$C_{0.74}$:$H_{0.17}$:$D_{0.09}$ samples (data given out to $30\mathring{A}$ only to emphasise lower Q region showing structure). In each case, the measured total structure factor is composed of a weighted sum of Faber-Ziman partial structure factors where for a two component system containing elements a and b, $S(Q)^{FZ}$ is given by

$$S(Q)^{FZ} = \frac{c_a^2 b_a^2}{< b >^2} S(Q)_{aa} + \frac{c_b^2 b_b^2}{< b >^2} S(Q)_{bb} + \frac{2 c_a c_b b_a b_b}{< b >^2} S(Q)_{ab} \tag{8.6}$$

The coherent scattering cross-sections for carbon, hydrogen and deuterium are given in Table (8.2). Substituting for these values in Equation (8.6) it can be shown

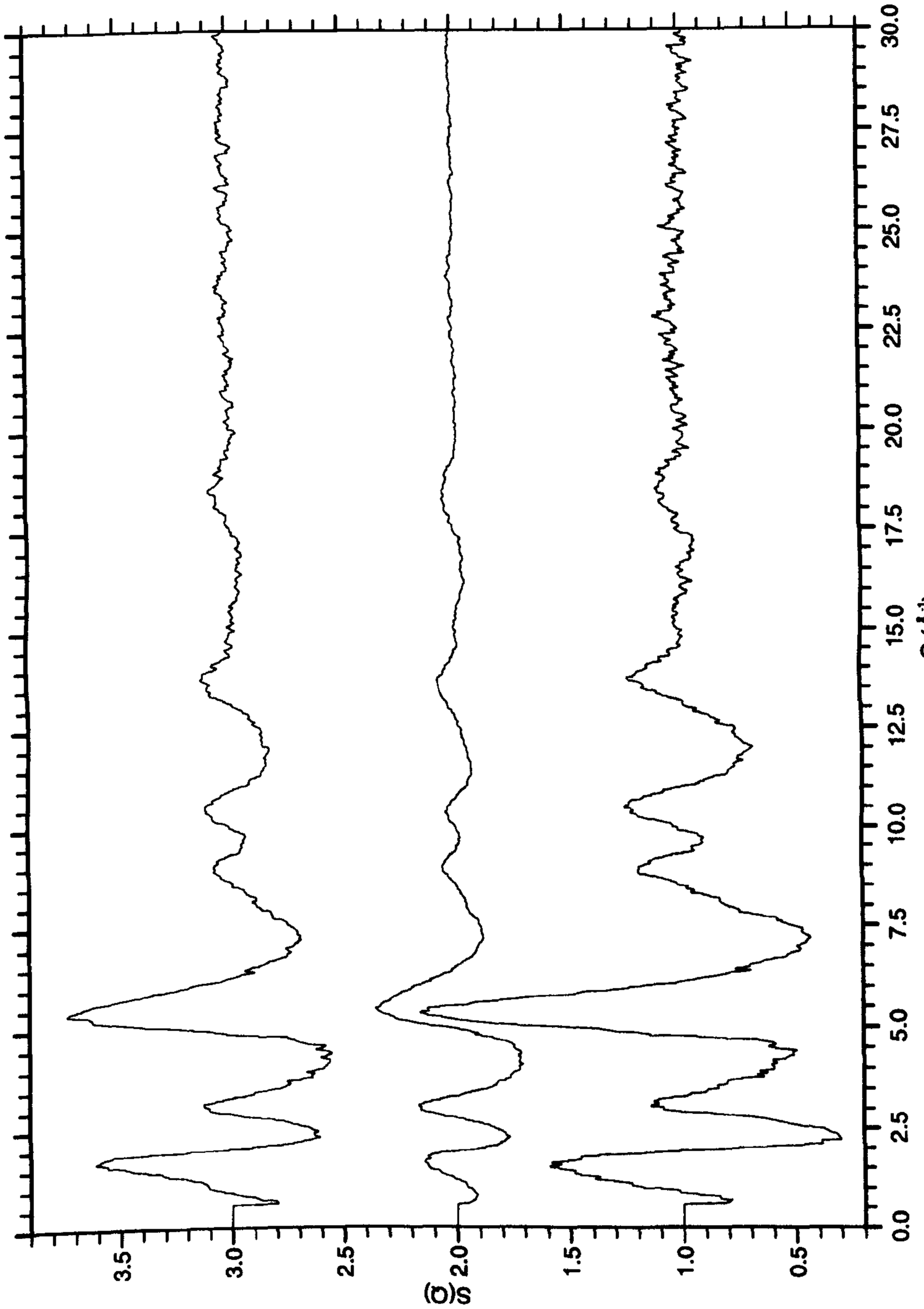

Figure 8.4: Total structure factor for samples a-$C_{0.74}$:$H_{0.17}$:$D_{0.09}$ (top), a-$C_{0.73}$:$D_{0.27}$ (middle) and a-$C_{0.75}$:$H_{0.25}$ (bottom).

that the weighting factors for the C-C, C-H(D) and H(D)-H(D) correlations for the fully hydrogenated and the fully deuterated samples are as given in Table (8.3).

Element	Scattering Length (10^{-12}cm) [49]
Carbon	0.6646
Hydrogen	-0.3739
Deuterium	0.6671

Table 8.2: Coherent scattering lengths for carbon, hydrogen and deuterium

Sample	W_{C-C}	$W_{C-H(D)}$	$W_{H(D)-H(D)}$
a-$C_{0.75}$:$H_{0.25}$	1.51	-0.56	0.05
a-$C_{0.73}$:$D_{0.27}$	0.53	0.40	0.07
a-$C_{0.74}$:$H_{0.17}$:$D_{0.09}$	1.01	-0.01	0.00

Table 8.3: Weighting factors for the C-C, C-H(D) and H(D)-H(D) partial contributions to the total structure factor for the isotopically substituted samples given.

By expansion of Equation (8.6) it can be shown that for a three component system such as a-$C_{0.74}$:$H_{0.17}$:$D_{0.09}$ the total structure factor is given by:

$$S(Q)^{FZ}_{a-C:H:D} = \frac{1}{(c_C b_C + (c_D b_D + c_H b_H))^2} \quad [\quad c_C^2 b_c^2 S(Q)_{CC} + (c_D b_D + c_H b_H)^2 S(Q)_{HH} + \quad (c_D b_D + c_H b_H) 2 c_C b_C S(Q)_{CH}] \qquad (8.7)$$

where the partial structure factor for C-H correlations has been taken to be equal to that for C-D correlations and the partial structure factor for H-H correlations taken to be equal to that for D-D correlations.

The term $(c_D b_D + c_H b_H)$ in Equation (8.7) represents the effective scattering length for hydrogen in the sample. For the "null mixture" sample, which has a measured

composition of a-$C_{0.74}$:$H_{0.17}$:$D_{0.09}$, the effective scattering length for hydrogen is

$$b_{eff}^{a-C_{0.74}:H_{0.17}:D_{0.09}} = -0.04 \times 10^{-12}\text{cm} \tag{8.8}$$

The resultant weighting factors for the partial correlation functions for this sample are given in Table (8.3). From this table it can be seen that, to the accuracy given, there are zero contributions to the total structure factor for the "null" sample from H-H correlations and a very small contribution from C-H correlations. In the following section the variation in the form of the structure factor for each of these samples is looked at.

Comparison between the total structure factors

Figures (8.5), (8.6) and (8.7) show the measured total structure factors for the fully hydrogenated, fully deuterated and the "null mixture" samples respectively (plotted individually to allow a more detailed comparison to be made). After removal of the incoherent scattering contribution to the data, the fully hydrogenated sample can be seen to display a first structure factor peak at $1.58\mathring{A}^{-1}$. Corresponding peaks in the structure factor for the a-C:D sample and the a-C:H:D sample occur at $1.62\mathring{A}^{-1}$ and $1.69\mathring{A}^{-1}$ respectively. In the case of the "null mixture" and the fully deuterated sample, a shoulder is observed on the first peak at $\sim 1\mathring{A}^{-1}$. This feature cannot be observed in the fully hydrogenated sample. However this sample does display a slightly broader first peak than that observed for the other two samples.

Each of the three samples also has a second peak at $3.1\mathring{A}^{-1}$ with the peak shape again varying between samples. For both the a-C:H and the a-C:H:D samples the second peak is slightly asymmetric and smaller than the first peak, the differential being greatest for the "null mixture" sample. In contrast, the corresponding peak for the fully deuterated sample is symmetric and of greater height than the first. This

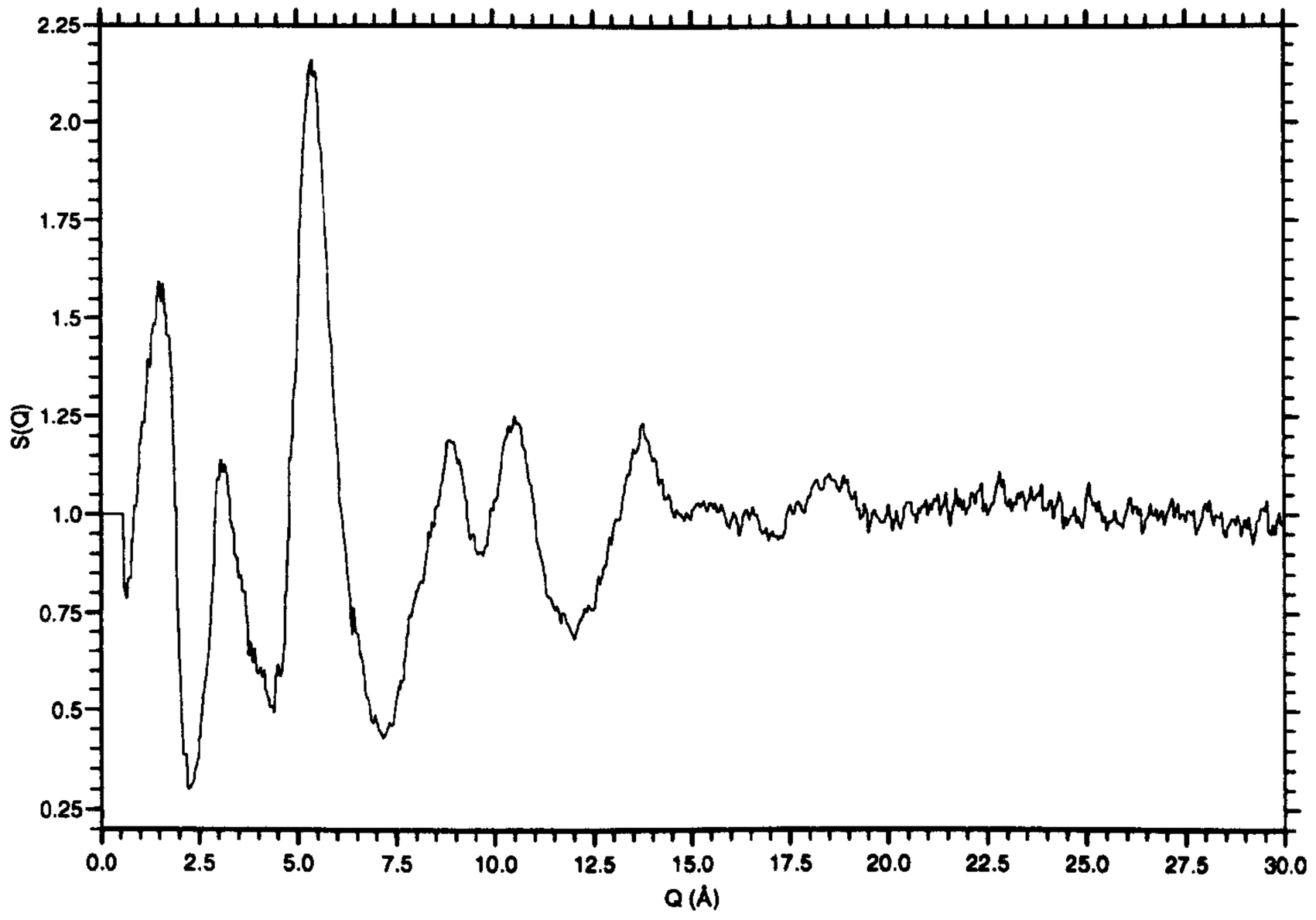

Figure 8.5: Total structure factor for a-$C_{0.75}$:$H_{0.25}$ as measured on the SANDALS diffractometer at the RAL.

may be the result of C-D correlations which would be expected to make a positive contribution to the scattering profile of this sample with a weighting close to that of the C-C correlations as shown in Table (8.3). If this is the case then corresponding C-H correlations in the a-C:H sample may be expected to lower the complementary peak height in this sample due to their negative weighting. However it can be seen from Table (8.3) that the ratio of C-H:C-C contributions to the scattering profile for the a-C:H sample is far smaller than the C-D:C-C ratio for the a-C:D sample.

In addition to the variation in the second peak height, a change in the relative size of the minima either side of this peak is also observed. In the a-C:H:D sample these minima are of similar depth; in the fully deuterated sample the second minima is more pronounced, and in the fully hydrogenated sample the reverse is true. This may again be indication of C-H(D) correlations at this point.

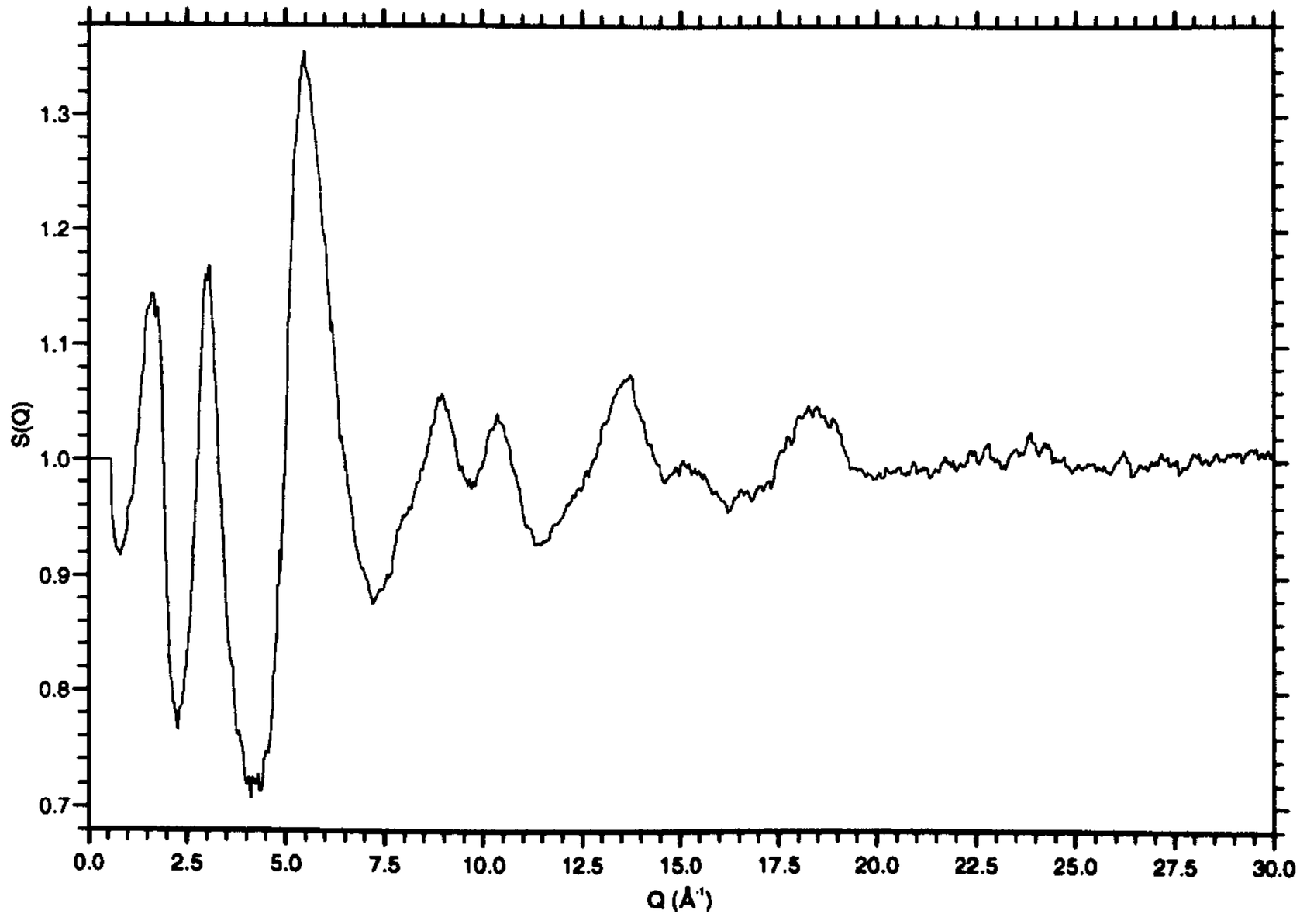

Figure 8.6: Total structure factor for a-$C_{0.73}$:$D_{0.27}$ as measured on the SANDALS diffractometer at the RAL.

A third peak in the structure factor of the fully hydrogenated sample is found to occur at $5.38\mathring{A}^{-1}$ close to that observed for the "null mixture" sample at $5.42\mathring{A}^{-1}$. The corresponding peak for the fully deuterated sample occurs at $5.50\mathring{A}^{-1}$. This peak is found to be most sharp in the case of the a-C:H sample. The remaining two samples display both a slight asymmetry in this peak and a small shoulder on the lower Q side. This latter effect is seen to be more pronounced in the fully deuterated sample and may again indicate the presence of C-H(D) correlations in this region.

Each of the three samples can be seen to display a fourth structure factor peak at $8.96\mathring{A}^{-1}$ which is followed by a peak at $10.57\mathring{A}^{-1}$ for the fully hydrogenated sample,$10.37\mathring{A}^{-1}$ for the fully deuterated sample and $10.49\mathring{A}^{-1}$ for the null mixture sample. A combination of peaks at $9.0\mathring{A}^{-1}$ and $11\mathring{A}^{-1}$ has previously been observed in diamond-like a-C:H samples deposited using a fast atom source [5]. These neutron

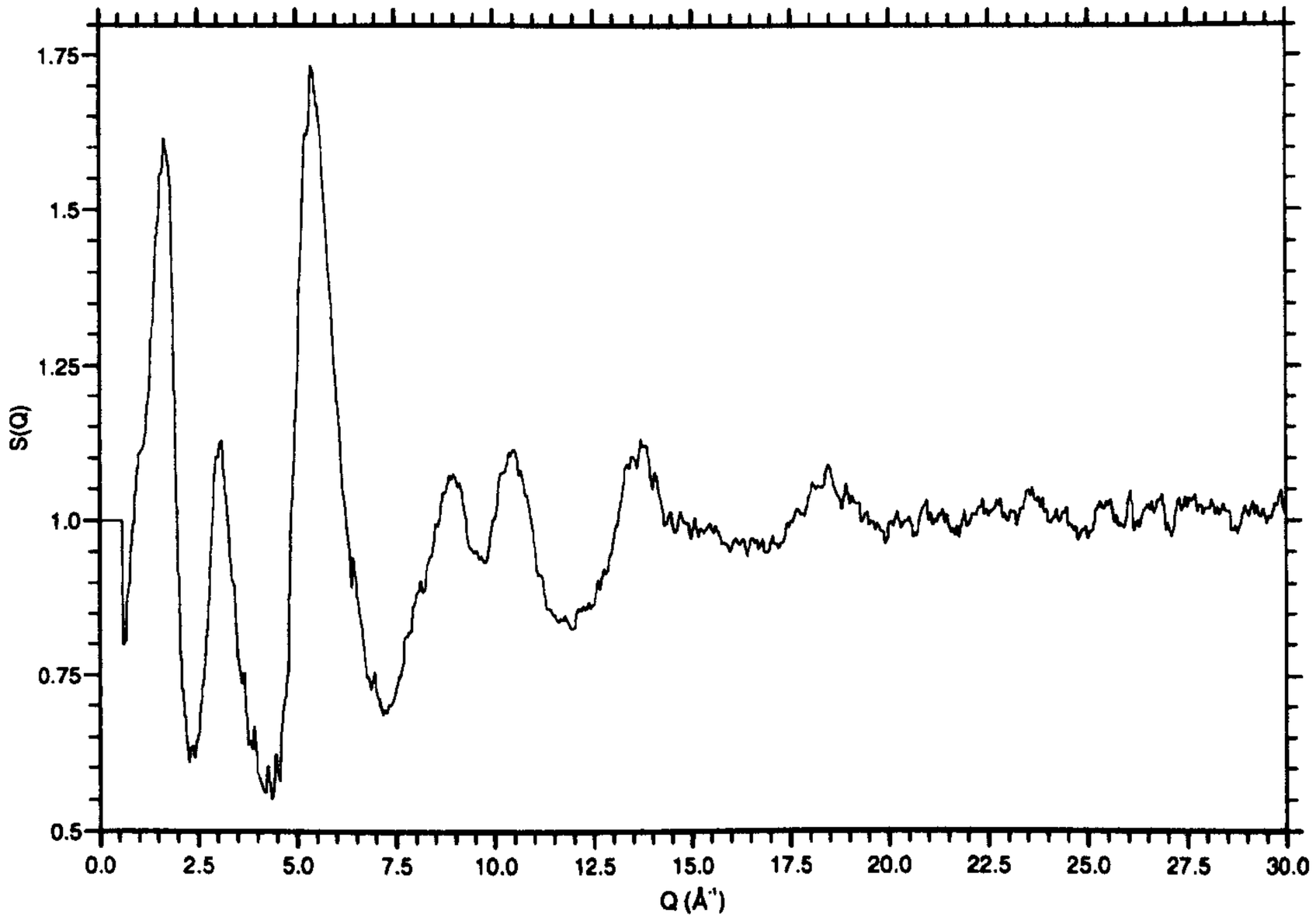

Figure 8.7: Total structure factor for a-$C_{0.74}$:$H_{0.17}$:$D_{0.09}$ as measured on the SANDALS diffractometer at the RAL.

scattering studies showed the minima between the fourth and fifth structure factor peaks to increase in amplitude with the hydrogen content of the a-C:H material indicating the presence of C-H correlations at this point. For the samples studied here this minima can be seen to be most pronounced for the fully hydrogenated sample and least for the fully deuterated. This therefore further endorses the assumption of such correlations in this Q range.

Out at higher Q still, each of the samples displays a peak at $\sim 13.8\mathring{A}^{-1}$ and $18.5\mathring{A}^{-1}$. A small peak can be clearly observed for the a-C:D sample at $15.2\mathring{A}^{-1}$ whereas only a complementary shoulder can be seen in the case of the "null mixture" sample. From Figure (8.5) some structure at $15.6\mathring{A}^{-1}$ and $16.5\mathring{A}^{-1}$ can be seen in the structure factor of the fully hydrogenated sample.

Before these structure factors are used to deduce the partial structure factors for

this phase of a-C:H it is useful first to look briefly at the real space correlations for each of the samples. In this way it can be ensured that these samples truly represent isotopically enriched forms of the same structural phase. The derivation of these real space correlations from the structure factors is detailed in the next section followed by a brief description of the results obtained.

8.1.4 Pair distribution functions for the isotopically substituted samples.

Figure (8.8) shows the total pair distribution function, g(r), for the a-$C_{0.75}$:$H_{0.25}$, a-$C_{0.73}$:$D_{0.27}$ and a-$C_{0.74}$:$H_{0.17}$:$D_{0.09}$ samples. These were obtained by Fourier transformation of the total structure factors given in Figure (8.4) where

$$g(r) = 1 + \frac{1}{2\pi^2\rho}\int_0^{Q_{max}} Q^2[S(Q)-1]\frac{sin(Qr)}{Qr}dQ \tag{8.9}$$

As for the total structure factors, these g(r) represent a sum of weighted partial pair distribution functions such that:

$$g(r) = W_{CC}g(r)_{CC} + W_{HH}g(r)_{HH} + W_{CH}g(r)_{CH} \tag{8.10}$$

where the relevant weighting factors for each sample are given by the corresponding partial structure factor weightings as given in Table (8.3).

Termination Errors

Transformation between reciprocal and real space can only be perfect if the structure factor S(Q) is known for an infinite range of Q values. In practice this is obviously not the case as the measured function terminates at a finite value Q_{max}. This may

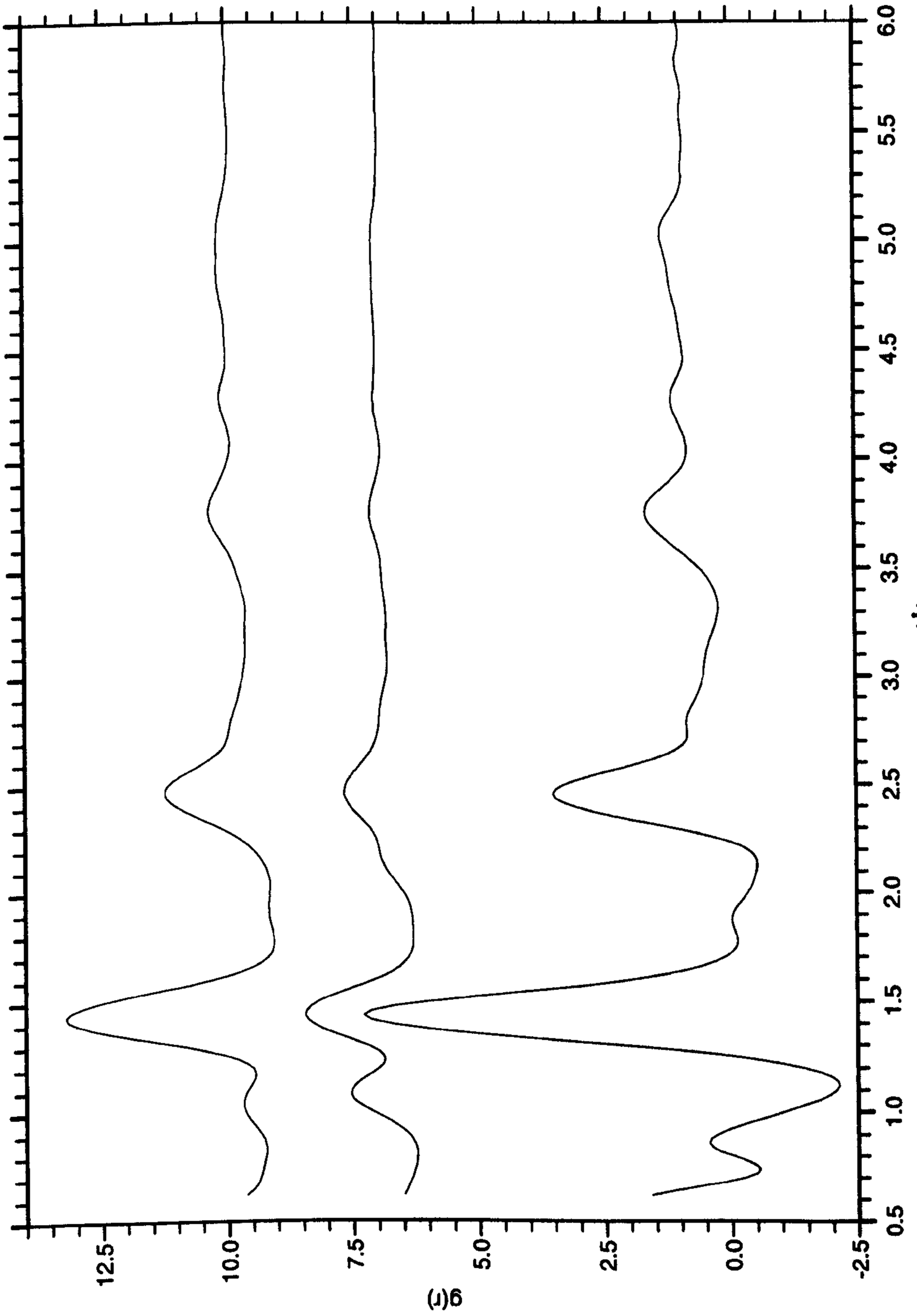

Figure 8.8: Total pair distribution function for a-$C_{0.74}$:$H_{0.17}$:$D_{0.09}$ (upper), a-$C_{0.73}$:$D_{0.27}$ (middle) and a-$C_{0.75}$:$H_{0.25}$ (lower).

be considered equivalent to the function S(Q) being multiplied by a modification function M(Q) where

$$\begin{aligned} M(Q) &= 1 \qquad Q \leq Q_{max} \\ &= 0 \qquad Q > Q_{max} \end{aligned} \tag{8.11}$$

so that

$$g(r) = 1 + \frac{1}{2\pi^2\rho}\int_0^\infty Q^2[S(Q)-1]M(Q)\frac{sin(Qr)}{Qr}dQ \tag{8.12}$$

The effect of such a finite Q range is to introduce "termination errors" into the Fourier transform. This occurs because the "true" g(r) which would occur for an infinite Q range becomes convoluted with the cosine transform of the modification function. For the step function, M(Q), given above the latter would be a sinc function $\frac{sin(Q_{max}r)}{\pi r}$. Such a convolution results in two effects: first a loss in resolution occurs as real space wavelengths below $\frac{2\pi}{Q_{max}}$ are lost, leading to a peak width of approximately $\frac{\pi}{Q_{max}}$, and secondly spurious termination ripples are introduced at values of $rQ_{max} \simeq \pm((4n+1)\pi)/2$ (where n is an integer), which decay with increasing r. This problem is reduced to a certain extent in time-of-flight neutron diffraction where S(Q) can be measured out to a high Q_{max}. In particular, for amorphous materials if the structure factor can be measured to beyond the point at which oscillations have died away (at least within the statistical accuracy of the data) then such a discontinuity in S(Q) does not occur. If this cannot be achieved, termination errors can be minimised by applying a damping factor which multiplies the measured S(Q) in the Fourier transform, replacing a sharp discontinuity at Q_{max} with a smoothly varying function. For the data given in this work a Lorch function [97] has been used where

$$M(Q)_{Lorch} = \frac{Q_{max}}{\pi Q}sin(\frac{\pi Q}{Q_{max}}) \tag{8.13}$$

This function is used at it reduces ripples rapidly. However it does cause some loss in real space resolution.

Comparison between the total pair distribution functions

From the total pair distribution functions given in Figure (8.8), the real space structure of the samples can be seen to correlate well. A negative peak corresponding to the C-H distance at $1.1\mathring{A}$ can be clearly seen in the fully hydrogenated sample and a corresponding positive C-D peak in the fully deuterated data. A small peak can be seen in the "null mixture" sample shifted to $1\mathring{A}$. Some of this contribution may be due to residual effects observed in the low r region of the data due to long range oscillations in the structure factor resulting from difficulties in fitting the polynomial to remove the incoherent and self contribution.

All three samples have a C-C first neighbour peak at $1.45\mathring{A}$ (c.f. C-C for graphite of $1.42\mathring{A}$ and that for diamond $1.51\mathring{A}$) which is to be expected for the energy range at which the samples were made. A shoulder can be seen in the deuterated data at $2.16\mathring{A}$ which corresponds to the C-C-D second neighbour distance. A corresponding trough is apparent in the hydrogenated sample and the two effects appear to cancel in the mixed sample, again implying that this has a "null" composition. Each of the samples has a second neighbour peak at $2.47\mathring{A}$.

The degree of correlation between the real space structure of these samples can be clearly seen in Figure (8.9) where the weighting of $g(r)_{CC}$ has been normalised to that of the "null" sample in each case. Having shown the structure of the samples to be consistent, the partial correlation functions for this phase of a-C:H may now be derived from the data for the three samples. This process and the results obtained are detailed in the second half of this chapter.

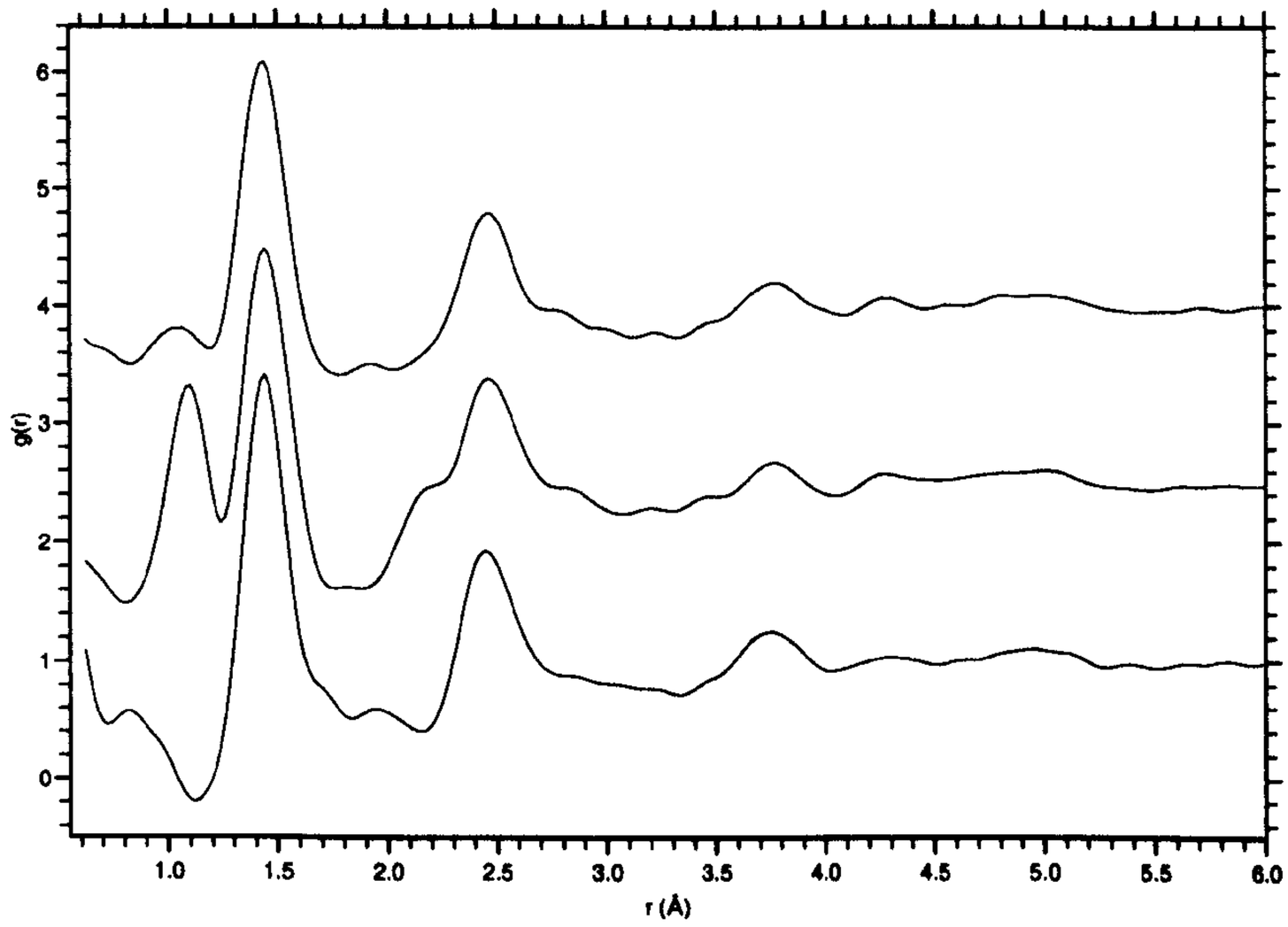

Figure 8.9: Total pair distribution functions for samples a-$C_{0.74}$:$H_{0.17}$:$D_{0.09}$ (top), a-$C_{0.73}$:$D_{0.27}$ (middle) and a-$C_{0.75}$:$H_{0.25}$ (bottom) having W_{CC} normalised to that of the "null" sample in each case.

8.2 Partial correlation functions for amorphous hydrogenated carbon

8.2.1 Determination of the partial structure factors

The interference function measured for the three isotopically substituted samples can be defined as follows:

$$I(Q) = c_C^2 b_H^2 [S(Q)_{CC} - 1] + c_H^2 b_H^2 [S(Q)_{HH} - 1] + 2c_C b_C c_H b_H [S(Q)_{CH} - 1] \quad (8.14)$$

where c_C and c_H represent the atomic concentrations of carbon and hydrogen(deuterium) in the samples. b_C and b_H represent the effective scattering length for carbon and hydrogen respectively. Having shown the structural similarity between the three isotopically substituted samples, their measured interference functions can be used

to represent three linear equations which may be solved for $S(Q)_{CC}$, $S(Q)_{CH}$ and $S(Q)_{HH}$. The equations to be solved may be written in matrix form as follows:

$$[A].[X(Q)] = [I(Q)] \tag{8.15}$$

where

$$[A] = \begin{bmatrix} c_C^2 b_C^2 & c_H^2 b_H^2 & 2c_C b_C c_H b_H \\ (c_C^*)^2 (b_C^*)^2 & (c_H^*)^2 (b_H^*)^2 & 2c_C^* b_C^* c_H^* b_H^* \\ (c_C^{**})^2 (b_C^{**})^2 & (c_H^{**})^2 (b_H^{**})^2 & 2c_C^{**} b_C^{**} c_H^{**} b_H^{**} \end{bmatrix} \tag{8.16}$$

$$[X] = \begin{bmatrix} S_{CC}(Q) - 1 \\ S_{HH}(Q) - 1 \\ S_{CH}(Q) - 1 \end{bmatrix} \tag{8.17}$$

and

$$[I(Q)] = \begin{bmatrix} I(Q)_1 \\ I(Q)_2 \\ I(Q)_3 \end{bmatrix} \tag{8.18}$$

For the samples detailed here, [A] is given by:

$$\begin{bmatrix} 1.51 & 0.05 & -0.56 \\ 0.53 & 0.07 & 0.40 \\ 1.01 & 0.00 & -0.01 \end{bmatrix} \tag{8.19}$$

The formal solution of Equation (8.15) is

$$[X(Q)] = [A]^{-1}.[I(Q)] \tag{8.20}$$

and $[A]^{-1}$ may be calculated to be [98]:

$$\begin{bmatrix} -0.11 & 0.03 & 4.32 \\ 41.19 & 20.60 & -61.79 \\ 7.42 & 2.15 & 5.56 \end{bmatrix} \tag{8.21}$$

From the measured functions $I(Q)_1, I(Q)_2$ and $I(Q)_3$ and the calculated value of $[A]^{-1}$, the partial structure factors $S(Q)_{CC}$, $S(Q)_{HH}$ and $S(Q)_{CH}$ were obtained. These partial functions are given in Figure (8.10) and are discussed in the following sections.

8.2.2 The carbon-carbon partial structure factor

As previously discussed in Chapter (2), the carbon atoms within these samples of a-C:H may exist in either an sp^3, sp^2 or sp^1 hybridisation state. If purely sp^3 bonds are present within the carbon matrix, the C-C bond length would be expected to be $1.54\mathring{A}$ and the average bond angle approximately 110°. Any sp^2 bonds present within the carbon network could take either of three forms: olefinic as in ethene (C_2H_4), aromatic as in benzene (C_6H_6) or graphitic. These three forms relate to each sp^2 hybridised carbon atom having one, two or three double bond links to its neighbouring carbon atoms respectively. The C-C nearest neighbour distance in an olefinic bond is found to be $1.34\mathring{A}$ whereas aromatic and graphitic carbon phases have a nearest neighbour distance of $1.39\mathring{A}$ and $1.42\mathring{A}$ respectively. The bond angle associated with each of these sp^2 bond configurations is 120°.

The lower profile in Figure (8.10) shows the C-C partial structure factor, $S(Q)_{CC}$, determined from the measured neutron scattering profiles for the three isotopically substituted samples. As the composition of the "null mixture" sample lies very close to that required for an a-C:H sample having a zero hydrogen neutron cross-section, $S(Q)_{CC}$ is given, to a close approximation, by the total structure factor for the "null" sample. The peak positions observed in this partial correlation function correspond, therefore, to those detailed for the "null" sample in Section (8.1.3)

It is useful to compare this partial structure factor with that for some known

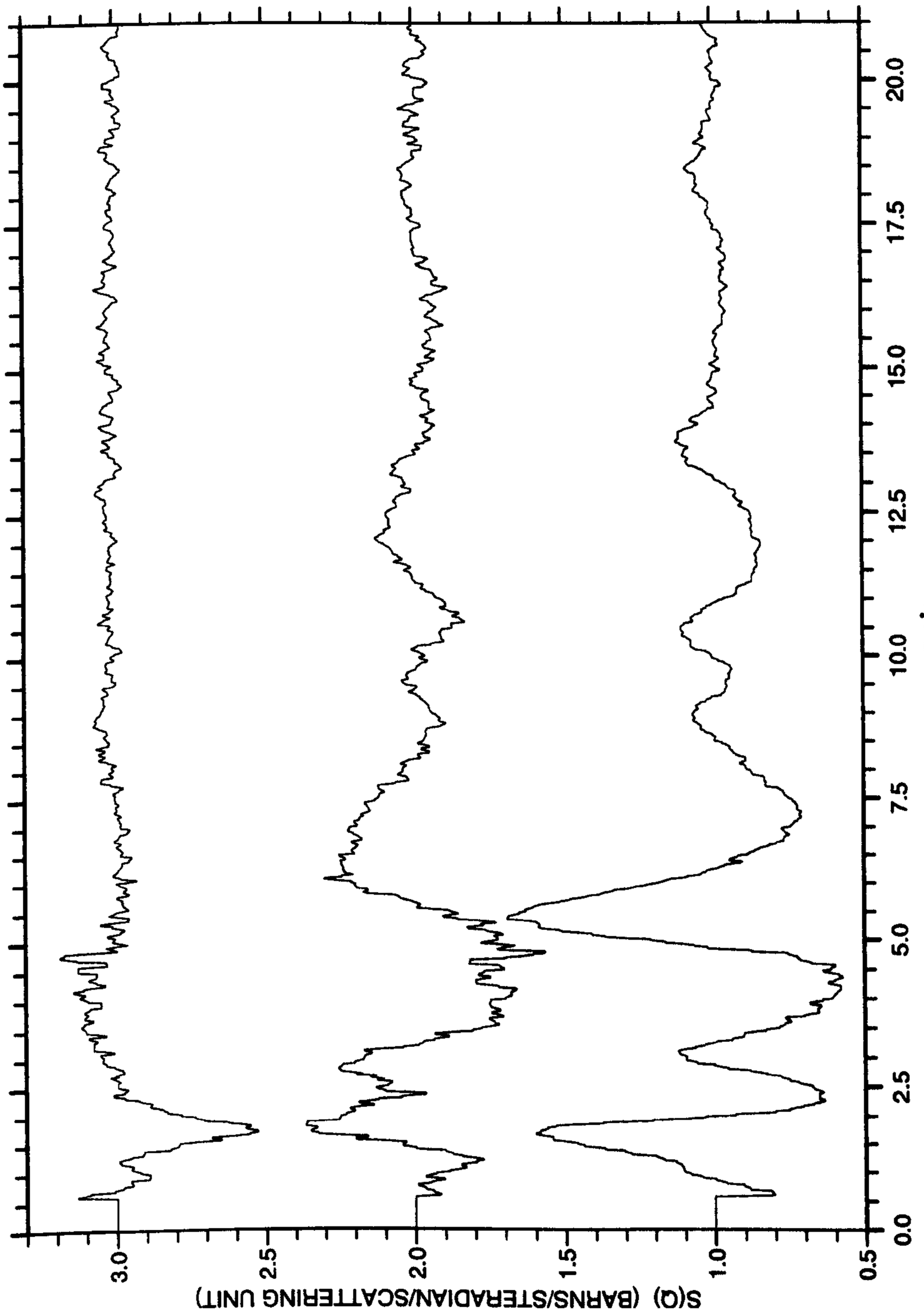

Figure 8.10: Partial structure factor for a-C:H: top $S(Q)_{HH}$; middle $S(Q)_{CH}$, and bottom $S(Q)_{CC}$.

carbon structures. Figure (8.11) shows the structure factor for both diamond and graphite powder samples as measured by $\theta : 2\theta$ X-ray diffraction on station 9.1 at the Daresbury Laboratory SRS (see Section (5.1.1)). The measured peak positions in the structure factor for these two samples and those measured by other workers [12] for several forms of amorphous carbon are given in Table (8.4). Also given are those measured for the C-C partial structure factor.

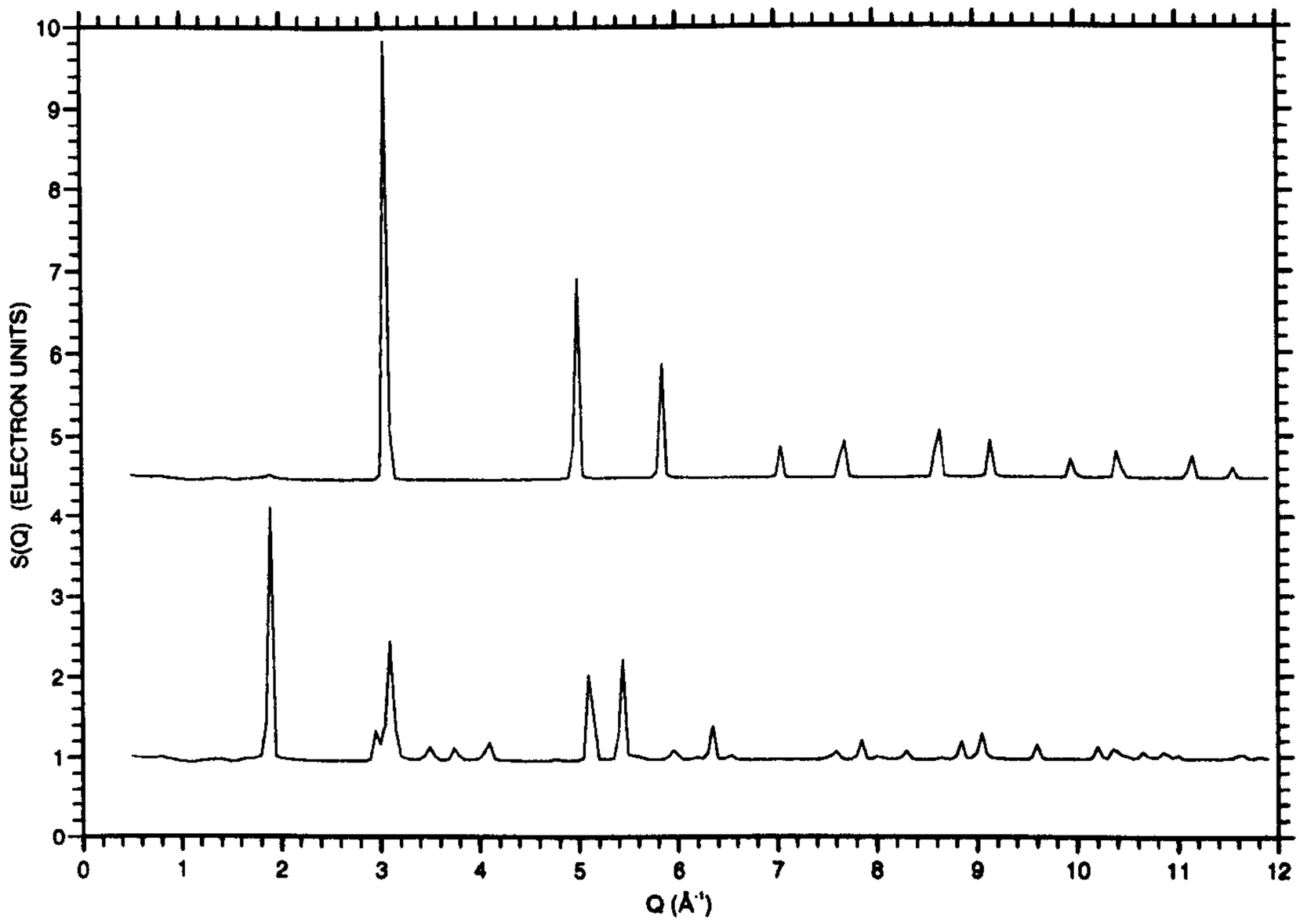

Figure 8.11: Structure factor for graphite (lower curve) and diamond (offset) powder samples as measured on station 9.1 at the Daresbury Laboratory SRS.

It can be seen from Table (8.4) that several of the measured peak positions in $S(Q)_{CC}$ correspond closely with those observed in graphite. As the latter represents a fully sp^2 bonded carbon network this may be taken to indicate the presence of a significant degree of sp^2 bonding within the carbon network of these samples. However some correlations between the structure factor peak positions for the carbon matrix and those for diamond may also be seen. Therefore some degree of sp^3 carbon bonding

Graphite	Diamond	$S(Q)_{CC}$	Glassy Carbon	a-C (evap)	a-C (sputt)	a-C (MSIB)
1.92	-	1.70	1.8	1.0	1.6	-
2.95	-	2.95 (shoulder)	2.98	2.96	2.95	3.0
3.13	3.08	3.15	3.1	-	-	"
5.12	5.03	5.2 (shoulder)	5.11	5.1	-	5.1
5.48	-	5.42	-	-	5.5	-
5.97	5.87	-	5.96	-	-	-
7.87	7.73	-	7.8	-	-	-
8.87/9.08	9.17	8.96	8.8	8.7	8.7	8.7
10.38	10.43	10.49	10.2	10.3	10.5	10.3

Table 8.4: Measured peak positions ($\AA^{-1}$) in the structure factor for graphite, diamond, $S(Q)_{CC}$, glassy carbon [99], evaporated carbon [100], sputtered carbon [5] and mass selected ion beam carbon [32].

within the matrix cannot be ruled out.

Comparing the structure factors for the two crystalline carbon samples shown in Figure (8.11) it can be seen that the graphite powder sample has a measured first diffraction peak at $1.9\AA^{-1}$ whereas the diamond powder sample shows no structure until $3.0\AA^{-1}$. This first diffraction peak for graphite originates from the $3.4\AA$ real space C-C interlayer separation displayed by this material (see Section (2.1.2)). The first peak in the structure factor for the carbon matrix can be seen to occur at $1.7\AA^{-1}$ close to that observed in graphite. However several explanations for the origin of structure in this region are possible. A first sharp diffraction peak occurring between 1 and $2\AA^{-1}$ is a commonly occurring feature in covalently bonded amorphous solids and liquids and has been assigned by Elliot [101] to result from the clustering of small interstitial voids around groups of atoms in such materials. In a material such as a-C:H, network termination by hydrogen must also result in some degree of void formation and therefore may contribute to a diffraction peak in this region. From

the partial structure factor measured for the carbon matrix (Figure (8.10)) it appears that there are two distinct features resulting in structure in this region. The most prominent results in a peak at $1.69\mathring{A}^{-1}$, close to that to be expected for a graphite C-C interlayer separation. The smaller structure at $\sim 1\mathring{A}^{-1}$ (corresponding to a real space correlation length of approximately $6\mathring{A}$) is more suggestive of some internal void structure in the material. If these assignments to the observed features are correct then the measured dominance of the $1.69\mathring{A}^{-1}$ peak is to be expected for such samples which have been deposited at a high impact energy. At such energies a significant degree of preliminary graphite-like structuring of the carbon network would be likely to occur leading to an increase in the intensity of this peak relative to that observed in samples deposited at a lower energy. Further it is reasonable to assume that in samples such as these, having a relatively low hydrogen(deuterium) content, a smaller void fraction would be observed than in those deposited at a lower impact energy and having, therefore, a higher percentage of hydrogen. In the following chapter X-ray scattering data is presented on both these isotopically substituted samples and two further samples deposited at a lower impact energy. These may be used to investigate the variation of this first peak with the hydrogen content of the film and therefore may provide further information on its structural origins.

From the degree of sp^2 bonding observed within the carbon matrix, this phase of a-C:H may be compared to glassy carbon. The latter quasi-amorphous material is known to contain a high degree of sp^2 bonded carbon in the form of convoluted graphitic sheets which are interlinked by sp^3 bonded carbon atoms and displays a first structure factor peak at $1.8\mathring{A}^{-1}$. Both this and the subsequent three higher order structure factor peaks measured for glassy carbon [99] compare well with that for the carbon matrix of this form of a-C:H as shown in Table (8.4). However beyond

$Q =\sim 5.4\mathring{A}^{-1}$ this relationship breaks down somewhat. These two materials do share a particularly low density (c.f. measured glassy carbon density of 1.49gcm^{-3}, these a-C:H(D) samples of 1.1gcm^{-3}, diamond 3.51gcm^{-3} and graphite 2.25gcm^{-3}) which may be related in the case of glassy carbon to its highly porous structure. Thus there are obvious similarities between the carbon matrices in these two materials. However the structure of the carbon atoms within these samples could not be said to reflect directly that of glassy carbon.

Also listed in Table (8.4) is data on evaporated carbon which is known to be trigonally bonded. The structure factor for this material displays much broader peaks [12] than those observed in $S(Q)_{CC}$ and the two materials do not appear similar, although the first structure factor peak for this material at Q=1$\mathring{A}^{-1}$ does correspond to the shoulder observed on that for $S(Q)_{CC}$. Likewise strong correlations between $S(Q)_{CC}$ and mass selected ion beam carbon are not obvious. This is not surprising as the latter represents a highly tetrahedrally bonded carbon network and such a structure would not usually be associated with materials such as these a-C:H(D) samples, deposited in this impact energy range .

What can be seen from Table (8.4) is the close proximity between the structure factor peak positions which occurs for materials known to display very different structural configurations. Therefore it is often more constructive to compare the real space correlation functions for the materials. In the following section the pair distribution function for the carbon matrix of the a-C:H(D) samples is detailed and discussed in the context of other carbon-based materials.

8.2.3 The carbon-carbon partial pair distribution function

Figure (8.12) shows the C-C and C-H partial pair distribution functions obtained by Fourier transformation of the data given in Figure (8.10). From the upper curve it can be seen that the C-C correlation function shows a first neighbour peak at 1.45$\mathring{A}$, close to that observed in graphite at 1.42$\mathring{A}$. However this peak is broad enough to include contributions from diamond-like sp^3, olefinic sp^2 or aromatic sp^2 carbon bonds (at 1.54$\mathring{A}$, 1.34$\mathring{A}$ and 1.39$\mathring{A}$ respectively). Previous studies on a-C:H samples deposited using a fast atom source at an impact energy in the region of 0.5kV have shown two distinguishable contributions to their first C-C peak. These contributions are found to occur at 1.34$\mathring{A}$ and 1.51$\mathring{A}$, indicating the presence of significant olefinic and diamond-like bonding. A single peak only is obvious for these samples deposited at $\sim$ 1kV indicating the movement of both carbon phases to a more graphitic structure with increasing impact energy.

From Figure (8.12) the C-C second neighbour distribution can be seen to peak at 2.47$\mathring{A}$. Combining this with the C-C first neighbour peak position an average bond angle of 117.2° is obtained for this phase of amorphous hydrogenated carbon. This then confirms the presence of a very high degree of sp^2 bonds within the carbon matrix.

C-C-C second neighbour peak position at this point in the pair distribution function and some of the possible options are given in Figure (8.13). As this peak is again broad it could incorporate second neighbour contributions such as those observed in diamond (2.51$\mathring{A}$), graphite (2.45$\mathring{A}$) or benzene (2.42$\mathring{A}$). The latter might be expected to occur on the edge of graphitic areas. Also possible would be a double/single bond combination as observed in the lower energy form of this material. In Table (8.5) the first and second neighbour distances are given for some of the forms of carbon

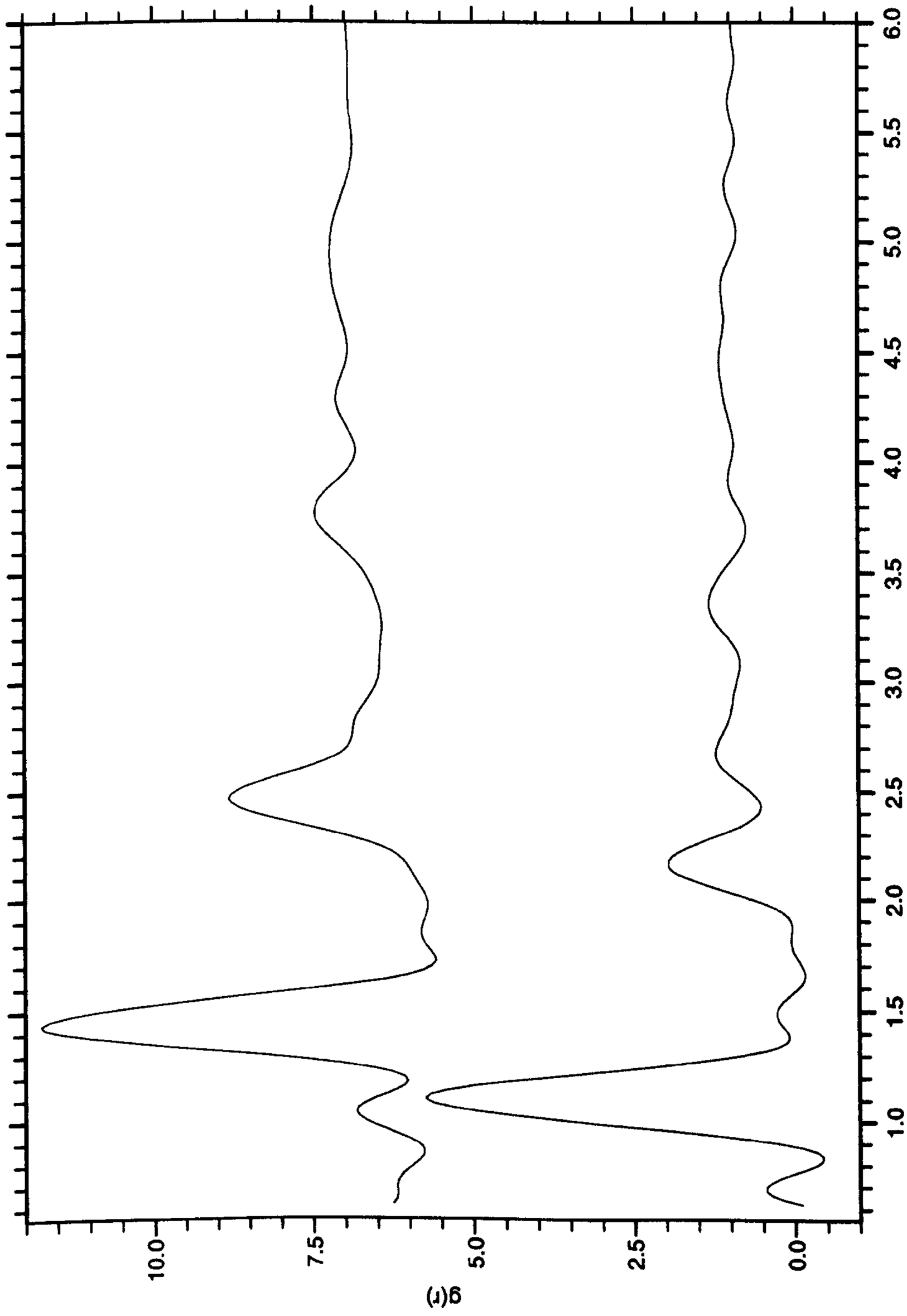

Figure 8.12: Partial pair distribution functions for a-C:H: top $g(r)_{CC}$, bottom $g(r)_{CH}$.

discussed in the previous section. It can be seen from these values that the carbon matrix for these a-C:H(D) samples appears to have a slightly higher sp^3 content than that for glassy or evaporated carbon but far below that of MSIB carbon. Further, from the second neighbour distances given, this material can be seen to show a greater proximity to glassy carbon than evaporated carbon (as indicated by their structure factors). This form of a-C:H(D) can be seen to result in first and second neighbour C-C distances very close to that measured by Li and Lannin [102] for a r.f. sputtered sample of a-C. This sample was measured to have an sp^2 content of between 10% and 20%.

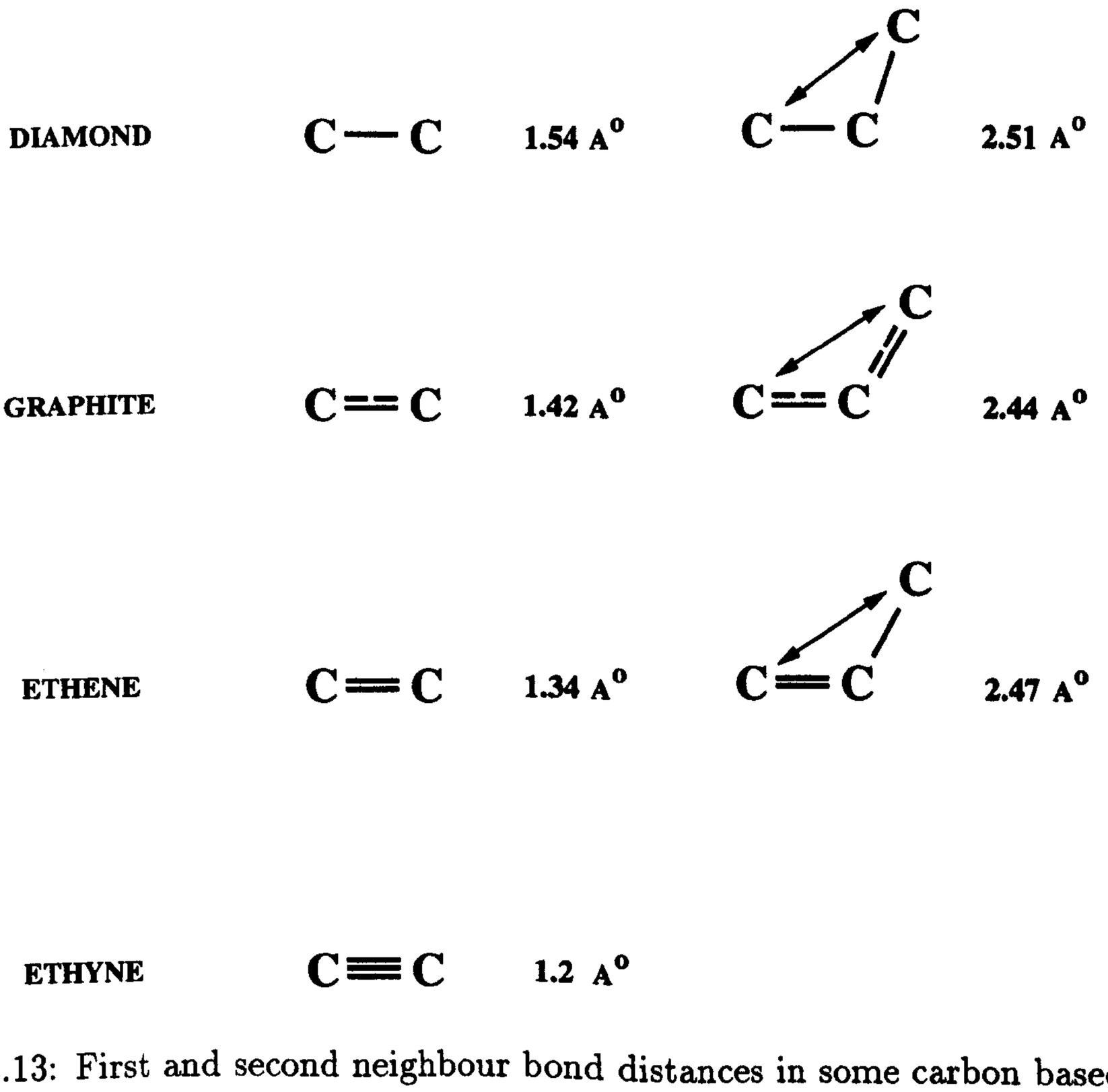

Figure 8.13: First and second neighbour bond distances in some carbon based materials

	r_1 ($\AA^{-1}$)	n_1	r_2 ($\AA^{-1}$)	n_2
Graphite	1.42	3	2.45	6
Diamond	1.54	4	2.51	12
Glassy Carbon [99]	1.425	2.99	2.45	6.1
a-C (evap) [100]	1.43	3.3	2.53	8.8
a-C (sputt) [102]	1.46	3.04	2.47	6.9
a-C (MSIB) [32]	1.534	4.0	2.517	11.47

Table 8.5: First and second neighbour bond distances (r) and coordination numbers (n) for several forms of carbon

From Figure (8.12) a shoulder can seen on the high r side of the second neighbour C-C peak at 2.85$\AA$. This would again be consistent with a C-C=C-C correlation length. Alternatively this could be representative of the cross-ring distance in graphite. The cross-ring distance for benzene would also be expected to occur in this region at 2.79$\AA$. This 2.85$\AA$ peak is noticeably absent in Li and Lannin's sample and this absence was taken by the latter as evidence of lack of graphitic ordering in their sample. A fourth neighbour peak can be clearly observed in $g(r)_{CC}$ at 3.77$\AA$ followed by two smaller peaks at 4.30$\AA$ and 4.96$\AA$. Difficulty again arises in assigning these higher order peaks due to the many different structural configurations which would result in similar interatomic separations. However, from Figure (8.14) it can be seen that each of these correlations is consistent with an intraplanar C-C distance observed in graphite.

What is noticeable about this partial pair distribution function is that the 3.4$\AA$ graphite interlayer distance is not observed. Although there is some evidence in the corresponding partial structure factor for graphite-like layer formation, the absence of this peak would seem to indicate that significant structuring of the carbon into graphite sheets has not occurred. This contrasts with glassy carbon which shows an

interplane correlation length of 5-15$\mathring{A}$ [103] and displays a marked shoulder at this point in its pair distribution function [99]. Recent MAS/NMR studies carried out on similar a-C:H samples, deposited at a lower impact energy, have led to the suggestion of a model for the a-C:H system by Jäger [13] depicting two distinct matrix types: one consisting of chains of alternately doubly and singly bonded carbons and a second of polymeric chains of sp^3 bonded carbons terminated by hydrogen atoms. This contrasts with Robertson's model for a-C:H which involves islands of graphitically bonded carbon interlinked by sp^3 bonded regions within which the hydrogen is incorporated. From the latter model some graphite-like layering of the carbon atoms would be expected to occur even for samples deposited in the medium impact energy range i.e. 500eV. At the higher impact energies associated with these samples any graphitic ordering would be expected to have increased and therefore the lack of distinct layer formation in these samples would seem to indicate that they are representative of a high energy form of a system closer to Jaeger's model. The structural configuration of these a-C:H(D) samples can be further defined through their C-C nearest neighbour coordination number. This is discussed in the following section.

8.2.4 The carbon-carbon radial distribution function

Figure (8.15) gives the radial distribution function for the carbon matrix where J(r) is given by

$$J(r) = 4\pi r^2 \rho(r) g(r) \tag{8.22}$$

and $\rho(r)$ is the sample density. The latter was determined, by a sink float method, to be $1.1 gcm^{-3}$ for these samples.

From the definition of J(r) it can be seen that J(r)dr represents the number of atoms to be found at a distance between r and r+dr from a carbon atom at the origin.

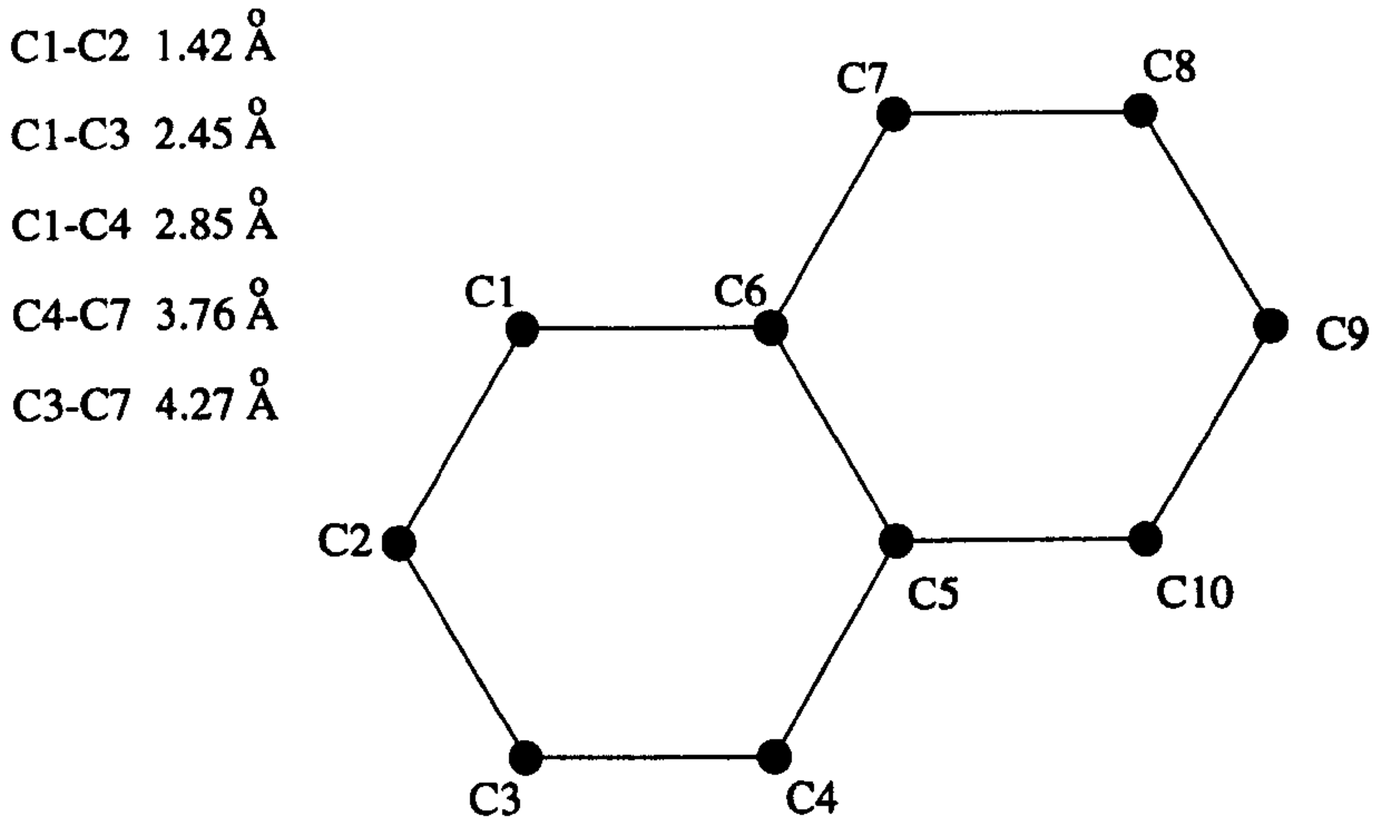

Figure 8.14: Intraplanar C-C distances for graphite.

Thus from the partial radial distribution function given in Figure (8.15) the average coordination number for the carbon matrix can be measured. From the fit to J(r) shown, a carbon first neighbour coordination number of 3 atoms was obtained. As each of the isotopically enriched samples contains 25% ± 1 hydrogen(deuterium), if the assumption is made that all the hydrogen(deuterium) is bonded to the carbon (i.e. that there is no significant proportion of molecular hydrogen in the sample) then the average coordination number for the carbon atoms within these samples would be 3.3 atoms. If it is further assumed that the samples contain only sp^2 and sp^3 bonded carbon, i.e. that the sp^1 contribution is negligible (very little has been found in a-C:H in general), then the fraction of sp^2 bonds within the matrix may be given by

$$\begin{aligned} \text{C-C coord. no.} &= 3sp^2 + 4(1 - sp^2) \\ 3.3 &= 4 - sp^2 \\ sp^2 &= 0.7 \end{aligned} \tag{8.23}$$

This gives an upper limit for the percentage of sp3 hybridised carbon within these samples of 30%. In practice, the presence of molecular hydrogen would result in a

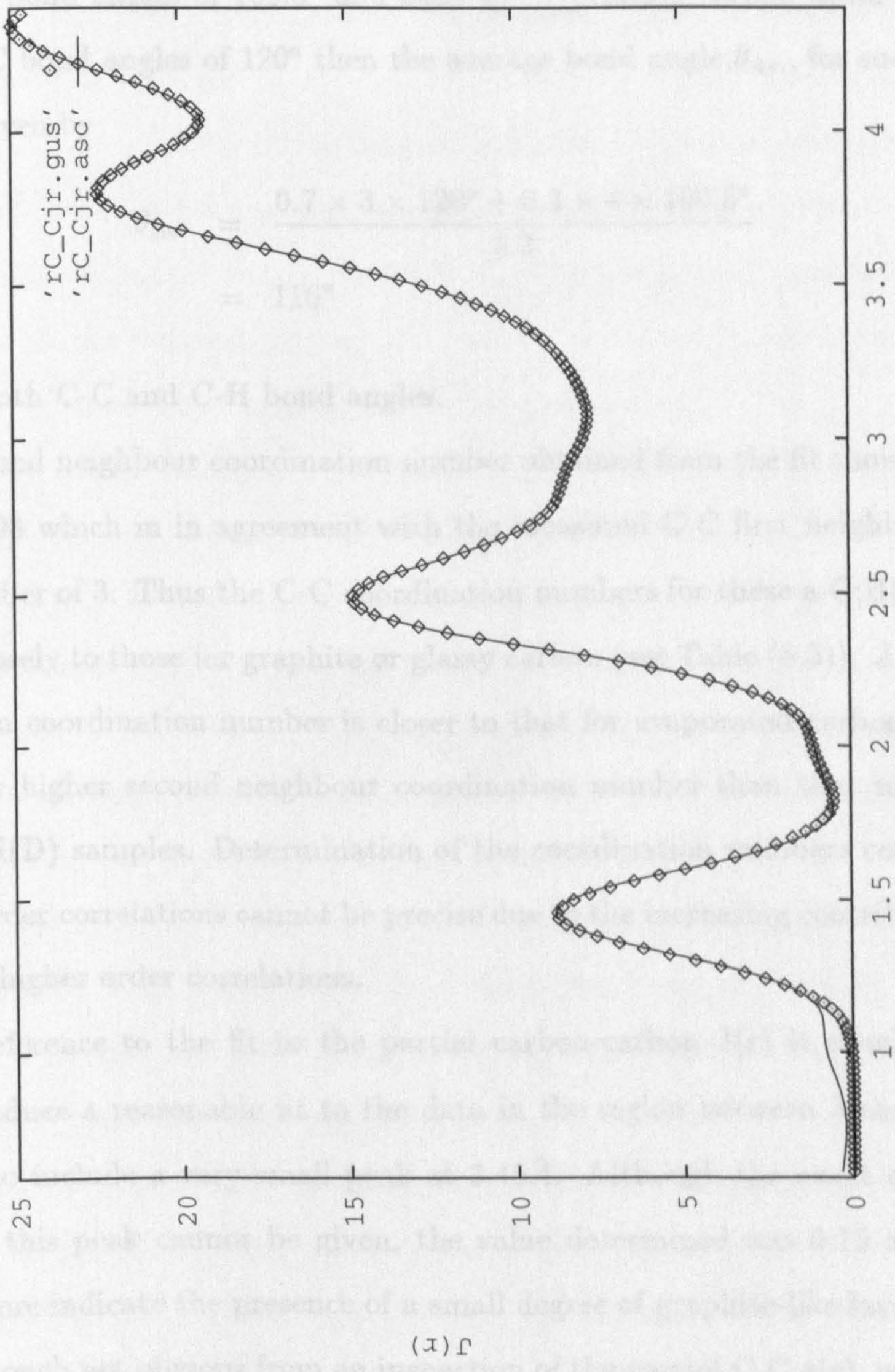

Figure 8.15: Partial carbon-carbon radial distribution function, $J(r)_{CC}$, for the a-C:H(D) samples (solid line data; starred line fit to data).

lower figure for this percentage. If each sp^3 carbon atom within the matrix results in 4 C-C-C bond angles of 109.5° and each sp^2 hybridised carbon atom contributes three C-C-C bond angles of 120° then the average bond angle,$\theta_{Av.}$, for such a system would be given by

$$\begin{aligned} \theta_{Av.} &= \frac{0.7 \times 3 \times 120° + 0.3 \times 4 \times 109.5°}{3.3} \\ &= 116° \end{aligned} \tag{8.24}$$

including both C-C and C-H bond angles.

The second neighbour coordination number obtained from the fit shown in Figure (8.15) is 5.98 which in in agreement with the measured C-C first neighbour coordination number of 3. Thus the C-C coordination numbers for these a-C:H(D) samples compare closely to those for graphite or glassy carbon (see Table (8.5)). Although the total carbon coordination number is closer to that for evaporated carbon, the latter shows a far higher second neighbour coordination number than that measured for these a-C:H(D) samples. Determination of the coordination numbers corresponding to higher order correlations cannot be precise due to the increasing contributions from other, still higher order correlations.

With reference to the fit to the partial carbon-carbon J(r) it should be noted that to produce a reasonable fit to the data in the region between 3 and 4$\mathring{A}$ it was necessary to include a very small peak at 3.45$\mathring{A}$. Although the exact coordination number of this peak cannot be given, the value determined was 0.75 atoms. This may therefore indicate the presence of a small degree of graphite-like layer formation which, although not obvious from an inspection of the partial C-C g(r), was indicated in the C-C partial structure factor. However it is possible that this feature results simply from termination errors in the transformation process.

8.2.5 The carbon-hydrogen partial structure factor

The hydrogen atoms within the carbon matrix of the isotopically substituted samples may be bonded to sp^3, sp^2 or sp^1 hybridised carbon atoms or they may even be present in the form of molecular hydrogen. Inelastic neutron scattering studies have shown evidence for such molecular hydrogen in a-C:H samples deposited in a fast atom source at an impact energy of 500eV [5]. The evidence for any such hydrogen environment in the samples studied here will be discussed in the following section detailing the measured hydrogen-hydrogen correlations.

The centre profile of Figure (8.10) shows the partial carbon-hydrogen structure factor, $S(Q)_{CH}$, for the a-C:H(D) samples. Two peaks can be clearly seen in $S(Q)_{CH}$ at Q=1.75$\AA^{-1}$ and 3.0$\AA^{-1}$ with broader features out at $\sim 6\AA^{-1}$, 9.7$\AA^{-1}$ and 12$\AA^{-1}$. It can be seen from Figure (8.10) that these first two peaks in $S(Q)_{CH}$ occur in close proximity to those for $S(Q)_{CC}$. The data in Figure (8.10) therefore illustrates the difficulty in assigning the partial scattering contributions to the data when only total scattering profiles are available for samples such as these.

Comparison of the total structure factors for the a-C:H(D) samples had indicated the presence of a C-H correlation peak at Q=$\sim$ 3$\AA^{-1}$ and this can be clearly seen in $S(Q)_{CH}$. This data also gives direct evidence for the existence of C-H correlations at Q=$\sim$ 10$\AA^{-1}$ which had been suggested by previous studies on diamond-like a-C:H samples [104]. The data in Figure (8.12) also shows the C-H structural configuration to be more broadly distributed, the structure for the carbon matrix being defined by a sharper structure factor function. This may be the result of the increased level of freedom of the hydrogen atoms as network terminators.

Bond	Configuration	Bond length ($\AA$) [105]
Csp^3-H	C-C-H_3	1.06
	C_2-C-H_2	1.09
	C_3-C-H	1.10
Csp^2-H	C-C=C-H	1.08
C*ar*-H	C*ar*-H	1.08

Table 8.6: C-H bond lengths for various configurations

8.2.6 The carbon-hydrogen partial pair distribution function

Figure (8.12) shows the partial C-H distribution function, $g(r)_{CH}$ derived from $S(Q)_{CH}$. A C-H first neighbour peak is clearly visible in this function at $1.1\AA$ as well as a significant contribution at $2.18\AA$ corresponding to the shoulder observed in the total pair distribution function for the fully deuterated sample. Higher order peaks can also be observed at $2.7\AA$ and $3.4\AA$.

Table (8.6) gives the C-H bond distances associated with possible different hybridisation states of the carbon atom. The measured first peak position in $g(r)_{CH}$ at $1.12\AA$ can be seen to lie closest to that for a CH or CH_2 group having the hydrogen atom bonded to an sp^3 hybridised carbon atom. The slightly higher bond length than those given in Table (8.6) may result from some small residual inelasticity effects. Taking the first and second C-H neighbour distances from $g(r)_{CH}$ and assuming the hydrogen to be bonded to an sp^3 hybridised carbon, an average C-C-H bond angle of 109.1° is obtained which is very close to that expected for a hydrogen atom bonded to a tetrahedrally coordinated carbon atom.

The coordination numbers corresponding to the first few peaks in $g(r)_{CH}$ have been determined from the corresponding radial distribution function, $J(r)_{CH}$, given

in (8.16) and are listed in Table (8.7). It can be seen from Table (8.7) that the C-H first coordination number is 1.77 atoms indicating the presence of a large number of CH_2 and/or CH_3 groups within the samples. If the presence of CH_3 groups is neglected this would infer a 3:1 ratio of CH_2:CH groups which is surprisingly high for materials having a relatively small atomic percentage of hydrogen. Previous infrared absorption studies on a-C:H samples deposited in a fast atom source at 500eV have indicated a ratio of CH_2:CH groups in the region of 1.1:1 with little evidence of CH_3 [5]. An anomalous rise in the CH_2 percentage was observed for the lowest hydrogen content film (29%) in this study. This was combined with a drop in the sample density to 1.98 g/cm^{-3}. The samples studied here also have a very low measured density at $\sim$1.5g/cm^{-3}. Preliminary NMR studies on this phase of a-C:H have indicated the presence a significant number of CH_3 groups. $CH_{2,3}$ groups forming natural voids within the material may therefore contribute to the unexpectedly low measured density for these samples. Further infra red studies of the material are suggested to confirm the CH_3 presence indicated in the NMR measurements.

This work on hard a-C:H samples also showed the hydrogen to be predominantly bonded to sp^3 hybridised carbon atoms which is in agreement with Robertson's model in which the hydrogen is seen to stabilise the sp^3 bonded network. Jaeger's model for a-C:H, based on the study of the latter material has been previously described (namely, two matrices: one consisting of chains of alternately doubly and singly bonded carbons and a second of sp^3 bonded carbons terminated by hydrogen atoms). If the materials studied here represent a higher energy form of Jaeger's material it is reasonable to assume that the olefinically bonded regions would move towards a graphitic structure more readily. Thus the materials here may represent a system with a predominant graphite-like phase interspersed by a much smaller sp^3 region within

Bond	First Neighbour Distance ($\mathring{A}$)	Coord. No.	Second Neighbour Distance ($\mathring{A}$)	Coord. No.
C-C	1.45	3.00	2.48	5.98
C-H	1.13	1.77	2.18	2.63

Table 8.7: Measured partial coordination numbers for a-C:H samples

which the hydrogen is incorporated. This would therefore be akin to Robertson's model for much lower energy diamond-like carbon phases.

8.2.7 The hydrogen-hydrogen partial structure factor

The upper profile in Figure (8.10) shows the partial H-H structure factor, $S(Q)_{HH}$, measured for the isotopically substituted samples. Very little structure can be seen in this profile beyond a negative spike at $1.75\mathring{A}^{-1}$. Significant correlations in this function would be surprising as the hydrogen atoms within the system act as network terminators dispersed in a carbon dominated matrix where they may have a large degree of freedom in their orientational distribution. However the significant proportion of CH_2 and CH_3 groups indicated to be present in the matrix from the C-H partial radial distribution function would suggest that some short range correlations should be observable. Figure (8.17) shows the partial H-H pair distribution function, $G(R)_{hH}$, obtained by Fourier transform of $S(Q)_{HH}$. This function can be seen to be very noisy. However two features are noticeable. Firstly a shoulder can be observed in the data at $\sim 0.8\mathring{A}$ close to that expected for molecular hydrogen at $0.75\mathring{A}$. Although the region below $1\mathring{A}$ is less reliable due to termination errors in the transformation process, this feature is not obvious in either the C-C or the C-H partial structure factors. As previously stated, inelastic neutron scattering data collected on similar

for, although such effects would be expected to be minimal. Similarly dead time and multiple scattering effects should be negligible. Multiple refraction effects due to the incident and scattered beam passing through not only the surface of the film but also the surface film/substrate interface should also be considered and accounted for.

7.4 Conclusions

Grazing angle X-ray diffraction has been carried out on a series of carbon based thin films mounted on crystalline substrates and has shown that depth profiling of the sample/substrate system can be achieved. Two thin Films of amorphous hydrogenated carbon have been studied and preliminary results for the experimental technique appear encouraging, showing that scattering profiles for these low Z, amorphous systems can be obtained from films of only 1μm thickness. However a more rigorous examination of the data collected and the correction procedures required is necessary before conclusive results can be drawn from the data.

Suggested further work would involve the production of a series of a-C:H thin films in the energy range of 100eV to 1.5keV. Grazing angle X-ray diffraction could be used to study the structural variation in the thin films as a function of the incident energy of the impacting particles.

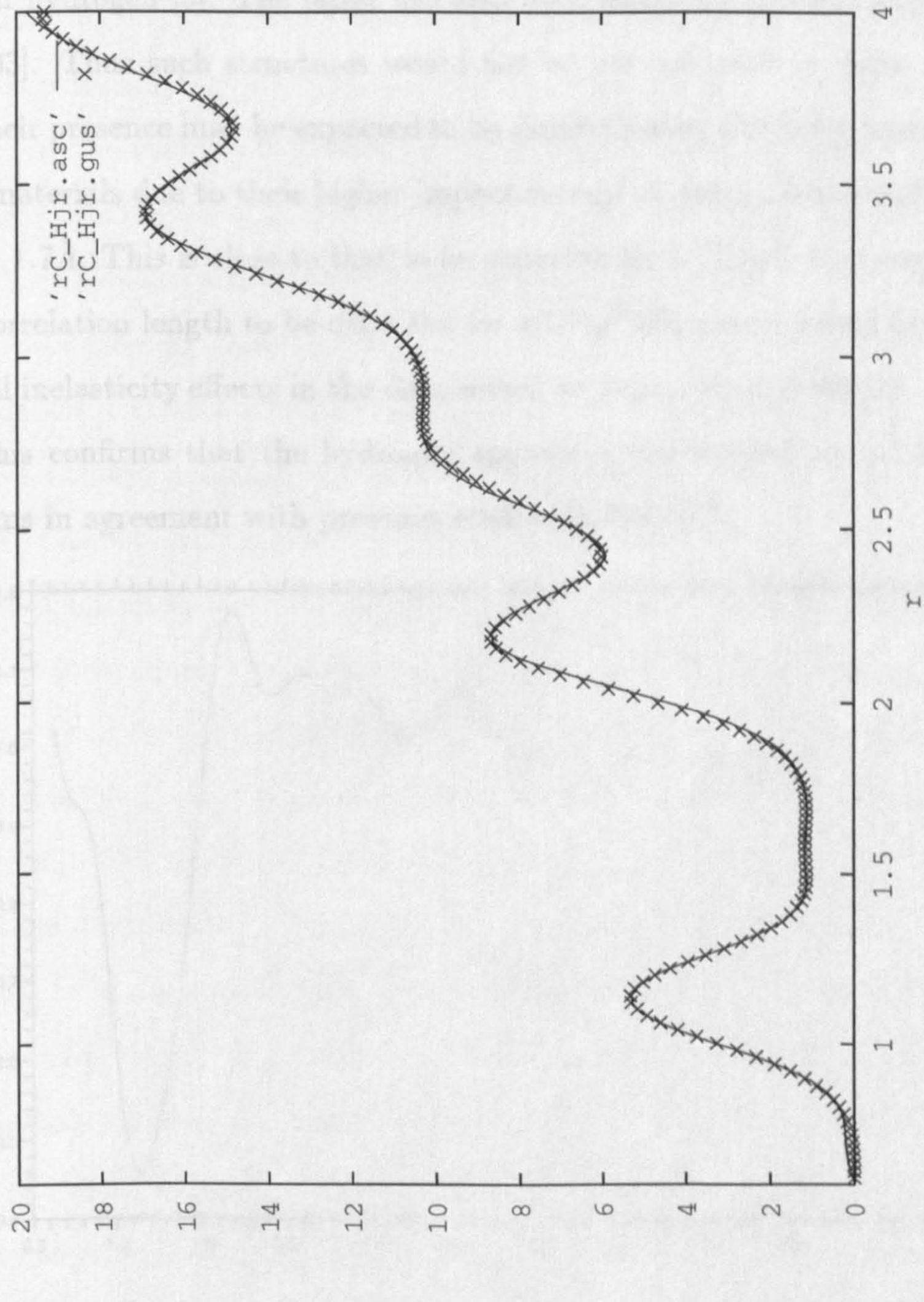

Figure 8.16: Partial carbon-hydrogen radial distribution function for the a-C:H(D) samples (solid line data; starred line fit to data).

samples deposited at a lower impact energy has provided evidence for the presence of molecular hydrogen [5]. The latter has also been indicated in some MSIB carbon samples [103]. Thus such structures would not be unreasonable in these materials, although their presence may be expected to be diminished by the lower hydrogen content these materials due to their higher impact energy. A second feature of $g(r)_{HH}$ is the peak at $1.7\mathring{A}$. This is close to that to be expected for a $C(sp^3)$-H_2 group at $1.8\mathring{A}$. The H-H correlation length to be expected for a $C(sp^2)$-H_2 group would be $1.9\mathring{A}$. As any residual inelasticity effects in the data would be expected to lower this measured distance, this confirms that the hydrogen appears to be bonded to sp^3 hybridised carbon atoms in agreement with previous studies [5,106,107].

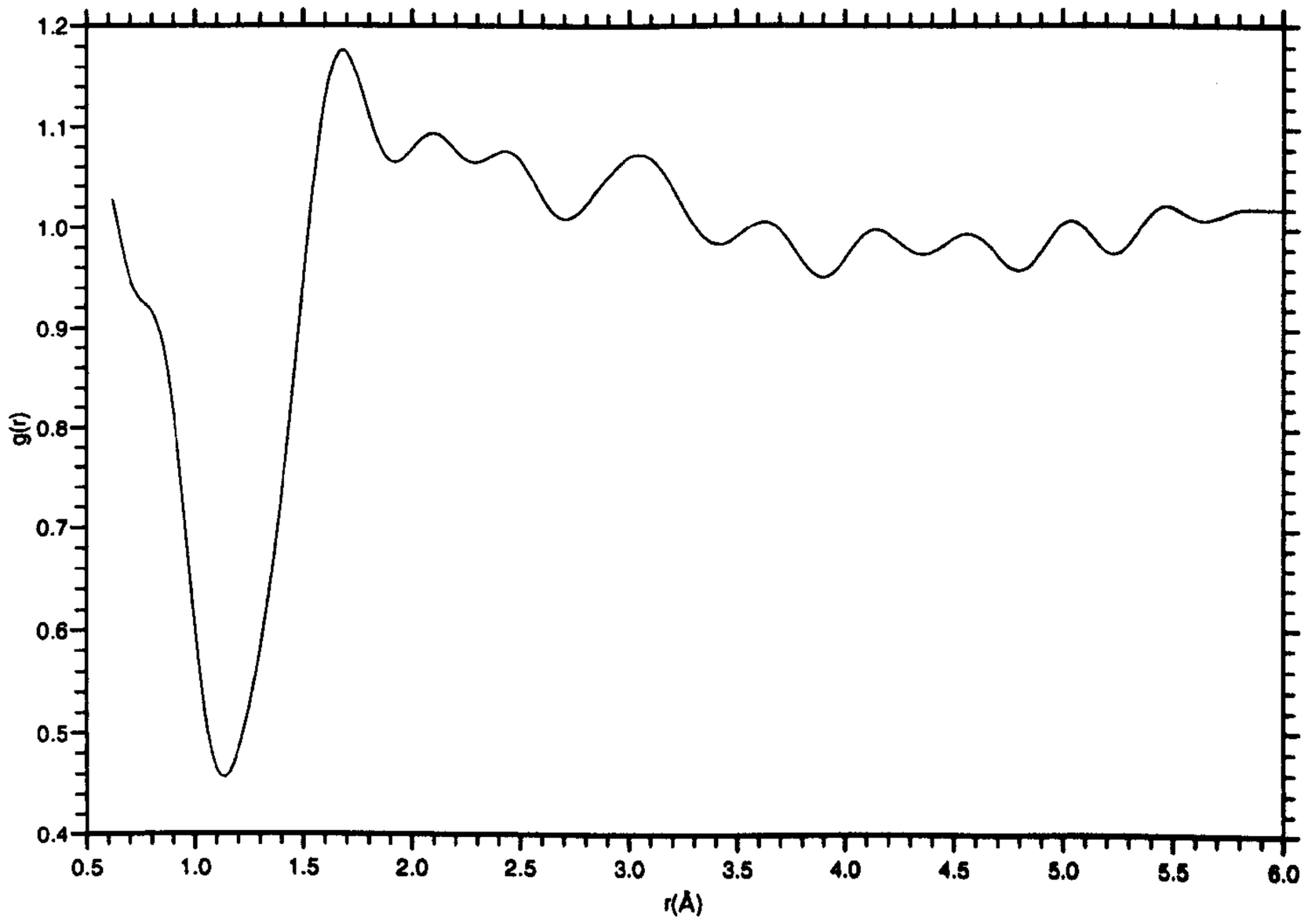

Figure 8.17: Partial pair distribution function for hydrogen, $g(r)_{HH}$.

8.2.8 Conclusions

Neutron scattering data has been collected on three samples of amorphous hydrogenated carbon having varying degrees of isotopic enrichment. This data has shown the structure of the samples to correspond, proving the use of a fast atom source for the production of such materials having a finely tuned degree of isotopic substitution. Furthermore, one of the samples has been shown to represent closely a sample with zero hydrogen scattering cross-section. This is the first sample of a-C:H of its kind and has allowed direct access to the scattering function for the carbon matrix. These samples have allowed a unique definition of the structural origin of the individual components of the neutron scattering profile for this material. Partial structure factors have been obtained for the C-C, C-H and H-H correlations within the sample matrix. These have shown the carbon matrix to be predominantly trigonally bonded with an upper limit for the percentage of sp^3 hybridised carbon atoms within the carbon matrix of 30%. The sp^2 bonded carbons have been shown to display a significant degree of graphite-like interlayer hexagonal structure. However intralayer correlations are still weaker than those observed in glassy carbon (intralayer correlation length 5-15$\AA$). This is in agreement with previous studies of a-C:H which have shown a transition towards a more structured graphite-like atomic arrangement for materials such as these deposited at an impact energy of ~1kV. The partial C-H correlations have revealed the hydrogen to be predominantly bonded to sp^3 hybridised atoms as suggested by most current models of this material. These have also revealed a surprisingly high degree of $CH_{2,3}$ bonds within the hydrogenated carbon matrix. It is suggested that further inelastic neutron scattering and/or infra-red studies be carried out on these samples to verify this ratio. Such a high degree of $CH_{2,3}$ bonds has been suggested to contribute to the measured density for these materials lying below

that to be expected for such low hydrogen content samples. The degree and form of any void structure within these materials could also be usefully investigated using small angle X-ray scattering techniques. The H-H partial structure factor has shown direct evidence for the presence of a small degree of molecular hydrogen trapped within the void structure of the material. This is in agreement with previous studies on diamond-like a-C:H samples deposited at a lower impact energy [5]. This partial structure factor has also shown contributions from the H_2 groups bonded to the carbon atoms that were observed in the C-H partial pair distribution function. The use of the SANDALS diffractometer at the Rutherford Appleton Laboratory has been shown to minimise the inelasticity effects within the measured neutron scattering profiles. This has therefore overcome a particular problem of accessing the structure factor for such materials through elastic neutron scattering techniques. The minimisation of such effects gives further clarification to the validity of the measured C-H and H-H partial correlation functions.

Determination of the partial radial distribution functions for this material has allowed a direct measurement of the C-C and C-H first and second neighbour coordination numbers. These have been shown to be 3 and 1.77 atoms respectively. It is suggested that further work be carried out on the deposition of similar isotopically substituted samples deposited using a fast atom source for a deposition energy in the range $\sim$ 500eV. In this way direct investigation of the carbon and hydrogen matrix of the so-called "diamond-like" a-C:H structure may be investigated.

Chapter 9

X-ray Scattering Results for a-C:H(D)

9.1 Introduction

Amorphous hydrogenated carbon has a vast number of potential applications as detailed in Chapter (2). However to exploit these possibilities fully [4], [108] a deeper understanding of the atomic level structure of this material is required. Moreover, questions still remain with regard to the relationship between sample composition, deposition parameters and structural configuration. In the following chapter results are presented of an X-ray study of five a-C:H(D) samples. These samples were deposited in a fast atom source at a deposition energy ranging from 500eV to 1.2keV from one of three hydrocarbon precursor gases. As such they may be used to investigate the interaction between a number of different sample specifications and the resultant structural configuration.

The X-ray data presented in this chapter was collected on station 9.1 at the Daresbury Laboratory SRS. In Chapter (5) details were given of the analysis procedures required to extract the structurally sensitive information from the experimentally measured X-ray scattering profiles. In the following sections the structural information obtained is detailed and discussed.

Three of the five samples studied here correspond to the isotopically substituted samples investigated in Chapter (8) using neutron scattering techniques. Thus the X-ray scattering results obtained may be contrasted with this complementary data to provide a broader picture of this material.

9.2 Isotopically substituted samples

In Chapter (8) results from a neutron scattering study carried out on the three isotopically substituted samples a-$C_{0.75}$:$H_{0.25}$, a-$C_{0.74}$:$H_{0.17}$:$D_{0.09}$ and a-C:$_{0.73}$:$D_{0.27}$ were presented. This work allowed information to be gained on the atomic level structural configuration of this phase of a-C:H. These results revealed the carbon within this material to be predominantly sp^2 bonded with an average C-C nearest neighbour coordination number of 3.0 atoms. The hydrogen atoms were found to be predominantly bonded to the carbon atoms with the ratio of CH_2 to CH groups being 3:1. Evidence of a trace of molecularly bonded hydrogen was also found. X-ray scattering measurements have also been carried out on these three samples to provide complementary information on the structure of this material.

As X-rays scatter from the electrons in an atom, the profiles collected at the Daresbury Laboratory SRS for these three samples are dominated by scattering from the carbon matrix. In addition, as by definition the isotopically substituted samples should provide the same electron profile to the incoming beam, the scattering profiles

for each of the three should correspond.

As the carbon and hydrogen elements contain only six and one electrons per atom respectively, the X-ray scattering cross-section for this material is expected to be low. Further, a dramatic fall in this cross-section occurs with scattering angle (or wavevector transfer vector Q). Thus a synchrotron source was chosen for these experiments to provide an intense incident X-ray beam and thus enhance the intensity of the scattered beam. A second advantage of the synchrotron source chosen for these experiments is the high incident beam intensity available in the region below $1\mathring{A}$ allowing scattering data to be collected out to Q=$\sim 18\mathring{A}^{-1}$. Although this does not compete with that available on a pulsed neutron source such as ISIS, over the Q range available X-rays have the advantage that they do not suffer from the troublesome inelasticity effects encountered in corresponding neutron scattering measurements.

9.2.1 Data reduction

In Chapter (5) the X-ray scattering methods carried out on these samples are described. Two techniques were used: standard transmission ($\theta : 2\theta$) X-ray scattering was used to measure the total scattering profiles for each sample and the Warren-Mavel fluorescence detection technique was used to measure the coherent scattering profiles only. Following the data reduction process detailed in Chapter (5), the sample scattering profiles were first corrected for sample independent effects namely: detector dead time, scattering volume, the polarization factor and the variation of the incoming beam intensity with time. As previously stated, a synchrotron source was chosen for these experiments so as to overcome the particularly difficult scattering intensity problem that would have been experience with a laboratory source for such low Z amorphous materials. Further, as the Warren-Mavel technique also results in

a relatively weak scattered beam intensity the need for such a source becomes more important still. The use of such a source proved highly successful in this case and statistically good scattering profiles were collected for each of the samples in a total data collection time of $\sim$ 2 hours for the standard transmission data and $\sim$ 6 hours for the Warren-Mavel data. In fact the synchrotron beam intensity obtained on station 9.1 was such that for one sample the intensity of the scattered beam at low 2θ was too high to allow dead time corrections to retrieve the original form of the data at the detector. The scattering data on this sample was collected early on in the beam life time where the intensity is at its maximum.

Having carried out the sample independent corrections, the standard transmission data was scaled to the level of the Warren-Mavel data to allow the difference profile for the two to be obtained. The scaling factor used was chosen such that the latter displayed a minimum of residual structure from the two scattering profiles and tended to zero at $2\theta = 0$. The Warren-Mavel and scaled transmission data for the a-$C_{0.74}$:$H_{0.17}$:$D_{0.09}$ sample were shown in Chapter (5), Section (5.4.6). Also shown (Figure (5.17)) was the difference profile obtained for this sample. This profile should represent the form of the incoherent scattering for this material. It may also contain contributions from the diffraction pattern of the Mo foil used as a filter (as detailed in Section (5.4.6)). However no such contributions are obvious in the difference profile. What is noticeable about the form of this profile is the fall off in the data above $2\theta =\sim 70°$ as theoretical Compton profiles would predict a rise to a plateau [68]. However this fall-off may be present due to the fact that the profile has not been corrected for absorption effects. As the spread in the wavelength of the Compton component of the scattering profile would be expected to extend to longer wavelengths with increasing 2θ and absorption in the sample also increases

with wavelength, this effect would be expected to cause some fall-off in the data at higher scattering angles.

Once the Compton scattering profile has been obtained from the collected data, this profile can be removed from the standard transmission data to yield a statistically improved form of the Warren-Mavel data. In practice a fit is made to the measured Compton profile and it is this that is removed from the standard data (see Section (5.4.6)). In this way combined noise from the standard transmission and the Warren-Mavel profiles is not introduced to the Compton subtracted profile. As previously detailed in Chapter (5), Warren and Mavel estimated that they removed only 90% of the incoherent scattering from their data by using the fluorescence method. Previous workers using this technique [109] have measured both the standard transmission and the Warren-Mavel diffraction profile so that the Compton profiles obtained can be used to remove any further incoherent scattering from the Warren-Mavel scattering profiles. To investigate whether any further incoherent scattering needs to be removed from the Warren-Mavel data, the latter is scaled to the theoretical self-scattering curve for the material as the coherent data should oscillate about this curve. If it does not, further incoherent scattering can be removed from the Warren-Mavel profile. For the case of the isotopically substituted samples studied here, the Warren-Mavel or Compton subtracted standard transmission data were found to oscillate very well about the theoretical self-scattering curve. Therefore no further incoherent scattering was removed from the data. The reduction in the incoherent scattering contribution to the Warren-Mavel data collected in this work results from the excellent control over the incident wavelength possible at the Daresbury Laboratory SRS. A wavelength of $0.6185\mathring{A}$ was set at the monochromator, just $0.015\mathring{A}$ below the K_α edge of the Mo foil filter. Warren and Mavel were limited in their work to the available laboratory

source wavelength of 0.615$\AA$ i.e. 0.05$\AA$ below the K_α edge of the Mo foil also used in their work.

The coherent and self-scattering profiles for the fully hydrogenated and the "null mixture" sample are given in Figures (9.2) and (9.1) respectively. The data for the fully hydrogenated sample can be seen to be the noisier of the two. This is because only the Warren-Mavel data was available for this sample. For the "null mixture" sample the Compton subtracted standard transmission data was used to represent the coherent scattering profile.

Scaling of the coherent scattering profile to the self-scattering curve also serves to convert the former to electron units. Once this scaling procedure has been carried out, the self-scattering contribution is removed from the coherent scattering profile and the average scattering factor for the sample divided out so as to give the structure factor S(Q). For a material containing M atomic species with the atomic concentration of species i denoted by x_i and it's scattering factor by f_i, S(Q) is then defined as follows

$$S(Q) = \frac{1}{(\sum_{i=1}^{M} x_i f_i(Q))^2}[x_i^2 f_i^2(Q)S(Q)_{ii} + x_j^2 f_j^2(Q)S(Q)_{jj} + x_i f_i(Q) x_j f_j(Q) S(Q)_{ij}] \quad (9.1)$$

It can be seen from Equation (9.1) that, in contrast to the corresponding neutron scattering structure factor (Equation (8.6)), the scattering factor for each of the elements is Q dependent. The structure factor obtained for each of the three isotopically substituted samples is discussed in the following section.

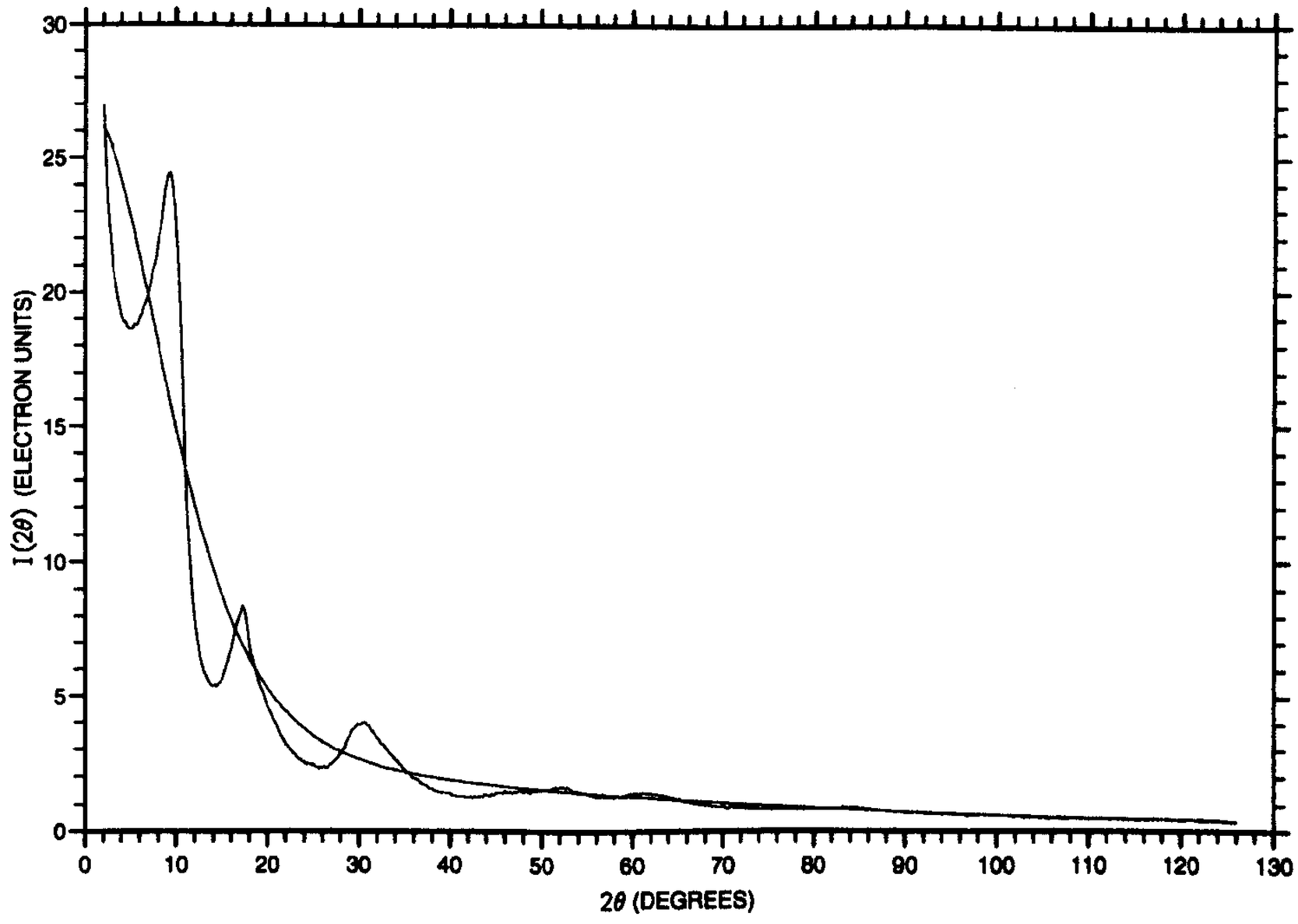

Figure 9.1: Coherent and self-scattering curves for sample a-$C_{0.74}$:$H_{0.17}$:$D_{0.09}$.

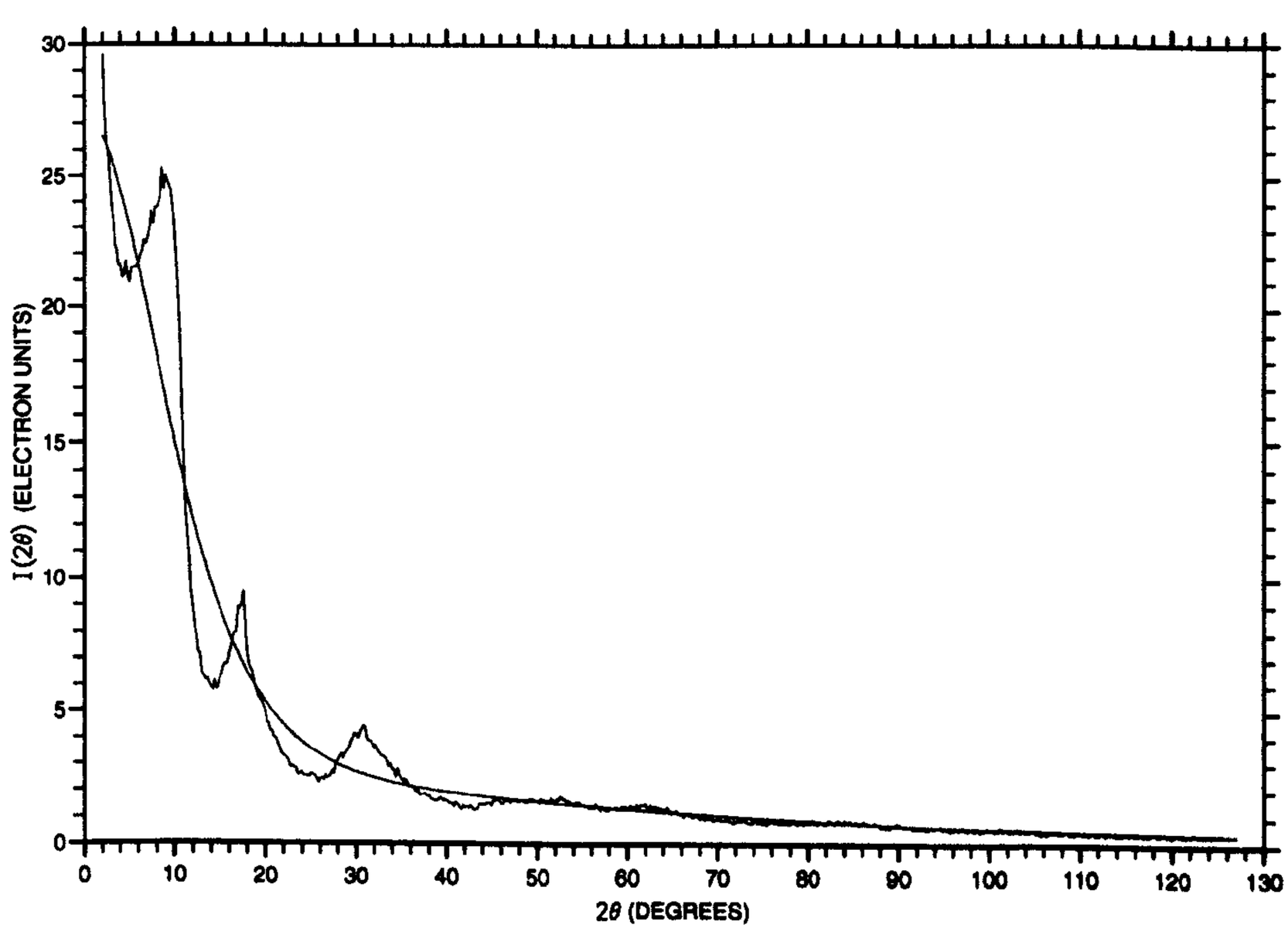

Figure 9.2: Coherent and self-scattering curves for sample a-$C_{0.75}$:$H_{0.25}$.

9.2.2 The X-ray total structure factor for the a-C:H(D) samples

As previously discussed the total X-ray structure factor for each of the isotopically substituted samples would be expected to be identical. In Figure (9.3) the measured S(Q) for each of these samples is given. It can be seen from this data that there appears to be some difference in the form of the first diffraction peak for the fully deuterated sample. For this sample the peak is seen to be broader and less sharp than that observed for the fully hydrogenated or the "null mixture" sample. Such a noticeable contrast in form was not obvious in the corresponding neutron diffraction data collected on these samples. However in the latter case the measured total S(Q) contains significant contributions from C-H and H-H correlation in this region. In the X-ray scattering experiments these contributions are relatively weak. The fully deuterated sample is one of the two isotopically substituted samples deposited at the slightly lower impact energy of 1.1keV. It also has the lowest carbon content of the three. Although the variation over the three samples is only small at 2 atomic percent this would nevertheless indicate that, of the three, this sample would have had the lowest effective impact energy. The impact energy region within which these samples were deposited lies on the transitional border between the diamond-like carbons and a more structured graphitic phase (as shown by the neutron scattering data). It therefore would not be surprising if the structure of the materials deposited in this region were highly sensitive to the impact energy chosen. The fast atom source from which these samples were deposited had a tendency to drift slightly downwards in voltage setting over time. This was accounted for by a manual adjustment of the voltage parameters. The suggested lower impact energy for the deuterated sample may therefore be a consequence of this.

As previously discussed in Chapter (8) this Q region may provide information on the medium range order within the samples. In particular the form of the first diffraction peak may indicate the degree of porosity or graphite-like layer formation within the sample. In both the fully hydrogenated and the "null mixture" sample the first structure factor peak in Figure (9.3) is found to occur at $1.7\mathring{A}^{-1}$. This corresponds to that for the first diffraction peak in the C-C partial structure factor measured using neutron diffraction techniques on these samples. It also lies quite close to that for the interlayer graphite peak at $1.92\mathring{A}^{-1}$. For the fully deuterated sample this peak occurs at $1.6\mathring{A}^{-1}$ and may indicate the beginning of a movement towards a more porous structure. This would be difficult to assign for such a small change in hydrogen content and impact energy. In the second half of this chapter data is presented for samples containing up to 35 % hydrogen, deposited at an impact energy of $\sim$ 500eV. By comparison with this data the possible structural changes indicated by the form of the diffraction data in this region may be investigated.

Beyond the first diffraction peak, the three structure factors in Figure (9.3) can be seen to be very similar indicating that the short range structural order is the same for each of the samples.

The use of X-ray scattering techniques has provided further information on these samples to complement that already obtained by neutron diffraction. It is also useful to directly compare the data collected by each technique. Such a comparison is carried out in the following section.

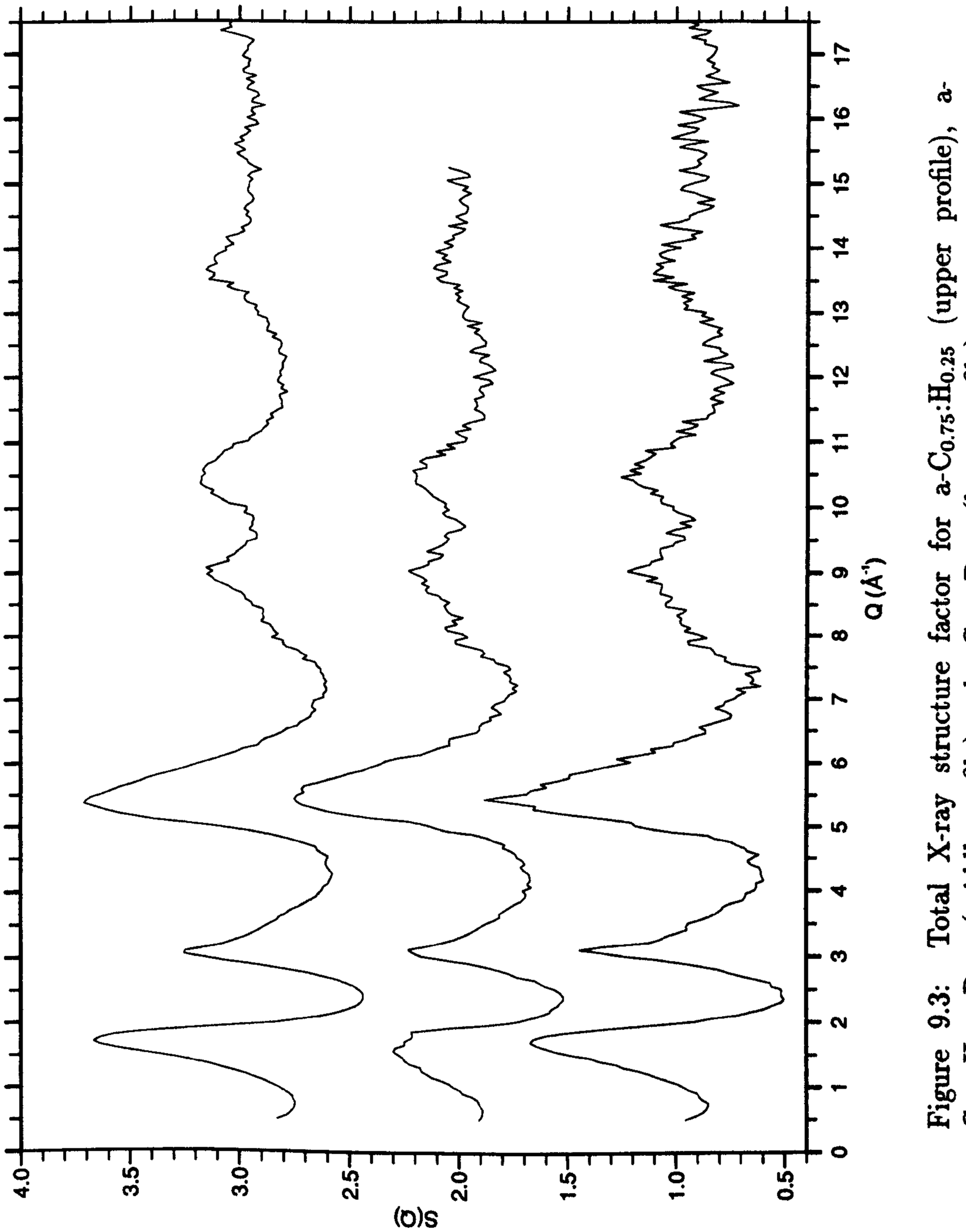

Figure 9.3: Total X-ray structure factor for a-$C_{0.75}$:$H_{0.25}$ (upper profile), a-$C_{0.74}$:$H_{0.17}$:$D_{0.09}$ (middle profile) and a-$C_{0.73}$:$D_{0.27}$ (lower profile).

9.2.3 Comparison between X-ray and neutron structure factors

The X-ray weighting factors for the partial structure factors which contribute to the data in Figure (9.3) are given in Equation (9.1). Unlike the corresponding neutron weighting factors these vary with Q. Theoretical X-ray scattering factor curves are available for carbon and hydrogen as detailed in Section (5.5). These may be used to determine the weighting factors for the C-C, C-H and H-H contributions to the X-ray structure factors as a function of Q. In Figure (9.4) the variation of the weighting factors for each of the three components is given for the "null mixture" sample, a-$C_{0.74}H_{0.17}$:$D_{0.09}$. These were determined using Stewart, Davidson and Simpson's analytical approximation as detailed in Section (5.5). It can be seen from Figure (9.4) that, as expected, the C-C correlations dominate the structure factor. However contributions from the C-H partial structure factor should be visible below Q=$\sim 6\mathring{A}^{-1}$. It would not be expected to see H-H correlations.

A direct comparison of the X-ray data collected on these samples with that collected using corresponding neutron techniques can be made by weighting the partial structure factors obtained by the latter with the X-ray weighting factors given in Figure (9.4). In this way the accuracy of these neutron partial structure factors can be examined. Figures (9.5),(9.6) and (9.7) each show a plot of the X-ray structure factor and the neutron partial structure factors weighted with the relevant theoretical X-ray scattering factors for the fully hydrogenated, "null mixture" and fully deuterated samples respectively.

From Figure (9.5) it can be seen that the structure factor peak positions for the X-ray and neutron scattering data correspond very well. A small scale factor difference occurs between the peak amplitudes measured by the two techniques. In each case

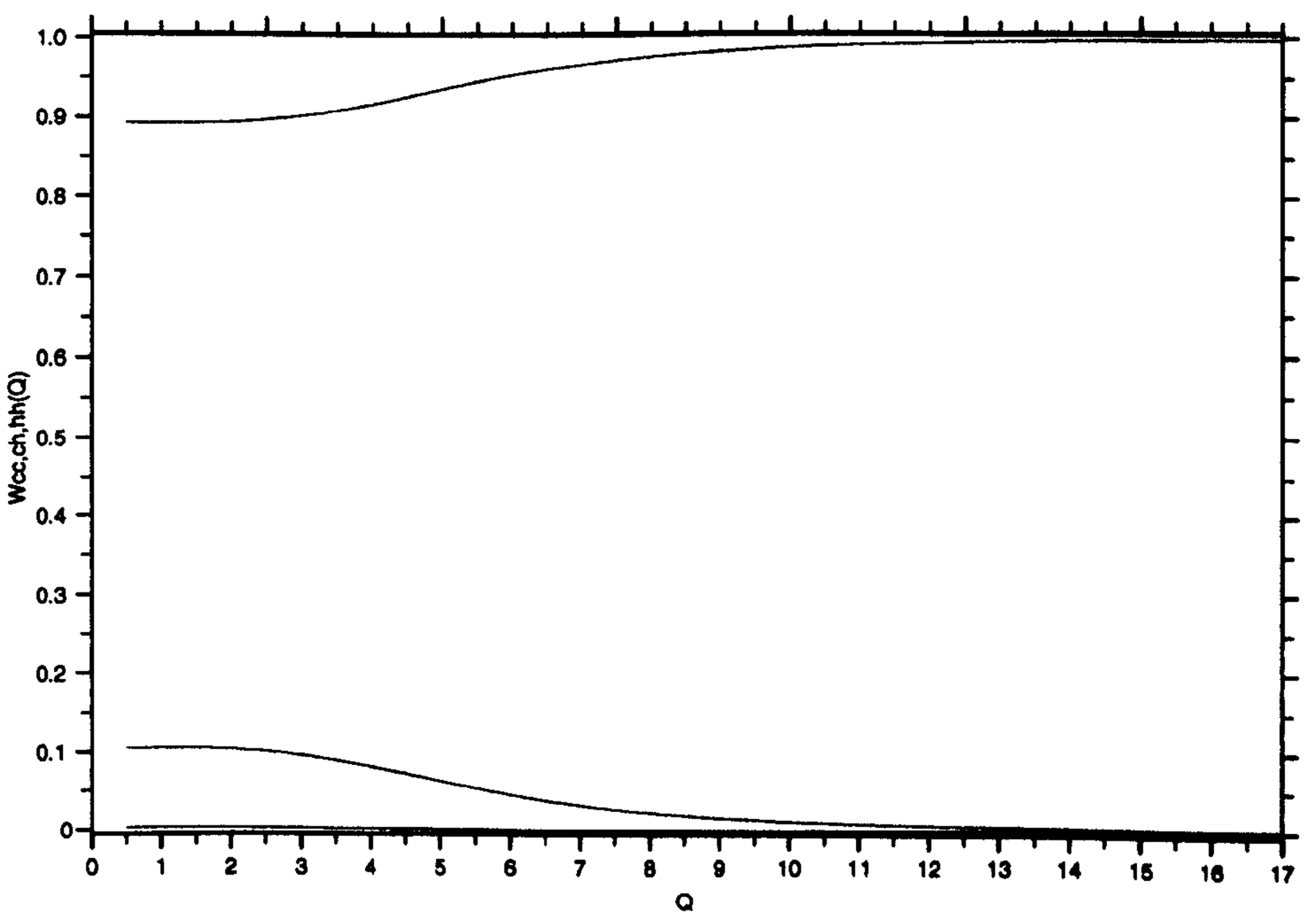

Figure 9.4: X-ray weighting factors for the partial C-C (upper curve), C-H (middle curve) and H-H (lower curve) structure factors for sample a-$C_{0.74}$:$H_{0.17}$:$D_{0.09}$.

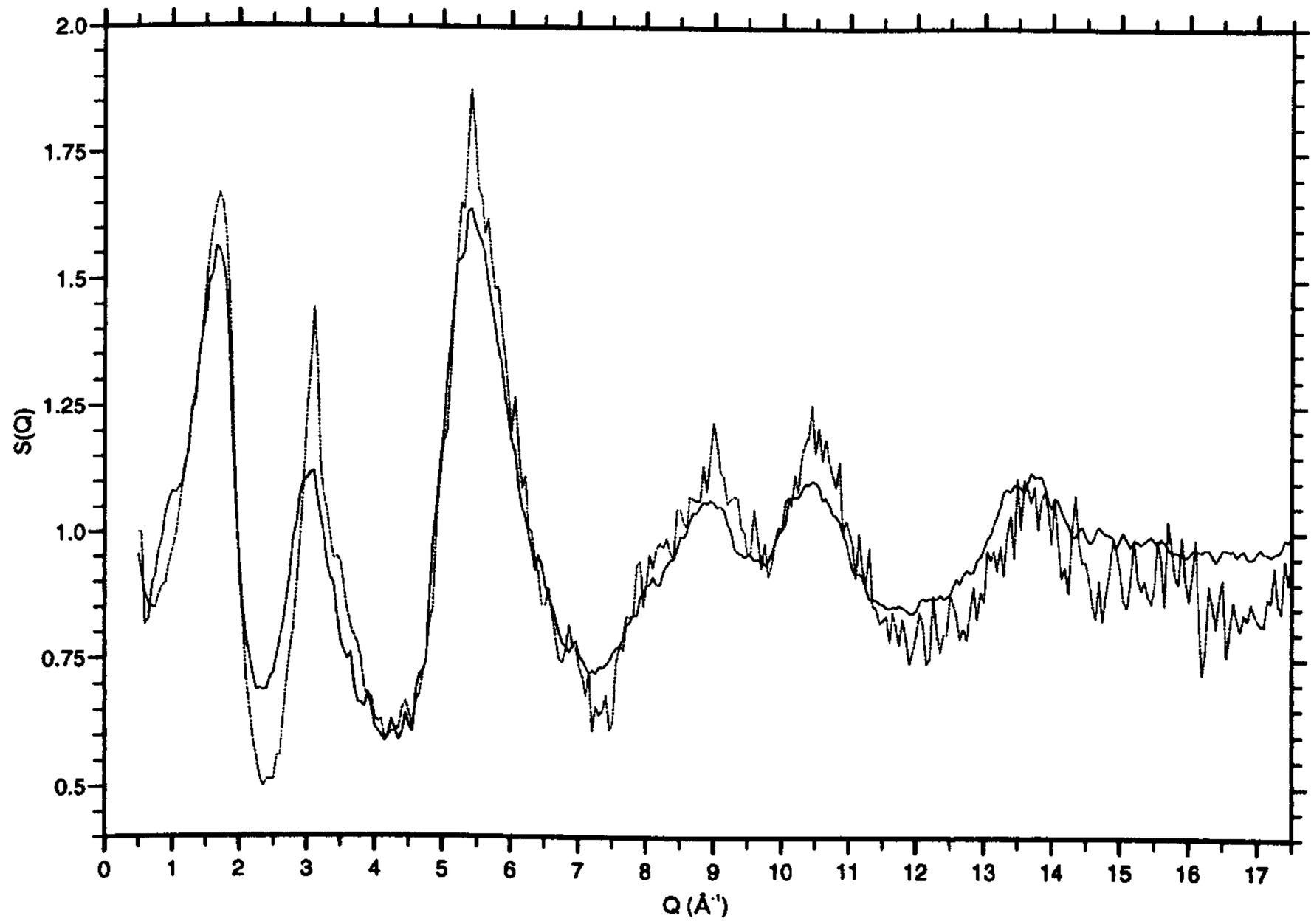

Figure 9.5: X-ray structure factor (broken line) compared to neutron partial structure factors weighted with theoretical X-ray scattering factors (solid line) for sample a-$C_{0.75}$:$H_{0.25}$.

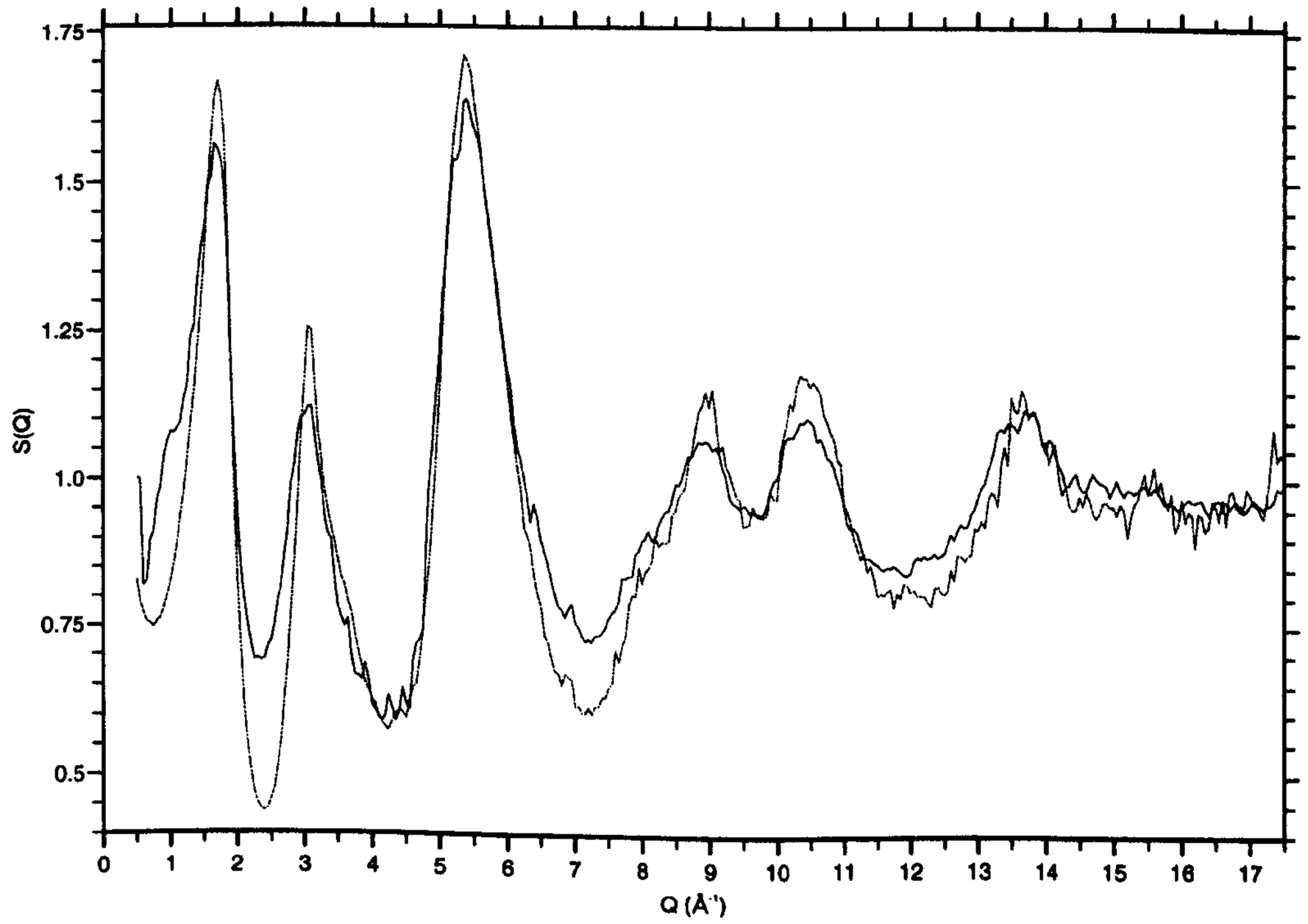

Figure 9.6: X-ray structure factor (broken line) compared to neutron partial structure factors weighted with theoretical X-ray scattering factors (solid line) for sample a-$C_{0.74}$:$H_{0.17}$:$D_{0.09}$.

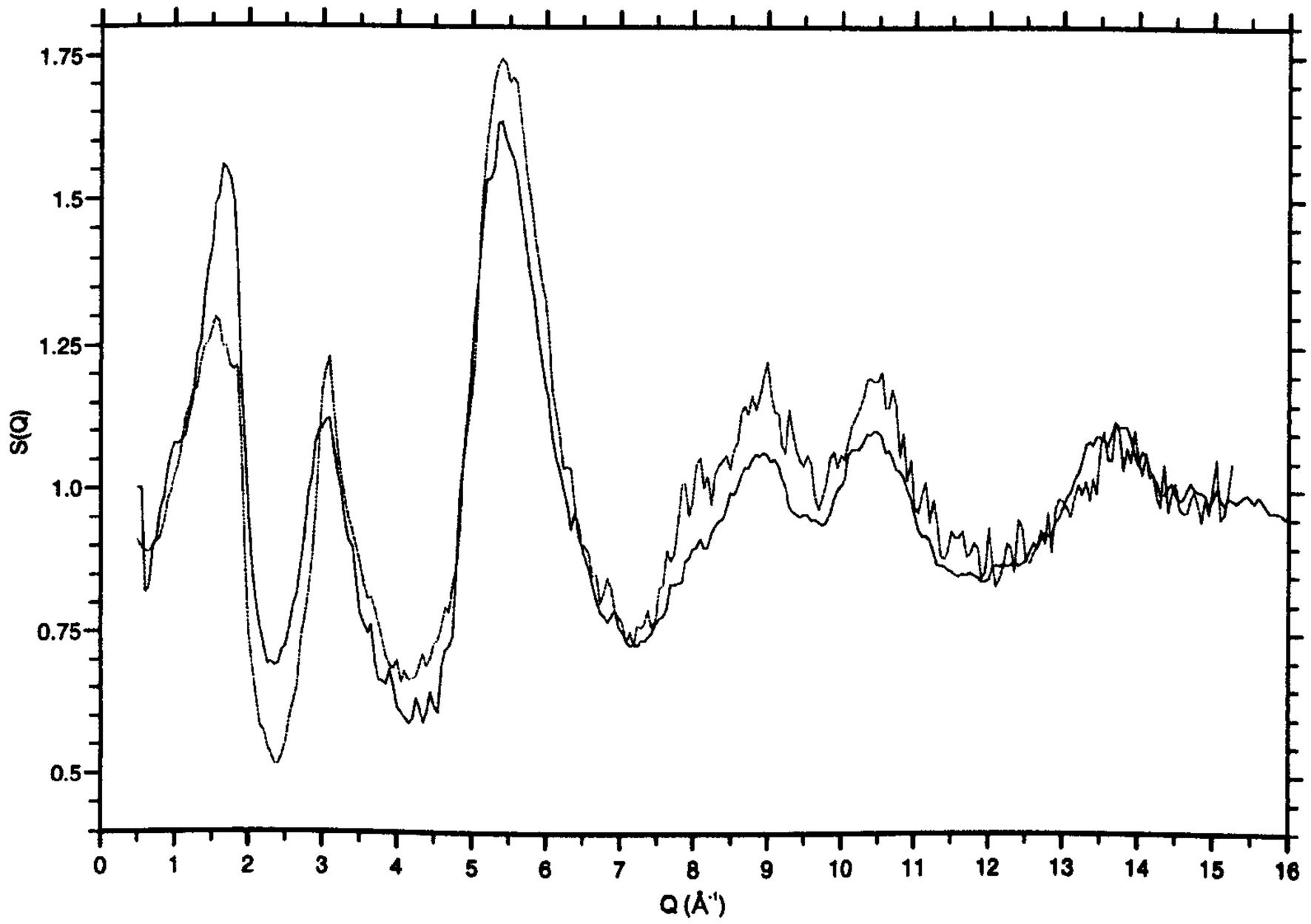

Figure 9.7: X-ray structure factor (broken line) compared to neutron partial structure factors weighted with theoretical X-ray scattering factors (solid line) for sample a-$C_{0.73}$:$D_{0.27}$.

the neutron scattering amplitudes are seen to be smaller. However, for each of the samples the neutron and X-ray peak amplitude for the 13.7$\AA^{-1}$ peak corresponds more closely than those at lower Q. For both the fully hydrogenated and the "null mixture" sample the X-ray and neutron profiles maintain the same relative peak amplitudes up to Q=12.5$\AA^{-1}$. For the fully deuterated sample a variation in the amplitude of the first structure factor peak can be clearly seen between that derived using X-ray diffraction and that using neutrons. For both the hydrogenated and the "null mixture" samples the shoulder on the low Q side of the first diffraction peak in the neutron data is noticeably missing on the corresponding X-ray data. For the fully deuterated sample this peak is broader and it is possible that it is present in the X-ray data unresolved from the peak at 1.7$\AA^{-1}$. The possible association of this shoulder with a porous structure has been discussed in Section (8.2.2). Thus there appears further indication that of the three the fully deuterated sample has the more porous structure.

For each of the samples the distribution of the second diffraction peak is shifted to lower Q values for the neutron data. This may result from the difficulty in fitting a polynomial to the neutron data in this region or possibly the effect of "absent" C-H correlations. However, when taking into account the different analysis procedures and corrections carried out on the X-ray and neutron data the scattering profiles collected by each technique actually correspond well. No obvious effects on the neutron data due to residual inelasticity effects appear present. This therefore vindicates the choice of the SANDALS diffractometer for the neutron diffraction experiments.

9.2.4 The X-ray total pair distribution function

Figure (9.8) gives the X-ray total pair distribution function for each of the isotopically substituted samples. Comparison between the three profiles shows their structure to be quite similar. The features in the pair distribution function for the fully deuterated sample can be seen to be slightly broader than those for the fully hydrogenated and the "null mixture" sample. Some of this effect is due to the smaller maximum Q value for the fully deuterated sample. However some is also due to the slight structural difference of this sample as indicated by its structure factor. Each of the samples has a first neighbour peak at $1.45\mathring{A}$ corresponding to that measured for the C-C partial neutron scattering function. The second neighbour distance of $2.47\mathring{A}$ observed for each sample is also in agreement with this function. For both the fully hydrogenated and the "null mixture" sample a small peak can be seen between the first and second neighbour distances at $\sim 1.9\mathring{A}$. There is no evidence of this feature in the pair distribution function for the fully deuterated sample. This is very interesting as the existence of C-C bond lengths in this region can be associated with the transition of a carbon matrix from a diamond structure to a rhombohedral graphite structure [110]. Fahy et al studied the minimum energy transition between these two crystalline forms of carbon and found that the borderline between preferred sp^2 rhombohedral graphite formation and local tetrahedral coordination occurs when the distance between hexagonal rings is between $2.1\mathring{A}$ and $2.3\mathring{A}$. It is therefore possible that the appearance of this feature in the fully hydrogenated and the "null mixture" sample indicates the presence of a significant transitional phase between diamond-like carbon structures and a graphite-like trigonally bonded layered structure. This phase is not obvious in the fully deuterated sample indicating that the latter represents an structural phase less well progressed towards a graphitic structure.

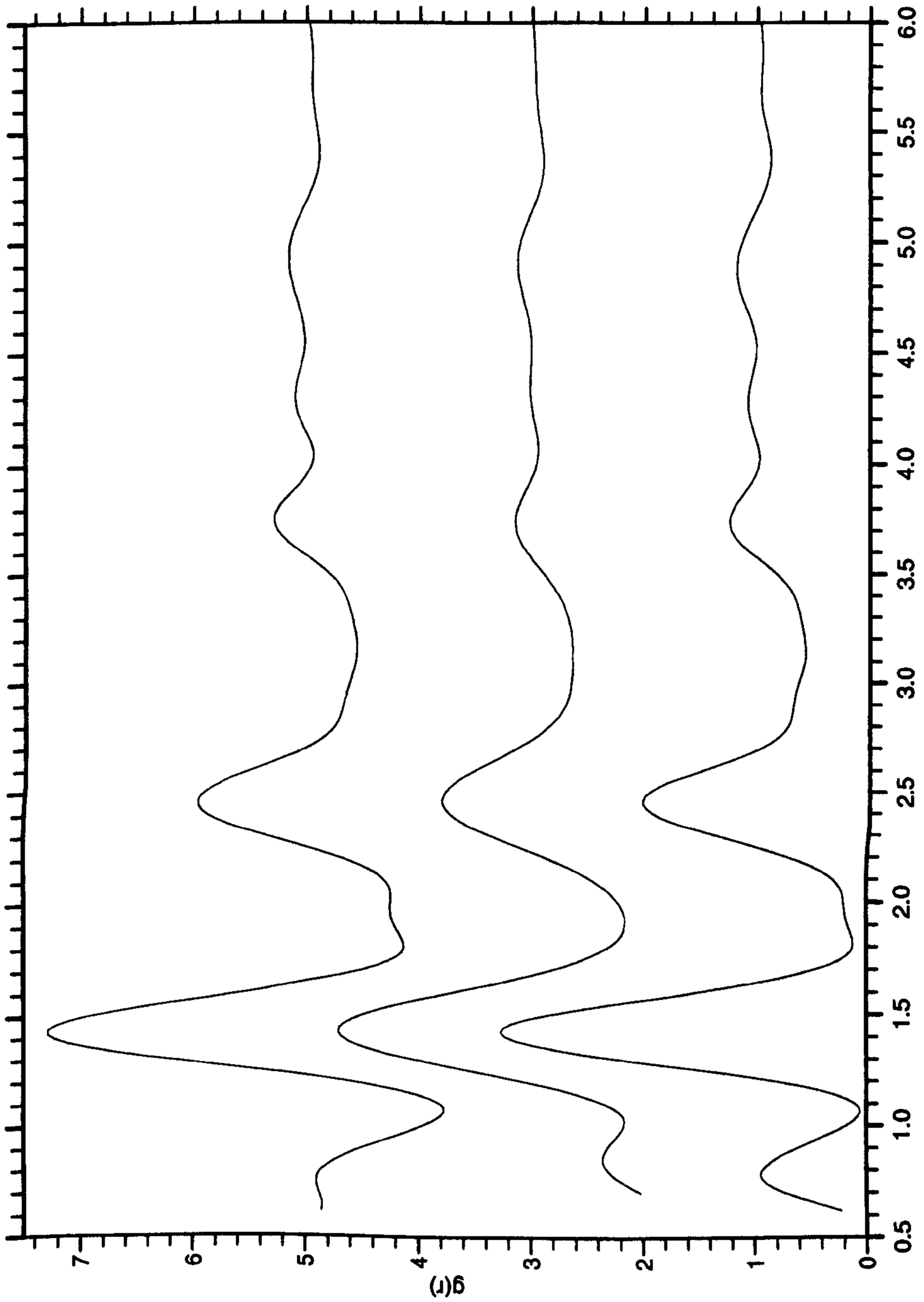

Figure 9.8: Total X-ray pair distribution function for samples a-$C_{0.75}$:$H_{0.25}$ (bottom), a-$C_{0.73}$:$D_{0.27}$ (middle) and a-$C_{0.74}$:$H_{0.17}$:$D_{0.09}$ (top).

The region between the second and third peak in the g(r)s given in Figure (9.8) shows a feature at $\sim 2.9\mathring{A}$ for the fully hydrogenated and "null mixture" samples. This cannot be seen clearly in the profile for the fully deuterated sample. In the neutron scattering data, this feature in $g(r)_{CC}$ was associated with the cross-ring distance in graphite. It is possible that there is some contribution in this region to the profile for the a-C:D sample but it is less pronounced.

Beyond the second neighbour distance, features can be seen in each of the profiles in Figure (9.8) at $3.75\mathring{A}$, $4.30\mathring{A}$ and $4.9\mathring{A}$. Each of these corresponds with features measured in the C-C partial pair distribution function detailed in Chapter (8). An average bond angle of 117° is again obtained for these samples, indicating the high degree of sp^2 bonding within the carbon matrix. The $4.3\mathring{A}$ peak is again less pronounced in the fully deuterated sample than in the fully hydrogenated or "null" mixture samples. The loss in intensity of this peak, associated with an inter-ring distance in graphite (see Figure (8.14)), again indicates the lesser degree of hexagonal layer structuring in the fully deuterated sample.

Overall, the X-ray pair distribution functions measured for the isotopically substituted samples indicate that although their structure is similar, the fully deuterated sample varies slightly from that of the fully hydrogenated and the "null mixture" sample. The former is found to be less well progressed towards a graphitic structure. This data therefore provides evidence not only of the occurrence of a transitional stage to rhombohedral graphite-like structures within this deposition region, but also the highly sensitive nature of the deposition process to the incident beam energy over this energy range. In the following sections X-ray diffraction data is presented on two a-C:H samples deposited in the medium energy range. The structural information gathered on these materials can therefore be used to provide a broader view of the

impact of deposition energy on the subsequent material.

9.3 X-ray diffraction from diamond-like a-C:H

The X-ray scattering techniques carried out on the isotopically substituted samples and detailed in the previous sections have also been used to collect data on two samples of a-C:H deposited in a fast atom source at an impact energy of ~500eV. In Table (9.1) the deposition parameters and the measured atomic composition and density for these two samples are given. The atomic composition for these samples was measured by combustion analysis in a Carlo-Erba CHN analyser and the density measurements were made using a residual volume technique [5]. At the deposition energies used for these samples a higher degree of tetrahedral bonding of the carbon matrix would be expected to occur than that observed in the isotopically substituted samples. It is from this bonding and the associated physical and electronic properties that the term "diamond-like" evolves. The samples detailed in Table (9.1) were deposited in a cylindrically symmetrical fast atom source as opposed to the planar symmetrical source configuration described previously [48]. For the former, the effective impact energy has been measured to be 0.45% of the source voltage [111]. Thus these samples were deposited at a source voltage of $\sim$ 1.1kV.

	Precursor Gas	Deposition Energy (eV)	Composition	Density (g/cm^3)
Sample 1	Acetylene (C_2H_2)	$\sim$ 500	a-$C_{0.65}$:$H_{0.35}$	1.81
Sample 2	Propane (C_3H_8)	$\sim$ 500	a-$C_{0.68}$:$H_{0.32}$	1.99

Table 9.1: Deposition parameters, atomic compositions and density for the diamond-like carbon samples.

It can be seen from Table (9.1) that although Sample 1 has the lowest hydrogen:carbon precursor gas ratio, it has the highest hydrogen atomic composition. Furthermore, as the impact energy per carbon atom would be greater for Sample 1, it might be expected to display the lower hydrogen content of the two. However, exact figures on the impact energy at which these two samples were deposited are not available. It is therefore possible that Sample 2 was deposited at a slightly higher impact energy. Without precise knowledge of the relative deposition energies of the two samples it is difficult to comment, in complete detail, on their resultant hydrogen content.

In the same way as for the isotopically substituted samples, both standard ($\theta : 2\theta$) transmission X-ray data and Warren-Mavel fluorescence detection technique data was collected for each sample. The data reduction procedures necessary to access the structure factor from the raw data collected for the two samples has been detailed in the previous sections. The standard data collected for Sample 2 could not be used as the intensity of the scattered beam at the detector was so high that dead-time corrections could not be accurately carried out, hence only the lower count rate fluorescence radiation data was used in this case. In Figures (9.9) and (9.10) the coherent scattering profile and the self scattering curves for Samples 1 and 2 are given respectively. Although the coherent scattering profiles can be seen to oscillate about the theoretical self scattering curve in each case, the experimental data for Sample 1 can be seen to deviate from the self scattering curve at high 2θ.

Figure (9.11) shows the X-ray structure factors for Samples 1 and 2. The S(Q) for the acetylene sample is shown only up to a maximum Q value of $13\mathring{A}^{-1}$ and that for the propane sample up to Q=$15\mathring{A}^{-1}$. Although data was collected up to Q=$18\mathring{A}^{-1}$ for both, an error in the gradient of the theoretical scattering curve relative to that of the

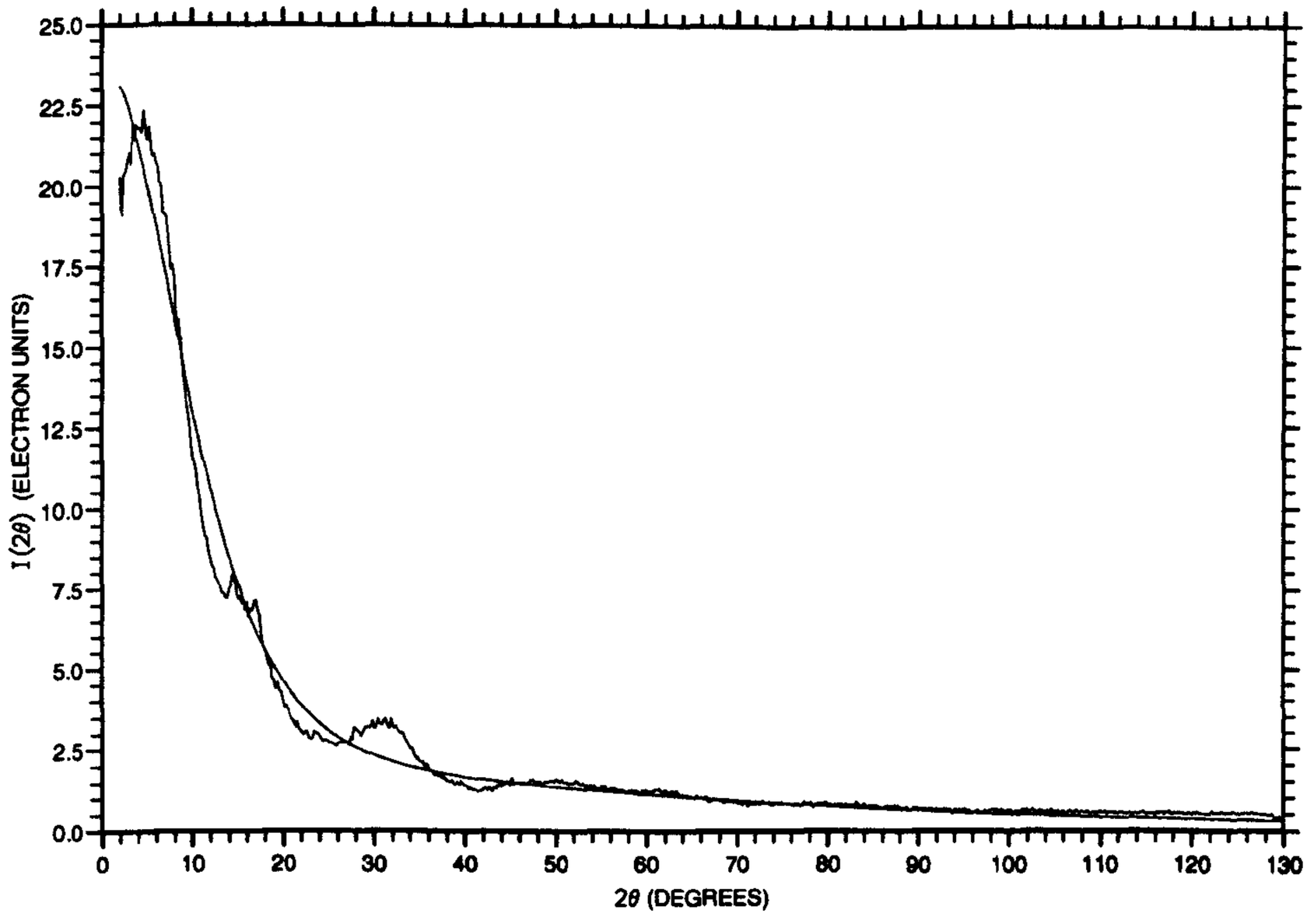

Figure 9.9: Coherent and self scattering curves for sample a-$C_{0.65}$:$H_{0.35}$.

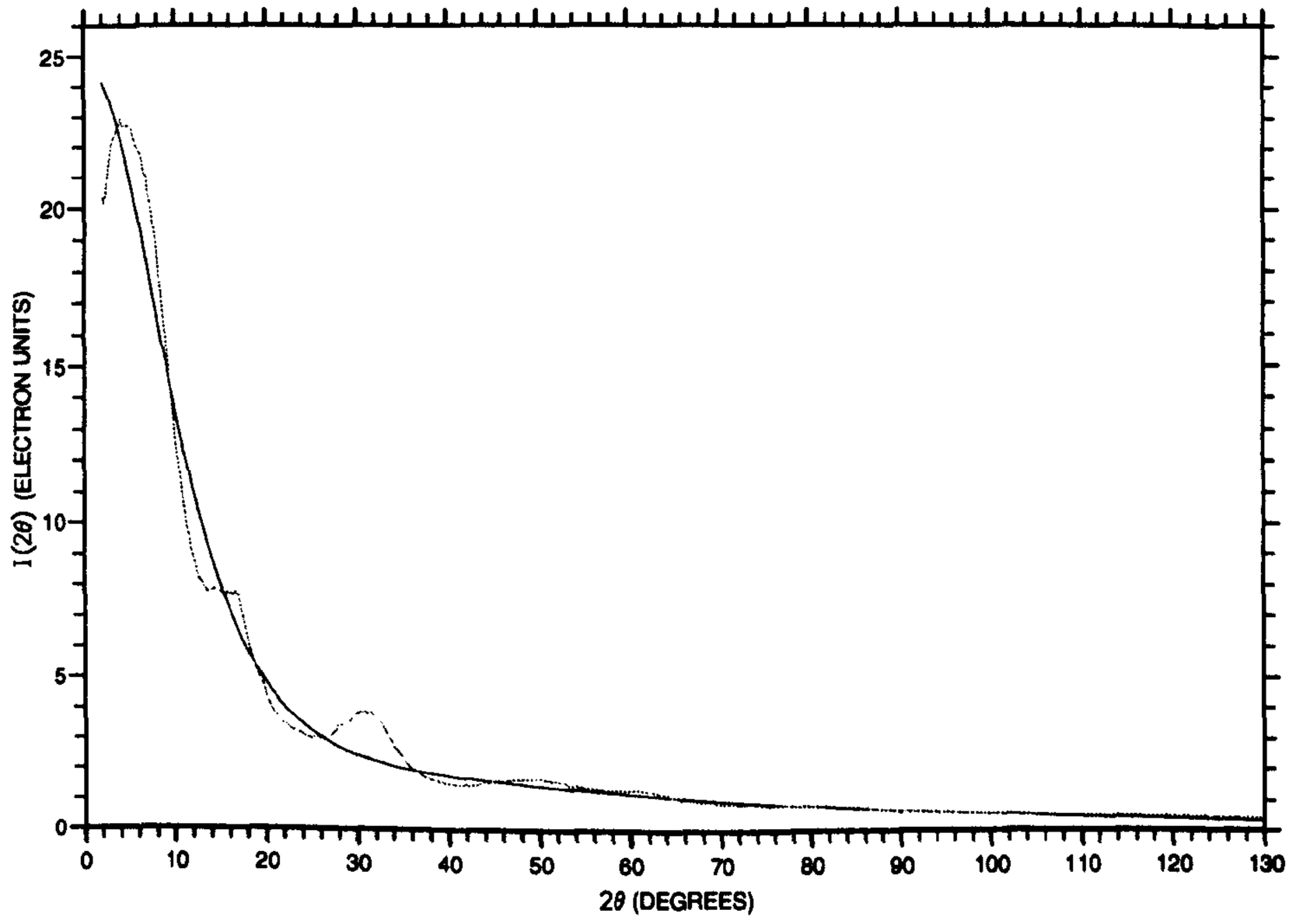

Figure 9.10: Coherent and self scattering curves for sample a-$C_{0.68}$:$H_{0.32}$.

measured data caused the structure factor, S(Q), to deviate significantly from unity at high Q. This problem had been previously found to occur for the fully deuterated isotopically substituted sample, though to a lesser extent. The scattering angle at which this effect becomes most pronounced is found to decrease as the hydrogen content of the samples increases, indicating that the problem results from the theoretical hydrogen scattering factor curves used. The theoretical atomic form factor curves of Stewart et al [67, 66] were chosen in this work as the latter have been calculated specifically for the case of hydrogen terminally bonded to carbon, taking into account the distortion of the electron density function of the hydrogen atom. Stewart et al assume a spherical density for the bonded H atom but "float" this spherical distribution $0.07\mathring{A}$ off the proton into the bond. For the five a-C:H(D) samples studied in this work the form of the electron density distribution may vary as the structural composition and the bonding state of the carbon atoms to which the hydrogen atoms are attached varies between samples. Thus these materials pose a particular problem in defining the form of the hydrogen form factor. The use of the Warren-Mavel technique to remove the incoherent scattering from the X-ray diffraction data therefore appears to have been so successful in this case that the limiting factor in determining the structure factor for these samples now appears to lie in determining the self scattering curves for the materials.

Comparing the measured structure factors for Samples 1 and 2 shown in Figure (9.11) the latter can be seen to correspond very closely in both amplitude and phase across the Q range sampled. What is immediately noticeable about the structure factors for these two samples is the smaller, broader first peak relative to that measured for the isotopically substituted samples (Figure (9.3)). In fact a small variation occurs between the form of this peak for the structure factors given in Figure (9.11).

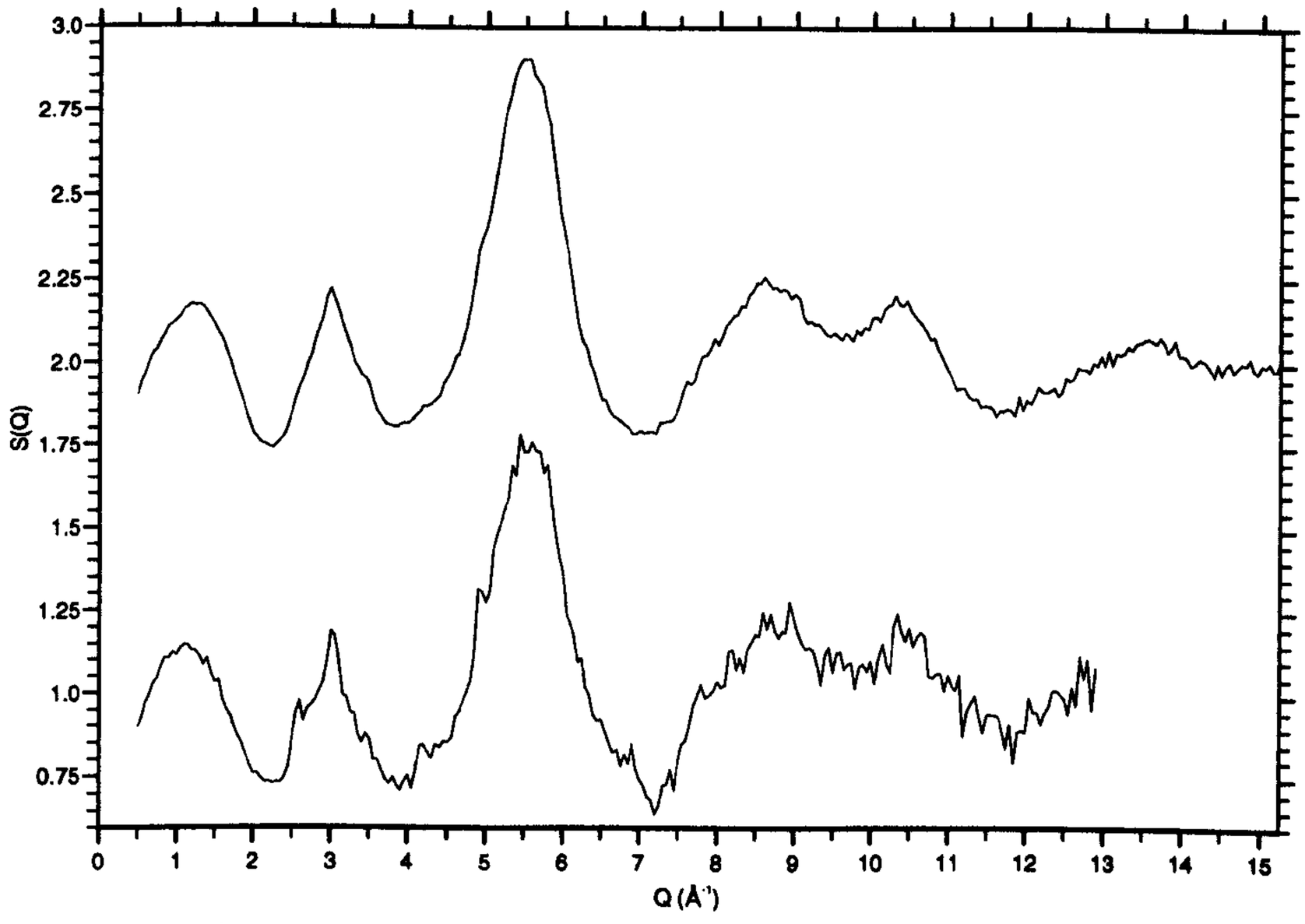

Figure 9.11: Total X-ray structure factor for samples a-$C_{0.68}$:$H_{0.32}$ (upper profile) and a-$C_{0.65}$:$H_{0.35}$ (lower profile).

For Sample 2 this peak occurs at $1.26\mathring{A}^{-1}$; for sample 1 it occurs at $1.14\mathring{A}^{-1}$ and the amplitude has dropped slightly. In Section (9.2.2) the first peak in S(Q) for the a-$C_{0.73}$:$D_{0.27}$ sample was seen to have fallen in amplitude and moved to a lower Q value relative to the "null mixture" and fully hydrogenated samples. It was suggested that this effect may be due to the fully deuterated sample having a smaller deposition energy. From the first diffraction peak observed for Samples 1 and 2 this trend can indeed be associated with a lower impact energy. Having observed this change in the form of the first peak, it is useful to make a direct comparison of the structure factors for both the isotopically substituted samples and the "diamond-like" samples.

9.3.1 Comparison between the X-ray structure samples for each of the a-C:H(D) samples

Figure (9.12) shows the structure factors for the a-$C_{0.75}$:$H_{0.25}$, a-$C_{0.73}$:$D_{0.27}$, a-$C_{0.68}$:$H_{0.32}$ and a-$C_{0.65}$:$H_{0.35}$ samples, plotted consecutively for comparison. From the data shown, S(Q) for each of the samples can be seen to correlate well beyond Q=$7.5\mathring{A}^{-1}$. Moving below this point, the third diffraction peak can be seen to be most sharp for sample a-$C_{0.75}$:$H_{0.25}$ which has the lowest hydrogen content and reflects the increased structural order within this sample. Sample a-$C_{0.68}$:$H_{0.32}$ displays the greatest amplitude and width for this peak. For the high deposition energy samples, a-$C_{0.75}$:$H_{0.25}$ and a-$C_{0.73}$:$D_{0.27}$, this peak occurs at $5.4\mathring{A}^{-1}$ whereas for the 500eV samples, a-$C_{0.65}$:$H_{0.35}$ and a-$C_{0.68}$:$H_{0.32}$, it occurs at $5.5\mathring{A}^{-1}$.

The second diffraction peak is again seen to be very sharp for the lowest hydrogen content sample. Although, the deuterated sample can be seen to have a similar width at this point, it has a smaller amplitude. Both the a-$C_{0.65}$:$H_{0.35}$ and a-$C_{0.68}$:$H_{0.32}$ samples can be seen to display a similar amplitude and width at this point, smaller

and broader than the higher energy samples respectively.

Comparing the first diffraction peak for each sample, a trend can be clearly seen in the form of the data in this region, the latter dropping in amplitude and moving down in Q as the hydrogen content of the sample increases. This indicates a marked breakdown of any graphite-like interlayer structural correlations within the carbon matrix as the deposition energy falls. Furthermore, this is accompanied by a progressive change in the configuration of the void structure of the material which may be associated with the corresponding increase in hydrogen content of the material. The latter would be an inevitable consequence of the increased network termination as the atomic percentage of hydrogen atoms within the material increases. Small angle X-ray scattering measurements have been carried out on the two "diamond-like" samples [112] and indicate a significant pore structure with a broad distribution of pore sizes. It would be interesting to contrast these results with that for the a-$C_{0.75}$:$H_{0.25}$ and a-$C_{0.73}$:$D_{0.27}$ samples. The first diffraction peak for the data shown in Figure (9.12) indicates a structural change over a range corresponding to real space correlation lengths from 3.65$\AA$ to 5.51$\AA$. SAXS studies would allow this length scale to be increased and provide a wider view of the changes taking place within the materials.

In the following section the measured pair distribution function for Samples 1 and 2 is given and compared to that measured for the isotopically substituted samples.

9.3.2 Pair distribution function for the diamond-like a-C:H samples

Figures (9.13) and (9.14) show the X-ray pair distribution functions for Samples 1 and 2 respectively. Neither sample displays a split first peak as was shown in the corresponding neutron diffraction data collected on these samples [5]. This is not

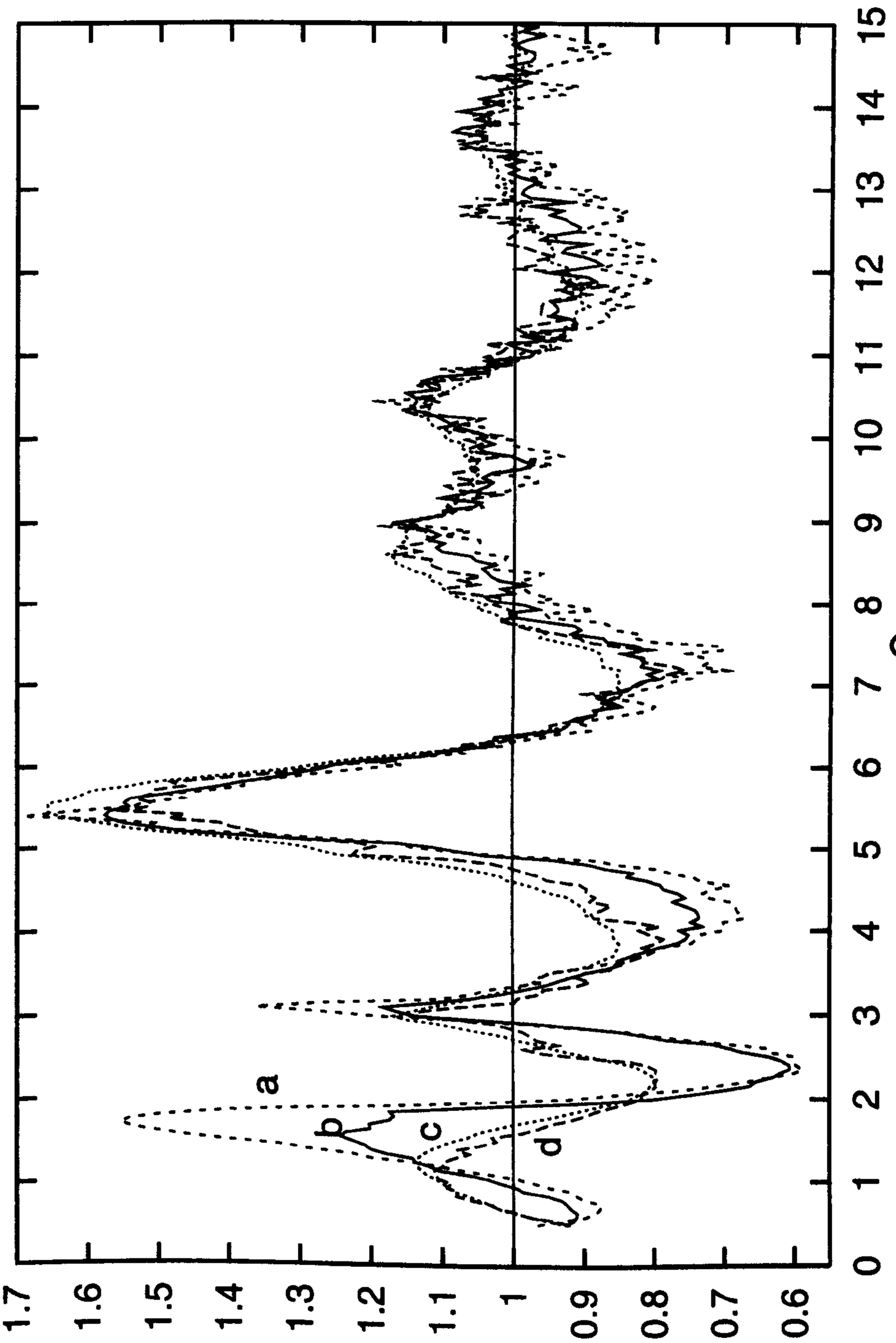

Figure 9.12: X-ray structure factors for sample a) a-$C_{0.75}$:$H_{0.25}$, b) a-$C_{0.73}$:$D_{0.27}$, c) a-$C_{0.68}$:$H_{0.32}$ and d) a-$C_{0.65}$:$H_{0.35}$.

surprising as the resolution for these pair distribution functions is much poorer than the corresponding neutron functions due to the limited Q range available for the X-ray data (c.f. neutron diffraction data Q_{max} of $50\mathring{A}^{-1}$). Sample 2 shows a first neighbour correlation distance of $1.47\mathring{A}$. Averaging the peak distances measured by neutron diffraction and weighting them according to their neutron diffraction radial distribution function peak areas also gives a value of $1.47\mathring{A}$ for this sample. Sample 1 shows a first neighbour C-C distance of $1.46\mathring{A}$, somewhat below that expected at $1.47\mathring{A}$. However the peak positions in the pair distribution function for Sample 1 must be treated with care due to the particularly limited Q range sampled (Q_{max}=$13\mathring{A}^{-1}$), which would give an expected resolution of no better than ± 0.02. The measured second neighbour distance for Sample 2 occurs at $2.50\mathring{A}$ closer to that of diamond ($2.51\mathring{A}$) than that measured for the isotopically substituted samples ($2.47\mathring{A}$). The corresponding peak for Sample 1 occurs at $2.48\mathring{A}$ again lower than to be expected. Higher order peaks occur for Sample 2 at $3.74\mathring{A}$, $4.77\mathring{A}$ and $5.9\mathring{A}$. For the isotopically substituted samples peaks were observed at $3.75\mathring{A}$, $4.3\mathring{A}$ and $4.9\mathring{A}$ where each of these could be associated with a graphite intralayer C-C correlation length (see Figure (8.14)). From the higher order correlations measured for Sample 2, it does not appear to exhibit the hexagonal ring structure evident for the isotopically substituted samples and can be seen to represent a material having a more diamond-like structure. Corresponding peaks for Sample 1 occur at $3.70\mathring{A}$, $4.85\mathring{A}$ and $5.83\mathring{A}$ again showing little evidence for hexagonal ring formation. In particular neither the X-ray or neutron data for these samples shows evidence for the $2.85\mathring{A}$ graphite cross-ring distance (although for the X-ray data this may be washed out by the limited Q range sampled). Thus as the deposition energy falls from ~1kV to ~ 0.5kV a structural transformation from a graphite-like to a more "diamond-like" structure has been shown to occur.

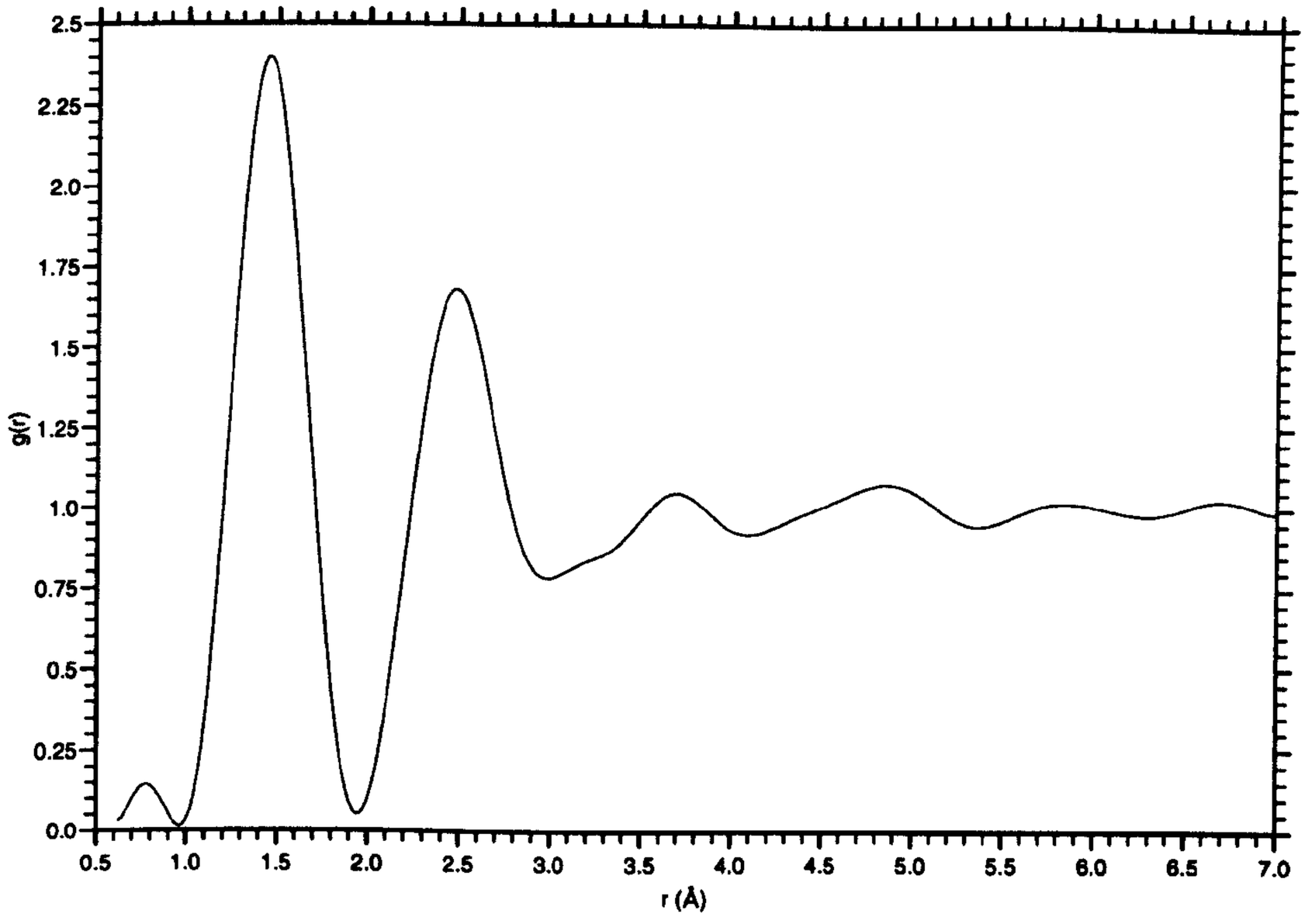

Figure 9.13: X-ray pair distribution function for sample a-$C_{0.65}$:$H_{0,35}$.

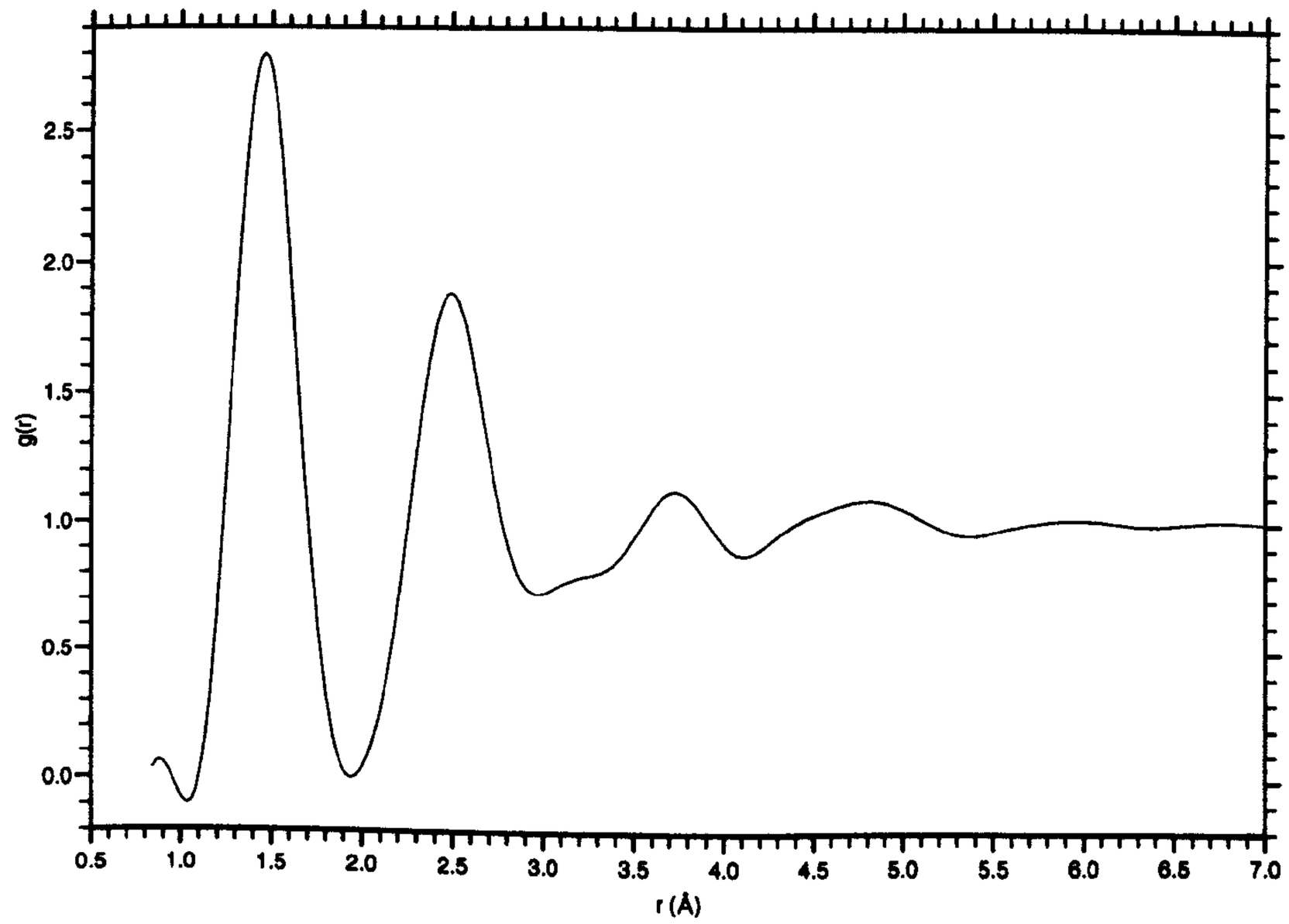

Figure 9.14: X-ray pair distribution function for sample a-$C_{0.68}$:$H_{0.32}$.

9.3.3 High energy acetylene sample

In the previous sections comparison has been made of samples deposited at high and medium impact energies from different precursor gases. Data will be presented here on a second sample deposited from acetylene at a higher impact energy than Sample 1. The sample concerned was deposited at an impact energy of 0.85kV (source voltage 1kV) and it's structure factor is given in Figure (9.15). This sample has a measured atomic composition a-$C_{0.78}$:$H_{0.22}$. Its structure factor can be seen to display a split first diffraction peak. The latter consists of a broad peak at $1.53\mathring{A}^{-1}$ and a sharper feature at $1.89\mathring{A}^{-1}$. From this sharp peak there is obvious graphite layer formation within this sample. The lower peak indicates a residual presence of the void structure indicated in Sample 1. Although the second diffraction peak position for this sample corresponds to that measured for the lower energy acetylene sample, the third peak at $5.47\mathring{A}^{-1}$ lies between that measured for the diamond-like and that for the isotopically substituted samples. All higher order peaks correspond with those measured for Sample 1.

Figure (9.16) gives the pair distribution function for this 0.85kV acetylene sample. The C-C first neighbour distance is found to occur at $1.48\mathring{A}$, above that measured for the lower deposition energy acetylene sample, indicating that the shift in the g(r) for the latter sample was due to the limited Q range available. The second neighbour distance is found to occur at $2.49\mathring{A}$ below that for Sample 2 and further from that for diamond at $2.51\mathring{A}$. This therefore lies between that for the "diamond-like" and the isotopically substituted samples. The third neighbour peak at $3.74\mathring{A}$ again corresponds to that measured for Sample 2, lying above that measured for the 0.5kV acetylene sample at $3.70\mathring{A}$. Higher order correlations can be seen to occur in the g(r) given in Figure (9.16) at $3.74\mathring{A}$, $4.39\mathring{A}$ and $4.91\mathring{A}$. Thus this sample displays

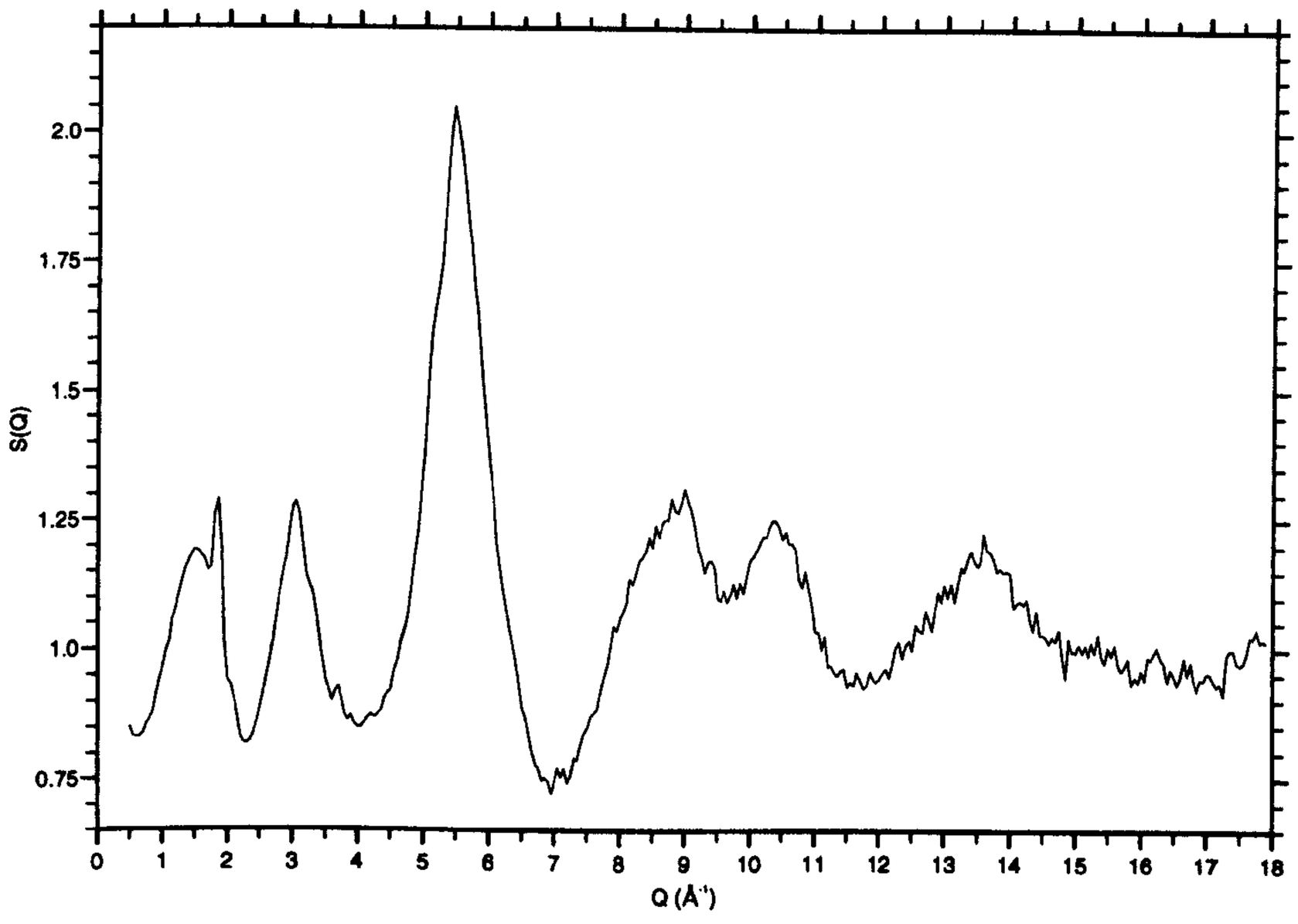

Figure 9.15: X-ray structure factor for 0.85kV acetylene sample, a-$C_{0.78}$:$H_{0.22}$.

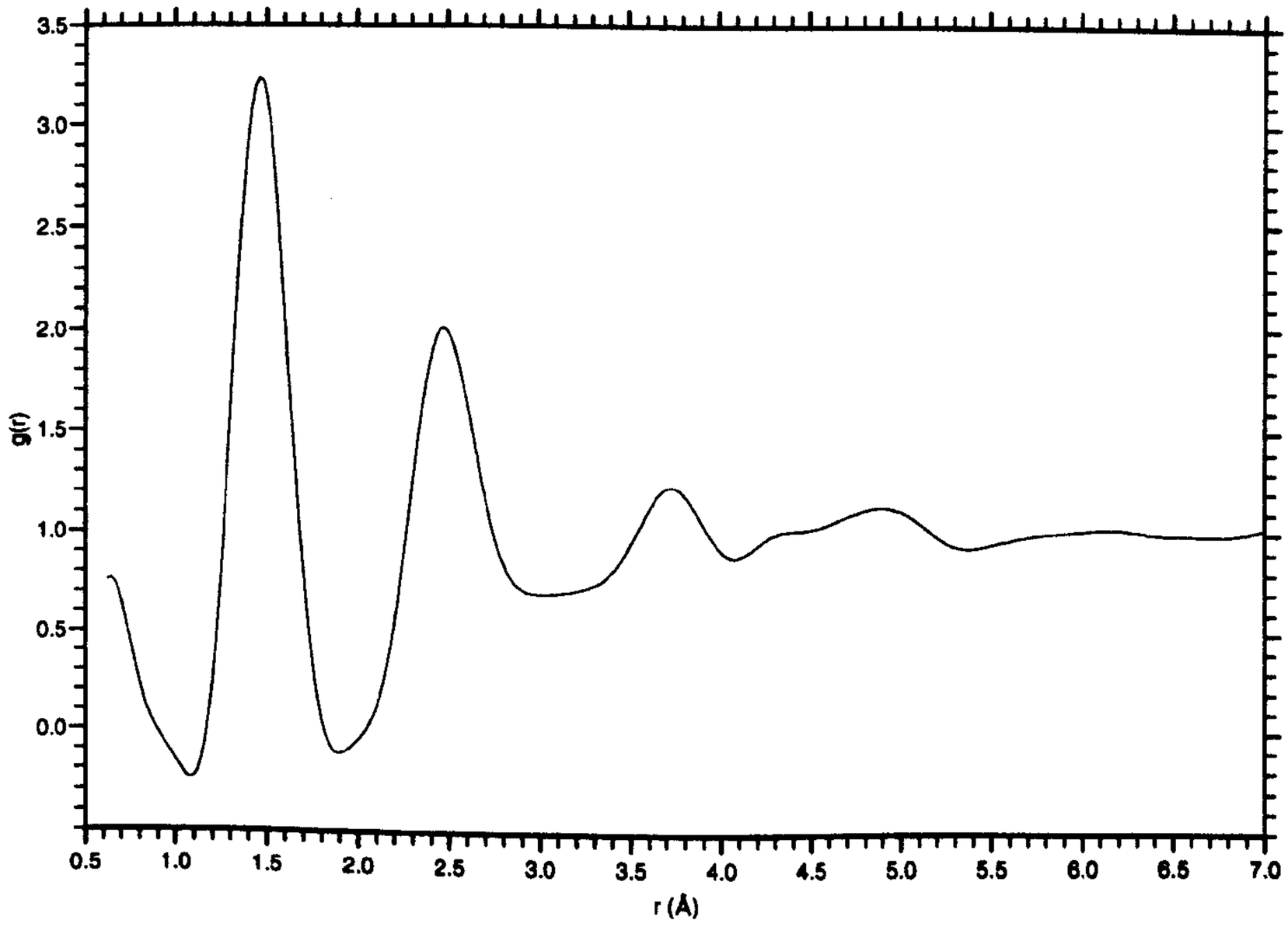

Figure 9.16: X-ray pair distribution function for 0.85kV acetylene sample, a-$C_{0.78}$:$H_{0.22}$.

features similar to those associated with the hexagonal graphite-like intralayer structure observed in the isotopically substituted samples. However for the 0.85kV sample these features do not correspond as closely to those for graphite. Thus this sample has been shown to show structure intermittent to that measured for the isotopically substituted samples and the "diamond-like" samples, and illustrates the interplay between all deposition parameters, including both energy and precursor gas.

9.4 Conclusions

X-ray diffraction data has been collected on a series of a-C:H(D) samples deposited over an impact energy range between 0.5keV and 1.2keV, having a hydrogen(deuterium) content varying between 35% and 22%. Three of these samples, a-$C_{0.75}$:$H_{0.25}$, a-$C_{0.74}$:$H_{0.17}$:$D_{0.09}$ and a-C:$_{0.73}$:$D_{0.27}$, have been been studied using neutron diffraction techniques (see Chapter (8)) and found to represent structurally similar, isotopically enriched materials. However, complementary information on the carbon network within these materials, determined from the X-ray data collected, has shown the structural form of the a-C:$_{0.73}$:$D_{0.27}$ to vary somewhat from the a-$C_{0.75}$:$H_{0.25}$ and a-$C_{0.74}$:$H_{0.17}$:$D_{0.09}$ samples. Sample a-C:$_{0.73}$:$D_{0.27}$ has been shown to represent a structural phase slightly less well progressed towards a fully graphitic configuration. This is suggested to result from the fully deuterated sample having a lower deposition impact energy (witnessed by its higher deuterium content). Although the variation in impact energy for this sample from that of the other two isotopically substituted samples is only slight, clear evidence of a change in the void structure for the fully deuterated sample has been shown. This X-ray data has therefore highlighted the extreme sensitivity of the deposited materials to the impact energy parameter in this transitional region.

Comparison has been made between the X-ray data collected on the isotopically substituted samples and a combination of the partial C-C, C-H and H-H structure factors, determined from neutron diffraction studies on these samples, weighted according to the appropriate theoretical X-ray scattering factors. In each case, the theoretically weighted neutron structure factors were found to correspond well with those measured using X-ray diffaction. This has therefore given merit to the accuracy of the partial structure factors determined for this phase of a-C:H using the isotopic substitution method.

X-ray diffraction data has also been presented on two samples of a-C:H deposited at an impact energy of 0.5keV. Comparison with the isotopically substituted samples, deposited at $\sim$ 1.1keV has provided evidence for a marked breakdown in graphite-like inter- and intra-layer structural correlations and a move towards a more diamond-like atomic arrangement as the deposition energy falls between these values. Furthermore, a progressive change in the void structure within the samples has been found to accompany the transition between diamond-like and graphite-like phases. Further work has been suggested involving small angle X-ray diffraction studies on these samples to provide comparative information on the structural features within these materials above $\sim 10\mathring{A}$ in size.

Data has been presented on two samples of a-C:H deposited from the same precursor gas (acetylene), deposited at an impact energy of 0.5kV and 0.85keV respectively. A progression towards a more graphitic structure at higher impact energies is again witnessed. Further work is suggested involving a series of samples deposited from the same precursor gas at a range of impact energies between say 0.3keV and 1keV to allow the structural reconfigurations to be closely followed.

The Warren-Mavel fluorescence technique has been shown to provide a highly efficient method for the removal of the incoherent scattering contribution to the measured X-ray profiles. In fact, it has been so successful that it has highlighted the difficulty in obtaining accurate theoretical self scattering profiles for the hydrogen within these amorphous hydrogenated carbon samples. This has been shown to be particularly so for the "diamond-like" form of this material, where the complex bonding enviroment present lead to particular difficulties in defining the electron distribution of the bonded hydrogen.

Chapter 10

Conclusions

A fast atom source plasma deposition system, commissioned as part of this work, has been used to produce a series of highly compositionally tuned samples of a-C:H, including three isotopically substituted, structurally similar samples. Neutron diffraction studies have been carried out on these samples on the SANDALS diffractometer at the Rutherford Appleton Laboratory's pulsed source, ISIS. The data collected has afforded an insight into the structural configuration of this phase of a-C:H of unique clarity by providing direct access to the partial C-C, C-H and H-H correlation functions for this material. The C-C partial correlation functions measured have shown the carbon matrix within these materials to be predominantly sp^2 bonded with a maximum sp^3 content of 30%. Distinct inter- and intra-layer graphite-like bond formation has been shown and an average C-C nearest neighbour coordination number of 3 measured. The C-H partial structure factor and pair correlation function has shown the presence of a large number of $CH_{2,3}$ groups, which is surprising for such low (25 atomic percent) hydrogen content samples. Further evidence for these groups has been provided by the partial H-H correlation functions. Infra red and inelastic

neutron scattering studies on these samples are suggested to investigate presence of such groups. The hydrogen atoms within the system have been found to be predominantly bonded to sp^3 hybridised carbon atoms. Evidence for the presence of a trace of molecular hydrogen within this phase of a-C:H has also been provided. The partial C-H coordination number has been shown to be 1.8 atoms.

The SANDALS diffractometer at ISIS was chosen for the neutron scattering measurements on these samples with the aim of minimising the inelastic contributions to the measured data. This proved very successful, the inelastic effects being so minimised that contributions to the partial structure factors, arising from residual effects in the total structure factors for the isotopically substituted samples, could not be detected.

X-ray diffraction measurements, carried out at the Daresbury Laboratory SRS, have provided complementary information on the carbon matrix within the materials. This is in agreement with the neutron scattering data, showing a significant graphite-like structuring of the carbon. As the X-ray data is uncomplicated by large C-H or H-H contributions, it has been able to highlight the slight structural difference of one of the isotopically substituted samples. This sample, a-$C_{0.73}$:$D_{0.27}$, has been shown to represent an amorphous phase less well progressed towards a graphitically ordered structure. Although the structural differences between this and the a-$C_{0.75}$:$H_{0.25}$ and a-$C_{0.74}$:$H_{0.17}$:$D_{0.09}$ samples is small, this data has shown evidence for the extreme sensitivity of the materials to deposition energy in this transitional region.

X-ray data has also been collected on a-C:H samples deposited at an impact energy of 0.5keV (in comparison to that of $\sim$ 1keV for the isotopically substituted samples). Samples deposited in this energy region have been shown to indicate a higher degree of sp^3 bonding and represent a more diamond-like phase of a-C:H.

Comparison of the isotopically substituted samples and these diamond-like samples indicates a progressive breakdown in the graphitic ordering, accompanied by a change in the void structure of the materials, as the deposition energy falls and the hydrogen content increases within this region. Further work is suggested involving small angle X-ray diffraction data to elucidate the effect of such restructuring on the medium range order within the samples.

The use of the Warren-Mavel fluorescence detection technique, in conjunction with a synchrotron X-ray source, has proved to be an extremely efficient method for the removal of the incoherently scattered Compton contribution to the X-ray scattering data. The high degree of control over the incident wavelength chosen at such a source allows the experimental parameters to be optimised and the Compton contribution to the data minimised. In fact, this technique has been so successful on the a-C:H samples studied, that it has highlighted the problem of providing accurate theoretical self scattering curves for the coherent data. It is suggested that this difficulty arises from the complex bonding environment within the matrix of the diamond-like materials, resulting in an electron density distribution for the bonded hydrogen not accounted for in the theoretical X-ray scattering factor curves. Although curves have been chosen in this work that take some account of the distortion of the hydrogen electron distribution on bonding to the carbon, deviation of the experimental self scattering curves from the theoretical curves are still apparent. Further work is suggested to investigate whether such deviations are as apparent in the X-ray scattering curves for more polymeric forms of a-C:H, as the latter form of a-C:H may be more closely represented by the theoretical X-ray scattering curves.

Preliminary studies have been carried out on a glancing angle X-ray diffraction technique for the *in situ* characterisation of a-C:H thin films. Two films of amorphous

hydrogenated carbon have been studied and have shown that not only can scattering profiles be collected from 1μm films of this low Z, diffusely scattering material, but depth profiling of the thin film/substrate system is possible.

Bibliography

[1] R. Zallen, *The Physics of Amorphous Solids*, Wiley, 1983.

[2] S. R. Elliott, *Physics of Amorphous Materials*, Wiley, New York, 1990.

[3] J. C. Angus, in J. Mort and F. Jansen, editors, *Plasma Deposited Thin Films*, chapter 4, CRC Press, Florida, 1986.

[4] A. H. Lettington, *Phil. Trans. R. Soc. Lond. A* **342**, 287 (1993).

[5] P. R. J. Honeybone, *Neutron Scattering Studies of Amorphous Hydrogenated Carbon and Silicon Carbon*, PhD thesis, University of Kent, 1992.

[6] N. R. S. Tait, D. W. L. Tolfree, P. John, I. M. Odeh, M. J. Thomas, M. J. Tricker, J. I. B. Wilson, I. B. A. England, and D. Newton, *Nucl. Instrum. Meth.* **176**, 433 (1980).

[7] H. Schellenmeier, *Z. Phys. Chem* **205**, 349 (1953).

[8] P. Koidl, A. Bubenzer, and B. Dischler, *Proc. Soc. Photo Opt. Instrum. Eng.* **381**, 186 (1983), Symposium on Optical Surface Technology.

[9] M. Kakuchi, M. Hikita, and T. Tamamura, *Appl. Phys. Lett.* **48**, 835 (1986).

[10] M. Rothschild, C. Arnone, and D. J. Erlich, *J. Vac. Sci. Technol.* **B4** (1986).

[11] P. W. Atkins, *Physical Chemistry*, Oxford University Press, 1990.

[12] J. Robertson, in *Diamond and Diamond-like Films and Coatings*, page 331, Plenum, New York, 1990.

[13] C. Jager, J. J. Titman, and R. J. Newport, *Thin Solid Films* **227**(1), 3 (1993).

[14] D. R. McKenzie, L. C. Botten, and R. C. McPhedran, *Phys. Rev. Lett.* **51**, 280 (1983).

[15] R. J. Newport, P. J. R. Honeybone, S. P. Cottrell, J. Franks, P. Revell, R. J. Cernik, and W. S. Howellls, *Surface and Coating Technology* **47**(1-3), 668 (1991).

[16] P. H. Gaskell, A. Saeed, P. Chieux, and D. R. McKenzie, *Phil. Mag. B* **66**(2), 155 (1992).

[17] D. C. Green, D. R. McKenzie, and P. B. Lukins, *Materials Science Forum* **52-53**, 103 (1989).

[18] R. R. Saxena and R. H. Bragg, *J. Non-Cryst. Solids* **28**, 45 (1978).

[19] N. Wada, P. J. Gaczi, and S. A. Solin, *J. Non-Cryst. Solids* **35-36**, 543 (1980).

[20] L. T. Ball, I. S. Falconer, D. R. McKenzie, and J. M. Smelt, *J. Appl. Phys.* **59**, 720 (1986).

[21] S. Aisenberg and R. Chabot, *J. Appl. Phys* **42**(7), 2953 (1971).

[22] H. R. Kaufman, *J. Vac. Sci. Technol.* **15**, 272 (1978).

[23] R. K. Srinandan, H. Wang, and J. W. Rabalais, *J. Vac. Sci. Technol.* **A6**(3), 1788 (1988).

[24] J. Ishikawa, Y. Takeiri, K. Ogawa, and T. Tagaki, *J. Appl. Phys.* **61**(7), 2509 (1987).

[25] E. A. Burgemeister, Thermal and optical measurements on vacancies in type II diamond, in *Diamond Conference*, page 23, 1980, England.

[26] Carter, *Ion Bombardment of Solids*, American Elsevier, New York, 1968.

[27] Selected Values of Chemical Thermodynamic Properties, Tech. Note 270-3, National Bureau of Standards, Washington D. C., 1968.

[28] A. R. Ubbelohde and R. A. Lewis, *Graphite and Its Crystal Compounds*, Clarendon Press, Oxford, 1960.

[29] R. C. Weast, editor, *Handbook of Chemistry and Physics*, CRC Press, Florida, 1974, 55th ed.

[30] C. Weissmantel, K. Bewilogua, K. Breuer, D. Dietrich, U. Ebersbach, H. J. Erler, B. Rau, and G. Reisse, *Thin Solid Films* **96**(1), 31 (1982).

[31] C. Weissmantel, *Thin Solid Films* **92**, 55.

[32] A. Saeed, P. H. Gaskell, and D. A. Jefferson, *Phil. Mag. B* **66**(2), 171 (1992).

[33] P. H. Gaskell, A. Saeed, and D. R. McKenzie, *Phil. Mag. B* **66**(2), 155 (1992).

[34] C. A. Davis, V. S. Veerasamy, G. A. J. Amaratunga, and W. I. Milne, *Phil. Mag. B* **69**(6), 1121 (1994).

[35] J. W. Zou, K. Reichelt, K. Schmidt, and B. Dischler, *J. Appl. Phys* **65**(10), 3914 (1989).

[36] E. T. Prince and M. M. Romach, *J. Vac. Sci. and Technol. A* **3**(3), 694 (1985).

[37] J. Tersoff, *Phys. Rev. B* **44**(21), 12039 (1991).

[38] K. Rowher, *J. Non-Cryst. Solids* **137-138**, 843 (1991).

[39] X. Jiang, *Phys. Rev. B* **43**(3), 2372 (1991).

[40] D. A. Anderson, *Phil. Mag.* **35**(1), 17 (1977).

[41] C. Jager, J. Gottwald, and H. W. Spiess, *Physical Review B* **50**(2), 846 (1994).

[42] C. Wild and P. Koidl, *Appl. Phys. Lett.* **51**(19), 1506 (1987).

[43] B. Dischler, page 189, les Editions de Physique, 1987.

[44] M. A. Petrich, *Materials Science Forum* **52**, 377 (1989).

[45] P. J. R. Honeybone, R. J. Newport, J. K. Walters, W. S. Howells, and J. Tomkinson, *Physical Review B* **50**(2), 839 (1994).

[46] A. H. McIllraith, *J. Vac. Sci. Technol.* **9**(1), 209 (1971).

[47] J. Franks, *J. Vac. Sci. Technol. A* **7**(3), 2307 (1989).

[48] J. Franks, *J. Vac. Sci. Technol.* **16**(2), 181 (1979).

[49] V. F. Sears, *Thermal-Neutron Scattering Lengths and Cross Sections For Condensed-Matter Research*, Atomic Energy of Canada Ltd, June 1984.

[50] F. Mandl, *Statistical Physics*, Wiley, London, 1971.

[51] G. L. Squires, *Introduction to the Theory of Thermal Neutron Scattering*, Cambridge University Press, 1978.

[52] W. Marshall and S. W. Lovesey, *Theory of Thermal Neutron Scattering*, Clarendon Press, Oxford, 1971.

[53] P. A. Egelstaff, *Thermal Neutron Scattering*, Academic Press, 1965.

[54] G. E. Bacon, *Neutron Diffraction*, Clarendon Press, Oxford, 1962.

[55] S. W. Lovesey, *Theory of Neutron Scattering from Condensed Matter*, Clarendon Press, 1984.

[56] L. V. Hove, *Phys. Rev.* **95**, 249 (1954).

[57] J. P. Hansen, *Theory of Simple Liquids*, Academic Press, London, 1976.

[58] G. Placzek, *Phys. Rev.* **86**, 377 (1952).

[59] T. E. Faber and J. M. Ziman, *Phil. Mag.* **11**, 153 (1965).

[60] B. E. Warren, *X-ray Diffraction*, Addison-Wesley, Reading, 1969.

[61] B. K. Agarwal, *X-ray Spectroscopy*, Springer-Verlag, New York, 1979.

[62] M. Magini, *X-ray Diffraction of Ion Aqueous Solutions: Hydration and Complex Formation*, CRC Press, 1988.

[63] P. A. Egelstaff, *An Introduction to the Liquid State*, Clarendon Press, Oxford, 1992.

[64] M. C. Fairbanks, A. N. North, and R. J. Newport, editors, *Neutron and X-ray Scattering: Complimentary Techniques*, IOP Publishing, Bristol, 1990.

[65] N. Cusack, *The Physics of Disordered Matter: an introduction*, IOP Publishing, 1987.

[66] C. H. MacGillavry and G. D. Rieck, editors, *International Tables of X-ray Crystallography*, 1952-74.

[67] R. F. Stewart, E. R. Davidson, and W. T. Simpson, *Journal of Chem. Physics* **42**(9), 3175 (1965).

[68] J. H. Hubbell, *Journal of Physical and Chemical Reference Data* **4**(3), 471 (1975).

[69] The SRS, SERC Daresbury Laboratory, Warrington WA4 4AD, 1991, Guide to Facilities.

[70] O. Glatter and O.Kratky, *Small Angle X-ray Scattering*, London, 1982.

[71] G. F. Knoll, *Radiation Dtection and Measurement*, Wiley, New York, 1989.

[72] G. Bushnellwye, Private Communication, 1993.

[73] B. E. Warren and G. Mavel, *Rev. of Scientific Inst.* **36**(2), 196 (1962).

[74] G. Bushnellwye, J. L. Finney, J. Turner, D. W. Huxley, and J. C. Dore, *Rev. of Sci. Instr. and Meth.* **63**(1), 1153 (1992).

[75] G. Margaritondo, *Introduction to Synchrotron Radiation*, Open University Press, Oxford, 1988.

[76] H. H. Paalman and C. J. Pings, *J. Appl. Phys.* **33**(8), 2635 (1962).

[77] W. H. Press, B. P. Flannery, S. A. Teukolsky, and W. T. Vetterling, *Numerical Recipes*, Cambridge University Press, 1986.

[78] C. W. Dwiggins Jr and D. A. Park, *Acta Cryst. A* **27**, 264 (1971).

[79] G. H. Vineyard, *Phys. Rev.* **96**(1), 93 (1954).

[80] A. Soper, W. Howells, and A. Hannon, *ATLAS-Analysis of Time-of-Flight Diffraction Data from Liquid and Amorphous Samples*, Rutherford Appleton Laboratory, RAL-89-046, 1989.

[81] C. G. Windsor, *Pulsed Neutron Scattering*, Academic Press, London, 1981.

[82] User Guide To Experimental Facilities, Technical report, Rutherford Appleton Laboratory, Chilton, Didcot, Oxon OX11 0QX, 1992.

[83] K. B. Winterbon, *Nucl. Inst. and Methods* **16**(4-5), 310 (1986).

[84] I. A. Blech and B. L. Averbach, *Phys. Rev. A* **137**(4), 1113 (1965).

[85] A. K. Soper and P. A. Egelstaff, *Nucl. Inst. and Meth.* **178**, 415 (1980).

[86] B. H. Meardon, A Monte Carlo Computer Program for Neutron *Elastic Scattering* Simulation, 1973, Rutherford Appleton Laboratory.

[87] J. G. Powles, *Molecular Physics* **26**(6), 1325 (1973).

[88] A. K. Soper, Private Communication, 1993.

[89] M. R. Spielgel, *Mathematical Handbook of Formulas and Tables*, McGraw-Hill, 1968.

[90] W. P. G. Lim and C. Ortiz, *J. Mater. Res.* **2**(4), 471 (1987).

[91] H. Dosch, *Phys. Rev. B* **35**(5), 2137 (1987).

[92] A. H. Compton, *Phil. Mag.* **45**, 1121 (1922).

[93] G. H. Vineyard, *Phys. Rev. B* **26**(8), 4146 (1982).

[94] W. C. Marra, P. Eisenberger, and A. Y. Cho, *J. Appl. Phys.* **50**(11), 6927 (1979).

[95] R. Cernik and M. Hart, *Nucl. Inst. Meth. A* **281**, 403 (1989).

[96] G. Arfken, *Mathematical Methods for Physicists*, Academic Press, 1970.

[97] E. Lorch, *J. Phys. C* **2**, 229 (1969).

[98] M. L. Boas, *Mathematical Methods in the Physical Sciences*, Wiley,New York, 1983.

[99] D. F. R. Mildner and J. M. Carpenter, *J. Non-Cryst. Solids* **47**, 391 (1982).

[100] B. T. Boiko, L. S. Palantik, and A. S. Deveryanchenki, *Sov. Phys. Dokl.* **13**, 237 (1968).

[101] S. R. Elliott, *Nature* **354**, 445 (1991).

[102] F. Li and J. S. Lannin, *Phys. Rev. Lett* **65**(15), 1905 (1990).

[103] J. Robertson, *Surface and Coatings Technology* **50**(3), 185 (1991).

[104] P. J. R. Honeybone, R. J. Newport, W. S. Howells, J. Tomkinson, S. B. Bennington, and P. J. Revell, *Chem. Phys. Lett.* **180**(3), 145 (1991).

[105] R. C. Weast, editor, *CRC Handbook of Chemistry and Physics*, CRC Press, 1988.

[106] A. Bubenzer, B. Dischler, G. Brandt, and P. Koidl, *J. Appl. Phys.* **54**, 4590 (1983).

[107] F. Demichelis, M. Fanciulli, G. Kaniadakis, A. Tagliaferro, E. Tresso, P. Rava, and E. Giamello, *J. Non-Cryst. Solids* **101**(2-3), 179 (1988).

[108] M. Simpson, *New Scientist* (1988).

[109] D. W. Huxley, *Diffraction Studies of Amorphous Materials*, PhD thesis, Univ. of Kent, 1990.

[110] S. Fahy, S. G. Louie, and M. L. Cohen, *Phys. Rev. B* **34**(2), 1191.

[111] J. Franks, Private Communication, 1993.

[112] J. S. Rigden, Private Communication, 1994.